Nonlinear optical responses of targeted phthalocyanines when conjugated with nanomaterials or fabricated into polymer thin films

A thesis submitted in fulfilment of the requirement for

the degree of

DOCTOR OF PHILOSOPHY

Of

RHODES UNIVERSITY

By

Njemuwa Nwaji Njoku

September 2018

Dedication

Dedicated to

My dear mother, late Mrs Janeth Nwankwo Nwaji whose transition occur at the beginning of this journey.

My lovely wife

Mrs Chidinma Nwaji

My sons

Kamsiyochukwu and Sopuluchukwu

and

my daughter

Zikoranibuchi

Acknowledgements

ABSTRACT

A number of zinc, gallium and indium metallophthalocyanines (MPcs) with diverse substituents have been synthesized and characterized using various characterization tools such as proton nuclear magnetic resonance (^{1}HNMR), matrix assisted laser desorption time of flight (MALDI-TOF) mass spectrometry, Fourier-transformed infra-red (FT-IR), Ultraviolet-visible (Uv-vis) spectrophotometry, magnetic circular dichroism and CHNS elemental analysis. The time dependent density functional theory was employed to probe the origin of spectroscopic information in these complexes. Complexes with gallium and indium as central metal showed higher triplet quantum yield compared to the zinc derivatives. Some of the MPcs were covalently linked to nanomaterials such as CdTe, CdTeSe, CdTeSe/ZnO, graphene quantum dots (GQDs) as well as metallic gold (AuNPs) and silver (AgNPs) nanoparticles. Others were either surface assembled onto AuNPs and AgNPs or embedded into polystyrene as polymer source. The phthalocyanine-nanomaterial composites (Pc-NMCs) were characterized with FT-IR, UV-visible spectrophotometry, transmission electron microscopy (TEM), dynamic light scattering (DLS), Raman spectroscopy, X-ray photoelectron spectroscopy (XPS) and X-ray diffractometry (XRD). The thickness of the thin films was determined by utilization of the knife edge attachment of the A Bruker D8 Discover X-ray diffraction.

The optical limiting properties (using the open-aperture Z-scan technique) of the MPcs and the Pc-NMCs were investigated. The investigated MPcs complexes generally showed good optical limiting properties.

The nonlinear optical response of the MPcs were improved in the presence of nanomaterials such as the semiconductor quantum dots (SQDs), graphene quantum dots (GQDs) as well as metallic AuNPs and AgNPs with MPc-QDs showing the best

Abstract

optical limiting behavior. The optical limiting properties of the MPcs were greatly enhanced in the presence of polymer thin films.

Table of contents

Table of contents

Table of contents

Table of contents

List of Abbreviations

Abbreviations

Abs	**-**	**absorbance**
DFT	**-**	**density functional theory**
DBU	**-**	**1,8-diazabicyclo-[5.4.0]-undec-7-ene**
DCM	**-**	**dichloromethane**
DCC	**-**	**dicyclohexycarbodimide**
DMAP	**-**	**dimethylaminopyridine**
DMF	**-**	**dimethyl formamide**
DMSO	**-**	**dimethyl sulfoxide**
DPBF	**-**	**1,3-Diphenylisobenzofuran**
ESA	**-**	**excited state absorption**
FRET	**-**	**Förster resonance energy transfer**
FT-IR	**-**	**Fourier transform infra-red**
FWHM	**-**	**full width at half-maximum**
GSH	**-**	**Glutathione**
HOMO	**-**	**highest occupied molecular orbital**
IC	**-**	**internal conversion**
IUPAC	**-**	**international union of pure and applied chemistry**
ISC	**-**	**intersystem crossing**
LUMO	**-**	**lowest unoccupied molecular orbital**
MALDI	**-**	**matrix-assisted laser desorption ionization**
MPcs	**-**	**metallophthalocyanines**
NIR	**-**	**near infra-red**
Nd-YAG	**-**	**neodymium-doped yttrium aluminium garnet**
NLA	**-**	**nonlinear absorption**

List of Abbreviations

NLO	-	**nonlinear optical**
NPs	-	**nanoparticles**
NLR	-	**nonlinear refraction**
NLS	-	**nonlinear scattering**
ODE	-	**ordinary differential equations**
OL	-	**optical limiting**
PACT	-	**photodynamic antimicrobial chemotherapy**
Pcs	-	**phthalocyanines**
PDT	-	**photodynamic therapy**
PL	-	**photoluminescent**
^{1}H-NMR	-	**proton nuclear magnetic resonance**
QDs	-	**quantum dots**
RSA	-	**reverse saturable absorption**
SA	-	**saturable absorption**
TCSPC	-	**time correlated single photon counting**
TEM	-	**Transmission Electron Microscope**
THF	-	**tetrahydrofuran**
TPA	-	**two photon absorptions**
TOF	-	**time-of-flight**
TEM	-	**transmission electron microscopy**
UV-vis	-	**ultraviolet visible**
VR	-	**vibrational relaxation**
XRD	-	**x-ray diffractions**

List of symbols

N_A	-	**Avogadro constant**
w_0	-	**beam waist**
ΔA_T	-	**change in absorbance in the triplet state**
B_{eff}	-	**effective nonlinear absorption coefficient**
L_{eff}	-	**effective path length**
Eff	-	**efficiency of energy transfer**
F_{sat}	-	**energy density of saturation**
δ_{exc}	-	**excited state absorption cross-section**
S_1	-	**first excited singlet**
T_1	-	**first excited triplet**
τ_F	-	**fluorescence lifetime**
Φ_F	-	**fluorescence quantum yield**
R_0	-	**Förster distance**
δ_0	-	**ground state absorption cross-section**
S_0	-	**ground singlet state**
ε_s	-	**ground state molar extinction coefficient**
I_0	-	**input irradiance**
Φ_{ic}	-	**internal conversion quantum yield**
τ_{isc}	-	**intersystem crossing time**
I_{lim}	-	**limiting threshold intensity**
α	-	**linear absorbance**
f	-	**Lorentz local field factor**
T_{Norm}	-	**normalized transmittance**
S_n	-	**nth excited singlet state**
T_n	-	**nth excited triplet state**

List of symbols

I_{00} - **on-focus peak input irradiance**

I_{out} - **output intensity**

J - **overlap integral**

L - **pathlength (thickness of sample holder)**

ϵ_0 - **permittivity of free space**

h - **Planck constant**

Z_0 - **Rayleigh length**

η - **refractive index**

z - **sample position**

δ_1 - **singlet state absorption cross-section**

γ - **second-order hyperpolarizability**

$I_m[\chi^{(3)}]$ - **third-order susceptibility**

δ_2 - **triplet state absorption cross-section**

τ_T - **triplet lifetime**

Φ_T - **triplet quantum yield**

ε_T - **triplet state molar extinction coefficient**

λ - **wavelength**

Chapter one: Introduction

1. Introduction

The design and development of materials which exhibit nonlinear optical (NLO) behavior (including optical limiting) is important in applications such as data storage, communications, and defense [**1–4**]. Optical limiters strongly attenuate high intense optical beam to a threshold level while maintaining linear transmittance at reduced intensity. These devices possess the ability to protect optical sensors including the human eyes from laser induced damage. Understanding the mechanisms of optical limiting is paramount in modulating the synthesis of new materials. Many and diverse materials has been investigated in the quest to develop efficient optical limiting materials. However, there has been no single material or combination of materials that satisfies the ideal material capable of protecting optical sensors from potential laser threat. Thus, it becomes of utmost important for further research toward developing materials with satisfactory optical limiting capacity.

The focus of this study is to design and develop materials with improved optical limiting properties using targeted phthalocyanine-based materials. To achieve this, diverse metallophthalocyanine (MPcs) were synthesized, characterized and tested for optical limiting application. The synthesized compounds were either linked to selected nanomaterial or embedded into polymer thin film to further improve the optical limiting properties. The nanomaterials employed include metallic nanoparticles (silver and gold), semiconductor quantum dots (SQDs) and carbon-based graphene quantum dots (GQDs).

1.1. METALLOPHTHALOCYANINES

1.1.1. Structure and applications

Phthalocyanines (Pcs) are planar aromatic tetrapyrrolic macrocycles possessing conjugated 18 π-electron system with four isoindoline units linked via nitrogen atom, [**5–8**] (**Scheme 1.1**)

More than 70 elements of the periodic table can be accommodated at the central cavity of phthalocyanine. The numbering of Pc ring is done following the International Union of Pure and Applied Chemistry (IUPAC) nomenclature of tetrapyrroles (**Scheme. 1.1**). The positions 1,4,8,11,15,18,22 and 25 within the structure of phthalocyanine are known as α or non-peripheral positions, while, 2,3,9,10,16,17,23 and 24 are known as β or peripheral positions. The optical and redox properties of phthalocyanine molecules can be altered via substitution with different functional groups on the periphery (α or β position). The wide range of applications of phthalocyanine is attributed to relative ease of architectural maneuvering on the structures, their chemical, thermal as well as photo-stability properties [**5,9,10**]. Pcs have been employed in many and diverse areas which include but not limited to catalysis [**11**], photodynamic therapy [**12**], nonlinear optics [**13**], electrochemical and optical sensors [**14,15**], thermal writing displays [**16**] and solar cells [**17**].

1.1.2. Synthesis of symmetric phthalocyanines

The synthesis of peripheral, non-peripheral and ball-type tetrasubstituted phthalocyanines can be achieved using different synthetic routes as indicated in **Schemes 1.1** and **1.2.**

phthalic acid derivative

diiminoisoindoline derivative

phthalimide derivative

phthalonitrile

phthalic anhydride derivative

o-cyanobenzamide derivative

dibromobenzene derivative

Conditions of reactions

-appropriate solvents, e.g 1-pentanol, quinoline nitrobenzene and others.
-reflux
-inert atmosphere (argon or nitrogen gas)
-presence or absence of metal salts
-appropriate catalysts, e.g 1, 8-diazobicyclo-[5.4.0]-undec-7-ene (DBU) urea.

R = substituent of choice (the choice of substituent is generally determined by intended application)
R = H for unstituted phthalocyanines
M = H_2 for metal free phthalocyanine
M = metal ion for metallated phthalocyanine
R on position 4 gives peripheral tetrasubstituted Pc
R on position 3 gives non-peripheral tetrasubstituted Pc

Scheme 1.1: General synthesis of peripherally or non-peripherally tetrasubstituted phthalocyanines.

The common synthetic route in the lab involves the use of substituted phthalic acid derivatives as starting materials (**Scheme 1.1**). The laboratory synthesis of α and β substituted tetrasubstituted Pcs requires the use of 4-nitrophthalonitrile for the latter, and 3-nitrophthalonitrile for the former as the starting materials. These phthalonitrile can be modified to afford different types of substituted phthalocyanines.

The ball-type Pcs are a relatively new class of macrocycle in which two Pc monomers are cofacially arranged with four bridging substituents on the peripheral positions of the benzene rings and were first reported by Tomilova's group in 2002 [**18,19**].

Ball-type phthalocyanine

Conditions of reaction

i: -appropriate solvent, e.g Dimethylformamide (DMF), Dimethylsofoxide (DMSO)
  - Na_2CO_3 as base
  - sometimes with heating at 50-100^{0}C
ii: - appropriate solvent, e.g 1-petanol, hexanol etc
  - catalyst, e.g DBU, urea
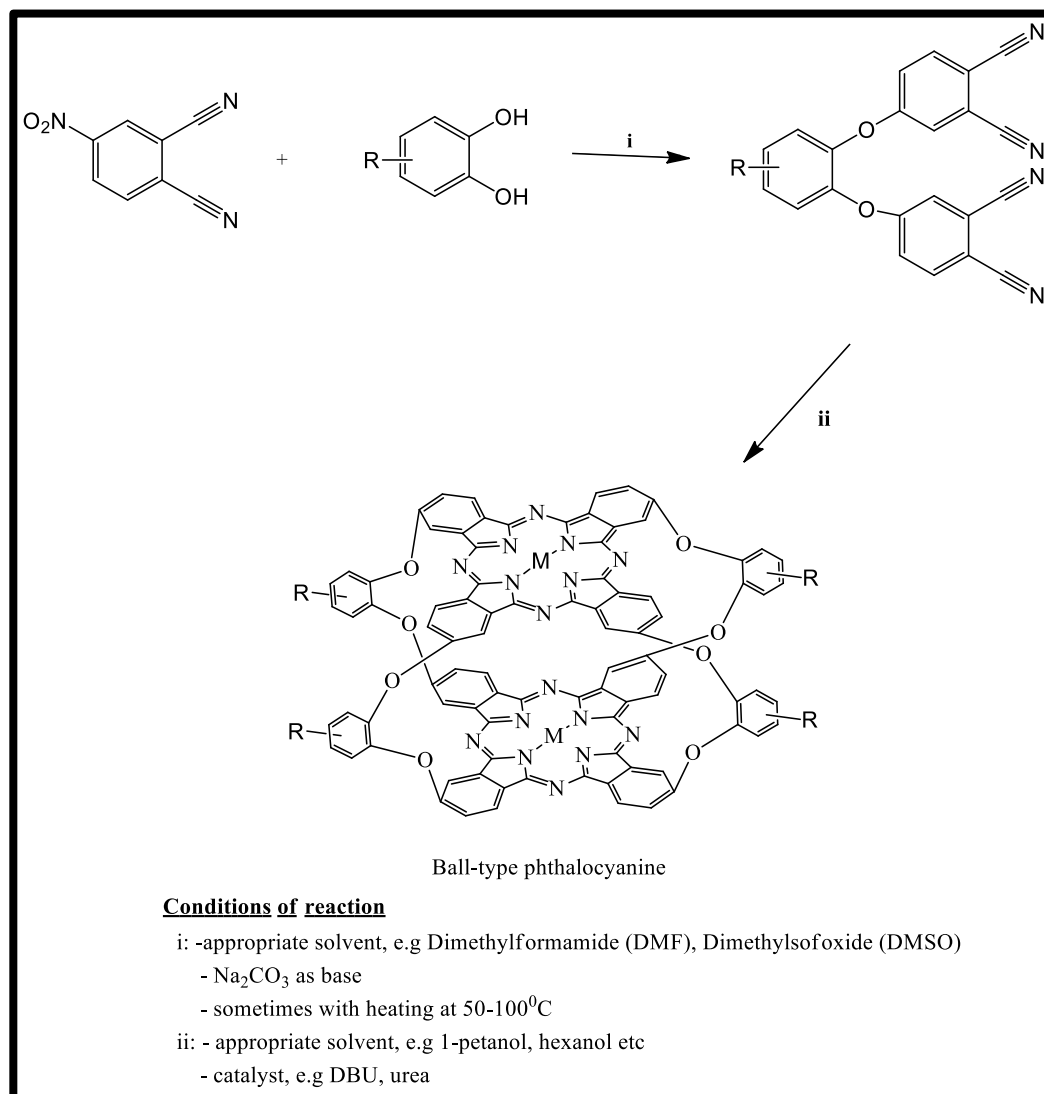
Scheme 1.2: Synthetic route for ball-type phthalocyanines

The binuclear ball-type phthalocyanines are usually prepared by tetracyclization of the precursor bisphthalonitriles using appropriate reaction conditions (**Scheme 1.2**). The precursor phthalonitriles are generally synthesized through the reaction of diols with excess of 4-nitrophthalonitrile using dimethylformamide (DMF) or dimethylsofoxide (DMSO) in the presence of K_2CO_3 as a base (**Scheme 1.2**) at 25-100^0 C and time duration of 60-96 h [**18,19**]. Worthy of note is that all the ball-type phthalocyanine reported in literature were bridged by substituted benzene rings.

A series of ball-type phthalocyanines were synthesized and studied in this work for optical limiting applications. The non-benzene substituted bridging linker ball-type Pcs having long alkyl chain as the linker were also synthesized in this work for the first time. The use of ball-type Pcs as nonlinear optical materials is relatively new with only one literature report showing the optical limiting properties of this class of macrocycles [**20**]. The ball-type Pcs could be potential optical limiting materials due to possession of enhanced π-conjugated system compared to corresponding monomers, which is the one generally accepted property of good optical limiting materials.

It is pertinent to note that the practical applications of symmetrical Pcs is sometimes limited where specific binding or coordination with other molecules are needed due inherent uniformity of this macrocycles [**21**]. There has been a rising research interest in the synthesis of asymmetric phthalocyanine with a single anchor moiety fixed at a specific position because of enhanced physicochemical properties with valuable applications in material science, optical signal detection and optical limiting [**22–24**]. The asymmetric A₃B-type Pc possess three identical (A) and one different (B) isoindole unit. Though many synthetic routes such as the statistical mixed condensation [**21,25,26**], subphthalocyanine ring expansion route [**21,27,28**], and polymeric support based route [**21,29,30**] have been reported, the statistical condensation method (**Scheme 1.3**) remains the most widely used due to its

simplicity. The individual phthalonitrile are usually combined in ratio of 3:1 or 9:1 (A: B) which usually affords a mixture of six compounds but favors the formation of asymmetrical Pcs (**Scheme 1.3**).

The different reactivities of the substituent group sometimes leads to the use of a combination ratio of 10:1 or even 40:1 (A:B) of the corresponding phthalonitrile [**31**]. Although A$_3$B-type Pcs have been widely prepared using this method, it is often tedious due to the difficulty usually encountered during separation and purification process.
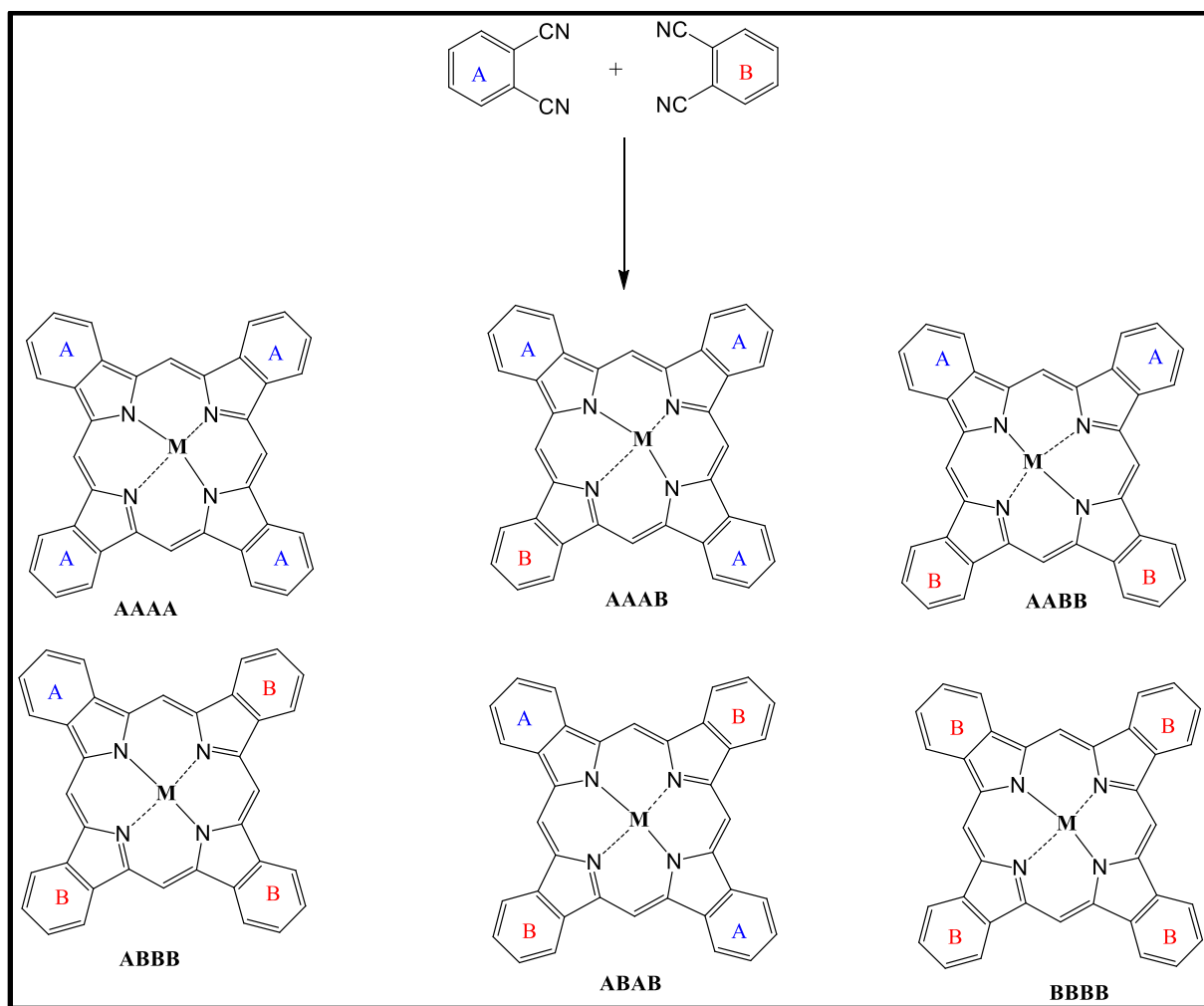
Scheme 1.3: Synthetic route for asymmetrical phthalocyanines
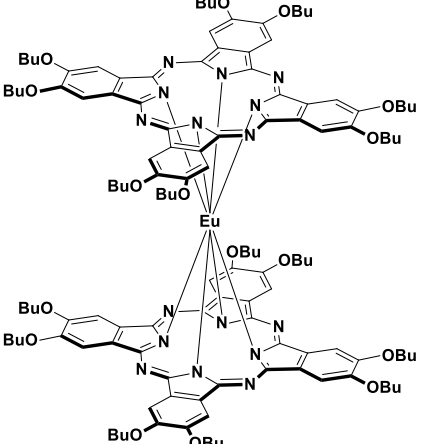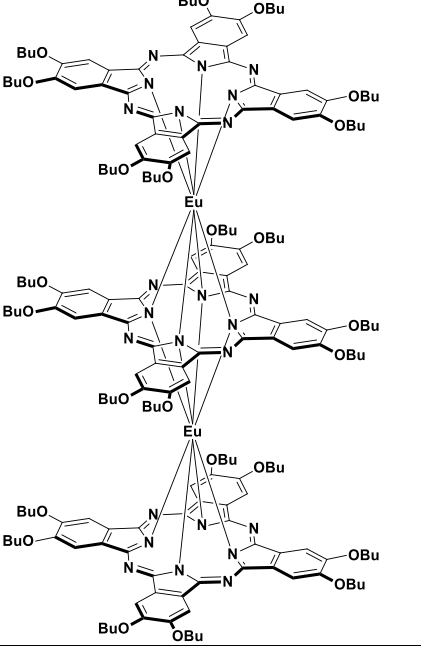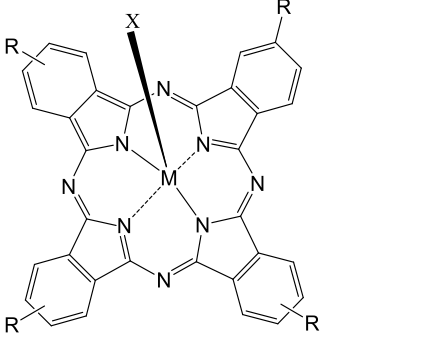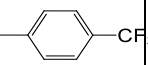
1.1.3.Nonlinear optical applications of phthalocyanines
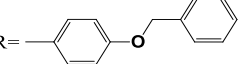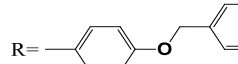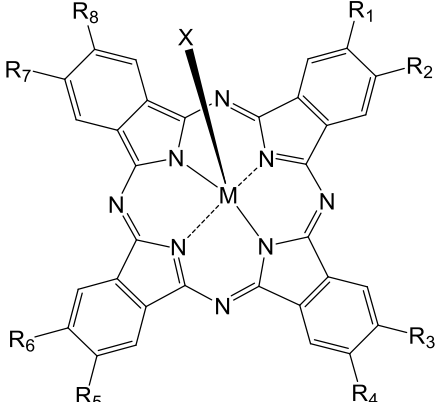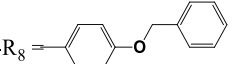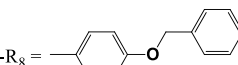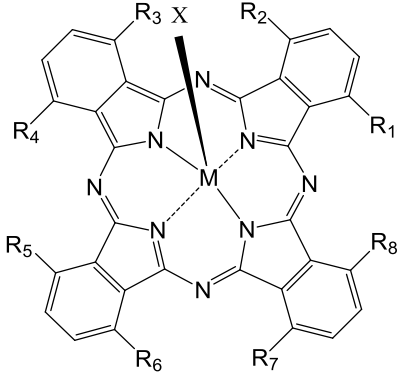
The possession of highly delocalized π-electron systems confer strong optical nonlinearities in organic molecules [**32**–**36**] and phthalocyanine with their extended two dimensional 18 π-electron system fulfil the requirement. Research in nonlinear optical properties of Pcs was triggered by the first report of optical limiting response in chloroaluminium phthalocyanine (ClAlPc) [**37**]. **Table 1.1** gives an overview of many and diverse phthalocyanine molecules that have been characterized for nonlinear optics/optical limiting applications [**13**,**38**-**58**] and the parameters are summarized in **Table 1.2**
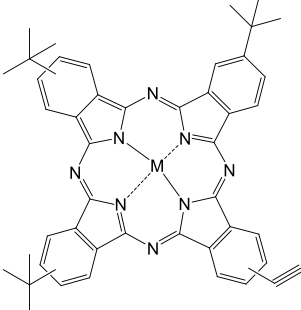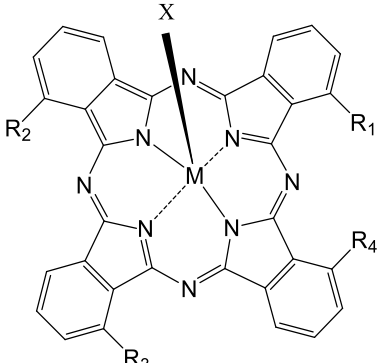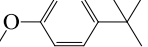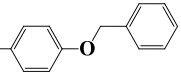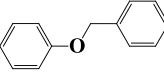
Attempts have been made to provide the experimental conditions employed during NLO measurement and intrinsic properties such as Q band absorption maxima and linear absorption coefficient for the Pc molecules presented in **Table 1.2.**
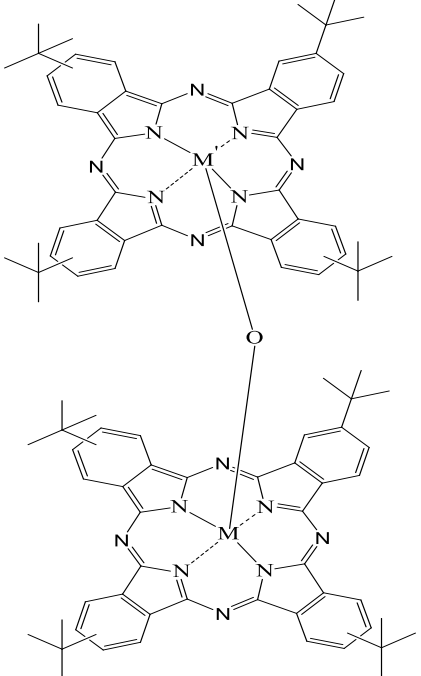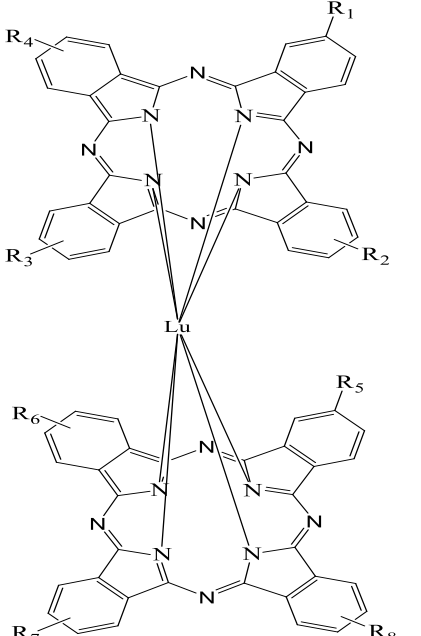
This information become vital since the NLO/OL performance of a Pc molecule depends strongly on the electronic properties of the molecule, and the experimental conditions under which they are studied.
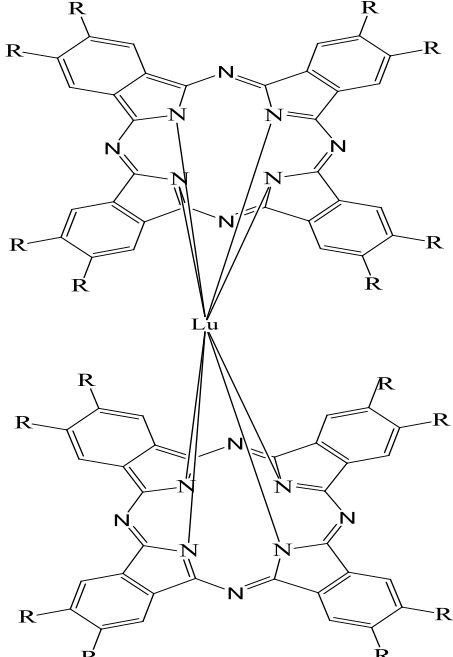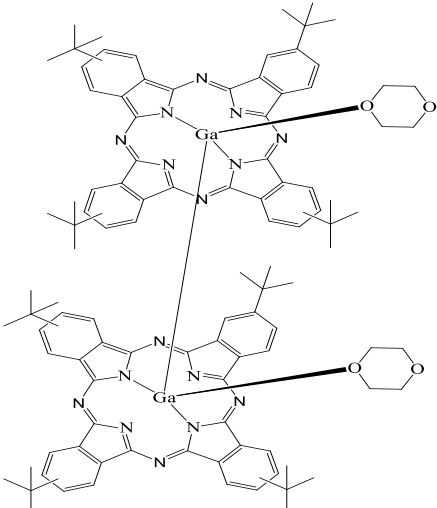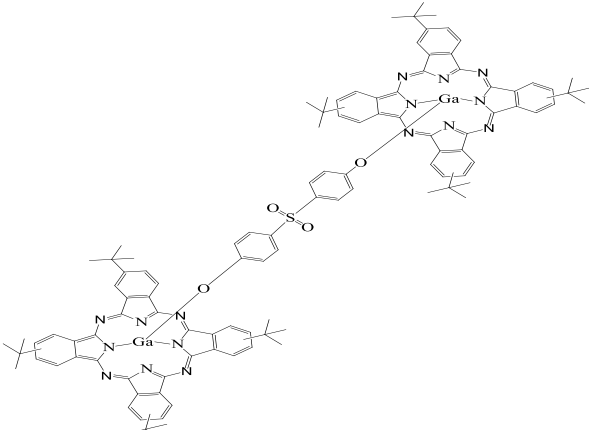
Table 1.1. Selected Phthalocyanine molecules that have been characterized for optical limiting application

Structure	No	Ref
	I BU =	[51]
	II BU =	[51]
	III: M = Ga, R = -C(CH$_3$)$_3$, X = CF$_3$ IV: M = Ga, R = -C(CH$_3$)$_3$, X = Cl V: M = In, R = -C(CH$_3$)$_3$, X = Cl VI: M = Zn, R = -C(CH$_3$)$_3$, X= nil	[38-42, 50]

	VII: M=Ga, R= [structure: 4-(benzyloxy)phenyl] X=Cl	
	VIII: M=In, R= [structure: 4-(benzyloxy)phenyl] X=Cl	
	IX: M = Zn, R_1 - R_8 = $-OSO_2C_3H_7$, X = nil	**[38-42,44, 47-49]**
	X: M = Ni, R_1 - R_8 = $-OSO_2C_3H_7$, X = nil	
	XI: M = Co, R_1 - R_8 = $-OSO_2C_3H_7$, X = nil	
	XII: M = Co, R_1 - R_8 = $-OSO_2C_8H_{17}$, X = nil	
	XIII: M = Zn, R_1 – R_6 = $-OSO_2C_3H_7$, R_7 = I, R_8 = H, X = nil	
	XIV: M = Co, R_1 – R_6 = $-OSO_2C_3H_7$, R_7 = I, R_8 = H, X = nil	
	XV: M = Co, R_1 – R_6 = $-OSO_2C_8H_{17}$, R_7 = I, R_8 = H, X = nil	
	XVI: M = Co, R_1 – R_6 = $-OC_4H_9$, R_7 = $-C\equiv CH$, R_8 = H, X = nil	
	XVII: M=Ga, R_1-R_8 = [structure: 4-(benzyloxy)phenyl] X=Cl	
	XVIII: M=In, R_1-R_8 = [structure: 4-(benzyloxy)phenyl] X=Cl	
	XIX: M = Pd, R_1 - R_8 = $-C_6H_{13}$, X = nil	**[13, 38, 43, 45]**
	XX: M = In, R_1 - R_8 = $-C_6H_{13}$, X = Cl	
	XXI: M = Zn, R_1 - R_8 = $-C_6H_{13}$, X = nil	
	XXII: M = Pb, R_1 - R_8 = $-C_6H_{13}$, X = nil	
	XXIII: M = Ni, R_1 - R_8 = $-C_6H_{13}$, X = nil	
	XXIV: M = Co, R_1 - R_8 = $-C_{10}H_{21}$, X = nil	
	XXV: M = Ni, R_1 - R_8 = $-C_{10}H_{21}$, X = nil	

	XXVI: M = Zn, R_1 - R_8 = -$C_{10}H_{21}$, X = nil **XXVII:** M = Zn, R_1 - R_8 = -iso-C_5H_{11}, X = nil **XXVIII:** M = Cu, R_1 - R_8 = -iso-C_5H_{11}, X = nil **XXIX:** M = Co, R_1 - R_8 = -iso-C_5H_{11}, X = nil	
	XXX: M = Zn **XXXI:** M = Ga	**[38, 46]**
	XXXII: M=In, R_1-R_4 = , X=Cl **XXXIII:** M=Ga, R_1-R_4 = X=Cl **XXXIV:** M=In, R_1-R_4 = X=Cl	**[40, 52]**

	XXXV: M = M'= Ga **XXXVI:** M = M'= In **XXXVII:** M =Ga, M'= In	**[53]**
	XXXVIII: R_1-R_4 = X=Cl **XXXIX:** $R_1 - R_4$ = -C(CH$_3$)$_3$, $R_5 - R_8$= H	**[54, 55]**

	XL: R =	**[56]**
	XLI	**[57]**
	XLII	**[52]**

	XLIII: M =Zn, n=1 **XLIV:** M =Co, n=1 **XLV:** M =Zn, n=2 **XLVI:** M =Co, n=2	**[58]**
	 XLVII: M= Zn, R= CH$_3$, R$_1$ =	**[20]**

Table 1.2: Nonlinear optical data of phthalocyanine molecules that have been reported in literature as potential material for optical limiting application. The laser excitations wavelength was mostly at 532 nm and nanosecond pulse duration unless otherwise stated. All the data taken were those obtained with the Z scan technique.

Pc	Solv.	Conc. (g L^{-1})	λ_{max} Q band (nm)	α_0 (cm^{-1})	β_{eff} (cm/GW)	$I_m[\chi^3]$ × 10^{-11} (esu)	Y ×10^{-33} (esu)	k (δ_{ex}/δ_0)	F_{sat} (J.cm^{-1})
I	DCM	2.5^a	640	NA	10.9	0.93	NA	NA	NA
II	DCM	2.5^a	685	NA	21.0	0.18	NA	NA	NA
III	T	0.5	696	0.91	29.0 ±5.0	1.1 ±0.2	8.7 ±1.7	13.6 ±0.4	8.4 ±0.4
IV	T	0.5	695	1.10	32.0 ±6.0	1.2 ±0.2	8.4 ±1.6	13.5 ±0.4	27.0 ±1.0
V	T	0.5	697	0.53	44.0 ±9.0	1.6 ±0.3	13.0 ±2.0	27.4 ±0.6	24.0 ±0.8
VI	C	0.4	NA	NA	420.0	7.1	NA	NA	NA
VII	C	1.0	699	0.48	62.0 ±12.0	NA	NA	22.8 ±0.8	NA
VIII	C	1.0	701	0.30	59.0 ±11.0	NA	NA	23.1 ±0.8	NA
IX	T	1.0	685	2.11	14.0 ±3.0	0.64 ±0.1	3.2 ±0.6	5.4 ±0.1	17.6 ±0.7
X	T	1.0	675	1.39	7.4 ±1.4	0.28 ±0.05	1.6 ±0.3	8.7 ±0.2	16.5 ±0.8
XI	C	1.0	676	1.86	13.0 ±3.0	0.45 ±0.09	3.0 ±0.6	8.1 ±0.2	27.0 ±1.0
XII	T	1.0	676	2.20	0.073 ±0.014	0.0028 ±0.0005	0.023 ±0.004	1.1 ±0.2	40.0 ±70
XIII	T	1.0	704	1.28	15.0 ±3.0	0.57 ±0.11	3.2 ±0.6	13.4 ±0.3	18.1 ±0.6
XIV	T	1.0	694	1.17	0.58 ±3.0	0.022 ±0.004	0.12 ±0.02	2.4 ±0.4	35.0 ±19
XV	T	1.0	694	2.21	0.23 ±0.04	0.0085 ±0.0017	0.062 ±0.012	1.7 ±1.2	160 ±100
XVI	T	0.5	677	1.80	7.2 ± 1.4	0.27 ±0.05	2.3 ±0.4	4.9 ±0.3	32.0 ±3

Pc	Solv.	Conc. (g L^{-1})	λ_{max} Q band (nm)	α_0 (cm^{-1})	β_{eff} (cm/GW)	$I_m[\chi^3]$ × 10^{-11} (esu)	Y ×10^{-33} (esu)	k (δ_{ex}/δ_0)	F_{sat} (J.cm^{-1})
XVII	C	1.0	700	0.86	190.0 ± 50	NA	NA	18.1 ±1.1	3.4 ±0.8
XVIII	C	1.0	702	0.62	130.0 ± 40	NA	NA	20.0 ±0.9	3.2 ±0.7
XIX	T	1.0	687	2.60	96.0 ± 19.0	3.6 ±0.7	21.0 ±4.0	5.9 ±0.1	2.1 ±0.1
XX	T	1.0	730	0.93	32.0 ± 6.0	1.2 ±0.2	7.3 ±1.4	16.1 ±0.3	10.1 ±0.5
XXI	T	1.0	705	1.17	40.0 ± 8.0	1.5 ±0.3	8.6 ±1.7	11.4 ±0.3	7.1 ±0.3
XXII	T	1.0	741	0.83	29.0 ± 6.0	1.1 ±0.2	7.0 ±1.4	16.1 ±0.3	9.8 ±0.3
XXIII	T	1.0	702	1.05	1.6 ± 0.3	0.059 ±0.011	0.34 ±0.06	2.4 ±0.2	18.0 ±3.0
XXIV	T	1.0	700	0.83	0.16 ± 0.03	0.0059 ±0.0011	0.45 ±0.009	2.2 ±0.7	95 ±70
XXV	T	1.0	702	0.94	1.5 ± 0.3	0.055 ±0.011	0.42 ±0.08	2.1 ±0.1	13.3 ±2.0
XXVI	T	1.0	705	1.17	24.0 ± 4.0	0.91 ±0.18	6.9 ±1.3	11.7 ±0.3	13.6 ±0.5
XXVII	T	1.0	703	1.05	40.0 ± 8.0	1.5 ±0.3	7.9 ±1.5	12.2 ±0.3	6.6 ±0.2
XXVIII	T	1.0	705	1.63	64.0 ± 10.0	2.4 ±0.4	13.0 ±2.0	8.8 ±0.1	4.6 ±0.1
XXIX	T	1.0	696	2.74	0.85 ± 0.17	0.032 ±0.006	0.17 ±0.03	0.85 ±0.17	170.6 ±190
XXX	T	0.5	684	1.95	35.0 ± 7.0	1.3 ±0.2	8.3 ±1.6	8.9 ±0.3	13.9 ±0.7
XXXI	T	0.5	673	1.76	1.4 ± 0.3	0.051 ±0.01	0.32 ±0.06	3.3 ±0.8	76 ±30
XXXII	D	NA	714	NA	NA	4.37	1020	NA	NA
XXXIII	C	1.0	726	0.22	36.0 ± 7.0	NA	NA	23.5 ±0.9	2.6 ±0.6
XXXIV	C	1.0	728	0.18	41.0 ± 8.0	NA	NA	25.7 ±0.8	2.6 ±0.6
XXXV	T	0.5	693	1.60	NA	1.3 ±0.2	0.18 ±0.03	11.3 ±1.0	13.5 ±1.0

Pc	Solv.	Conc. (g L⁻¹)	λmax Q band (nm)	α₀ (cm⁻¹)	βeff (cm/GW)	Im[χ³] × 10⁻¹¹ (esu)	Y ×10⁻³³ (esu)	k (δex/δ₀)	Fsat (J.cm⁻¹)
XXXVI	T	0.5	697	1.13	NA	1.5 ±0.3	0.24 ±0.04	12.4 ±0.3	7.6 ±0.3
	T	0.5	696	1.02	NA	1.1 ±0.2	0.15 ±0.03	10.0 ±0.2	14.6 ±0.6
XXXVIII[b]	DF	3.4 m	696	NA	NA	0.42	0.0000011	NA	NA
XXXIX[b]	C	9.6 m	NA	NA	NA	NA	2.79	1.44	NA
XL[b]	DF	2.7 m	674	NA	NA	0.027	0.0000071	NA	NA
XLI	T	0.5	NA	1.30	NA	1.3 ± 0.2	21.0 ± 3.0	10.4 ± 0.3	8.9 ± 0.4
XLII	T	0.5	692	3.13	NA	0.73 ± 0.1	11.3 ± 2.0	4.8 ± 0.6	7.9 ± 0.8
XLIII	T	0.5	678	1.06	12.0 ± 2.0	0.46 ± 0.08	5.8 ± 1.1	3.0 ± 0.1	1.9 ± 0.1
XLIV	T	0.5	677	1.22	5.6 ± 1.1	0.21 ± 0.04	2.6 ± 0.5	1.8 ± 0.1	1.3 ± 0.1
XLV	T	0.5	709	1.19	23.0 ± 5.0	0.87 ± 0.16	11.0 ± 2.0	5.4 ± 0.2	3.9 ± 0.3
XLVI	T	0.5	691	1.60	35.0 ± 7.0	1.3 ± 0.2	17.0 ± 3.0	11.8 ± 0.1	9.5 ± 0.1
XLVII[b]	C	1.0 m	697	1.51	14.0	NA	NA	16.2	10.1

T= toluene, C= chloroform, D= DMSO, DF= DMF.

[a]Absorbance at Q-band maxima

[b]m= 10⁻⁴ for sample **XXXVIII, XXXIX, XL** and **XLVII**.

NA= not available

NOTE: The respective equation employed to obtain the presented parameters in table 1.2 will be presented at the appropriate place in results and discussion section.

A critical look at **Table 1.1** shows that most of the studied complexes are symmetrical with only few asymmetrical and only one ball-type derivative. The use of ball-type Pcs as NLO materials is desired due to enhanced π-conjugated system as well as the ability to host two central metal within the cavity compared to the monomeric analogues. On the other hand, the use asymmetric Pcs for optical limiting applications is still in the minority due to problems associated with purification and isolation of desired products. The presence of permanent dipole moment in asymmetric Pcs offers greater advantage as optical limiting materials since this improves polarizability which is beneficial in nonlinear optical study [**13**,**23**].

Table 1.1 also showed that only few heavy metals such as gallium and indium have been employed for NLO, hence are employed in this work. The introduction of heavy atom has been known to induce spin orbit coupling which results in enhanced triplet population and consequently improved optical limiting properties of Pcs [**59**–**61**]. The effect of zinc, gallium and indium central metal ions on the optical limiting performance of diverse functional group substituted phthalocyanines were investigated in this thesis.

1.1.4.Phthalocyanines used in this work

Diverse targeted phthalocyanine complexes possessing different functional substituents were synthesized in this work (**Table 1.3**) for optical limiting applications. The numbering of the complexes considers the 9 different phthalonitrile precursors used for the synthesis of Pcs, which will be discussed in chapter 2. Thus, the numbering of the complexes will start from **10** (**Table 1.3**).
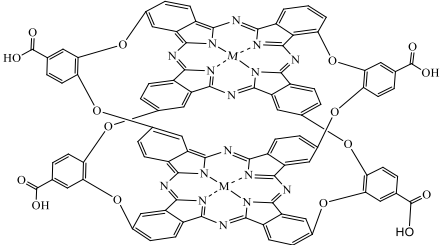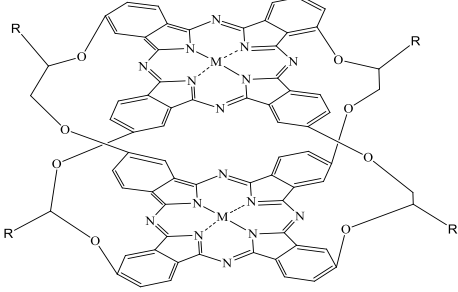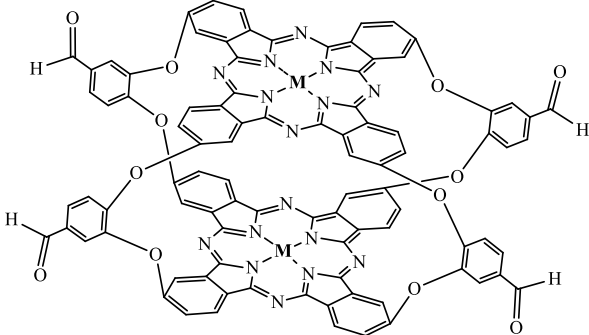
The complexes can be generally classified into three major groups: (1) the ball-type complexes **10**-**21**
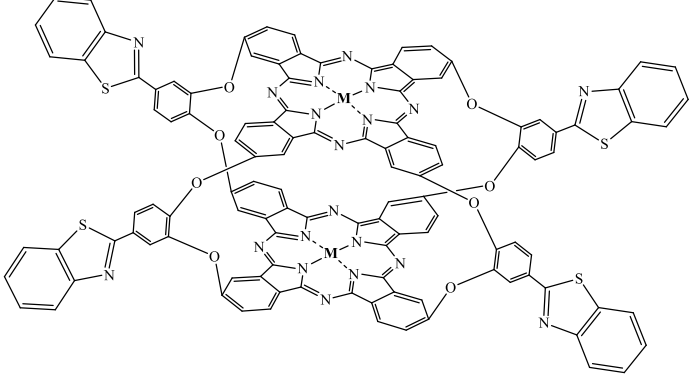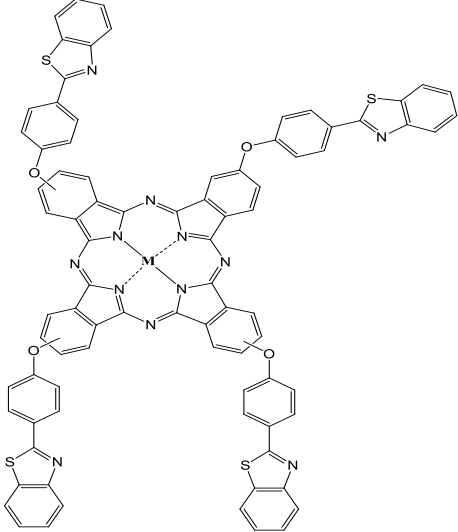
(2) the symmetric complexes **22**-**33** and (3) the asymmetric complexes **34**-**36**.
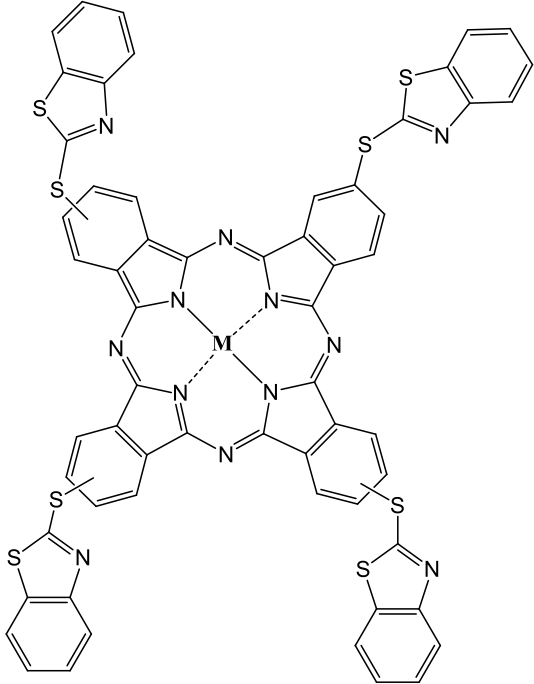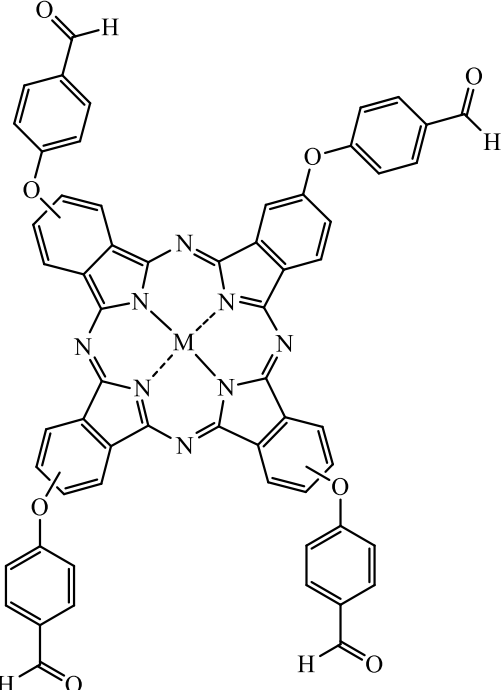
All the complexes in this work are reported for the first time apart from complex **22** and **25**, which has been previously reported [**62**,**63**]. The optical limiting properties of all the complexes are also investigated for the first time.
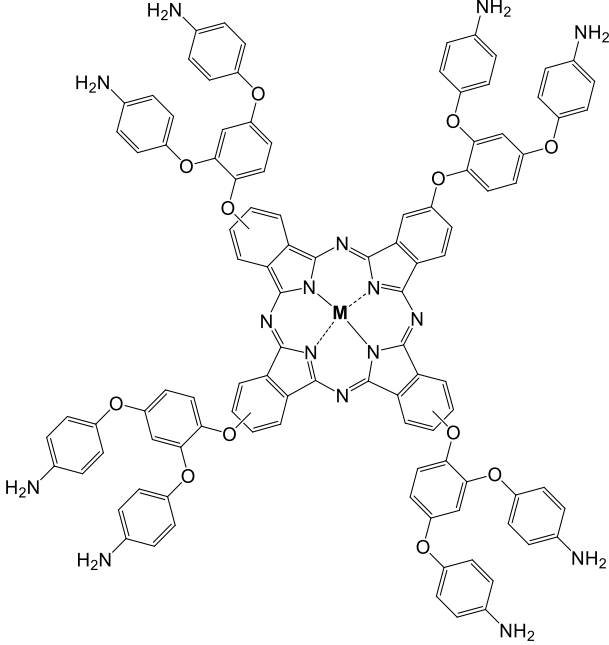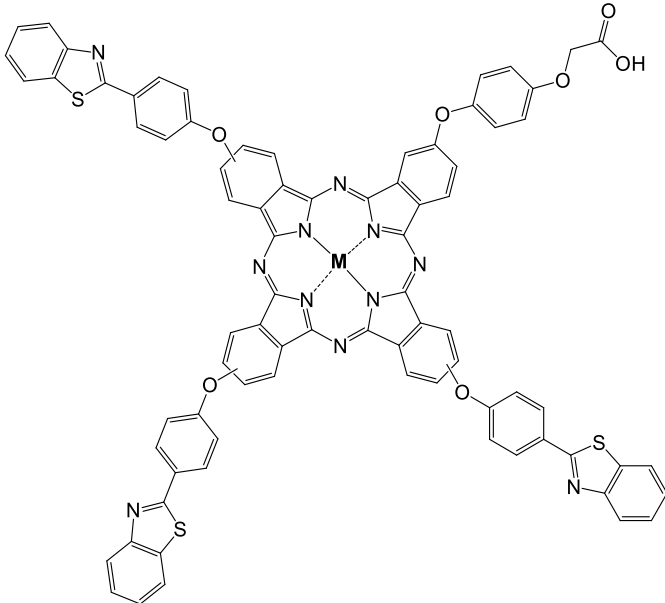
- For the group 1 (ball-type complexes), different bridging linkers were chosen to study their effect on the NLO response.

- Carboxylic acid linker (**10**-**12**) was chosen due to its polarizable electron which enhances NLO response.

- The long alkyl substituted linker (**13**-**15**) was chosen to increase solubility.

- The aldehyde linker (**16**-**18**) was chosen in order to compare the optical limiting effect with the corresponding aldehyde monomers (**28**-**30**)

- The benzothiazole linker (**19**-**21**) was chosen to enhance NLO response since benzothiazole small molecules has been reported to possess second order nonlinear optical properties [**64**]. The NLO response these dimers with corresponding monomers (**22**-**24**) will be compared.

- The bis(aminophenoxy)phenoxyl Pc complexes (**31**-**33**) were chosen for solubility and to study effect of covalent linkage and surface assembly to metallic nanoparticles.

- The asymmetric complexes (**34**-**36**) were chosen to compare NLO response with the symmetrical counterparts **22**-**24** as well as to study effect of covalent linkage and surface assembly to metallic nanoparticles.

Table 1.3: Summary of different phthalocyanine complexes used in this work

Molecular structure	Study with nanohybrid or thin fims

M = Zn (**10**)
   = GaCl (**11**)
   = InCl (**12**)
	12 was covalently linked to glutathione (GSH) capped silver and gold nanoparticles (AgNPs, AuNPs), CdTe, CdTeSe, CdTeSe/ZnO QDs and graphene quantum dots (GQDs) through amide bond formation
	
	10 and **11** were covalently linked to CdTe and GQDs

R= ~~~~~~~~~
M = Zn   (**13**)
   = GaCl (**14**)
   = InCl   (**15**)
	Formulated into polystyrene polymer thin films

M = Zn   (**16**)
   = GaCl (**17**)
   = InCl   (**18**)
	Formulated into polystyrene polymer thin films

M = Zn   (**19**)
   = GaCl (**20**)
   = InCl   (**21**)
	Surface assembled on metallic Au and Ag nanoparticles (NPs)

M = Zn   (**22**) [**62**]
   = GaCl (**23**)
   = InCl   (**24**)
	Surface assembled on metallic Au and Ag nanoparticles and formulated into polystyrene polymer thin films

M = Zn   (**25**) [**63**]
   = GaCl (**26**)
   = InCl   (**27**)
	Surface assembled on metallic Au and Ag nanoparticles and formulated into polystyrene polymer thin films

M = Zn   (**28**)
   = GaCl (**29**)
   = InCl   (**30**)
	Formulated into polystyrene polymer thin films

M = Zn   (**31**)
   = GaCl (**32**)
   = InCl   (**33**)
	(a) **31** was surface assembled and covalently linked to metallic Au and Ag nanoparticles
	(b) All were covalently linked to GSH capped CdTe QDs

M = Zn   (**34**)
   = GaCl (**35**)
   = InCl   (**36**)
	(a) **34** was surface assembled and covalently linked to metallic Au and Ag nanoparticles
	(b) All covalently linked to GSH capped CdTe QDs

1.1.5.Electronic Absorption in phthalocyanines

The nonlinear optical activity in phthalocyanines is expected to have strong dependence on the electronic structure as well as location of optical absorption spectra. The ground state optical absorptions in Pcs are dominated by two major absorption bands in the visible or near infrared (IR) (670 – 1000 nm) and the UV (325 – 370 nm) regions of the spectrum corresponding to the Q and the B bands [**65**] (**Fig. 1.1**)
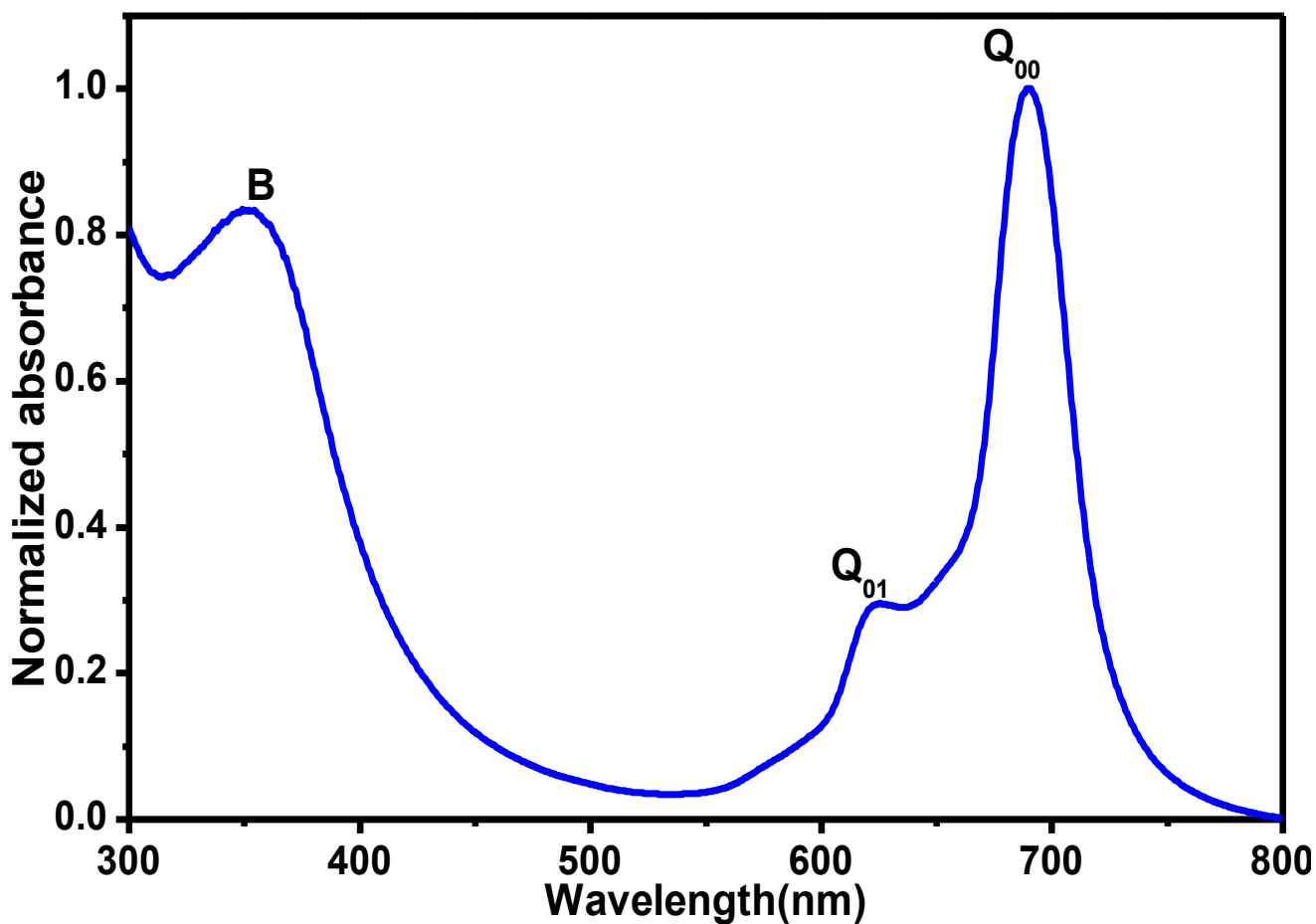
Figure 1.1: Electronic ground state absorption spectrum of MPc (unpublished data)

The Q and B bands are assigned in accordance with the Gouterman's four-orbital model [65,66] with Q band (Q_{00}) being characterized by a high molar extinction coefficient (ε) usually found to be of the order of 10^5 $M^{-1}.cm^{-1}$, with accompanying vibrational band (Q_{01}) (**Fig. 1.1**). The B band is less intense compared to the Q band, and lies at considerably higher energies around 350 nm. In metallated Pcs, the single intense Q band arising from D_{4h} symmetry is observed due to π-π^* transition from the a_{1u} of the highest occupied molecular orbital (HOMO) to e_g of lowest unoccupied molecular orbital (LUMO) of the MPc ring (**Fig. 1.2**). The Q band for unmatallated Pcs (H_2Pcs) on the other hand is split into two (Q_x and Q_y) due to D_{2h} reduced symmetry and this is due to transitions from a_{1u} the HOMO to the non-degenerate b_{2g} and b_{3g} of LUMO respectively (**Fig. 1.2**). The B bands occur due to transitions from a_{2u} and b_{2u} to e_g.

Substitution on the Pc ring results in shift in the Q band absorption maxima (blue or red shift depending on substituent type) relative to the unsubstituted Pc. In ball-type Pcs, a splitting and/or broadening is expected at the Q band due to intermolecular interaction between the Pc rings [67–69] depending on the conformation of the two Pc rings. Broadening and splitting results from the staggered rather than eclipsed conformation [70].

The theoretical approach has been a subject of interest for the past decades with the aim of better understanding and interpreting the electronic spectra in MPcs complexes [71–73]. The main aim in this field is to study the excited state properties of Pcs in finite and extended system using established theoretical and computational methodologies especially those based on the electronic density such as the Density Functional Theory (DFT). A great effort has been made on the study of the spectroscopic techniques by means of the time-dependent extension of the density functional theory. The time dependent density functional theory (TD-DFT) has been

shown to provide accurate results for transitions with significant charge transfer character [**74**], hence was employed in this work for spectra interpretations.
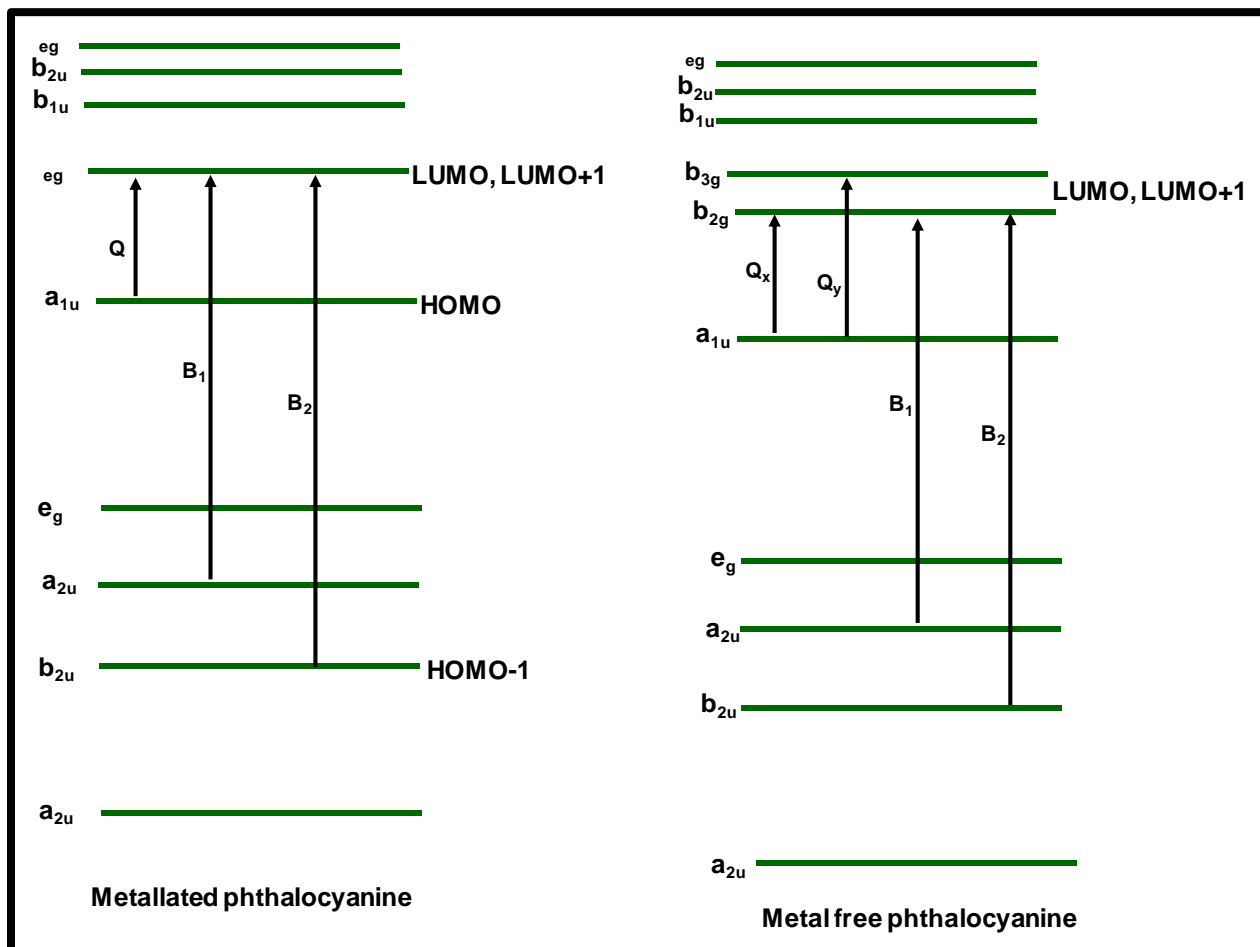
Figure 1.2: Electronic energy levels in phthalocyanine complexes showing the origin of Q and B bands

1.1.6. Photophysics of phthalocyanine

The Jablonski diagram (**Fig. 1.3**) describes the processes occurring after electronic excitation of Pc molecules.

Upon irradiation, Pc molecule in the ground singlet state (S_0) gets excited to the higher energy singlet state (S_1), and subsequently to S_n state as shown in **Fig. 1.3** [**75,76**]. In the S_n states, molecules are short-lived due to collisions, and undergo

vibrational relaxation (**VR**) to the first level of the S_1 state. Once in S_1 state, the molecule can either loose energy by emitting light through fluorescence with lifetime τ_0, undergo internal conversion by releasing heat to the surrounding or undergoes intersystem crossing to the excited triplet state T_1. Subsequent absorption by molecules in the first excited triplet lead to excitation to higher excited triplet T_n.
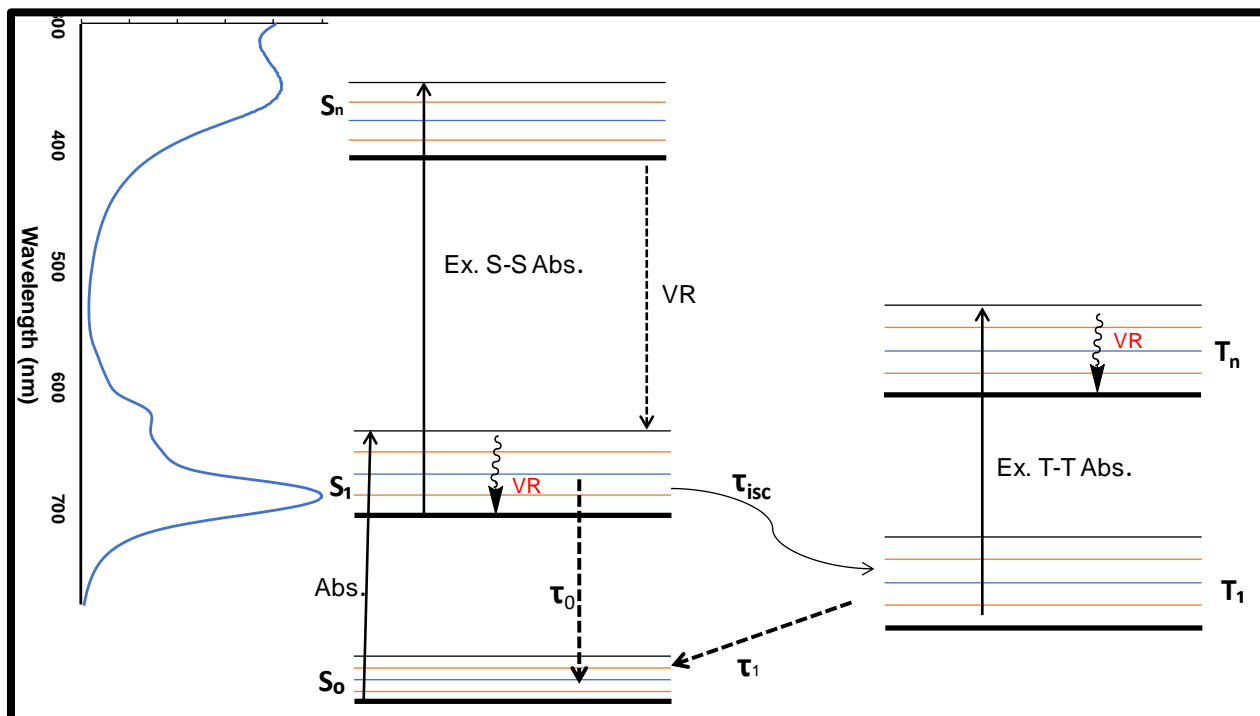
Figure 1.3: Modified Jablonski diagram illustrating the transition between the ground state singlet (S_0) and electronic excited (Ex) states (S_1 and T_1). Excited state singlet-singlet absorption (Ex S-S abs), Excited state triplet-triplet absorption (Ex T-T abs), fluorescence lifetime (τ_0), triplet lifetime (τ_1), intersystem crossing lifetime (τ_{isc}), vibrational relaxation (VR), intersystem crossing (ISC)

The accurate knowledge of excited state dynamics such as fluorescence quantum yield (Φ_F) and lifetime (τ_F), triplet quantum yield (Φ_T) and lifetime (τ_T) and the intersystem crossing time (τ_{ISC}) become paramount in understanding the NLO behavior of phthalocyanine based materials.

1.1.6.1. Triplet quantum yields and lifetimes

The nonlinear absorption which results in reverse saturable absorption (RSA) process for optical limiting applications is dependent on the population of the excited triplet state, hence the excited state dynamic is vital in designing good nonlinear optical materials [13,60,61,77]. The nanosecond laser flash photolysis technique was used to determine the excited triplet state properties. This is based on the change in absorbance in the triplet state, which occurs because of the triplet-triplet transition ($T_1 \rightarrow T_n$) and is directly proportional to the triplet quantum yield. The triplet quantum yield is generally determined by the comparative method using unsubstituted zinc phthalocyanine (ZnPc) as standard [75] and calculated as shown in **equation 1.1**

$$\Phi_T = \Phi_T^{std} . \frac{\Delta A_T . \varepsilon_T^{std}}{\Delta A_T^{std} . \varepsilon_T} \qquad\qquad (1.1)$$

where ΔA_T and $\Delta A_T{}^{std}$ are the changes in the triplet state absorbance of the sample and the standard, respectively. ε_T and ε_T^{std} are the respective triplet state molar extinction coefficients for the sample and the standard. Φ_T^{std} is the triplet quantum yield of the standard ZnPc. The molar extinction coefficient of the sample (ε_s) and standard (ε_s^{std}) and the respective change in triplet state absorbance of sample (ΔA_T) and standard (ΔA_T^{std}) are used to determine ε_T and ε_T^{std} according to **equation 1.2** and **1.3**

$$\varepsilon_T = \varepsilon_s . \frac{\Delta A_T}{\Delta A_s} \qquad\qquad (1.2)$$

$$\varepsilon_T^{std} = \varepsilon_S^{std} . \frac{\Delta A_T^{std}}{\Delta A_S^{std}} \qquad\qquad\qquad (\textbf{1.3})$$

1.1.6.2. Fluorescence quantum yield and lifetime

Fluorescence quantum yield (Φ_F) measures the efficiency of an emission process and it may be defined as the ratio of the number of photons emitted, to the number of photons absorbed [**78**]. The determination of Φ_F in this study was done using comparative method with unsubstituted ZnPc as reference standard, where the quantum yield of the Pc is related to that of the standard by **Equation 1.4**.

$$\Phi_F = \Phi_F^{std} . \frac{F . A_{std} . n^2}{F_{std} . A . n_{std}^2} \qquad\qquad\qquad (\textbf{1.4})$$

where F and F_{std} are the areas under the fluorescence emission curves of the sample and standard respectively. A and A_{std} are the respective absorbance of the sample and standard at the excitation wavelength, while n and n_{std} are the refractive indices of the solvents for the sample and standard, respectively.

Fluorescence intensity varies linearly to absorbed light intensity but nonlinearly with the concentration of the Pc. However, if the absorbance at the wavelength of excitation is ≤ 0.05, then a linear dependence can be assumed between the Pc concentration and the fluorescence intensity, which is important to prevent the inner-filter effects [**79**]. The inner filter effects result in self-quenching of the fluorescence, and a decrease in the Φ_F values.

The fluorescence lifetime (τ_F) is the measure of the average time spent by the fluorophores in the excited singlet state. It can be measured using time-correlated single-photon counting (TCSPC) technique among others [**80,81**].

1.1.7. Förster resonance energy transfer (FRET)

The Forster Resonance Energy Transfer (FRET) is an important phenomenon for studying the energy transfer interactions between two molecules within several nanometers [82]. The mechanism of FRET involves a non-radiative energy transfer from a donor fluorophore in an excited electronic state to a nearby acceptor chromophore through long-range dipole-dipole interactions, resulting in formation of donor-acceptor pair. **Figure 1.4** illustrates a FRET energy transfer process between a suitable excited donor molecule (QDs) and an acceptor molecule (MPcs) in a close proximity. Energy transfer from donor to acceptor molecule is generally accompanied by loss or decrease in the fluorescence quantum yield and lifetime of the donor leading to enhancement in the fluorescence properties of the acceptor.
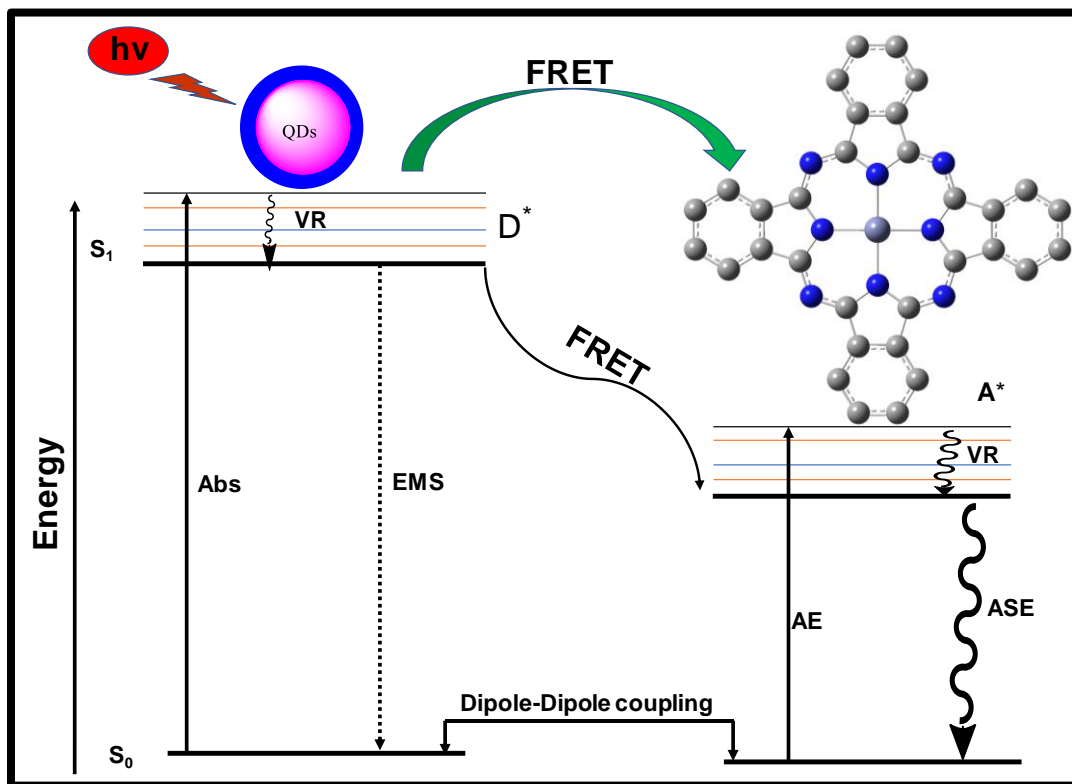
Figure 1.4: FRET diagram illustrating energy transfer from quantum dots QDs (Donor, D) to MPc (Acceptor, A): Abs = absorption, Ems = emission, AE = non- radiative acceptor excitation, ASE = acceptor stimulated emission, S_0 = singlet ground state, S_1 = singlet excited states, VR = vibrational relaxation.

An overlap in the fluorescence emission spectrum of the donor fluorophore with the absorption spectrum of the acceptor is prerequisite for FRET to occur. FRET is also dependent on the relative orientation of the transition dipole moments of the donor and acceptor as well as the quantum yield of the donor [**78,83**]. The FRET efficiency (Eff) can be determined experimentally either from the fluorescence quantum yield of the donor in the absence ($\Phi_{F(A)}$) and presence ($\Phi_{F(P)}$) of acceptor or from the photoluminescence lifetime of the donor in the absence (τ_A) and presence (τ_p) using **equation 1.5 and 1.6**

$$Eff = 1 - \frac{\Phi_{F(P)}}{\Phi_{F(A)}} \qquad\qquad (\textbf{1.5})$$

$$Eff = 1 - \frac{\tau_P}{\tau_A} \qquad\qquad (\textbf{1.6})$$

The amplitude weighted average lifetime obtained from **equation 1.7** are used in solving **equation 1.6**

$$\tau = \sum \alpha_i \tau_i \qquad\qquad (\textbf{1.7})$$

where α_i is the relative amplitude contribution to the lifetime τ_i. The Eff is dependent on centre to centre distance r (Å) between the donor and acceptor through a 6th order inverse law as shown in **equation 1.8** due to dipole-dipole coupling [**78,84**].

$$Eff = \frac{R_0^6}{R_0^6 + r^6} \qquad\qquad (\textbf{1.8})$$

where R_0 is the Förster distance (Å) defined as the critical distance between the donor and the acceptor molecules for which efficiency of energy transfer is 50% and depends on the quantum yield of the donor according to **equation 1.9**.

$$R_0^6 = 8.8 \ x \ 10^{23} k^2 n^{-4} \Phi_{F(A)} J \qquad\qquad (\textbf{1.9})$$

where κ is the dipole orientation factor, n is the refractive index of the medium, $\Phi_{F(A)}$ is the fluorescence quantum yield of the donor in the absence of the acceptor, and J is the Förster overlap integral that is calculated using **Equation 1.10**

$$J(\lambda) = \frac{\int_0^\infty F_D(\lambda)\varepsilon_A\lambda^4\partial\lambda}{\int_0^\infty F_D\partial\lambda} \qquad\qquad (1.10)$$

where F_D is the normalized intensity of QDs emission spectrum and ε is the molar extinction coefficient (M^{-1} cm^{-1}) of the acceptor. λ is the wavelength (nm) at the absorption maximum of the acceptor i.e. the Q-band. The PhotochemCAD® software [**85,86**] was used for the calculation of FRET parameters in this work.

1.2. Introduction to nanomaterials

Apart from synthesizing new materials with potential NLO attributes as inherent properties, an alternative approach for efficient materials with enhanced nonlinear optical response could be achieved through the fabrication of composites of materials that have already been identified as good optical limiters, such as MPcs and the nanomaterials mentioned above. Thus, part of the focus of this work was to enhance the optical limiting properties of the MPcs either through covalently linkage or surface assembly of the complexes to metallic gold and silver nanoparticles, semiconductor quantum dots or carbon-based graphene quantum dots to form new nanohybrid materials. Additionally, the optical limiting performance of the MPcs were investigated in solid polymer support through the conversion of Pc-polymer blend into thin films using drop and dry method. This is because the polymer confers high photodegradation threshold on the materials, hence making them able to withstand high input laser beam fluence for a long period.
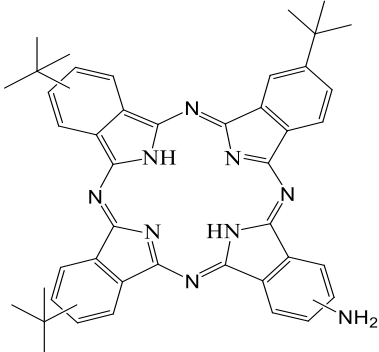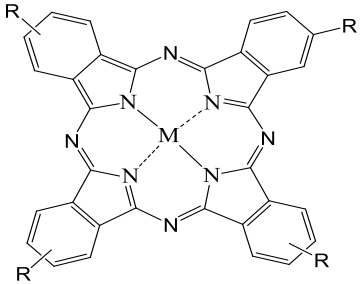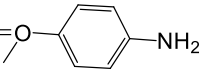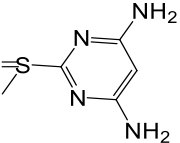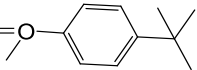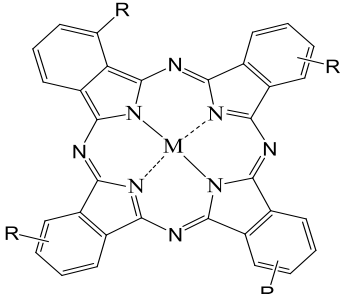
1.2.1.Quantum dots
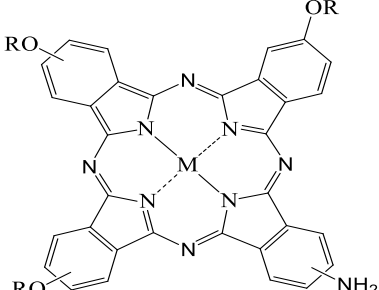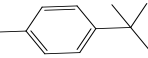
Semiconductor quantum dots (SQDs) are zero-dimensional inorganic semiconductor nanocrystals usually synthesized from group 12-16 (II-VI), 13-15 (III-V) or 14-16 (IV-VI) elements of the periodic table. They are known as zero-dimensional semiconductor material due to the quantum confinement of their electrons in three dimensions [87,88]. The energy levels in SQDs are confined to discrete values resulting in a decrease in nanocrystal size with increase in band gap energy.

SQDs have found wide and diverse applications in many areas of science and technology such as nonlinear optics [89–93], optical sensing [94,95], engineering solar device [96], labelling and bio-imaging [97], bioanalytical applications [98] and many others [99–102].

Though independent optical limiting investigation of SQDs [89–93] and metallated phthalocyanine [13,38,47,58,60] are known, the nonlinear optical study of covalently linked MPc-QDs dyad are still limited. In this work, complexes 10-12, 31-33, 34, and 35-36 were covalently linked to glutathione functionalized CdTe SQDs. Table 1.4 showed Pcs molecules that have been previously combined with nanomaterials for optical limiting applications [103-113]. This thesis reports for the first time the covalent linkage of ball-type Pcs to SQDs as well as the optical limiting behavior of ball-type-SQDs nanohybrids. The glutathione functionalized SQDs were chosen since glutathione possess both carboxylic acid and amine functional group which confer dual functional properties. The carboxylic acid functional group will be utilized when linking complexes that possess primary amine groups while the amine group will be employed when linking complexes that have carboxylic acid functional group.

Table 1.4: Selected Phthalocyanine molecules that have been combined with nanomaterials for optical limiting application

	Encapsulated into silica core shell	[**103**]
	M=Al, R=H (π-conjugated to multiwalled carbon nanotubes) M= Zn, R=NH$_2$ (covalently linked to graphene oxide (GO) NPs) M = Zn, R = (covalently linked to silica coated magnetic NPs) M = Zn, R = (surface assembled onto metallic Ag/Au nanoalloy) M = Zn, R = (π-conjugated to graphene oxide NPs)	[**104, 105, 108, 109, 112, 113**]
	M= Zn, R= -NH$_2$ (covalently linked to GO NPs) M= Zn, R= -O-(CH$_2$)$_5$OH (covalently linked to GO NPs) M = Zn, R= -O-CH$_2$CH$_2$OCH$_2$CH$_2$OH (covalently linked to GO NPs)	[**105, 106**]

	M = InOH, R = H (Covalently linked to CdTe/ZnS QDs) M = Zn, R = ⬡ (benzene with tert-butyl) (Covalently linked to graphene QDs and GO NPs)	[**107**, **110**, **111**]

Graphene quantum dots (GQDs) on the other hand are the fragmented pieces of larger and multi-layered graphene sheet with size range between 1-20 nm and also possess zero-dimensional (0D) framework [**114**–**116**]. The wide applications of GQDs such as in optoelectronic devices, energy-storage media and drug-delivery are due to their unique characteristics including but not limited to large surface area, high carrier transport mobility, superior mechanical flexibility and excellent thermal and chemical stability [**116**–**118**]. Thus, GQDs share similar excellent characteristics such as high photostability, size and wavelength tunable photoluminescence (PL) with SQDs [**114,119,120**]. Despite numerous literature reports on application of GQDs, the optical limiting study of Pc-GQDs for NLO are still limited. The nonlinear optical response of pristine GQDs covalently linked to MPcs was recently reported [**110**]. The optical limiting response of GQDs covalently linked to ball-type MPcs are reported in this work for the first time. Complexes **10**-**12** possessing carboxylic acid functional group were covalently coupled with amine functionalized GQDs to form new MPc-GQDs nanohybrids and the optical limiting response was compared with the corresponding MPc-SQDs nanohybrids formed by covalent linkage of the same MPc complexes to SQDs.

1.2.2. Silver (AgNPs) and gold (AuNPs) nanoparticles.

The recent years has witnessed significant research interest in noble metal nanoparticles because of their unusual optical properties and their potential applications in emerging optoelectronic and photonic technologies [**121,122**]

There has been a rapid progress in the study of potential optical limiting properties of metallic nanoparticles [**123**–**132**]. Among metal nanoparticle limiters, special and more attention has been given to metallic gold and silver nanoparticles [**125**–**129,131,132**], due to broad surface plasmon resonance (SPR) absorption band in the visible region of the electromagnetic spectrum. It has been shown that the optical properties of gold nanoparticles are mainly due to the surface plasma resonance (SPR), which result from the collective oscillation of particles' free electrons in the conduction band [**131**].

Despite various research reports in independent optical limiting applications of AgNPs and AuNPs, limited research studies have been done on nonlinear optical response of MPcs in combination with metallic nanoparticles. In this work, complexes **12**, **31** and **34** were covalently linked to glutathione functionalized AuNPs and AgNPs. Since complexes **19**-**27**, **31**- **33** and **34**-**36** all possess either terminal amino group or sulphur/nitrogen within the benzothiazole ring with high affinity for gold and silver, they were surface assembled on AuNPs and AgNPs. The effects of surface assembly versus covalent linkage of **31** and **34** on metallic gold and silver nanoparticles on photophysical and optical limiting properties were investigated for the first time.

1.3. Nonlinear optical processes

When light (electric field) of a given frequency passes through a material, oscillation of electrons occurs in response to applied field. With small electric field intensity, the polarization field is linearly dependent to incident electric field according to **equation 1.11** [**77**]

$$P = \varepsilon_0 \chi E \qquad (1.11)$$

where ε_0 is vacuum permittivity, χ is the electrical susceptibility and E is the applied electric field. However, for a stronger electric field, the polarization field no longer obeys the linear relationship given above because the susceptibility is now dependent on the electric field. Then polarization can be expanded in a Taylor series as shown in equation **1.12**

$$P = \varepsilon_0 (\chi^1 E + \chi^2 E^2 + \chi^3 E^3 + \cdots.) \qquad (1.12)$$

where χ^1 is the linear electric susceptibility, χ^2 is the second-order nonlinear susceptibility and χ^3 is the third-order nonlinear susceptibility [**133–136**]. In centrosymmetric media, χ^2 is absent because of the reversibility of polarization when the electric field is reversed. The dominant optical nonlinearity in this media is due to χ^3, which gives rise to third order nonlinear effects such as third-harmonic generation, self-phase modulation, self-focusing and four-wave mixing [**137,138**].

The third order nonlinear susceptibility has the real (χ^3_{Re}) and the imaginary (χ^3_{Im}) components as described in **equation 1.13**.

$$\chi^3 = \chi^3_{Re} + \chi^3_{Im} \qquad (1.13)$$

The real portion is responsible for NLO refraction processes while the imaginary portion give rise NLO absorption processes [**77**].

The limiting threshold (I_{lim}) is an important term in the optical limiting measurement and can be defined as the input fluence (or energy) at which the transmittance is 50%

of the linear transmittance [**13**]. Material for optical limiting applications perform better at lower limiting threshold. A more generally accepted indicator for evaluating the strength of good optical limiting material is the energy density at which the output fluence reaches its saturation value represented as F_{sat} [**38,53,57**]. A lower saturation energy density indicates efficient optical limiting materials.

The optical limiting effect of NLO material involves a decrease in transmittance under high intense irradiation. Thus, the transmission of an optical limiter is high at normal light intensities and becomes low when the illumination intensity is high [**13**,**139**]. Ideally, a linear rise in output energy of a limiter with increase input energy is expected until a threshold (I_{lim}) is reached as shown in **Fig. 1.5**. At a critical intensity, the output energy is attenuated to a constant value that can cause less damage to optical sensors. The three main mechanisms for optical limiting response are nonlinear absorption (NLA), nonlinear refraction (NR) and nonlinear light scattering (NLS). However, this work is focused on optical limiting that result from NLA processes using the Z-scan technique [**140,141**], which the set up will be described in the experimental section.
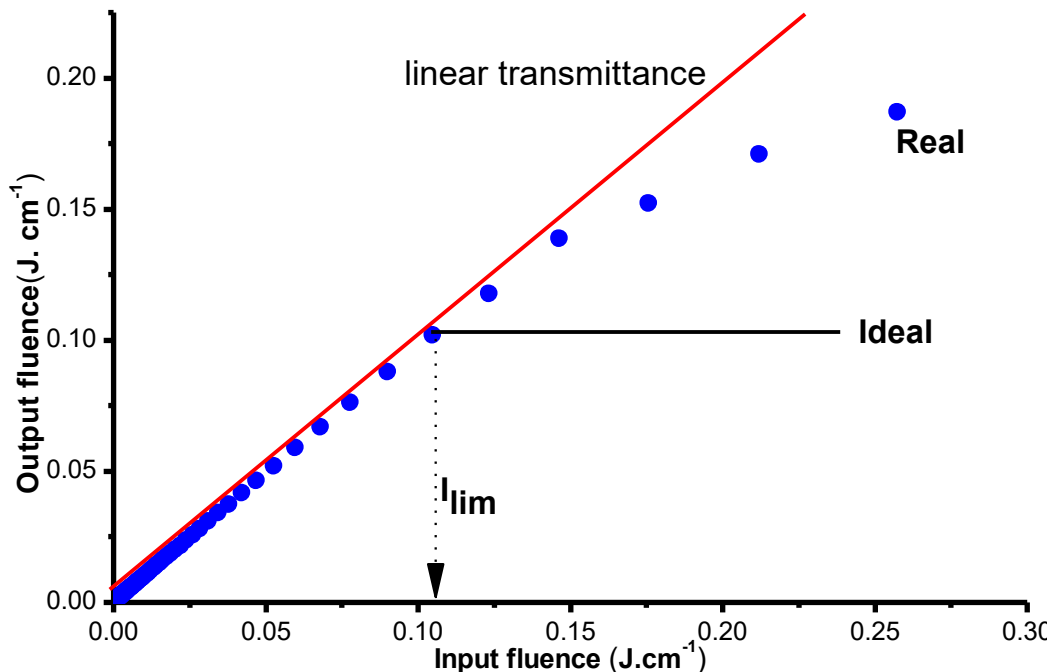
Figure 1.5: optical limiting behavior of real and ideal optical limiters

The difficulty in separating various nonlinear optical mechanisms such as: excited state absorption, two photon absorption, nonlinear scattering and nonlinear refraction responsible for RSA process has been a serious limitation of the z-scan technique. To solve this limitation, suitable equations for analysis of z-scan data have been developed, and the explanation of results from such analysis is usually given based on the nature of the investigated material and the properties (pulse width and repetition rate) of the laser beam employed. The appropriate equations employed for the analysis of the z-scan experimental will be discussed at results of this thesis.

1.4. SUMMARY OF AIMS OF THESIS

The aims of this thesis are summarized as follows:

1. Synthesis of co-facial ball-type phthalocyanines containing zinc-zinc, gallium-gallium and indium-indium central metals (complexes **10-21**) and investigation of the photophysical and NLO response of the complexes.

2. Synthesis of peripherally substituted Zn (II), Ga (III) and In (III) phthalocyanines containing benzothiazole, benzaldehyde and phenoxyl-bis(aminophenoxy) substituents (complexes **22-33**) and the detailed investigation of the photophysical and NLO properties.

3. Synthesis of asymmetric benzothiazole substituted Zn (II), Ga (III) and In (III) phthalocyanines with phenoxylacetic acid terminal (complexes **34**-**36**)

4. Synthesis of functionalized metallic nanoparticles.

5. Synthesis of functionalized semiconductor and graphene quantum dots

6. Covalent linkage appropriate phthalocyanine complexes to functionalized nanoparticles and study of the photophysical and NLO response.

7. Surface assembly of appropriate phthalocyanine complexes to metallic gold and silver nanoparticles and detail study of the NLO response of the new nanohybrids.

Chapter two: Experimental

2. Experimental

2.1. Materials

2.1.1. General Solvents

Ultra-pure water was obtained from a Milli-Q Water System (Millipore Corp, Bedford, MA, USA), spectroscopic dimethyl formamide (DMF), spectroscopic dimethyl sulfoxide (DMSO), deuterated (DMSO-d_6, CDCl$_3$-d_6), 1-pentanol, were purchased from sigma Aldrich®. Dichloromethane (DCM), tetrahydrofuran (THF), diethylether, absolute ethanol (abs. EtOH), chloroform, toluene, hexane, petroleum ether, ethyl acetate, and acetone were obtained from SAARCHEM®.

2.1.2. Chemical and reagents

Dicyclohexylcarbodiimide (DCC), 4-(dimethylamino)pyridine (DMAP), zinc acetate, gallium chloride, indium chloride, 1,8-diazabicyclo[5.4.0] undec-7-ene (DBU), 1,2-hexadecanediol, 4-(2,4-dichlorophenoxy)phthalonitrile, cetyltrimethylammonium bromide (CTAB), 2-aminothiophenol, 3,4-dihydroxybenzoic acid, 3, 4-dihydroxybenzaldehyde, 4-hydroxylbenzaldehyde, 4-aminophenol, 4-nitrophthalonitrile, polystyrene (Mw 192 000 g mol^{-1}), Rhodamine, 6G and 1, 3-diphenylisobenzofuran (DPBF) were purchased from Sigma Aldrich®.

2.2. Instrumentations and methods

- Ground state electronic absorption spectra were recorded on a Shimadzu® UV-2550 spectrometer (in solution) or Perkin-Elmer® UV/Vis/NIR spectrometer at 250 nm to 2500 nm range (for thin films).

- Fluorescence emission spectra were recorded on a Varian Eclipse spectrofluorimeter.

- Infra-red spectra (FT-IR) were collected Infrared (IR) spectra were recorded on a Bruker Alpha IR (100 FT-IR) spectrophotometer.

- ^{1}H-NMR spectra were recorded using a Bruker AVANCE 600 or 400 MHz NMR spectrometer in deutrated DMSO, THF or chloroform.

- Elemental analyses were obtained using a Vario-Elementar Microcube ELIII.

- Mass spectra data were recorded using a Bruker AutoFLEX III Smart-beam TOF/TOF mass spectrometer with α-cyano-4-hydrocinnamic acid as the matrix in the positive ion mode.

- The z-scan equipment used was fabricated at the University of Stellenbosch, South Africa. The laser pulses as the excitation sources were either produced by a tunable laser system consisting of a Nd-YAG laser (355 nm, 135 mJ/4–6 ns) pumping an OPO (30 mJ/3–5 ns) with a wavelength range of 420–2300 nm (NT-342B, Ekspla) and a pulse repetition rate of 20 Hz, or a frequency-doubled Nd-YAG laser (Quanta-Ray, 1.5 J/10 ns FWHM pulse duration) with a pulse repetition rate of 10 Hz and an energy range of 0.1 μJ–0.1 mJ, limited by the energy detectors D_1 and D_2 (Coherent J5-09) (**Fig. 2.1**). Both lasers were operated in a near Gaussian transverse mode at 532 nm (second harmonic) with low repetition rate of the lasers to prevent cumulative thermal nonlinearities. The beams were spatially filtered to remove the higher order modes and tightly focused with a 15 cm focal length lens. The liquid samples were placed in a cuvette cell with internal dimensions: 2 mm × 10 mm × 55 mm, 0.7 mL and a path length of 2 mm (Starna 21-G-2).
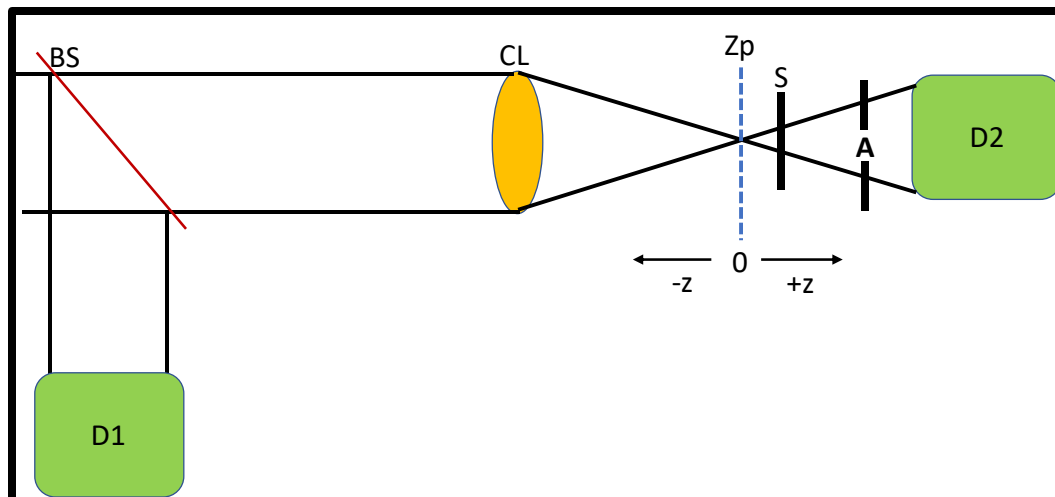
Figure 2.1: Schematic diagram of a basic Z-scan set-up Beam splitter (BS), convex lens (CL), zero position (ZP), sample holder (S), aperture (A), reference (D1) and probe detector (D2). The – z to + z describes the movement of sample along the z-axis through the focus (ZP) of the lens

- The nanosecond laser flash photolysis set-up (**Fig. 2.2**) used to determine the triplet state behaviors employed an Ekspla laser described below. The analyzing beam source was a Thermo Oriel 66902 xenon arc lamp, and a Kratos-Lis Projekte MLIS-X3 photomultiplier tube was used as detector. Signals were recorded with a two-channel, 300 MHz digital real time oscilloscope (Tektronix TDS 3032C). The kinetic curves were averaged over 256 laser pulses. The detailed procedure of the flash photolysis experiment is as follows: The Q band absorbance of solutions of the Pc alone and the standard ZnPc were set at ~1.0 (~0.5 for nanocomposites). The solution was de-aerated for 30 min inside a 1 cm path length UV-visible spectrophotometric cell. Thereafter the solution was sealed and irradiated using an appropriate excitation wavelength (the cross-over wavelength of the sample and the ZnPc standard). The maximum triplet absorption and singlet depletion wavelengths are determined from the transient curve
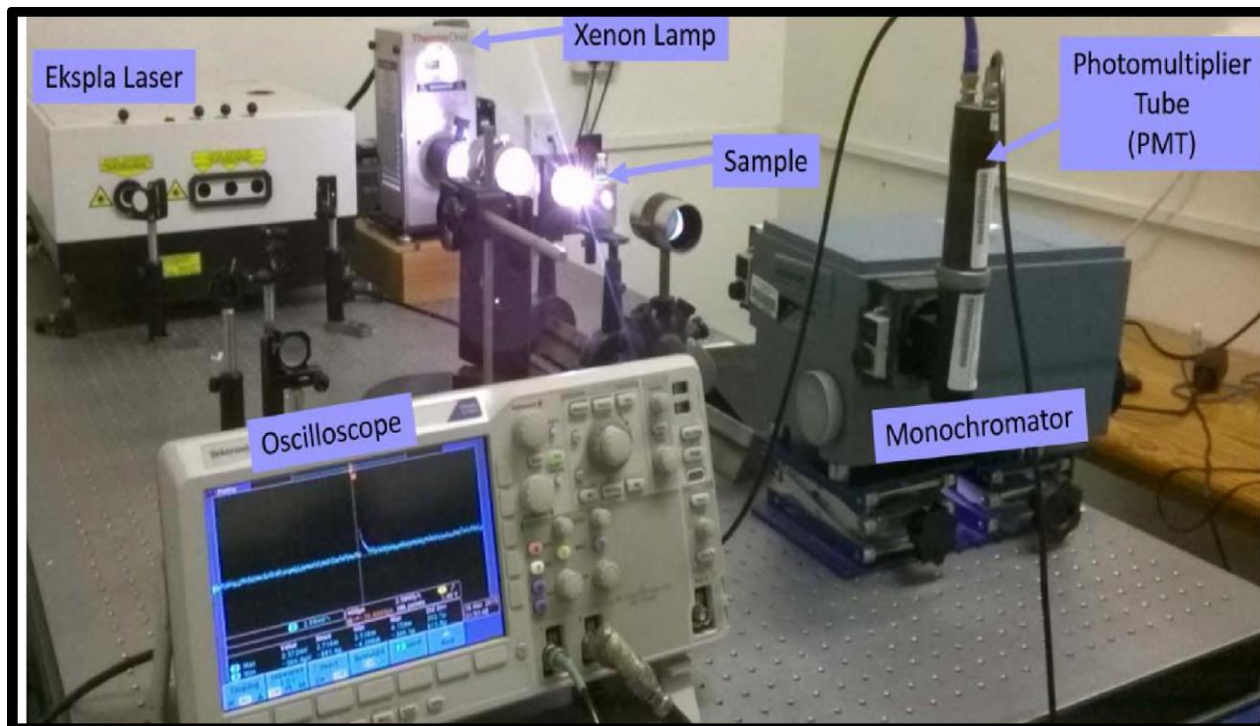
Figure 2.2: Schematic set up diagram for laser flash photolysis

- Fluorescence lifetimes were obtained using a time correlated single photon counting (TCSPC) setup (FluoTime 200, Picoquant GmbH or FluoTime 300). The excitation source was a diode laser (LDH-P-670 driven by PDL 800-B, 670 nm, 20 MHz repetition rate, 44 ps pulse width, Picoquant GmbH) for MPcs, MPcs-NPs and the excitation source was a diode laser (LDH-P-C-485 with 10 MHz repetition rate, 88 ps pulse width) for QDs. A monochromator with a spectral width of about 8 nm was used to select the required emission wavelength. The response function of the system, which was measured with a scattering Ludox solution (DuPont), had a full width at half-maximum (FWHM) of about 300 ps. The ratio of stop to start pulses was kept low (below 0.05) to ensure good statistics. The emission peak maxima were used for measurement of all luminescence decay curves. The data were analyzed with

the program FluoFit (Picoquant). The support plane approach was used to estimate the errors of the decay times.

- Raman spectra were obtained using a Bruker RAM II spectrometer equipped with a 1064 nm Nd-YAG laser and a liquid nitrogen cooled germanium detector. Samples were diluted with KBr before measurements.

- Transmission electron microscope (TEM) images were obtained using a Zeiss Libra TEM, 120 models and operated at 90 kV accelerating voltage. AuNPs, AgNPs, QDs, and composite samples for TEM were prepared separately by ultrasonication in abs. EtOH, H_2O or toluene.

- X-ray powder diffraction patterns were recorded on a Bruker D8 Discover, equipped with a LynxEye detector, using Cu Kα radiation (λ = 1.5405 Å, nickel filter). Scanning was at 10 min^{-1} with a filter time-constant of 2.5 s per step and a slit width of 6.0 nm. The data were obtained in the range from 2θ = 10° to 100°. The sample was placed in a zero-background silicon wafer slide. The X-ray diffraction (XRD) data analysis was carried out using Eva (evaluation curve fitting) software. Subtraction of spline fitted to the curved background was used for baseline correction of each diffraction pattern and the full width at half maximum (FWHM) values were obtained from the fitted curve.

- Magnetic circular dichroism (MCD) spectra were measured using a Chirascan plus spectrodichrometer equipped with a 1 T (Tesla) permanent magnet by using both the parallel and antiparallel fields.

- Thin-films were obtained using a special coating system (SCS), 6800 Spin Coater Series, coupled with a vacuum pump. The SCS system is connected to an air supply, without which it cannot function. The ramp and dwell times (in seconds), and the speed (in rpm), were varied to achieve the optimum

conditions for the best thin-film. The film thickness was determined by using the knife-edge attachment of a Bruker D8 Discover X-ray Diffraction (XRD) Spectrometer.

- Theoretical calculations were done using Gaussian 09 program with Intel/Linux cluster [**142**]. The Gausview 4.1 or Avogadro program was used for all visualization.

- The qualitative elemental compositions of the NPs and their conjugates with Pcs were obtained using INCA® PENTA FET coupled with VAGA TESCAM energy dispersive x-ray (EDX) spectrometer operated at 20 kV.

- The X-ray photoelectron spectroscopy (XPS) data were obtained using a Kratos Axis Ultra DLD, with an Al (monochromatic) anode, equipped with charge neutralizer and the operating pressure was kept below 5 x10-9 torr. The resolution was 10 eV pass energy in the slot mode. For the XPS wide scan, the following parameters were used: emission current was kept at 12.5 mA and the anode (HT) voltage at 15 kV. The resolution was maintained at 160 eV pass energy using a hybrid lens in the slot mode. For the high-resolution scans, the resolution was changed to 40 eV pass energy in the slot mode.

- Singlet oxygen quantum yields (Φ_Δ) were obtained using a general electric quartz lamp (300 W) with 600 nm ($\pm$ 3 nm) cut-off glass filter (Schott®) for ultra violet radiation and a water filter for infrared radiation. Interference filter of 700 nm with a band of 40 nm was placed before the sample chamber. Light intensities were measured with a POWER MAX 5100 (Molelectron® detector incorporated) power meter and were found to be 4.3 x 10^{15} photons cm^{-2} s^{-1}.

- Dynamic light scattering (DLS) experiments were done on a Malvern Zetasizer nanoseries, Nano-ZS90.

- Hydrothermal syntheses were carried out using a Berghof (Germany) High Pressure Laboratory Reactor (high preactor) BR-300, V.3.0 equipped with PT-100 temperature and pressure sensors, BTC-300 Temperature regulator and manometer and PTFE lining.

- A Metrohm Swiss 827 pH meter was used for pH measurements

2.3.   Synthesis of phthalonitriles

Out of the nine phthalonitrile employed in this work, 4-[4-(1,3-benzothiazol-2-yl)phenoxy] phthalonitrile (**5**), 4-{[1H-benzo(d)thiazol-2-yl]thio} phthalonitrile (**6**), 4-(4-formylphenoxy)   phthalonitrile   (**7**)   and   2-(4-(3,4-dicyanophenoxy)phenoxy)acetic acid (**9**) has been reported [**62**,**63**,**143**,**144**] The synthesis of the novel phthalonitriles (**1**-**4**, **8**) are hereby presented.

2.3.1. Synthesis of 3, 4-bis(3, 4-dicyanophenoxy)benzoic acid (1), Scheme 3.1

A   mixture   of   3,4-dihydroxybenzoic   acid   (1.78g,   11.55   mmol)   and   4-nitrophthalonitrile (2g, 11.55mmol) in dry DMF (20 mL) was stirred in 100 mL round bottom flask at 50 °C under inert atmosphere for 1hr. Dry K_2CO_3 (3g, 21 mmol) was added in six equal portions at 1 h interval and the reaction was allowed to stir undisturbed at ambient temperature for 7 days. The reaction was poured into ice water and the precipitated product was filtered under reduced pressure. The light-yellow   precipitate   was   purified   by   column   chromatography   using chloroform/methanol (9:1) as eluent to give a crystalline yellow solid. Yield: 1.35g, (49%), IR (ATR): ν (cm^{-1}): 3079 (OH stretch), 3034 (Ar–CH), 2230 (CN stretch), 1676 (C=O stretch). ^{1}H NMR (400 MHz, DMSO) (δ, ppm): 10.45 (s, J = 9.46, 1H, COOH), 8.01–7.93 (m, 3H, Ar–H), 7.78–7.69 (m, 5H, Ar–H), 7.53–7.47 (d, J = 7.69

Hz, 1H, Ar–H), ^{13}C NMR (600MHz, CDCl$_3$) δ 178.62, 161.20, 147.04, 140.92, 138.56, 134.70, 132.55, 129.13, 128.31, 126.08, 126.03, 126.01, 125.81, 125.64, 120.77, 120.54, 119.93, 116.64, 115.99, 115.07, 106.72, 106.33, 102.98. Anal. Calc. for C$_{23}$H$_{10}$N$_4$O4: C, 67.98; H, 2.48; N, 13.79; O, 15.75 Found: C, 67.82; H, 2.43; N, 13.76.

2.3.2.Synthesis of 4-(hexadecane-1,2-dioxyl)-bis(phthalonitrile) (**2**), Scheme 3.2

A mixture of 1,2-hexadecanediol (1.0 g, 3.86 mmol) and 4-nitrophthalonitrile (1.34 g, 7.72 mmol) in dry DMF (20 mL) was stirred in a 100 mL round bottom flask at 50°C under an inert atmosphere for 1 h. Dry K$_2$CO$_3$ (1.5 g, 10.5 mmol) was added in two equal portions at an interval of 6 h and the reaction was stirred undisturbed at ambient temperature for 7 days. The reaction mixture was poured into ice water and the precipitated product was filtered under reduced pressure. The light-yellow precipitate was purified by column chromatography using THF/methanol (9 :1) as the eluent to give a crystalline yellow solid. Yield: 0.95 g (41%), IR (ATR): v (cm^{-1}): 2914 (Ar–CH), 2233 (C≡N), 1595 (C = N/C = C), 1248–1095 (C–O–C). ^{1}H NMR (300 MHz, DMSO) δ 8.26–8.05 (d, J = 8.1 Hz, 2H, Ar–H), 8.04 (d, J = 7.6 3.9 Hz, 2H, Ar–H), 7.55 (d, J = 7.5, 3.7 Hz, 2H, Ar–H), 4.28–4.20 (d, J = 9.2, 8.6 Hz, 3H, alkyl-H), 3.25 (t, J = 8.8, 8.6, 7.5 Hz, 2H, alkyl-H), 1.30–1.23 (m, 24H, alkyl-H), 0.91 (s, 3H, alkyl-H). MALDI TOF-MS: calculated: 510.30; found: 510.39 [M + 1]$^+$.

2.3.3.Synthesis 4,4'-[(4-Formyl-1,2-bis(phenoxyl)diphthalonitrile] (**3**), **Scheme 3.3**

A mixture of 3, 4-dihydroxybenzaldehyde (1 g, 7.24 mmol) and 4-nitrophthalonitrile (2.51 g, 14.48 mmol) in dry DMF was stirred at 70°C under nitrogen inert gas for 2 h, followed by addition of dry K_2CO_3 (1 g, 7.24 mmol) in two equal portions within an additional period of 6 h. The reaction was then allowed to continue for further 120 h. The reaction mixture was poured into ice water and the precipitated product was filtered under reduced pressure and dried in vacuo to give a brownish solid. Yield, 2.6g (74%), IR (ATR): υ (cm^{-1}): 2937 (Ar–CH), 2231 (C≡N), 1595 (C=C), 1248–1095 (C–O–C). ^{1}H NMR (600 MHz, DMSO) δ 9.58 (s, 1H, Aldehyde-H), 8.09 – 7.98 (d, $J = 7.64$ Hz, 2H, Ar-H), 7.95 – 7.88 (d, $J = 7.52$ Hz, 2H, Ar-H), 7.61 – 7.57 (s, 1H, Ar-H), 7.53 – 7.39 (m, 4H, Ar-H). Anal. Calc. for ($C_{23}H_{10}N_4O_3$): C, 70.77; H, 2.58; N, 14.35. Found: C, 70.74: H, 2.62; N, 14.29.

2.3.4.Synthesis of precursor 3, 4-dihydroxybenzylbenzothiazole (Scheme 3.4)

A mixture of 3, 4-dihydroxybenzaldehyde (1 g, 7.2 mmol) and 0.14g (0.38 mmol) of CTAB was stirred in 50 mL of water at 80 ^{0}C for 30 min, followed with addition of 2-aminothiophenol (1.08 g, 8.69 mmol). The reaction mixture was allowed to reflux at 150 ^{0}C for 5 h. On cooling, the reaction mixture was diluted with ethyl acetate (EtOAc) (200 mL) and was transferred to a separating funnel. The organic layer was isolated and washed with $NaHCO_3$ (100 mL), and the aqueous layer further extracted with fresh EtOAc (3 x 100 ml). The combined organic extracts were washed with water (3 x 100 ml), isolated, dried using Na_2SO_4 and concentrated under reduced pressure. The crude product was purified using silica gel column chromatography with petroleum ether/ethyl acetate (9:1) as eluent to give bright

yellow solid. Yield: 1.6 g (82 %),), IR (ATR) (cm^{-1}) v_{max} 2973.17 (C-H from Ar-H stretch), 2934.37, 1519.56 (C=N stretch), 756.34 (C-S stretch), ^{1}H NMR (600 MHz, DMSO) δ 8.05 – 7.58 (dd, J = 8.2, 7.6 Hz, 2H, Ar-H), 7.54 – 7.07 (m, 4H, Ar-H), 7.0 – 6.58 (d, J = 7.5 Hz, 1H, Ar-H), 3.55 – 3.50 (s, 2H, H-hydroxyl group Anal. Calc. For C$_{13}$H$_9$NO$_2$S: C, 64.18; H, 3.73; N, 5.76; S, 13.18, Found: C, 64.22; H, 3.70; N, 5.78; S, 13.22.

2.3.5. Synthesis of 4,4'-((4-(benzo[d]thiazol-2-yl)-1,2-bis(phenoxy)) diphthalonitrile (4), Scheme 3.4

A mixture of 3, 4-dihydroxybenzylbenzothiazole (1.00 g, 4.11 mmol) and 4-nitrophthalonitrile (1.42 g, 8.22 mmol) in dry DMF (25 mL) was stirred in a 100 mL round-bottomed flask at 50 °C under an inert atmosphere for 1 h. Dry K$_2$CO$_3$ (3 g, 21 mmol) was added in six equal portions at 1 h intervals and the mixture was allowed to stir undisturbed at ambient temperature for 7 days. The mixture was poured into ice water and the precipitated product was filtered under reduced pressure. The light-yellow precipitate was purified by column chromatography using hexane/ethyl acetate (8:2) as eluent to give a crystalline yellow solid (3). Yield: 1.03 g, (42%), IR (ATR) (cm−1): 3034 (Ar-CH stretch), 2230 (C≡N stretch), 1676 (C=O stretch), 748 (C-S stretch). ^{1}H NMR (600 MHz, DMSO) δ 8.21 (d, J = 8.7 Hz, 5H, Ar-H), 8.16 (dd, J = 8.3, 4.8 Hz, 1H, Ar-H), 8.08 (d, J = 8.0 Hz, 1H, Ar-H), 7.96 (d, J = 2.5 Hz, 1H, Ar-H), 7.59–7.54 (m, 3H, Ar-H), 7.50–7.46 (m, 1H, Ar-H), 7.38 (d, J = 8.7 Hz, 1H, Ar-H). ^{13}C NMR (600 MHz, CDCl$_3$) δ 165.82, 160.52, 160.07, 153.84, 147.75, 145.57, 136.67, 132.47, 127.58, 127.15, 127.10, 126.30, 122.81, 122.64, 122.97, 122.80, 122.77, 122.75, 122.35, 122.28, 117.93, 116.25, 116.20, 115.67, 115.57, 109.86, 109.59, 109.33, 109.25. Anal. Calc. For C$_{29}$H$_{13}$N$_5$O$_2$S: C, 70.29; H, 2.64; N, 14.13; S, 6.47, Found: C, 69.08; H, 2.72; N, 14.09; S, 6.25

2.3.6.   Synthesis   of   4-(2,   4-bis   (4-aminophenoxy)phenoxy)phthalonitrile (8), Scheme 3.7

For the synthesis of **8**, a mixture of 4-(2, 4-dichlorophenoxyl)phthalonitrile (1g, 3.47 mmol) and 4-aminophenol (**3**) (0.76g, 6.94 mmol) in dry DMF was heated at 70 ^{0}C under argon for 72 h. The reaction mixture was precipitated in ice water, filtered and recrystalized in dry methanol. The resultant yellowish solid was dried under vacuum to yield 0.98 g (55.8%). IR (ATR): ν (cm^{-1}): 3286 (NH$_2$ stretch), 2928 (Ar–CH), 2231 (C≡N stretch), 1557, 1464 (C=N stretch of primary amine). ^{1}H NMR (600 MHz, DMSO-d6) (δ, ppm): 8.25-8.18 (m, 1H, Ar-H), 8.09-8.05 (d, J = 8.17 Hz, 1H, Ar-H), 7.88-7.83 (d, J = 8.28 Hz, 3H, Ar-H), 7.68 – 7.64 (m, 3H, Ar-H), 7.52 – 7.39 (m, 3H, Ar-H), 7.28 – 7.25 (m, 1H, Ar-H), 6.82 – 6.76 (d, 1H, J = 7.12 Hz, Ar-H), 6.71 – 6.68 (d, 1H, J = 6.23 Hz, Ar-H), 5.25 (s, 4H, NH$_2$ proton), Anal: Calc for C$_{26}$H$_{18}$N$_4$O$_3$, C, 71.88; H, 4.18; N, 12.90. Found: C, 71.81; H, 4.13; N, 13.02.

2.4.   Synthesis of phthalocyanines

The synthetic pathways for complexes **10**-**21**, **23**, **24**, **28**-**36** are shown in **Schemes 3.1-3.9**. The numbering considers the phthalonitrile compound **1**-**9**. While tetrakis[(4-benzo[d]thiazol-2-y phenoxy) phthalocyaninato]zinc(II) (**22**) and tetrakis[(4-benzo[d]thiazol- 2-ylthio) phthalocyaninato] zinc(II) (**25**) have been reported [**62**,**63**], the rest of the complexes are reported for the first time.

2.4.1. Complexes 10-12, Scheme 3.1

A mixture of zinc acetate (0.20 g, 1.09 mmol) for **10**, gallium chloride (0.2 g, 1.10 mmol) for **11**, indium chloride (0.2 g, 0.9 mmol) for **12** and   (3,4-bis (3,4-

dicyanophenoxy) benzoic acid (**1**) (0.25 g, 0.62 mmol), DBU (0.1 mL) and 1-pentanol (5 mL) was refluxed at 160 $^{\circ}$C for 24 h under nitrogen atmosphere. The product was precipitated using methanol and collected through centrifugation. The product was washed with methanol, ethanol and 1 M HCl. The dark green product was further purified by reverse phase column chromatography using dichloromethane and methanol (97:3) solvent mixture as eluent. The purified product was dried in enclosed fume hood.

Complex 10: Yield: 0.18 g (45%), IR (ATR): ν (cm^{-1}): 3327 (OH stretch), 3108 (Ar-CH), 1598 (C=O stretch). ^{1}H NMR (400 MHz, DMSO-d$_6$) δ 10.35 (s, 4H, COOH), 8.24 – 8.13 (m, 14H, Ar-H), 8.08 (d, J = 8.0 Hz, 3H, Ar-H), 7.96 (d, J = 2.5 Hz, 3H, Ar-H), 7.60 – 7.53 (m, 7H, Ar-H), 7.48 (t, J = 7.6 Hz, 3H, Ar-H), 7.38 (d, J = 8.7 Hz, 6H, Ar-H). Anal: Calc for C$_{92}$H$_{40}$Zn$_2$N$_{16}$O$_{16}$, C, 62.92; H, 2.30; N, 12.76. Found: C, 63.74; H, 2.25; N, 12.91. UV-vis., λ_{max}/nm (log ε): (DMSO), 688(5.86), 620 (4.75), 361 (5.32). MALDI TOF-MS: Calculated: 1756.22; Found: 1757.38

Complex 11: Yield: 0.15 g (38%), IR (ATR): ν (cm^{-1}): 3276 (OH stretch), 2983 (Ar-CH), 1564 (C=O stretch). 1H NMR (400 MHz, DMSO-d$_6$) δ 10.17 (s, 4H, COOH), 8.09 – 7.98 (m, 14H, Ar-H), 7.95 (d, J = 8.0 Hz, 3H, Ar-H), 7.83 (d, J = 2.5 Hz, 3H, Ar-H), 7.62 – 7.57 (m, 7H, Ar-H), 7.36 (t, J = 7.6 Hz, 3H, Ar-H), 7.14 (d, J = 8.7 Hz, 6H, Ar-H). Anal: Calc for C$_{92}$H$_{40}$Cl$_2$Ga$_2$N$_{16}$O$_{16}$, C, 60.19; H, 2.20; N, 12.21. Found: C, 61.03; H, 2.18; N, 12.37. UV-vis., λ_{max}/nm (log ε): (DMSO), 688(5.12), 620 (4.35), 361 (4.98). MALDI TOF-MS: Calculated: 1835.77; Found: 1836.02.

Complex 12: Yield: 0.13g (29%), IR (ATR): ν (cm^{-1}): 3215 (OH stretch), 3019 (Ar–CH), 1598 (C=O stretch). ^{1}H NMR (600 MHz, DMSO) (δ, ppm): 10.21 (s, J.9.32 Hz, 4H, COOH), 8.25-7.75 (m, 16H, Ar-H), 7.7-7.30 (m, 2H, Ar-H), 7.33 (m, 8H, Ar-H), 7.02-6.91 (m, 10H, Ar-H). Anal: Calc for C$_{92}$H$_{40}$Cl$_2$In$_2$N$_{16}$O$_{16}$, C, 57.37;

H, 2.09; N, 11.64. Found: C, 56.97; H, 1.83; N, 11.75; S, 8.49. UV-vis., λ_{max}/nm (log ε): (DMSO), 695(5.28), 620 (4.12), 361 (4.48). MALDI TOF-MS: Calculated: 1924.02; Found:1929.27 $[M+5]^{+}$.

2.4.2. Complexes 13-15, Scheme 3.2

A mixture of zinc (II) acetate (0.20 g, 1.4 mmol) for **13**, gallium (III) chloride (0.3g, 1.70 mmol) for **14**, Indium (III) chloride (0.2 g, 0.90 mmol) for **15** and 4-(hexadecane-1, 2-dioxyl)-bis(phthalonitrile) (**2**, 0.25 g, 0.49 mmol), DBU (3 drops) and 1-pentanol (5 mL) was refluxed at 140 ^{0}C for 24 h under argon atmosphere. On cooling, methanol was added and the precipitate was collected through centrifugation. The product was washed with methanol, ethanol and diethyl ether. The dark green product was further purified by column chromatography using THF and methanol (98:2) as eluent to give a green product. The purified product was dried in enclosed fume hood.

Complex 13: Yield: 0.09g (24%), IR (ATR): ν (cm^{-1}): 3017 (Ar–CH), 1613 (C=N/C=C), 1261–1138 (C–O–C). ^{1}H NMR (300 MHz, THF-δ_6) δ 8.68 (dd, J = 8.6, 2.3 Hz, 1H), 8.30 (d, J = 8.6 Hz, 1H), 7.88 (dt, J = 7.7, 3.8 Hz, 7H), 7.62 (dd, J = 24.2, 2.6 Hz, 8H), 7.39 (ddd, J = 30.5, 8.8, 2.6 Hz, 7H), 5.06 (dd, J = 6.1, 3.5 Hz, 3H), 4.53 – 4.27 (m, 6H), 2.61 (s, 3H), 1.97 – 1.80 (m, 6H), 1.49 – 1.20 (m, 97H), 0.91 (t, J = 6.6 Hz, 13H). Anal: Calc for $C_{128}H_{152}N_{16}O_8Zn_2$ C, 70.73; H, 7.05; N, 10.31; O, 5.89; Zn, 6.02. Found: C, 71.27; H, 6.88; N, 10.76. UV-vis., λ_{max}/nm (log ε): (THF), 682(5.24), 617 (4.62), 349 (5.18). MALDI TOF-MS: Calculated: 2173.52; Found: 2173.81 $[M+1]^{+}$.

Complex 14: Yield: 0.27g (49%), IR (ATR): ν (cm^{-1}): 3003 (Ar–CH), 1607 (C=N/C=C), 1258–1115 (C–O–C). ^{1}H NMR (300 MHz, THF) δ 8.52 (dd, J = 8.1, 2.5 Hz, 1H), 8.29 (d, J = 8.6 Hz, 1H), 7.74 (dt, J = 8.1, 3.7 Hz, 7H), 7.49 (dd, J =

22.1, 2.6 Hz, 8H), 7.59 (ddd, J = 28.5, 8.3, 2.7 Hz, 7H), 5.12 (dd, J = 6.8, 3.7 Hz, 3H), 4.61 – 4.32 (m, 6H), 2.52 (s, 3H), 1.89 – 1.76 (m, 6H), 1.52 – 1.09 (m, 97H), 0.95 (t, J = 6.9 Hz, 13H). Anal: Calc for $C_{128}H_{152}Cl_2Ga_2N_{16}O_8$ C, 68.24; H, 6.80; Cl, 3.15; Ga, 6.19; N, 9.95; O, 5.68. Found: C, 70.07; H, 6.13; N, 10.27. UV-vis., λ_{max}/nm (log ε): (THF), 697(5.37), 619 (4.69), 352 (5.21). MALDI TOF-MS: Calculated: 2253.07; Found: 2253.97 [M+1]$^+$.

Complex 15 : Yield: 0.21g (47%), IR (ATR): ν (cm^{-1}): 3063 (Ar–CH), 1623 (C=N/C=C), 1271–1185 (C–O–C). ^{1}H NMR (300 MHz, THF) δ 8.65 (dd, J = 8.7, 2.7 Hz, 1H), 8.37 (d, J = 8.5 Hz, 1H), 7.94 (dt, J = 8.0, 3.6 Hz, 7H), 7.58 (dd, J = 26.1, 2.8 Hz, 8H), 7.67 (ddd, J = 29.5, 8.5, 2.6 Hz, 7H), 5.32 (dd, J = 6.9, 3.3 Hz, 3H), 4.81 – 4.42 (m, 6H), 2.60 (s, 3H), 1.92 – 1.81 (m, 6H), 1.57 – 1.13 (m, 97H), 1.03 (t, J = 7.1 Hz, 13H). Anal: Calc for $C_{128}H_{152}Cl_2In_2N_{16}O_8$ C, 65.61; H, 6.54; Cl, 3.03; In, 9.80; N, 9.56; O, 5.46. Found: C, 66.12; H, 6.82; N, 10.02. UV-vis., λ_{max}/nm (log ε): (THF), 705(5.14), 642 (4.72), 356 (5.13). MALDI TOF-MS: Calculated: 2343.26; Found: 2344.02 [M+1]$^+$.

2.4.3.Complexes 16-18, Scheme 3.3

A mixture of zinc acetate (0.2 g, 1.4 mmol) for **16**, gallium (III) chloride (0.2 g, 1.14 mmol) for **17**, indium (III) chloride (0.2 g, 0.90 mmol) for **18** and 4,4'-[(4-formyl-1,2-bis(phenoxyl)diphthalonitrile] (**3**) (0.3 g, 0.77 mmol), DBU (0.2 mL) and 1-pentanol (7 mL) was refluxed at 180 °C for 18 h under an nitrogen atmosphere. Upon cooling, the product was precipitated using methanol and collected by centrifugation. The dark green product was washed with methanol, ethanol and diethyl ether and purified by column chromatography using DCM and methanol (8:2) as eluent. The purified product was dried in an enclosed fume hood.

Complex 16: Yield: 0.21 g (42%), IR (ATR): ν (cm^{-1}): 2892 (Aldehyde C-H stretch), 2832, 1624 (C=O stretch), 1577, 1177. ^{1}H NMR (600 MHz, DMSO) (δ, ppm): 10.08 – 9.99 (s, 4H, aldehyde-H), 8.26 – 8.23 (m, 1H, Ar-H), 8.15 (d, J = 7.1 Hz, 1H, Ar-H), 8.10 (dd, J = 15.1, 7.4, Hz, 6H, Ar-H), 7.99 (dd, J = 8.4, 1.9 Hz, 4H, Ar-H), 7.94 (dd, J = 6.4, 2.2 Hz, 7H, Ar-H), 7.88 (t, J = 3.2 Hz, 4H), 7.59 (t, J = 7.6 Hz, 4H, Ar-H), 7.55 (dt, J = 7.7, 3.9 Hz, 4H, Ar-H), 7.50 (dt, J = 8.2, 4.1 Hz, 5H, Ar-H). Anal. Calc. for $C_{92}H_{40}N_{16}O_{12}Zn_2$: C, 65.30; H, 2.38; N, 13.24. Found: C, 64.71; H, 2.41; N, 13.37. UV-vis, λ_{max}/nm (log ε): (DMSO), 684(5.12), 616 (4.09), 358 (5.02). MALDI TOF-MS: Calculated: 1692.22; Found: 1693.08 [M+1]$^+$.

Complex 17: 0.19 g (38%), IR (ATR): ν (cm^{-1}): 2842 (Aldehyde C-H stretch), 2855, 1708 (C=O stretch), 1564, 1169. ^{1}H NMR (600 MHz, DMSO) (δ, ppm): 10.12 – 9.95 (s, 4H, aldehyde-H), 8.23 – 8.07 (m, 1H, Ar-H), 8.17 (d, J = 7.1 Hz, 1H, Ar-H), 8.22 (dd, J = 15.1, 7.4, Hz, 6H, Ar-H), 7.99 (dd, J = 8.4, 1.9 Hz, 4H, Ar-H), 7.92 (dd, J = 6.4, 2.2 Hz, 7H), 7.75 (t, J = 3.2 Hz, 4H), 7.62 (t, J = 7.6 Hz, 4H), 7.55 (dt, J = 7.7, 3.9 Hz, 4H, Ar-H), 7.53 (dt, J = 8.2, 4.1 Hz, 5H, Ar-H). Anal. Calc. for $C_{92}H_{40}N_{16}O_{12}Cl_2Ga_2$: C, 62.37; H, 2.28; N, 12.65. Found: C, 62.98; H, 2.26; N, 12.72.   UV-vis, λ_{max}/nm (log ε): (DMSO), 691(5.31), 619 (4.11), 347 (5.23). MALDI TOF-MS: Calculated: 1771.84; Found: 1772.94 [M+1]$^+$.

Complex 18:   Yield: 0.26 g (52%), IR (ATR): ν (cm^{-1}): 2835 (Aldehyde C-H stretch), 2799, 1712 (C=O stretch), 1571, 1173. ^{1}H NMR (600 MHz, DMSO) (δ, ppm): 10.07 – 9.98 (s, 4H, aldehyde-H), 8.31 – 8.10 (m, 1H, Ar-H), 8.25 (d, J = 7.1 Hz, 1H, Ar-H), 8.17 (dd, J = 15.1, 7.4, Hz, 6H, Ar-H), 7.96 (dd, J = 8.4, 1.9 Hz, 4H, Ar-H), 7.92 (dd, J = 6.4, 2.2 Hz, 7H, Ar-H), 7.71 (t, J = 3.2 Hz, 4H, Ar-H), 7.69 (t, J = 7.6 Hz, 4H, Ar-H), 7.60 (dt, J = 7.7, 3.9 Hz, 4H, Ar-H), 7.58 (dt, J = 8.2, 4.1 Hz, 5H, Ar-H). Anal. Calc. for $C_{92}H_{40}N_{16}O_{12}Cl_2In_2$: C, 59.35; H, 2.17; N, 12.04. Found:

C, 59.89; H, 2.19; N, 12.15. UV-vis, λ_{max}/nm (log ε): (DMSO), 696(5.21), 626 (4.23), 363 (5.24). MALDI TOF-MS: Calculated: 1861.97; Found: 1863.02 $[M+1]^+$.

2.4.4. Complexes 19-21, Scheme 3.4

A mixture of zinc acetate (0.2 g, 1.4 mmol) for **19**, gallium (III) chloride (0.28g, 1.6 mmol) for **20**, indium (III) chloride (0.20g, 0.90 mmol) for **21** and 4,4'-((4-(benzo[d]thiazol-2-yl)-1,2-bis(phenoxy))diphthalonitrile (**3**) (0.3g, 0.61 mmol), DBU (0.3 mL) and 1-pentanol (10 mL) was refluxed under argon atmosphere at 180 °C for 24 h . The reaction mixture upon cooling was precipitated using methanol and the precipitate was collected by centrifugation. The green product was subsequently washed with methanol, ethanol and diethyl ether and purified by column chromatography using THF and methanol (9:1) as eluent. The product was dried under fume hood.

Complex 19: Yield: 0.12 g, (24%), IR (ATR): (cm^{-1}): 3047 (Ar-C-H stretch), 1477 - 1655 cm^{-1} (C=C stretch), 1496–1560 cm^{-1} (C=N stretch), 748 (C-S stretch). ^{1}H NMR (600 MHz, DMSO) δ 8.15-8.05 (dd, J = 8.5, 5.7 *Hz*, 11H, Ar-H), 8.00–7.98 (d, J = 7.6 *Hz*, 5H, Ar-H), 7.96-7.94 (m, 5H, Ar-H), 7.90–7.88 (m, 4H, Ar-H), 7.80 (m, 4H, Ar-H), 7.55-7.50 (t, J = 6.8 *Hz*, 6H, Ar-H), 7.45-7.40 (t, J = 7.2 *Hz*, 6H, Ar-H), 7.35 (m, 5H, Ar-H), 7.20 (d, J = 7.2 *Hz*, 6H, Ar-H). Anal. Calc. for $C_{116}H_{52}N_{20}O_8S_4Zn_2$: C, 65.94; H, 2.48; N, 13.26, S, 6.07. Found: C, 64.89; H, 3.05; N, 13.93, S, 5.85. UV-vis, λ_{max}/nm (log ε): (DMSO), 681(5.44), 612 (4.77), 341 (5.36). MALDI TOF-MS: Calculated: 2112.86; Found: 2113.92 $[M+1]^+$.

Complex 20: Yield: 0.15 g (26%), IR (ATR): (cm^{-1}): 3052 (Ar-C-H stretch), 1451 - 1636 cm^{-1} (C=C stretch), 1487–1560 cm^{-1} (C=N stretch), 754 (C-S stretch). ^{1}H NMR (600 MHz, DMSO) δ 8.05–7.97 (dd, J = 8.5, 5.7 *Hz*, 11H, Ar-H), 7.95–7.84

(d, $J = 7.6$ *Hz*, 5H, Ar-H), 7.82–7.77 (m, 5H, Ar-H), 7.75-7.68 (m, 4H, Ar-H), 7.65 (m, 4H, Ar-H), 7.56–7.51 (t, $J = 6.8$ *Hz*, 6H, Ar-H), 7.47–7.41 (t, $J = 7.2$ *Hz*, 6H, Ar-H), 7.28 (m, 5H, Ar-H), 7.23 (d, $J = 7.25$ *Hz*, 6H, Ar-H). Anal. Calc. for $C_{116}H_{52}N_{20}O_8S_4Ga_2Cl_2$: C, 63.55; H, 2.39; N, 12.78, S, 5.85. Found: C, 64.81; H, 2.97; N, 13.22, S, 6.09. UV-vis, λ_{max}/nm (log ε): (DMSO), 698(5.59), 624 (5.07), 370 (5.52). MALDI TOF-MS: Calculated: 2192.43; Found: 2193.17 $[M+1]^+$.

Complex 21: Yield: 0.18 g (36%), IR (ATR): (cm^{-1}): 3052 (Ar-C-H stretch), 1459 - 1633 cm^{-1} (C=C stretch), 1491–1564 cm^{-1} (C=N stretch), 751 (C-S stretch). ^{1}H NMR (600 MHz, DMSO) δ 8.11–8.02 (dd, $J = 8.5, 5.7$ *Hz*, 11H, Ar-H), 7.98–7.93 (d, $J = 7.6$ *Hz*, 5H, Ar-H), 7.88–7.83 (m, 5H, Ar-H), 7.78–7.70 (m, 4H, Ar-H), 7.63 (m, 4H, Ar-H), 7.58–7.50 (t, $J = 6.8$ *Hz*, 6H, Ar-H), 7.52–7.46 (t, $J = 7.2$ *Hz*, 6H, Ar-H), 7.32 (m, 5H, Ar-H), 7.29 (d, $J = 7.2$ *Hz*, 6H, Ar-H). Anal. Calc. for $C_{116}H_{52}N_{20}O_8S_4In_2Cl_2$: C, 61.04; H, 2.30; N, 12.27, S, 5.61. Found: C, 62.31; H, 3.07; N, 13.11, S, 6.11. UV-vis, λ_{max}/nm (log ε): (DMSO), 701(5.39), 624 (4.97), 370 (5.24). MALDI TOF-MS: Calculated: 2282.61; Found: 2283.71 $[M+1]^+$.

2.4.5. Complexes 23, 24, Scheme 3.5

A mixture of gallium (III) chloride (0.2 g, 1.14 mmol) for **23**, indium (III) chloride (0.2 g, 0.90 mmol) for **24** and 4-[4-(1,3-benzothiazol-2-yl)phenoxy]phthalonitrile (**5**) (0.3 g, 0.849 mmol), DBU (3 drops) and 1-pentanol (5 mL) was refluxed at 160 ^{0}C for 24 h under argon atmosphere. On cooling, methanol was added and the precipitated was collected through centrifugation. The product was washed with methanol, ethanol and diethyl ether. The dark green product was further purified by column chromatography using chloroform and methanol (95:5) as eluent to give a green powder.

Complex 23: Yield: 0.123g (41%), IR (ATR): ν (cm^{-1}): 3071 (Ar–CH), 1620 (C=N/C=C), 753 (C–S), 1234–1170, 1091–1048 (=C–O–C). ^{1}H NMR (300 MHz, DMSO) (δ, ppm): 8.90 (m, 8H, Ar-H), 7.93 (m, 8H, Ar-H), 7.42 (m, 28H, Ar-H). Anal: Calc. C, 66.43; H, 2.92; Cl, 2.33; N, 11.07; O, 4.21; S, 8.45. Found: C, 66.51; H, 2.85; N, 10.98; S, 8.01. UV-vis., λ_{max}/nm (log ε): (DMSO), 688(5.28), 617 (4.36), 318 (5.12). MALDI TOF-MS: Calculated: 1516.14; Found: 1518.05 [M+2]$^{+}$.

Complex 24 : Yield: 0.27g (54%). IR (ATR): ν (cm^{-1}): 3077 (Ar–CH), 1623 (C=N/C=C), 749 (C–S), 1238–1162, 1087–1048 (=C–O–C). ^{1}H NMR (300 MHz, DMSO-d_6) (δ, ppm): 8.18 (m, 8H, benzothiazole Ar-H), 8.14 (m, 8H, benzothiazole Ar-H), 8.09-8.06 (m, 4H, Ar-H), 8.04 (m, 4H, Ar-H), 7.58 (m, 8H, Ar-H), 7.54 (dd, *J=7.62, 7.58,* 4H, Ar-H), 7.48(m, 8H, Ar-H). Anal. Calc. for C$_{84}$H$_{44}$N$_{12}$S$_4$O$_4$InCl: C, 67.76; H, 3.10; N, 7.18; S, 8.22 Found: C, 66.71; H, 3.55; N, 7.33; S, 7.17. UV-vis, λ_{max}/nm (log ε): (DMSO), 688(5.32), 617 (4.06), 318 (4.72). MALDI TOF-MS: Calculated: 1563.8; Found: 1564.05 [M+1]$^{+}$.

2.4.6. Complexes 26, 27, Scheme 3.5

A mixture of gallium (III) chloride (0.2 g, 1.14 mmol) for **26**, indium (III) chloride (0.2 g, 0.90 mmol) for **27** and 4-{[1H-benzo(d)thiazol-2-yl]thio}phthalonitrile (**6**) (0.3g, 0.85 mmol), DBU (3 drops) and 1-pentanol (5 mL) was refluxed at 160 ^{0}C for 24 h under argon atmosphere. On cooling, methanol was added and the precipitated was collected through centrifugation. The product was washed with methanol, ethanol and diethyl ether. The dark green product was further purified by column chromatography using chloroform and methanol (95:5) as eluent to give a green powder.

Complex 26: Yield: 0.118g (39%). IR (ATR): ν (cm^{-1}): 3027 (Ar–CH), 1611 (C=N/C=C), 757 (C–S), ^{1}H NMR (400 MHz, DMSO) (δ, ppm): 8.61–8.52 (m, 9H, Ar–H), 8.50–8.07 (m, 11H, Ar–H), 8.01–7.24 (m, 8H, Ar–H). Anal: Calc. C, 56.36; H, 2.21; N, 13.15; S, 20.06. Found: C, 57.01; H, 2.08; N, 13.73; S, 20.51. UV-vis., λ_{max}/nm (log ε): (DMSO), 692(5.11), 618 (4.39), 314 (4.48). MALDI TOF-MS: Calculated: 1275.93; Found: 1279.02 [M+3]$^+$.

Complex 27: Yield: 0.18g (36%). IR (ATR): ν (cm^{-1}): 3005 (Ar–CH), 1623 (C=N/C=C), 749 (C–S). ^{1}H NMR (400 MHz, DMSO-d_6) (δ, ppm): 8.52 – 8.48 (m, 9H, Ar-H), 8.45 – 8.40 (m, 11H, Ar-H), 8.01 - 7.54 (m, 8H, Ar–H). Anal. Calc. for $C_{60}H_{28}N_{12}S_8InCl$: C, 58.24; H, 2.44; N, 8.49; S, 19.44. Found: C, 57.99; H, 2.25; N, 8.62; S, 19.57. UV-vis, λ_{max}/nm (log ε): (DMSO), 692(5.11), 618 (4.39), 314 (4.48). MALDI TOF-MS: Calculated: 1323.74; Found: 1324.08 [M+1]$^+$.

2.4.7. Complexes 28-30, Scheme 3.6

A mixture of zinc acetate (0.2 g, 1.4 mmol) for **28**, gallium (III) chloride (0.2 g, 1.14 mmol) for **29**, indium (III) chloride (0.2 g, 0.90 mmol) for **30** and 4-(4-formylphenoxy)phthalonitrile (**7**) (0.3 g, 1.2 mmol) , DBU (0.2 mL) and 1-pentanol (7 mL) was refluxed at 180 °C for 18 h under an nitrogen atmosphere. Upon cooling, the product was precipitated using methanol and collected by centrifugation. The dark green product was washed with methanol, ethanol and diethyl ether and purified by column chromatography using DCM and methanol (8:2) as eluent. The purified product was dried in an enclosed fume hood.

Complex 28: Yield 0.33 g (66%), IR (ATR): ν (cm^{-1}): 2836 (Aldehyde C-H stretch), 2810, 1719 (C=O stretch), 1581, 1190. ^{1}H NMR (600 MHz, DMSO) (δ, ppm): 10.01 (s, 4H), 8.19 (d, J = 8.7 Hz, 4H), 8.05 – 7.96 (m, 12H), 7.60 (d, J = 7.4 Hz,

4H), 7.37 (d, J = 8.2 Hz, 8H). Anal. Calc. for $C_{60}H_{32}N_8ZnO_8$: C, 68.09; H, 3.05; N, 10.59. Found: C, 68.78; H, 3.07; N, 10.68. UV-vis, λ_{max}/nm (log ε): (DMSO), 679 (5.17), 626 (4.18), 363 (4.73). MALDI TOF-MS: Calculated: 1058.36; Found: 1058.97 $[M+1]^+$.

Complex 29: Yield 0.27 g (54%), IR (ATR): ν (cm^{-1}): 2872 (Aldehyde C-H stretch), 2861, 1723 (C=O stretch), 1602, 1159. ^{1}H NMR (600 MHz, DMSO) (δ, ppm): 10.12 (s, 4H), 8.17 (d, J = 8.7 Hz, 4H), 8.03 – 7.96 (m, 12H), 7.49 (d, J = 7.4 Hz, 4H), 7.25 (d, J = 8.2 Hz, 8H). Anal. Calc. for $C_{60}H_{32}N_8O_8ClGa$: C, 65.63; H, 2.94; N, 10.20. Found: C, 64.95; H, 2.96; N, 10.32. UV-vis, λ_{max}/nm (log ε): (DMSO), 689(5.26), 620 (4.31), 367 (4.43). MALDI TOF-MS: Calculated: 1098.14; Found: 1099.02 $[M+1]^+$.

Complex 30: Yield 0.27 g (54%), IR (ATR): ν (cm^{-1}): 2866 (aldehyde C-H stretch), 2839, 1742 (C=O stretch), 1591, 1174. ^{1}H NMR (600 MHz, DMSO) (δ, ppm): 10.06 (s, 4H), 8.22 (d, J = 8.7 Hz, 4H), 8.15 – 7.81 (m, 12H), 7.61 (d, J = 7.4 Hz, 4H), 7.33 (d, J = 8.2 Hz, 8H). Anal. Calc. for $C_{60}H_{32}N_8O_8ClGa$: C, 63.04; H, 2.82; N, 9.80. Found: C, 63.85; H, 2.79; N, 9.69. UV-vis, λ_{max}/nm (log ε): (DMSO), 695(5.12), 627 (4.38), 352 (4.51). MALDI TOF-MS: Calculated: 1143.23; Found: 1144.37 $[M+1]^+$.

2.4.8. Complexes 31-33 (Scheme 3.7)

A mixture of zinc acetate (0.25 g, 1.1 mmol) for **31**, gallium chloride (0.3g, 1.70 mmol) for **32**, indium chloride (0.3 g, 1.36 mmol) for **33** and 4-(2, 4-bis(2, 4-bis(4-aminophenoxy)phenoxyl)phthalonitrile (**8**) (0.3 g, 0.7 mmol), DBU (0.25 mL) and 1-pentanol (5 mL) was refluxed at 170 °C for 24 h under

argon atmosphere. On cooling, methanol was added and the precipitate was collected through centrifugation. The product was washed with methanol, ethanol and diethyl ether. The dark green product was further purified by column chromatography using THF and methanol (96:4) solvent mixture as eluent. The purified product was dried in enclosed fume hood.

Complex 31: Yield: 0.18 g (34%), IR (ATR): ν (cm^{-1}): 3326 (NH$_2$ stretch), 2928 (Ar–CH), 1595, 1473 (C=N stretch of primary amine). ^{1}H NMR (600 MHz, DMSO-d$_6$) (δ, ppm): 8.15-8.00 (m, 10H, Ar-H), 7.96 - 7.80 (m, 13H, Ar-H), 7.65-7.50 (m, 8H, Ar-H), 7.50 – 7.35 (m, 12H, Ar-H), 7.30 – 7.15 (m, 3H, Ar-H), 6.92 – 6.75 (m, 5H, Ar-H), 6.75 – 6.65 (m, 5H, Ar-H), 5.18 (s, 16H, NH$_2$ proton). Anal: Calc for C$_{104}$H$_{72}$N$_{16}$O$_{12}$Zn, C, 69.42; H, 4.57; N, 12.11; O, 10.37; Zn, Found: C, 69.28; H, 4.62; N, 11.97, UV-vis., λmax/nm (log ε): (DMSO), 681(5.08), 616 (4.10), 348 (4.50). MALDI TOF-MS: Calculated: 1803.21; Found: 1802.75.

Complex 32: Yield: 0.19 g (32%), IR (ATR): ν (cm^{-1}): 3401 (NH$_2$ stretch), 3021 (Ar–CH), 1592, 1480 (C=O stretch of primary amine). ^{1}H NMR (400 MHz, DMSO-d$_6$) (d, ppm): 8.21–8.02 (m, 9H, Ar–H), 7.95–7.86 (m, 3H, Ar–H), 7.65–7.60 (m, 6H, Ar–H), 7.49 –7.38 (m, 3H, Ar–H), 7.30–7.26 (m, 7H, Ar–H), 6.91–6.80 (m, 14H, Ar–H), 6.71–6.59 (m, 14H, Ar–H), 5.49-4.95 (s, 16H, NH$_2$ proton). Anal. calc. for C$_{104}$H$_{72}$N$_{16}$O$_{12}$Ga, C, 67.78; H, 3.94; N, 12.16; found: C, 69.11; H, 3.65; N, 11.99, UV-vis., λ_{max}/nm (log ε): (DMSO), 687 (5.09), 617 (4.13), 354 (4.92). MALDI TOF-MS: calculated: 1842.91; found: 1843.20.

Complex 33: Yield: 0.22 g (36%), IR (ATR): ν (cm^{-1}): 3276 (NH$_2$ stretch), 2930 (Ar–CH), 1592, 1477 (C=O stretch of primary amine). ^{1}H NMR (600 MHz, DMSO-d$_6$) (d, ppm): 8.17–8.02 (m, 9H, Ar–H), 7.93–7.86 (m, 3H, Ar–H), 7.65–7.64 (m,

6H, Ar–H), 7.48 –7.36 (m, 3H, Ar–H), 7.30–7.24 (m, 7H, Ar–H), 6.90–6.80 (m, 14H, Ar–H), 6.71–6.59 (m, 14H, Ar–H), 5.49-5.00 (s, 16H, NH_2 proton). Anal. calc. for $C_{104}H_{72}N_{16}O_{12}In$, C, 65.53; H, 3.91; N, 11.76; found: C, 64.96; H, 4.06; N, 11.25, UV-vis., λ_{max}/nm (log ε): (DMSO), 691 (5.14), 620 (4.15), 356 (4.83). MALDI TOF-MS: calculated: 1887.69; found: 1888.09.

2.4.9. Complex 34-36 (Scheme 3.8)

A mixture of 4-(4-(1,3-benzo[d]thiazol-2-yl)phenoxy)phthalonitrile (**5**) (1 g, 2.83 mmol), 2-(4-(3,4-dicyanophenoxy)phenoxy)acetic acid (**9**) (0.28 g, 0.94 mmol), zinc acetate (0.4 g, 2.19 mmol) for **34**, gallium chloride (0.35 g, 1.99 mmol) for **35**, indium chloride (0.20 g, 0.90 mmol) for **36**, DBU (3 drops) and 1-pentanol (10 mL) was refluxed at 140 ^{0}C for 24 h under argon atmosphere. On cooling, methanol was added and the precipitate was collected through centrifugation. The product was washed with methanol, ethanol and diethyl ether. Column chromatography showed several fractions using THF and methanol (98:2) as eluent. The desired A_3B product was identified through mass spectrometry and ^{1}HNMR. The purified product was dried in enclosed fume hood.

Complex 34: Yield: 0.28g (21%). IR (ATR): ν (cm^{-1}): 3395 (COOH), 3005 (Ar–CH), 1623 (C=N/C=C), 735 (C–S). ^{1}H NMR (600 MHz, DMSO- d_6) (δ, ppm): 10.25 (s, 1H, COOH proton), 8.25 – 8.19 (m, 6H, Ar-H), 8.15 - 8.10 (m, 6H, Ar–H), 8.09 - 8.01 (d, *J = 8.68* Hz, 3H, Ar–H), 7.98 - 7.90 (d, *J = 8.68* Hz, 3H, Ar–H), 7.60 – 7.55 (m, 13H, Ar–H), 7.50 - 7.45 (t, *J = 8.22* Hz, 3H, Ar–H), 7.40-7.30 (m, 6H, Ar-H), 4.18 - 4.10 (s, 2H, CH_2) . Anal. Calc. for $C_{79}H_{43}N_{11}$: C, 66.83; H, 3.05; N, 10.85; S, 6.78. Found: C, 67.57; H, 3.08; N, 10.74; S, 6.85. UV-vis, λ_{max}/nm (log ε): (DMSO), 680(5.31), 610 (4.15), 319 (4.38). MALDI TOF-MS: Calculated: 1419.42; Found: 1417.82 [M+1]$^+$.

Complex 35: Yield: 0.28 g (19%). IR (ATR): ν (cm^{-1}): 3183 (COOH-stretch) 2987 (Ar–CH), 1704 (C=N/C=C), 745 (C–S). ^{1}H NMR (600 MHz, DMSO-d_6) (δ, ppm): 10.23 (s, 1H, COOH proton), 8.22 – 8.18 (m, 6H, Ar-H), 8.13 - 8.11 (m, 6H, Ar–H), 8.09 - 8.01 (d, $J = 8.68$ Hz, 3H, Ar–H), 7.96 - 7.91 (d, $J = 8.68$ Hz, 3H, Ar–H), 7.61 – 7.56 (m, 13H, Ar–H), 7.50 - 7.45 (t, $J = 8.22$ Hz, 3H, Ar–H), 7.42-7.30 (m, 6H, Ar-H),   4.08 - 4.02 (s, 2H, CH$_2$) .Anal. Calc. for C$_{79}$H$_{43}$N$_{11}$S$_3$: C, 65.01; H, 2.97; N, 10.56; S, 6.59. Found: C, 66.07; H, 2.86; N, 10.78; S, 6.61. UV-vis, λ_{max}/nm (log ε): (DMSO), 689(5.23), 615 (4.28), 319 (5.08).   MALDI TOF-MS: Calculated: 1457.15; Found: 1458.01 [M+1]$^+$.

Complex 36: Yield: 0.31g (21%). IR (ATR): ν (cm^{-1}): 3275 (COOH-stretch), 2988 (Ar–CH), 1714 (C=N/C=C), 749 (C–S). ^{1}H NMR (600 MHz, DMSO-d_6) (δ, ppm): 10.25 (s, 1H, COOH proton), 8.21 – 8.19 (m, 6H, Ar-H), 8.11 - 8.10 (m, 6H, Ar–H), 8.09 - 8.00 (d, $J = 8.68$ Hz, 3H, Ar–H), 7.97 - 7.91 (d, $J = 8.68$ Hz, 3H, Ar–H), 7.62 – 7.58 (m, 13H, Ar–H), 7.50 - 7.45 (t, $J = 8.22$ Hz, 3H, Ar–H), 7.41-7.32 (m, 6H, Ar-H),   4.07 - 4.00 (s, 2H, CH$_2$).   Anal. Calc. for C$_{79}$H$_{43}$N$_{11}$S$_3$: C, 63.06; H, 2.88; N, 10.24; S, 6.39. Found: C, 62.91; H, 2.71; N, 9.89; S, 6.08. UV-vis, λ_{max}/nm (log ε): (DMSO), 693(5.03), 617 (4.57), 319 (4.97).   MALDI TOF-MS: Calculated: 1503.12; Found: 1504.22 [M+1]$^+$.

2.5. Procedure for conjugation of phthalocyanines with nanoparticles

2.5.1. Covalent linkage of phthalocyanine to nanoparticles to form Pc-NPs (complexes 10-12 and 31-36), Scheme 3.9 and 3.10

The synthesis of GSH capped CdTe [145], CdTeSe, CdTeSe/ZnO [146], GQDs [147], AuNPs and AgNPs [148] has been reported.

The conjugation was performed follows: complexes **10** (0.025 g, 0.014 mmol), **11** (0.025 g, 0.014 mol), and **12** (0.025 g, 0.13 mol), **34** (0.020 g, 0.01 mmol), **35** and **36** (0.03 g, 0.02 mmol) each were separately   dissolved in 10 ml of DMF, followed by addition of DCC (0.015 g, 0.072 mmol) to activate the carboxylic acid functional group in **10**-**12** and **34**-**36**. The reaction mixture was stirred for 48 h at ambient temperature. After this time, DMAP (0.025 g, 0.082 mmol) and 0.01 g of glutathione (GSH) functionalized CdTe QDs were added (**Scheme 3.9**) and the reaction was allowed to stir for further 48 h at ambient temperature. Complexes **10**-**12** was also linked to amine functionalized GQDs and **12** to GSH capped CdTeSe, CdTeSe/ZnO, AuNPs and AgNPs while **31** and **34** were also linked to GSH capped AuNPs and AgNPs, all using the same procedure.

For the covalent linkage of **31**-**33** that possess amine functional group, a 0.05g each of the GSH functionalized CdTe were separately dissolved in 10 ml of DMF, followed by addition of DCC (0.015 g, 0.072 mmol) to activate the carboxylic acid of the nanoparticles (**Scheme 3.10**). After this time, a mixture of each of **31** (0.04g, 0.02 mmol), **32** (0.03g, 0.02 mmol) or **33** (0.03g, 0.02 mmol) and DMAP (0.025 g, 0.082 mmol) were added and allowed to stir for further 48 h. The formed nanoconjugates were precipitated out of solution with methanol and collected through centrifugation, washed several times using ethanol and dried in enclosed fume hood.

2.5.2.Surface assembly of phthalocyanine on metallic nanoparticles (**complexes 19-27**, **31** and **34**), **Scheme 3.11**

The synthesis of olyamine capped AuNPs and AgNPs was has been reported [**148**]. The attachment of the phthalocyanine onto the nanoparticles was carried out using reported method [**148**] with slight modification. Briefly, 1 mg of the oleyamine (OA) functionalized AuNPs or AgNPs in 2 ml of toluene was added to a refluxing solution of 5 mg of each of the complexes in 10 ml of toluene and the mixture was allowed at reflux for 2 h. The mixture was cooled to the room temperature while stiring and subsequently left stirring at room temperature for a further 12 h for ligand exchange of loosely bound OA on the surface of nanoparticles with the complexes. The mixture was diluted with methanol and the Pc-nanoconjugates were collected by centrifugation at 500 rpm for 10 min. The products were washed with methanol and ethanol and then dried in enclosed fumehood.

2.6.   Preparation of polymer thin films (complexes 13-18, 22-30)

Polystyrene (200 mg) was weighed into clean vials containing 4 mL of chloroform and the mixture was sonicated for 30 min. Then 1×10^{-2} moles of each of the complexes (**13**-**15**, **16**-**18**, **22**-**30**) were separately dissolved in 1 mL of chloroform and transferred into the vials, followed by stirring for 24 h. A homogenous mixture of Pc-polystyrene was coated on thin glass slides. The coated glass slides were air dried to remove the chloroform. The resultant thin films are labelled as **13**-TF, **14**-TF, **15**-TF, **16**-TF, **17**-TF, **18**-TF, **22**-TF, **23**-TF, **24**-TF, **25**-TF, **26**-TF, **27**-TF, **28**-TF, **29**-TF and **30**-TF respectively. The knife edge attachment of a Bruker D8 Discover X-ray diffraction (XRD) instrument was used to determine that the thicknesses of the thin films. The thickness of the thin films was reported as 0.015

mm (**13**-TF), 0.021 mm (**14**-TF), 0.017 mm (**15**-TF), 0.031 mm (**16**-TF), 0.027 mm (**17**-TF), 0.032 mm (**18**-TF), 0.044 mm (**28**-TF), 0.027 mm(**29**-TF) and 0.039 mm (**30**-TF), 0.014 mm (**3**-TF), 0.019 mm (**4**-TF), 0.016 mm (**5**-TF) and 0.014 mm (**6**-TF).

Chapter three: Synthesis and characterization

Chapter four: Photophysicochemical properties

Chapter five: Nonlinear optical properties

Chapter six: Conclusion and future perspective

The results discussed in the subsequent chapters have been published or accepted for publication in peer-reviewed journals.

1. **N. Nwaji**, D. O. Oluwole, J. Mack, M. Louzada, S. Khene, J. Britton, T. Nyokong Improved nonlinear optical behaviour of indium ball type phthalocyanine linked to glutathione capped nanoparticles *Dyes Pigm*ents 140 (2017) 417-430

2. **N. Nwaji**, J. Mack, J. Britton, T. Nyokong, Synthesis, Photophysical and Nonlinear Optical Properties of a Series of Ball-type Phthalocyanines in Solution and Thin Films. *New J. Chem*., 41 (2017) 2020-2028

3. **N. Nwaji**, O. M. Bankole, J. Britton, T. Nyokong, Photophysical and Nonlinear Optical Study of Benzothiazole Substituted Phthalocyanine in Solution and Thin Film, *J. Porphyrins Phthalocyanines* 21 (2017) 263-272

4. **N.Nwaji**, B. Jones, J. Mack, D. O. Oluwole, T. Nyokong Nonlinear optical dynamics of benzothiazole derivatized phthalocyanines in solution, thin films and when conjugated to nanoparticles, *J. Photochem. Photobiol. A*: 346 (2017) 46-59

5. **N. Nwaji**, T. Nyokong, Nanosecond optical nonlinearities in low symmetry phthalocyanine nanoconjugates studied using the Z-scan technique *J. Lumn.*, 192 (2017) 1167–1179

6. **N. Nwaji**, John Mack, T. Nyokong, 4-Bis (4-aminophenoxy)phenoxy derivitized phthalocyanine conjugated to metallic nanoparticles, searching for enhanced optical limiting materials, *New J. Chem* **14** (2017) 14351-14361

7. **N. Nwaji**, J. Mack, T. Nyokong, Photophysical and strong optical limiting properties of ball-type phthalocyanines dimers and their monomeric analogues, *J. Photochem. Photobiol A*, 352 (2018) 73-85

8. **N. Nwaji**, O. Achadu, T. Nyokong, Photo-induced resonance energy transfer and nonlinear optical response in ball-type phthalocyanine conjugated to semiconductor and graphene quantum dots, *New J. Chem.,* 42 (2018) 6040--6050

9. **N. Nwaji**, J. Mack, T. Nyokong Enhanced Nonlinear optical response of Benzothiazole substituted ball-type phthalocyanines in the presence of metallic nanoparticles, *Optical Mat.*, 82 (2018) 93-103

10. **N. Nwaji**, S. Dingiswayo, J. Mack, T. Nyokong, Phototophysical and enhanced nonlinear optical response in assymetric benzothiazole substituted phthalocyanine covalently linked to semiconductor quantum, *Spectrochim. Acta.*, 204 (2018) 629–639

11. **N. Nwaji**, J. Mack, T. Nyokong, Optical limiting study in aminophenoxy substituted phthalocyanine in the presence of semiconductor quantum dots, *J. Luminescence*, 203 (2018) 247–256

Side publications

12. G. Fomo, **N. Nwaji**, T. Nyokong, Low symmetric metallophthalocyanine modified electrode via click chemistry for simultaneous detection of heavy metals, *J. Electroanal. Chem 813 (2018) 58-66*

13. B. P. Ngoy, Z. Hlatshwayo, **N. Nwaji**, G. Fomo, J. Mack, T. Nyokong Photophysical and optical limiting properties at 532 nm of BODIPY dyes with

p-benzyloxystyryls at the 3,5-positions, *J. Porphyrins Phthalocyanines*, 22 (2018) 413–422

14. E. Dube, **N. Nwaji**, D. O. Oluwole, J. Mack, T. Nyokong, Investigation of photophysicochemical properties of zinc phthalocyanines conjugated to metallic nanoparticles, *J. Photochem. Photobiol A*, 349 (2017) 148–161

15. E. Dube, D. O. Oluwole, **N. Nwaji**, T. Nyokong**,** Glycosylated zinc phthalocyanine-gold nanoparticle conjugates for photodynamic therapy: Effect of nanoparticle shape, *Spectrochim Acta*, 203 (2018) 85-95**.**

16. N. Nwahara, **N. Nwaji**, T. Nyokong, Enhanced photophysical parameters of folate-targeted phthalocyanine-nanoparticles composites as potential drug delivery nanosystems, *J. Photochem. Photobiol***.** submitted 31-03-2018

17. E. Dube, **N. Nwaji**, J. Mack, T. Nyokong, Photophysicochemical behavior of symmetric and asymmetric zinc phthalocyanines, surface assembled onto gold nanotriangles, *New J. Chem.*, 42 (2018) 14290 - 14299

18. D. O. Oluwole, **N. Nwaji**, L. Nene, L. Mokone, E. Dube, T. Nyokong, Novel nano–dyad of homoleptic sandwich–type phthalocyanines with nitrogen doped graphene quantum dots for nonlinear optics, *New J. Chem*. 42 (2018) 10124-10133

19. R. Matshitse**, N. Nwaji,** M. Mananga, E. Prinsloo and T. Nyokong, Effect of number of positive charges on the photophysical and photodynamic therapy activities of quarternary benzothiazole substituted zinc phthalocyanine, *J. Photochem. Photobiol A*, (In press)

20. N. Nnaji**, N. Nwaji,** G. Fomo, J. Mack and T. Nyokong, Inhibition of chloride ion induced aluminium corrosion using benzothiazole derived phthalonitrile and phthalocyanine, *Coordination chemistry*, (Submitted)

21. Dube, D. O. Oluwole, **N. Nwaji**, E. Prinsloo, T. Nyokong Combined photothermal and photodynamic therapy effects of phthalocyanine-gold speckled silica nanoparticle conjugates, *J. Photochem. Photobiol. A*, submitted 16-07-2018.

Chapter three: Synthesis and characterization of Pcs and conjugates

The synthesis of complexes **22** and **25** have already been reported elsewhere [**62,63**], hence will not be discussed here. The rest of the complexes (**10-12**, **13-15**, **16-18**, **19-21**, **23**, **24**, **26**, **27**, **28-30**, **31-33**, **34-36**) will be discussed in detail.

3.1.   Phthalocyanines alone
3.1.1. Complexes 10-12

The synthetic route for complexes **10**-**12** is shown in **Scheme 3.1**. The structural characterization of this complexes using ^{1}H-NMR, Uv-vis, infra-red, MALDI-TOF mass spectroscopies and elemental analysis agreed well with the proposed structures. The formation of **10**-**12** was confirmed by the disappearance of CN peak observed at 2230 cm^{-1} in the FT-IR spectrum of **1**. ^{1}H NMR spectrum for complexes **10, 11** and **12** showed the singlet proton of the carboxylic acid at 10.35, 10.17 and 10.21 ppm respectively, which were integrated into a total of 4 protons for each. The aromatic protons appear at 8.24-7.38 ppm for **10**, 8.09 – 7.14 for **11** and 8.25-6.91 ppm for **12**, all integrated to give anticipated number of 36 protons (**Fig. A1**, **appendix**).

The Uv-vis of the complexes showed a monomeric behavior with single intense Q band, typical of metalated Pc with degenerate D_{4h} symmetry[**149**] (**Fig. 3.1**) The Q band maxima of gallium complex **11** and indium complex **12** lie at longer wavelength at 689 nm and 695 nm, respectively, more red-shifted compared to 682 nm observed for **10** containing zinc (**Table 3.1**). Red shifts in the Q band are typical for MPcs containing central metals with big atomic radius in the Pc cavity [**150**].
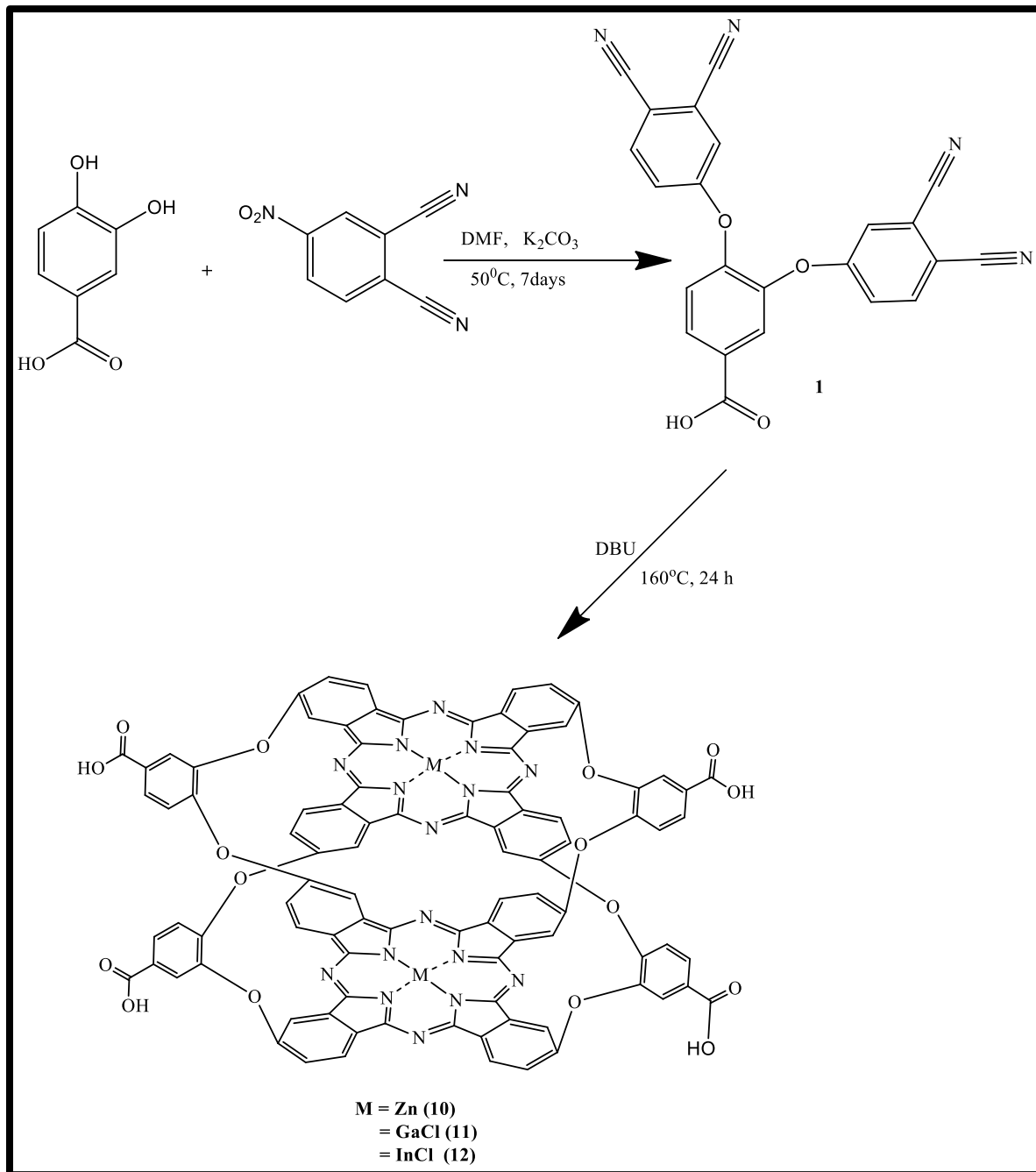
Scheme 3.1: Synthetic route for ball-type complexes 10-12

Table 3.1: Absorption wavelengths of ball-type Pcs 10-21 in DMSO

Complex	λ_{max}
Group 1 bearing Zinc central metal	
10	682
13	681
16	682
19	681
Group 2 bearing Gallium central metal	
11	689
14	697
17A	691
17B	689
20	698
Group 3 bearing Indium central metal	
12	695
15	707
18	696
21	701
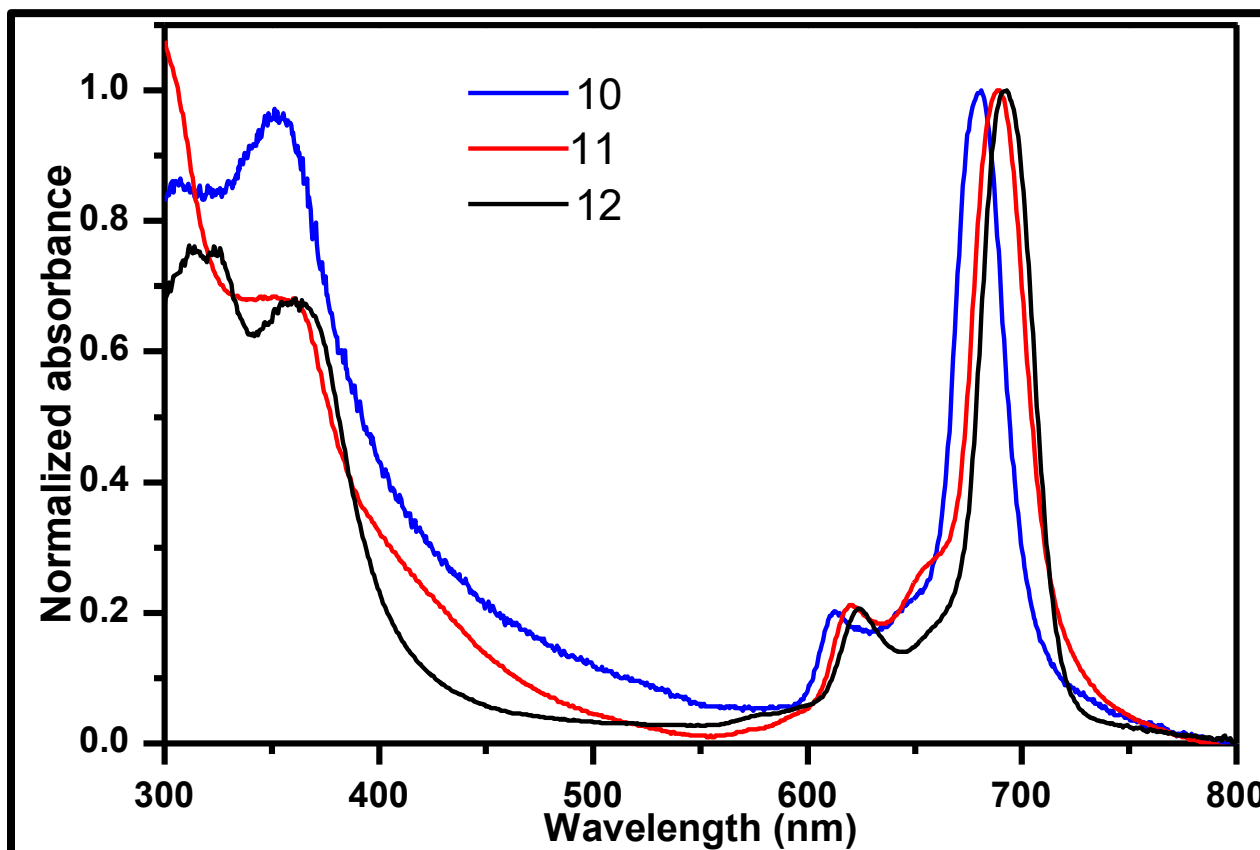
Figure 3.1: Electronic absorption spectra of 10-12 in DMSO

A splitting of molecular orbitals as well as lowering of symmetry is expected to result in splitting or broadening of the Q band due to strong intermolecular interaction between the Pc rings in ball-type Pcs [**69,151**]. There was no observed splitting in Q band of **10**-**12**. Non splitting of the Q band in ball-type Pcs is expected with dimers having eclipsed rather than staggered conformation [**70**] and have been observed before [**152**].

The absorption, excitation and fluorescence spectra of **10**-**12** are shown in **Fig. 3.2**. The absorption spectrum is similar to the excitation spectrum, and both are mirror images of the emission spectrum, suggesting that the nuclear configuration of the ground state is not affected by excitation wavelength of interest.
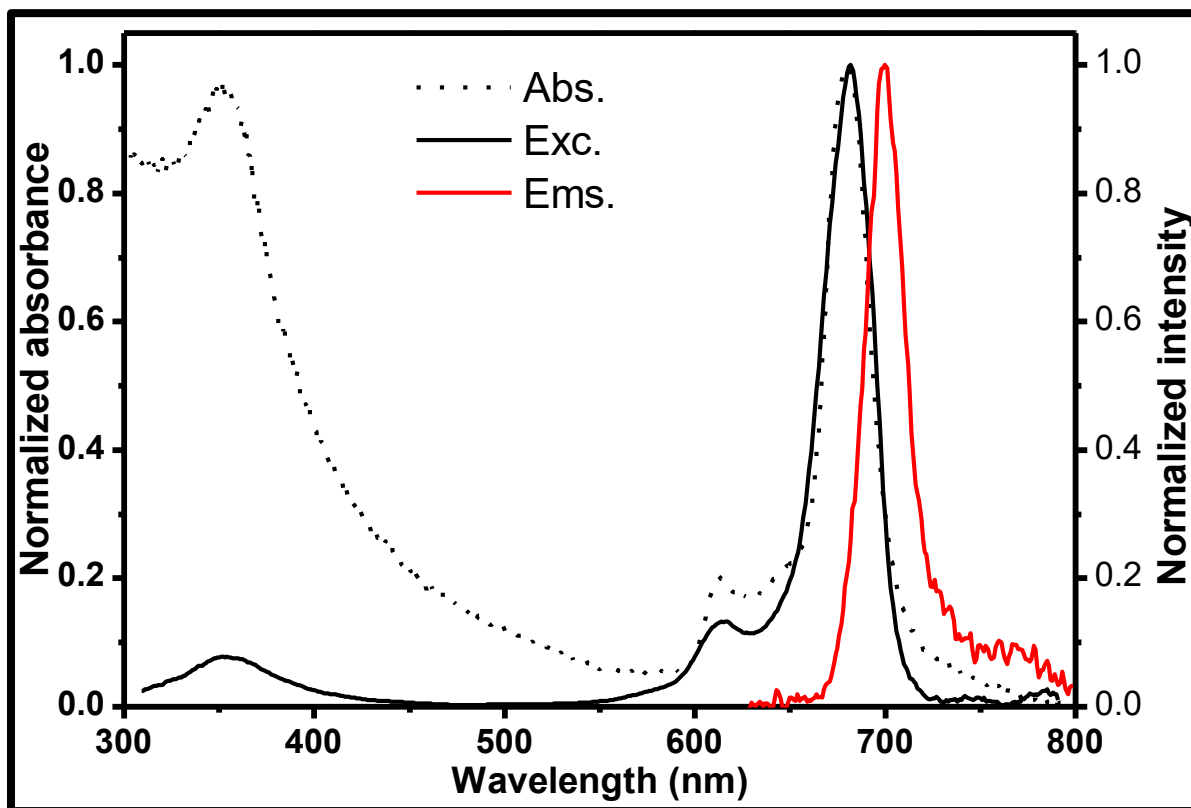
Figure 3.2: Absorption, fluorescence emission and excitation spectra of 10 in DMSO.

3.1.2. Complexes 13-15

Scheme 3.2 shows the pathway for the synthesis of hexadecane alkyl chain bearing ball-type complexes. The choice of long alkoxyl chain is due to its electron donating nature which can lead to increase in electron density and stabilizes the Pcs ring as well as to provide –C-O-C- bonds for rotational flexibility, which could result in symmetry distortion that favours NLO response. The structural analysis of the complexes was consistent with the proposed structure shown in **Scheme 3.2**. The ^{1}H NMR spectra for complex **13**-**15** were similar with only slight variation in chemical shift (**Fig A2, appendix**). The aromatic protons from the Pc ring were observed between 8.68 ppm – 7.39 ppm with corresponding signals integrated to give a total of 24 protons while the long alkyl chain length protons resonate around 5 ppm – 1 ppm integrated to give total of 128 protons. The elemental composition

was within the expected values. The expected mass to charge ration (m/z) for **13**, **14** and **15** were 2173.52, 2253.07 and 2343.26 respectively while the observed were 2173.81, 2253.97 and 2344.02 respectively all corresponding to $(M+1)^+$.
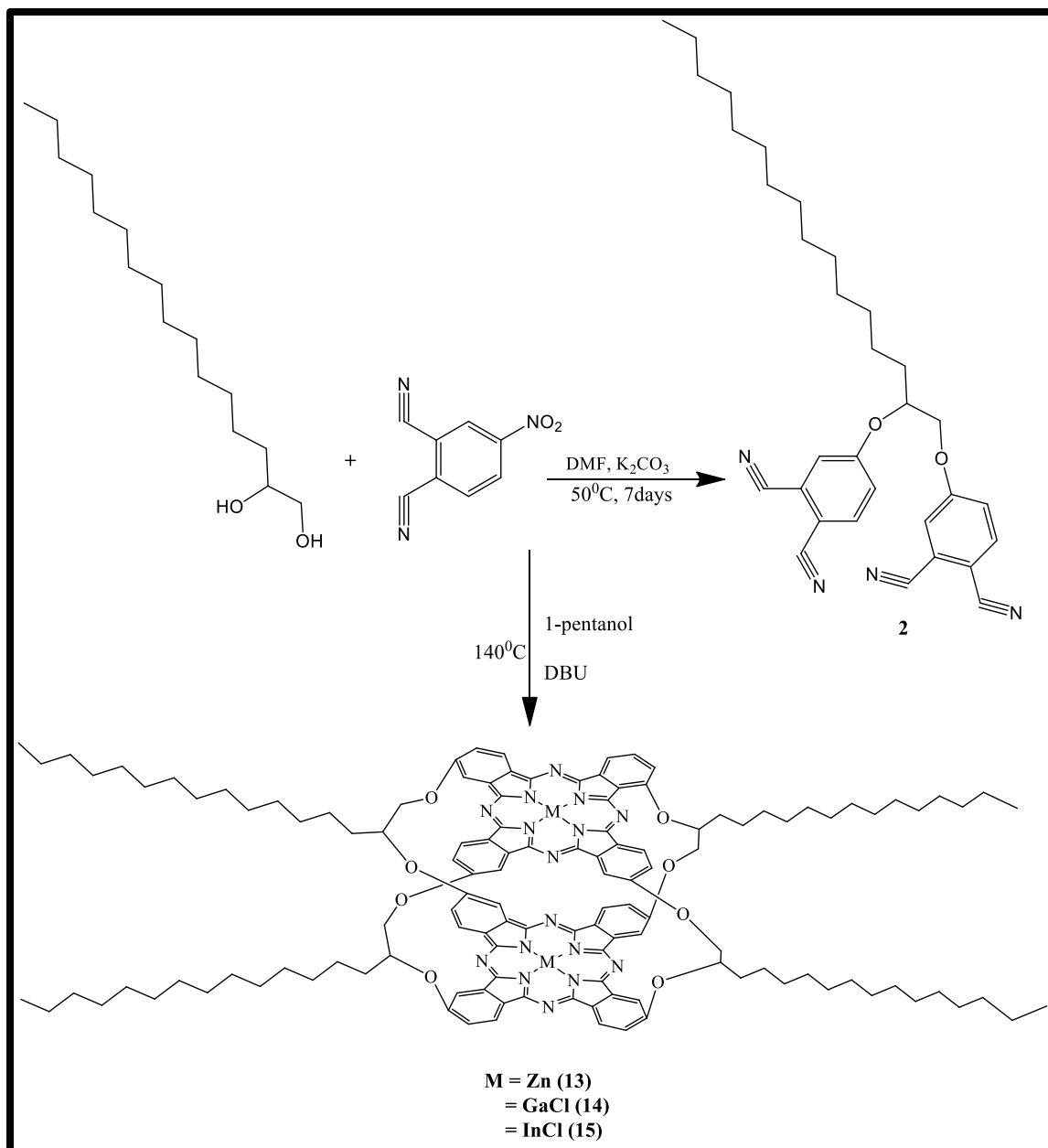
Scheme 3.2: Synthetic route for preparation of complex 13-15

A red shifting of absorption spectra as the atomic weight increases was observed (**Fig. 3.3**) as observed for **10**-**12**. The Q-bands were observed at 681 nm, 699 nm and 707 nm respectively for **13**, **14** and **15** respectively (**Table 3.1**),
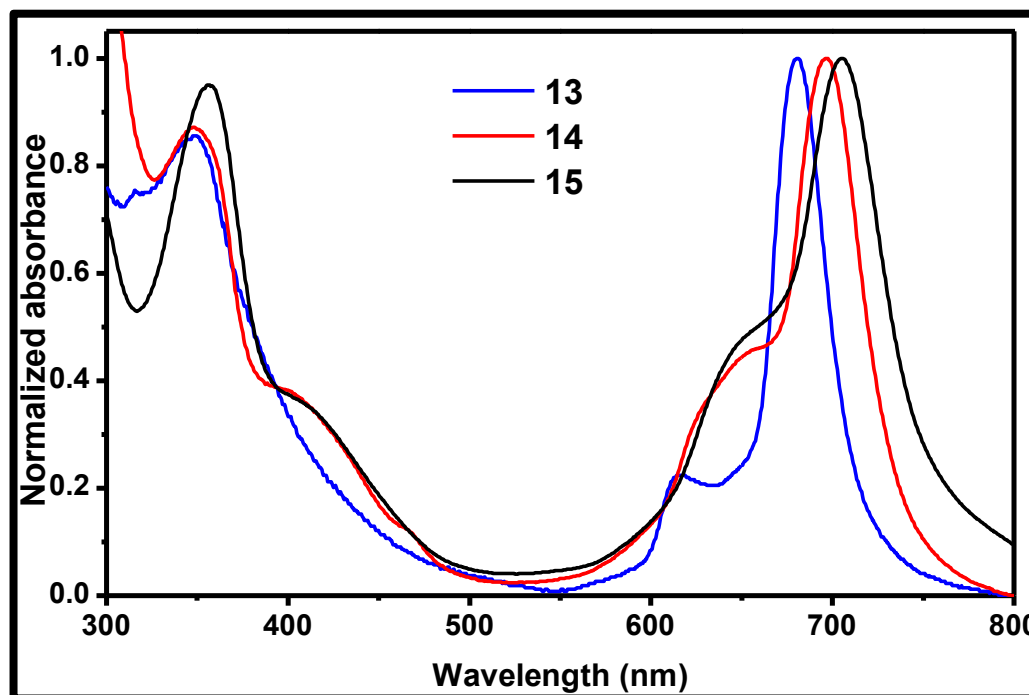
Figure 3.3: Absorption spectra for 13-15. Solvent = DMSO

The pronounced broadening witnessed for **14** and **15** compared to **13** could be due to the usual aggregation [**153**]. Ideally, aggregation should be less expected for **14** and **15** since axial ligation tend to reduce aggregation.

To probe into the probable cause of broadening, the absorption spectra of **13**–**15** were recorded at different concentrations in solution. The plots of concentration against absorbance obeyed the Beer–Lambert law confirming non-aggregated species (**Fig. 3.4**, using **13** and **14** as representatives).
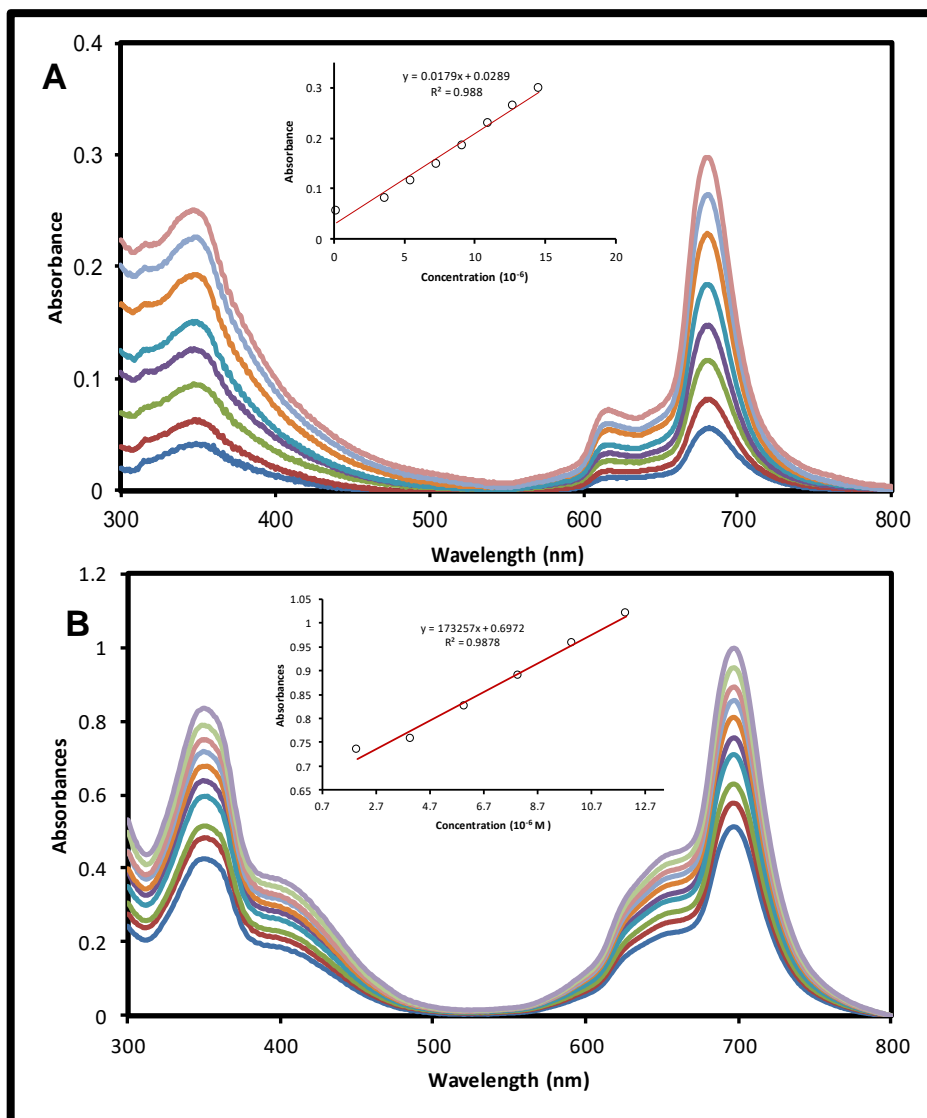
Figure 3.4: Absorption changes of (A) 13 and (B) 14 in solution at different concentrations. Solvent: DMSO

This indicate that the broadening of the Q band observed for **14** and **15** is not due to aggregation.

When **13**-**15** were formulated into polystyrene thin films, further broadening of the spectral bands was observed due aggregation of phthalocyanines in solid state (**Fig. 3.5**)
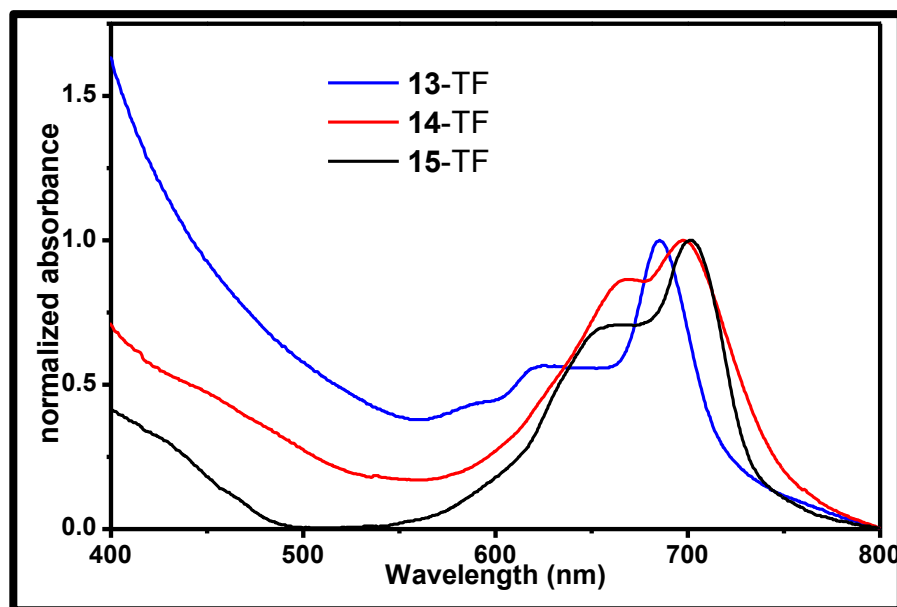
Figure 3.5: Absorption spectra of 13-15 in polymer thin films

Aggregation in thin films (TF) was judged by red-shifting of the Q band and the presence of high energy peaks at 620, 650 and 655 nm in **13**-TF, **14**-TF and **15**-TF respectively with loss of B bands (**Fig. 3.5**). A lack of clear B band and red-shifting of Q band peaks is typical of the solid-state spectra of phthalocyanines[**154**].

The principles of MCD spectroscopy is based on the analyses of the three Faraday terms, $\mathcal{A}_1$, $\mathcal{B}_0$ and $\mathcal{C}_0$ which provide information on state degeneracies and band polarizations that cannot be derived from the UV-visible absorption spectrum alone [**155**]. The MCD spectrum of **13** (**Fig. 3.6**) is very similar to what would normally be expected for a monomeric ZnPc [**156**] since pseudo-$\mathcal{A}_1$ terms are observed in the Q and B band regions with cross-over point at 681 nm that correspond to 681 nm

absorption maxima observed in Uv-vis spectra. The TD-DFT calculation for **13** (**Fig 3.6**) predict a single intense Q band transition of Gouterman's four orbital model [**65**] similar to what would be observed for monomeric $M^{11}Pc$ complexes. A similar spectrum was observed for **14** and **15** (**Fig. 3.6** for **14**, **Table A1, appendix**) with some minor differences in the B band region resulting from the effect of axial chloride ligands on the energy of $2a_{2u}$ molecular orbital of the parent D_{4h} symmetry ring.
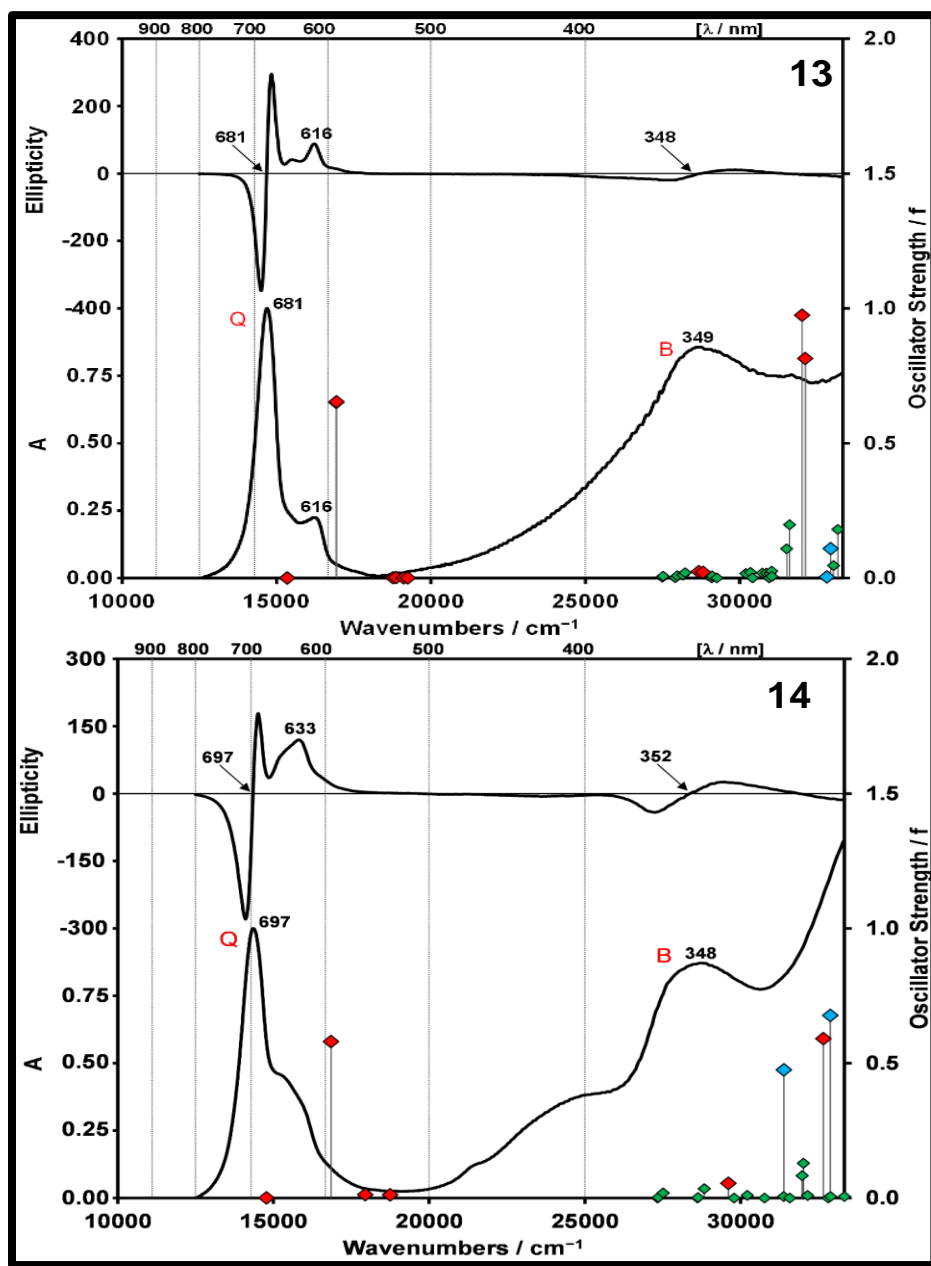
Figure 3.6: Absorption and MCD spectra of 13 and 14 in THF. The calculated TD-DFT spectrum of the isomer of 13 and 14 with four 3,3-position attachments is plotted against a secondary axis. Red diamonds are used to highlight bands associated with the Q and B bands of Gouterman's 4-orbital model while blue diamonds are used for transitions associated with what would be the $2a_{2u}$ MO of the Pc rings, if D_{4h} symmetry were assumed.

The frontier molecular orbital showed a decrease in energy gap between the highest occupied molecular orbital (HOMO) and lowest unoccupied molecular orbital (LUMO) in order of **13** > **14** > **15** (**Fig. 3.7**), which account for the red-shift in Q band absorption maxima of **14** and **15** compared to **13**. It is pertinent to note that the point of attachment of the bridging substituents in ball-type Pcs can either be in 3,3 or 3,4-position, hence there is scope for isomers.
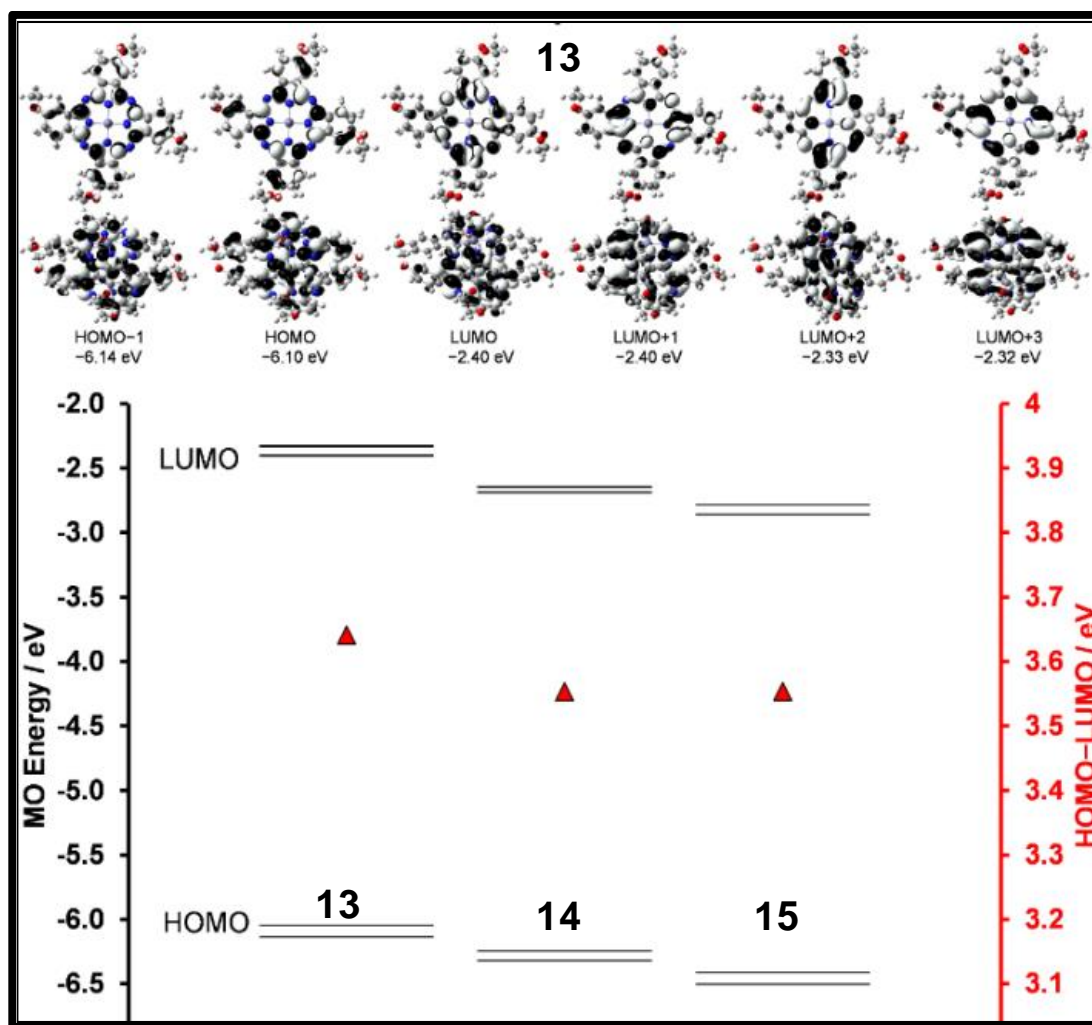
Figure 3.7: The angular nodal patterns and energies of the six frontier π-MOs of the isomer of 13 that are associated with the Q transition of Gouterman's 4-orbital model are shown from two perspectives (top). The MO energies and HOMO–LUMO gaps for the isomers of 13–15 with four 3,3-position attachments (bottom). The HOMO–LUMO gaps are highlighted with red diamonds and are plotted against a secondary axis.

To investigate if there are significant differences in spectra of the isomers, six different structures were modelled for **13**, two with either 3,3 or 3,4 attachments and four mixed structures arranged in 3:1, oppositely and adjacently arranged 2:2, and 1:3 arrangement (**Fig. 3.8**). Their energies were found to lie within 15 kcal mol^{-1}, so it is reasonable to anticipate that a mixture of these isomers is formed in each case. The calculated TD-DFT spectra are similar enough (**Fig 3.8**, **Table A1, appendix**) that it is reasonable to anticipate a single dominant pseudo-A_1 term in the Q and B band regions.
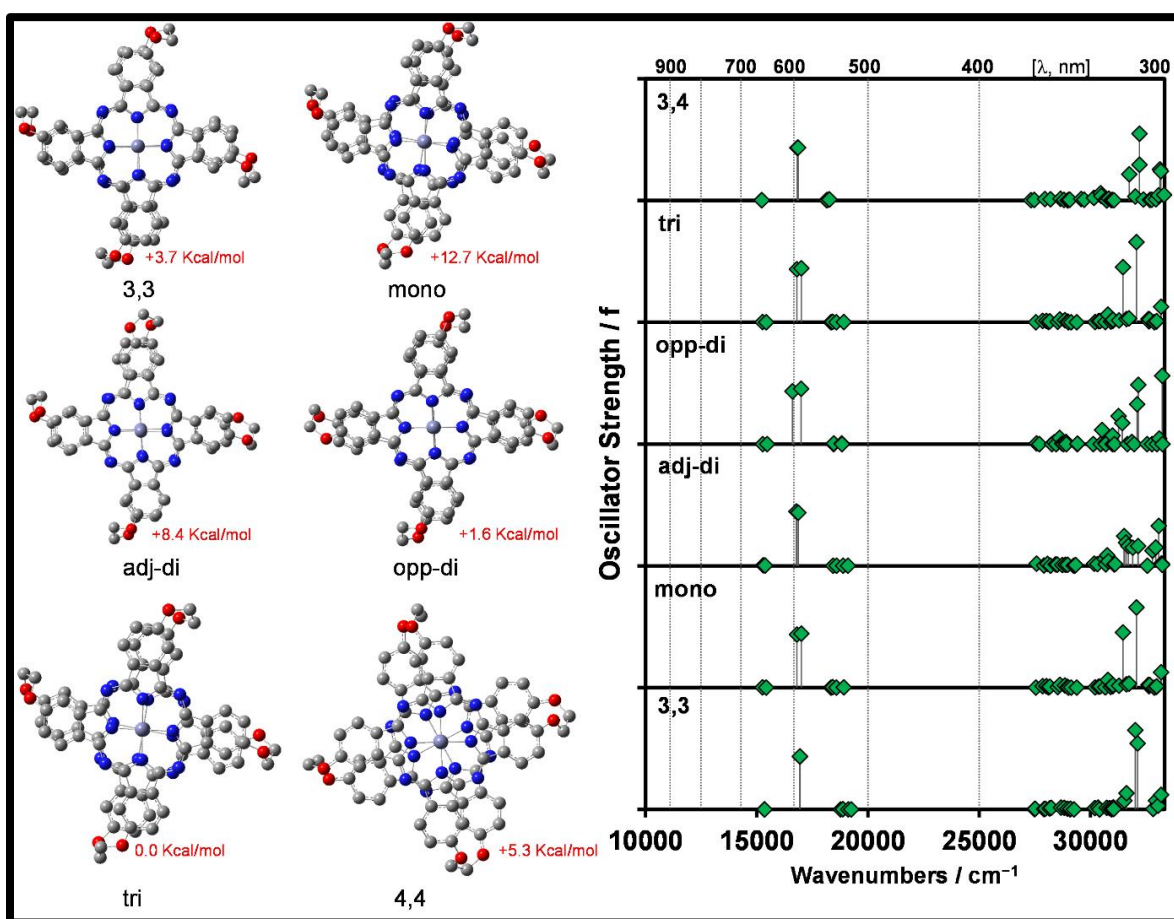
Figure 3.8: The structures and predicted relative energies calculated for B3LYP optimized geometries at the CAM-B3LYP/6-31G(d) level of theory for isomers of 4 with only either 3,3- and 3,4- attachments (3,3 and 3,4), and structures with both types of attachment arranged in a 3:1 manner (mono), in oppositely and adjacently arranged 2:2 structure (adj-di and opp-di), and a 1:3 manner (tri). The hydrogen atoms are omitted for clarity.

The TD-DFT predict presence of isomers and the possibility of weak intensity for the forbidden bands in the spectra as seen in **Fig. 3.6**, which explain the band broadening that is observed in the Q band region relative to the spectra of monomeric $M^{II}Pc$ complexes [**157**]. It is noteworthy in this regard that although the isomer with only 3,3-position attachments is predicted to be almost perfectly eclipsed, the other isomers are not (**Fig. 3.8**).

The absorption spectra of **14** and **15** differ somewhat from that of **13** (**Fig. 3.3**), because of the presence of axial chloride ligands and the larger Ga(III) and In(III) sitting out of the plane of the Pc π-system (**Fig. 3.9**). This leads to significant changes in the vibrational band envelope to the blue of the Q band (**Fig. 3.3**), and the differences observed at higher energy in the B band region can be readily explained by the TD-DFT calculations (**Fig. 3.6**), because the axial chloride ligands interact significantly with Pc ring MOs with $1a_{2u}$ and $2a_{2u}$ symmetry (under the D_{4h} symmetry of MPc monomers), since they have large MO coefficients on the pyrrole nitrogen atoms [**158**]. Thus, the broadening observed in **14** and **15** can be attributed the orientation of chloride axial ligand that tend to distort the electronic density of Pc ring.

13: isomer with four 3,3 position bridges

14: isomer with four 3,3 position bridges

15: isomer with four 3,3 position bridges
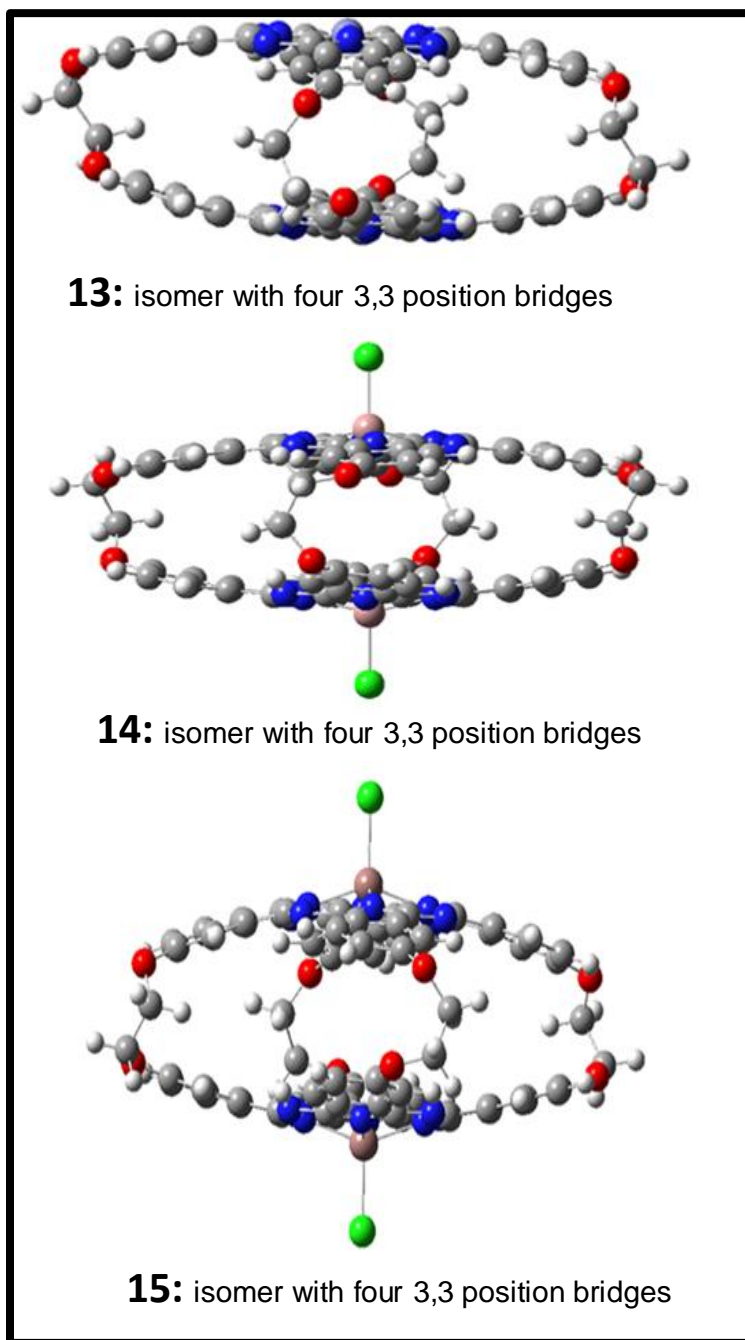
Figure 3.9: Side views of the B3LYP optimized geometries of 13-25 for isomers with four 3,3-position bridging moieties.

3.1.3. Complexes 16-18

Scheme 3.3 showed the synthetic route for **16**-**18**, which was accomplished through cyclotetramerization of 4, 4'-[(4-formyl-1,2 bis(phenoxyl)diphthalonitrile) (**3**) in the presence of catalytic amount of DBU using 1-pentanol as a solvent. In the ^{1}HNMR (**Fig. A3, appendix**), the characteristic protons due to aldehyde were observed at 9.95-10.12 ppm was integrated to give 4 protons. The rest of the aromatic protons were found between 8.31–7.50 ppm, and integrated to give anticipated number of protons. The elemental composition and mass spectral data of the complexes corresponded to the expected values.

Fig. 3.10 shows the absorption spectra of **16**-**18**. Two isomers of **17** were successfully isolated during chromatographic separation. The Q bands of the complexes were observed at 682, 691, 689 and 696 nm for **16**, **17**A, **17**B and **18** respectively (**Table 3.1**)

The broadening in the spectra was more pronounced in **17** compared to **16** and **18**, which could be due to conformational effect resulting from the axial chloride as explained before for **13**-**15**. Both the absorption and excitation spectra are similar and mirror images of the emission spectra (**Fig. 3.10**), suggesting that the ground state nuclear configurations are not affected by excitation. Complex **18** showed weak emission and excitation due to low fluorescence as will be discussed in chapter four.
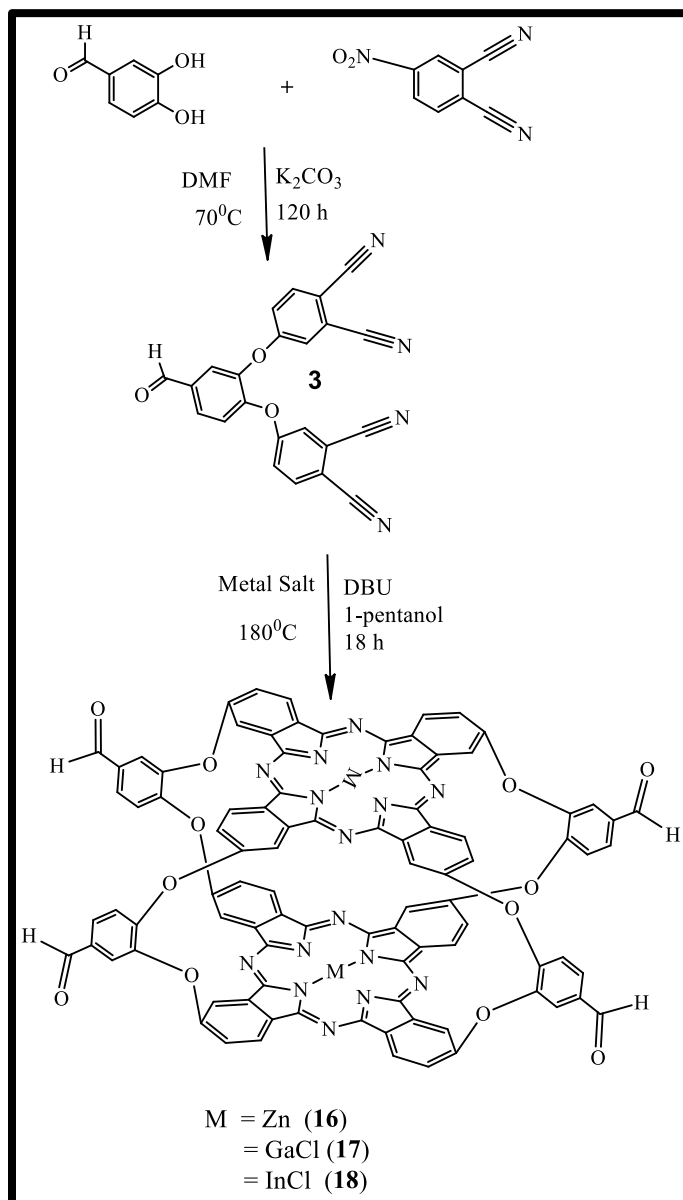
Scheme 3.3: Synthetic route for complexes 16-18
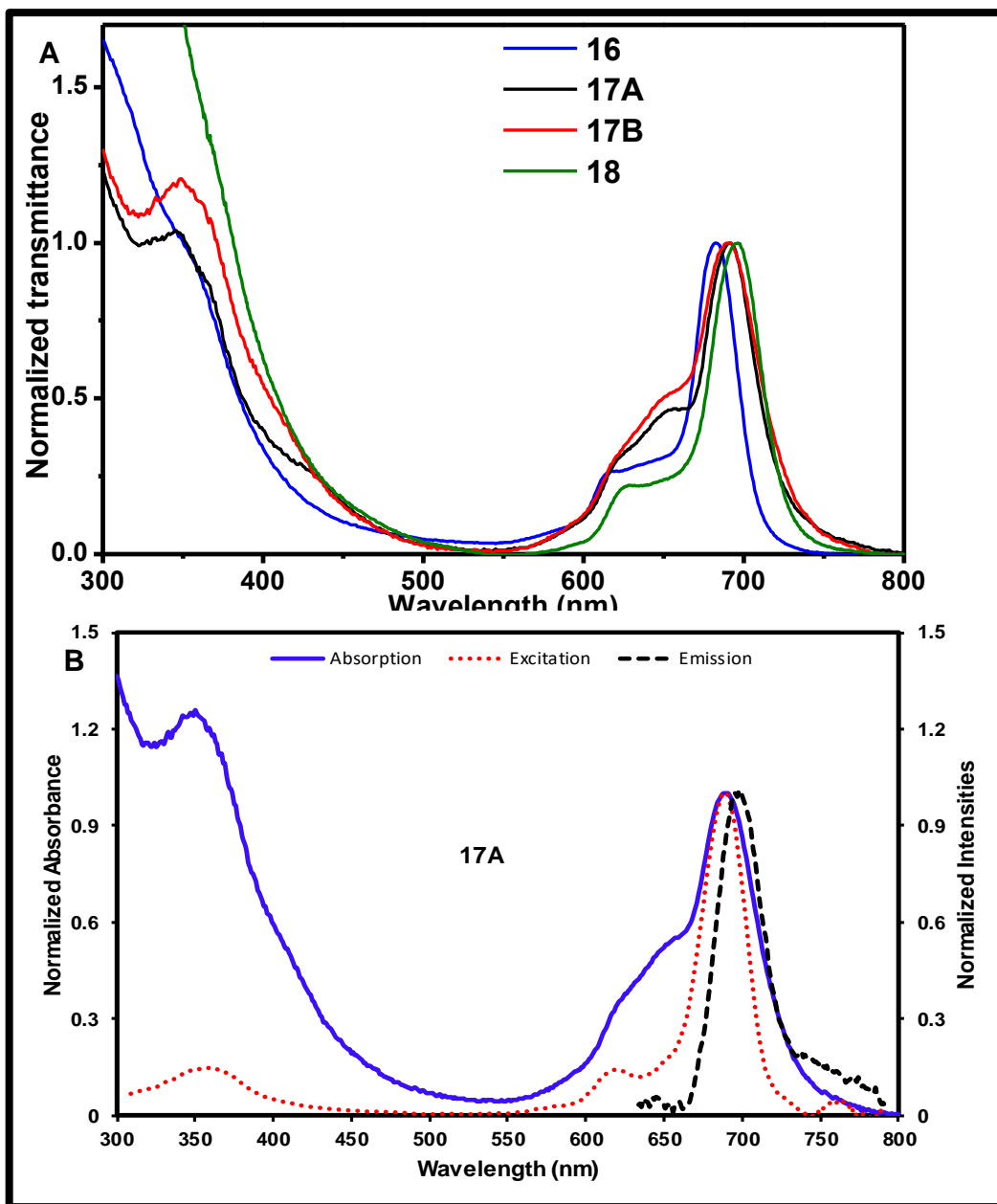
Figure 3.10: Absorption spectra of 16-18 (A) and absorption, emission and excitation spectra of 17A (B). Solvent: DMSO

A minus-to-plus sigmoid curve was observed in the MCD spectra of **16**-**18** (spectra not shown) with a cross-over point at 682, 690, 689 and 698 nm for **16**, **17A**, **17B** and **18** respectively as observed for **13**-**15**, which essentially correspond to the Uv-vis absorption maxima of the complexes.

It is anticipated that the most probable isomers observed in complex **17** (A and B) might arise due to rotation of one of the two axial chlorides inside the ring (**Fig. 3.11**) resulting in destabilization of the HOMO-LUMO gap. The TD-DFT predicts the two isomers to differ with 4 nm in the Q-band maxima, which is in close agreement with the 2 nm difference observed in the experimental UV–vis spectra (**Table 3.1**).
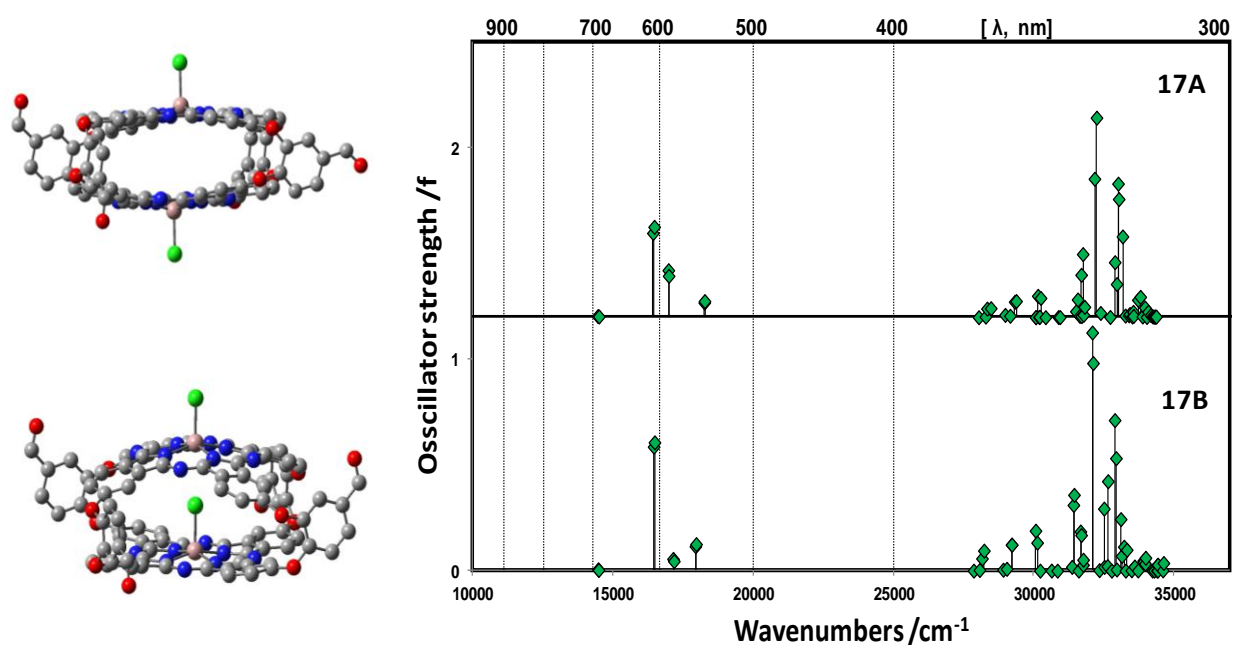
Figure 3.11: The structures and calculated for B3LYP optimized geometries at the CAM-B3LYP/6-31G(d) level of theory for two of the positional isomers of 17 that have only 3,3-attachments. Hydrogen atoms are omitted for clarity.

3.1.4.Complexes 19-21

Complexes **19**-**21** bearing benzothiazole bridged linker were prepared according to **Scheme 3.4** through cyclotetramerization of the 4,4'-((4-(benzo[d]thiazol-2-yl)-1,2-bis(phenoxy)) diphthalonitrile (**4**) using 1-pentanol as the solvent and DBU as a catalyst.
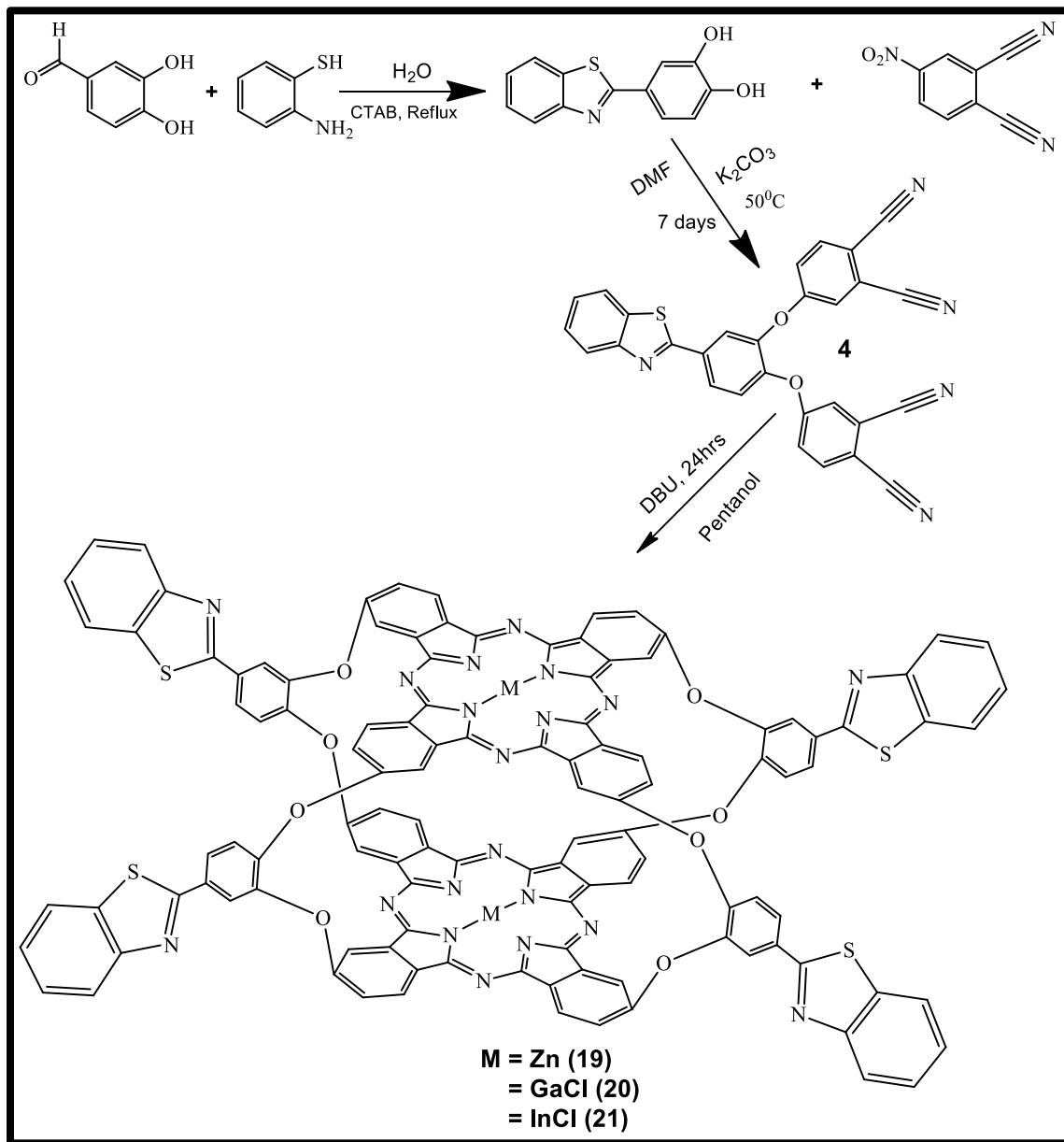
Scheme 3.4: Synthetic pathway for complexes **19**-**21**

The FT-IR spectra of **19**-**21** showed disappearance of the C≡N peak observed at 2230 cm^{-1} in the FTIR of **4**, confirming the formation of the target complexes. The FTIR spectra of the complexes showed C-H stretch of the benzothiazole which ranged from 3047 to 3052 cm^{-1}, while the C-S stretch ranged from 748 to 754 cm^{-1}. The ^{1}H NMR spectra (**Fig. A4, appendix**) showed aromatic ring protons between 8.15–7.20 ppm, all integrated to give the anticipated number of protons. The MALDI-TOF mass spectra of the complexes showed fragmentation with molecular ion peak as [M+1]$^+$. The CHNS elemental analysis of the complexes agrees with the proposed structure.

The Q bands of the complexes were observed at 681 nm, 698 nm and 702 nm (**Table 3.1**) (spectra not shown) without any sign of aggregation. The MCD and TD-DFT calculations for **19**-**21** also showed similar spectra pattern as observed for **13**-**15** and **16**-**18**.

3.1.5. Effect of nature of bridging substituents on absorption spectra (complexes 10-21)

The comparison of the spectra of the ball-type Pcs **10**-**21** indicate that the different substituents do not show any significant difference in the Q band absorption maxima of group 1 complexes bearing zinc (**Table 3.1**), suggesting that the bridging linkers have limited effect on the energy gap between the highest occupied molecular orbital (HOMO) and the lowest unoccupied molecular orbital (LUMO) that could have result in a visible shift in position.

For group 2 and 3 bearing gallium and indium central metal, a significant red-shift was observed for the electron donating alkyl substituted complex **14** and **15** as well as the benzothiazole **20** and **21** compared to corresponding electron withdrawing carboxylic acid (**11, 12**) and aldehyde (**17**, **18**) substituted complexes (**Table 3.1**)

3.1.6.Complexes 22-27

The MPcs **22**-**27** were prepared by cyclotetramerization of the phthalonitriles (**5** or **6**) with the corresponding metal salts (**Scheme 3.5**).

The ground state absorption spectra for complexes **22–27** showed that they are monomeric in DMSO (**Fig. 3.12**) with single Q-band absorption maxima between 681–697 (nm) in DMSO, **Table 3.2**.
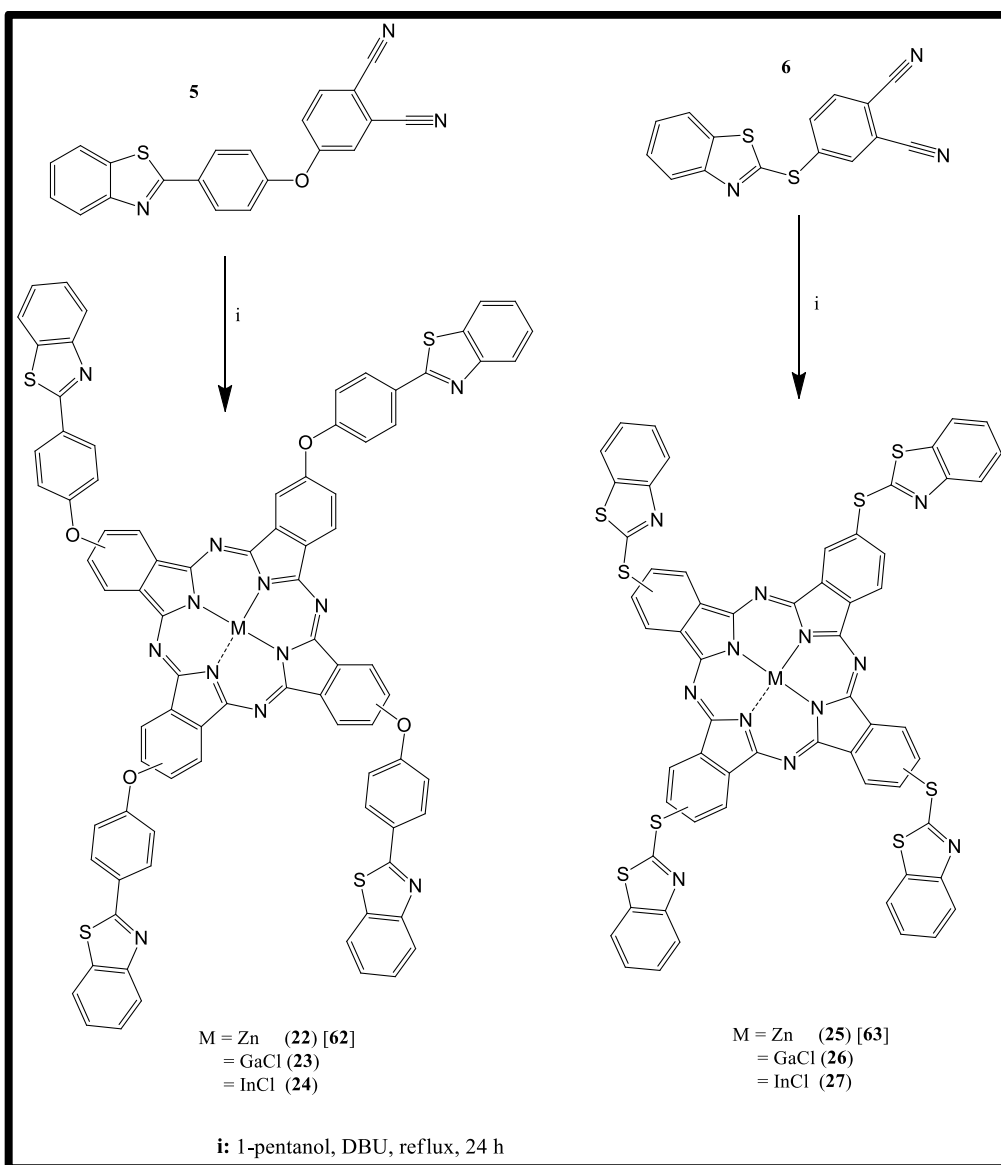
Scheme 3.5: Synthetic route for 22-27
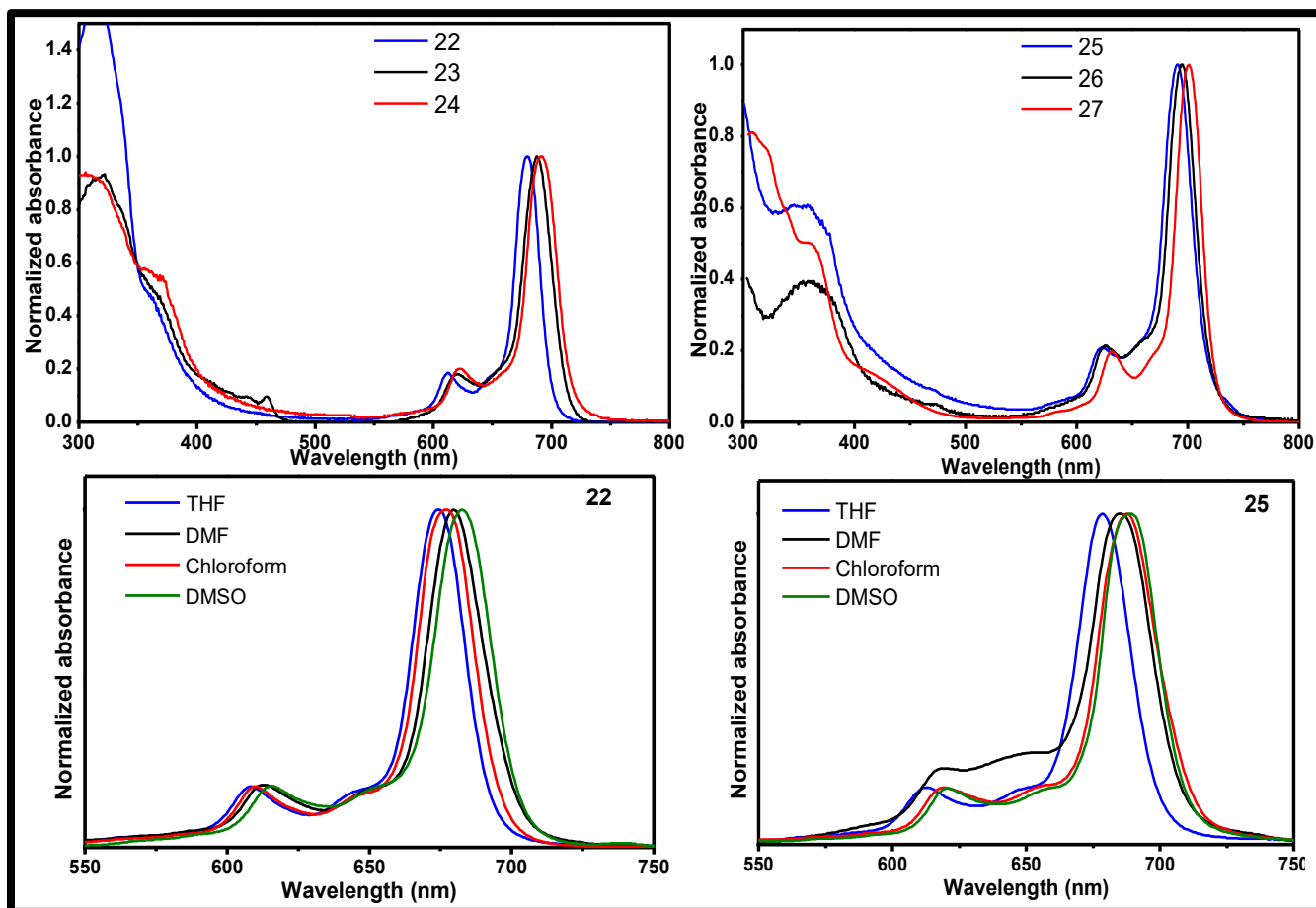
Figure 3.12: Absorption spectra of 22-27 in DMSO (Top), 22 and 25 in different solvents (Bottom)

For complexes **22**, **23** and **24** that bear the same substituent but only differ on the central metal, **23** and **24** shows a more red-shifted Q-bands due to the large size of gallium and indium [**159**] as discussed above. Similar trend was also observed for complexes **25**, **26** and **27** that have the same substituent. Complexes **25**-**27** bearing sulfur bridged benzothiazole show more red-shifted Q-band compared to the corresponding central metal oxygen bridged complexes **22**-**24** (**Table 3.3**). The presence of electron donating sulfur atom is known to result in red-shifting in phthalocyanines [**159**,**160**]. The absorption spectra in different solvents predominantly showed red-shifting of the Q bands as solvent polarity increases in order of DMSO > DMF > CHCl$_3$ > THF (**Fig. 3.12, Table 3.2**).

Table 3.2: Spectral data for complexes 22–27 in different solvents

Complex	Solvent	Q Band $\lambda_{max.}$ (nm)	Excitation $\lambda_{exc.}$ (nm)	Emission $\lambda_{em.}$ (nm)	Stoke Shift (nm)
22	DMSO	681	680	690	10
	DMF	679	684	693	9
	$CHCl_3$	677	680	689	9
	THF	674	677	687	10
23	DMSO	688	691	699	8
	DMF	686	690	700	10
	$CHCl_3$	685	688	698	10
	THF	682	685	701	16
24	DMSO	692	692	700	8
	DMF	691	693	698	5
	$CHCl_3$	689	688	701	13
	THF	686	686	697	11
25	DMSO	685	682	699	17
	DMF	683	682	694	12
	$CHCl_3$	681	683	692	9
	THF	679	681	691	10
26	DMSO	692	691	702	11

Complex	Solvent	Q Band $\lambda_{max.}$ (nm)	Excitation $\lambda_{exc.}$ (nm)	Emission $\lambda_{em.}$ (nm)	Stoke Shift (nm)
	DMF	690	694	705	11
	CHCl₃	688	691	699	8
	THF	687	691	700	9
27	DMSO	697	698	706	8
	DMF	693	693	707	14
	CHCl₃	690	692	701	9
	THF	686	687	697	10

All the complexes displayed similar fluorescence behavior with maximum emission and excitation peaks ranging from 699-706 nm and 682 nm - 698 nm respectively in DMSO. The observed stoke shift of 8-19 nm are typical of MPcs complexes in DMSO.

3.1.7. Complexes 28-30

Complexes **28**-**30** were obtained by cyclotetramerization of 4-(4-formylphenoxy) phthalonitrile (**7**) in the presence of catalytic amount of DBU using pentanol as solvent (**Scheme 3.6**). The sharp peak of C≡N stretch at 2234 cm⁻¹ in the FTIR spectra of **7** disappears after cyclotetramerization, confirming formation Pc complexes. The ¹H NMR spectra (**Fig. A5, appendix**) showed the protons due to aldehyde between 10.01–10.12 ppm integrated to give four protons in each complex. The rest of the aromatic protons were found between 8.22–7.25 ppm, and integrated

to give anticipated number of protons. The elemental composition and mass spectral data of the complexes corresponded to the expected values.
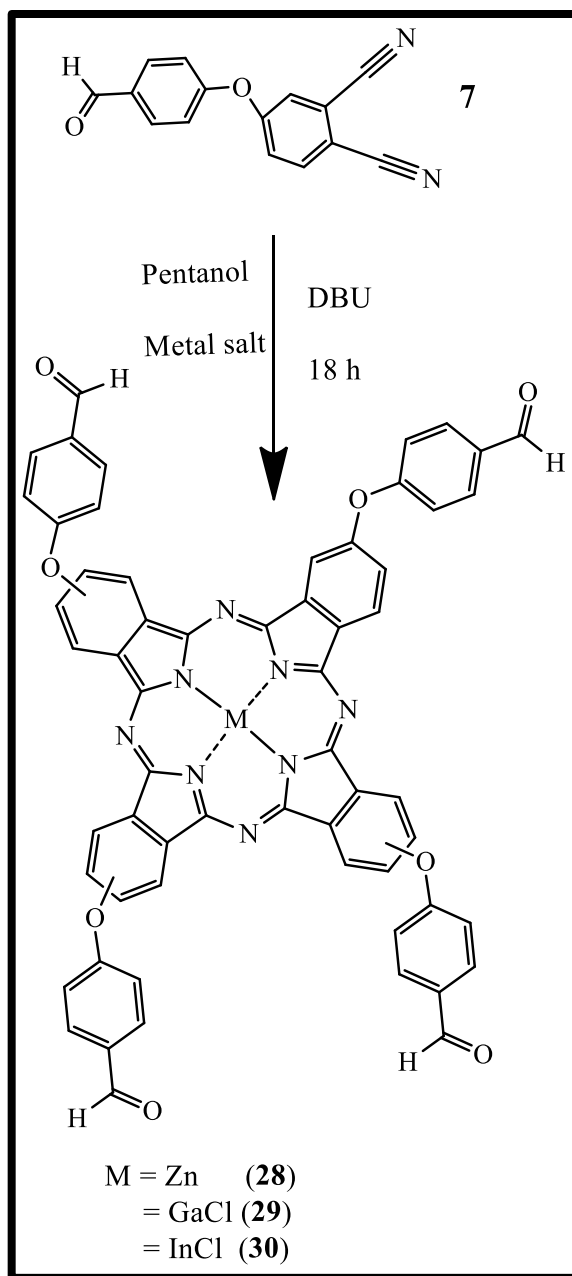
Scheme 3.6: Synthetic route for complexes 28-30

Table 3.3: Spectral data for complexes 22–36 in DMSO

Complex	λ_{max}
Phenoxylbenzothiazole substituted complexes	
22	681
23	688
24	692
Thiarybenzothiazole substituted complexes	
25	685
26	692
27	697
Aldehyde substituted complexes	
28	679
29	689
30	695
Aminophenoxyl substituted complexes	
31	680
32	687
33	691
Asymmetric benzothiazole substituted complexes	
34	680
35	687
36	693

The ground state electronic absorption spectra of the complexes showed monomeric behavior with absorption maxima at 679, 689 and 695 nm in DMSO for **28-30**, respectively (**Table 3.3**).

The excitation spectra are like absorption and both were mirror image of emission indicating that excitation at wavelength of interest did not change the ground state nuclear configuration of the complexes.

The TD-DFT calculation showed the frontier molecular orbital with the HOMO and LUMO localized within the pyrrole inner ring and the HOMO-LUMO energy gap narrowing as the atomic weight of the central metal increases as observed before which accounted for red-shifting for **29** and **30** compared to **28**.

3.1.8. Complexes 31-33

The synthetic route of complex **31-33** is depicted in **Scheme 3.7**. 4-(3,5-dichlorophenoxy)phthalonitrile was reacted to 4-aminophenol to give the precursor 4-(2,4-bis(4-aminophenoxy)phenoxy)phthalonitrile (**8**).

Cyclotetramerization of **8** using 1-pentanol as solvent, catalytic amount of DBU and appropriate metal salt give complex **31-33**. The disappearance of C≡N peak at 2232 cm^{-1} (for **8**) in the FT-IR spectrum of **31**-**33**, confirmed the formation of the complexes. The ^{1}H NMR spectra of **31**-**33** (**Fig. A6, appendix**) showed aromatic ring protons between 8.15 – 6.59 ppm while the amino proton was confirmed between 5.49-4.95 ppm integrated into 16 protons. MALDI-TOF mass spectra and elemental analyses agrees with the proposed structure. The Q band maxima for **31**, **32** and **33** was observed at 680, 687 and 691 nm respectively (**Table 3.3**).

A pseudo-Faraday A_1-term characterized with an S-shaped sigmoid curve (**Fig. 3.13**) with high intensity between 600−750 nm and lower intensity between 300−400 nm was observed in the MCD spectra of the complexes similar to all Pcs complexes.
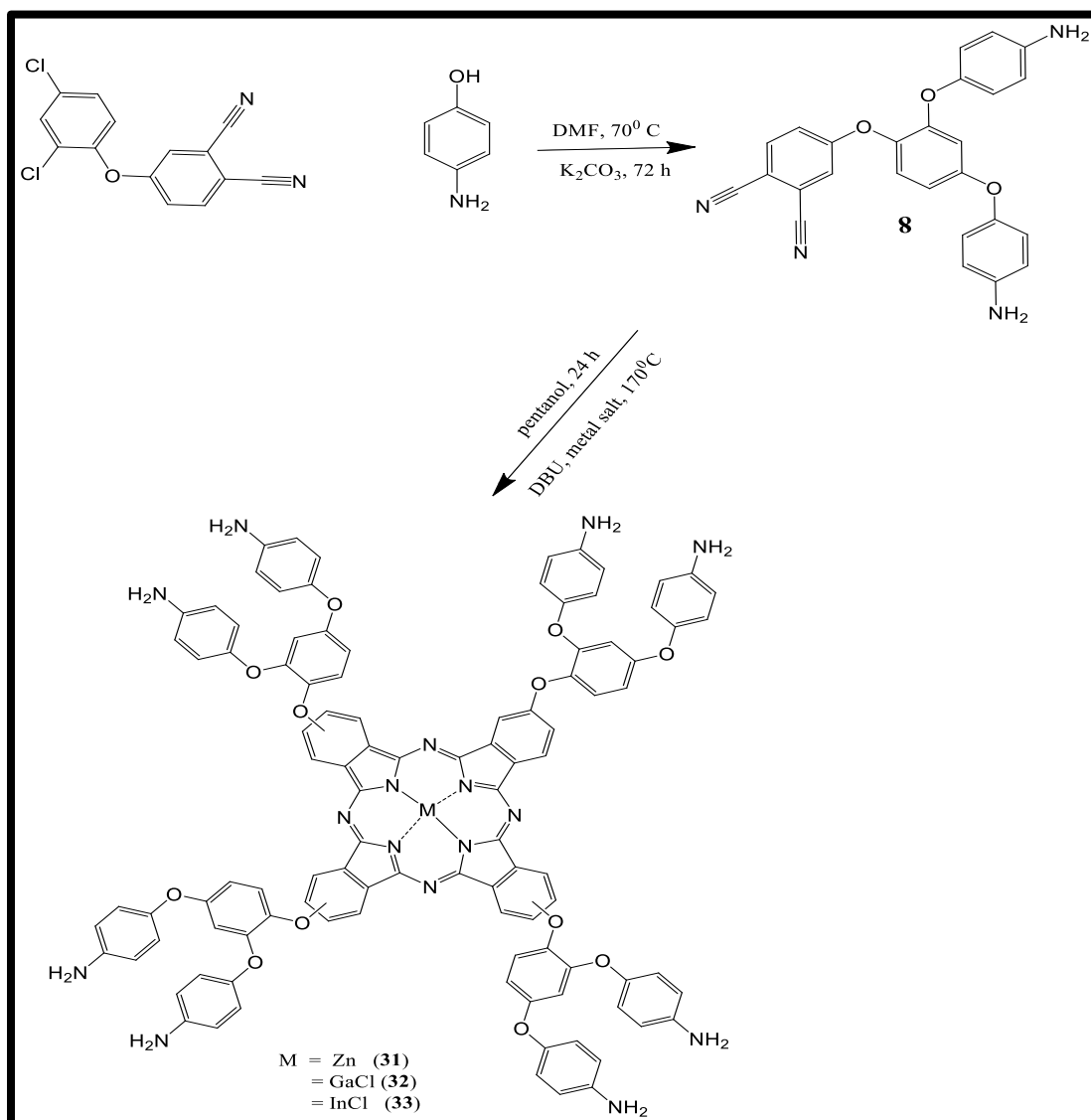
Scheme 3.7: Synthetic route for complexes 31-33

The crossover points in the Q band region at 681, 689 and 692 nm for **31**, **32** and **33** respectively essentially corresponding to absorption maxima at 680, 687 and 691 nm observed in the UV-visible absorption spectra of the complexes.

In the context of phthalocyanines, Gouterman's 4-orbital model has been modified to include two close-lying B_1 and B_2 bands, because of configurational interaction with other higher energy $\pi\pi^*$ states [**161**] (**Fig. 3.13 A**).
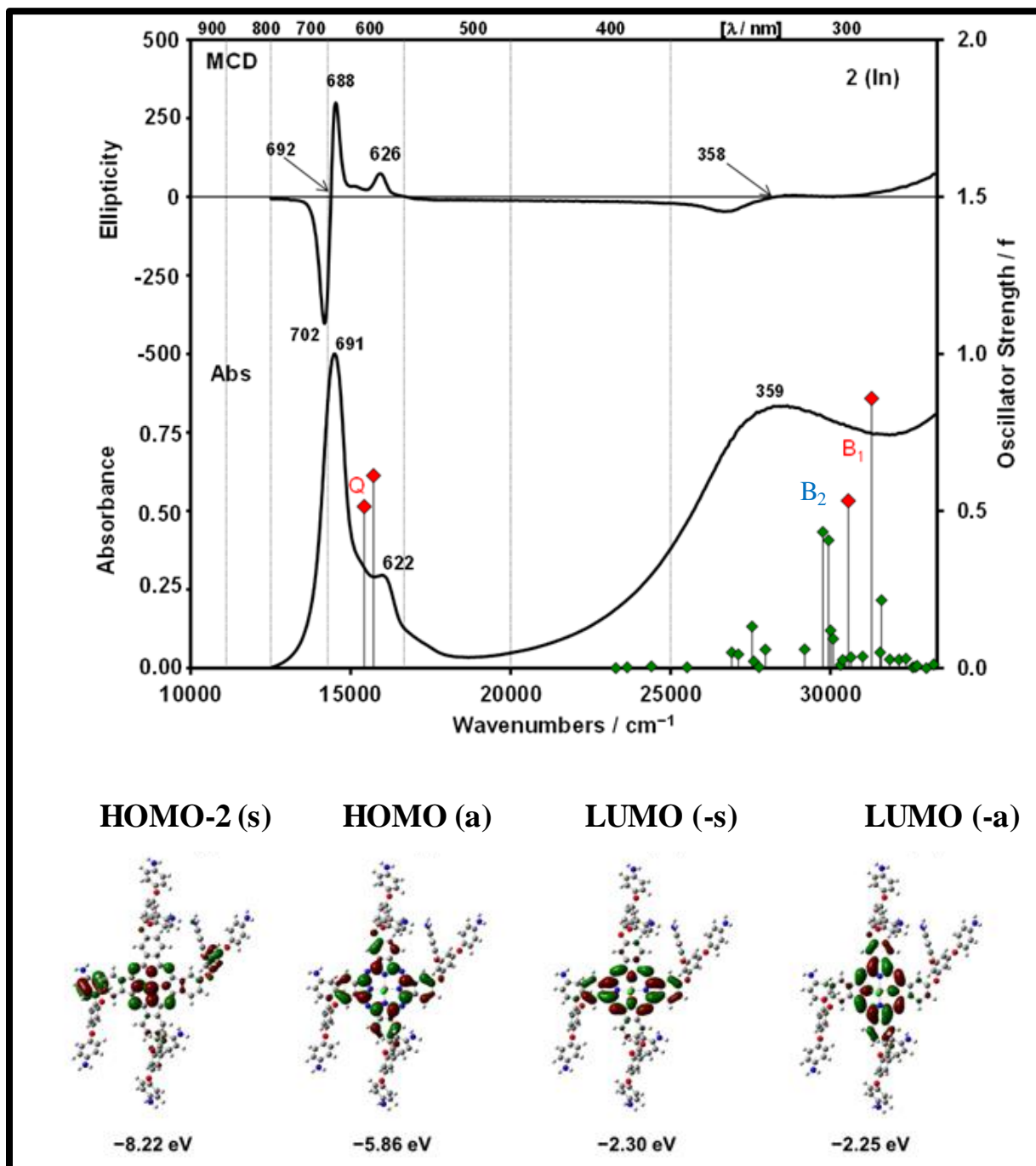
Figure 3.13: (A) Absorption and MCD spectra of **33** in DMSO with TD-DFT spectrum of the C_{4v} positional isomer of **33**. Red diamonds are used to highlight bands associated with the main Q and B bands of Gouterman's 4-orbital model that are associated with transition out of the $1a_{1u}$ and $1a_{2u}$ MOs into the $1eg^*$ LUMO. (B) The angular nodal patterns and energies of the frontier orbital of the D_{4h} positional isomer of complex **2** that are associated with the Q transition.

As is the case with other complexes, the TD-DFT calculations predict the presence of bands to the red of the main B_1/B_2 band envelopes in UV-visible absorption spectra and a set of relatively weak bands in the MCD spectra. Similar bands have been reported for Pcs containing alkoxy, phenoxy, thioalkyl and thiaaryl substituents and were attributed to either n→π* transitions that are associated with the lone pairs of electrons on the peripheral oxygen or sulfur atoms, or to π→π* transitions that are associated with low-lying occupied π-molecular orbital that are localized largely on the peripheral benzene rings, which are destabilized by the electron donating substituents [**161**]

There is a relative stabilization of the LUMO and LUMO+1 of **32** and **33**, which have similar nodal patterns that differ only by being rotated by 90° with respect to each other [**162,163**], due to the large MO coefficients on two of the pyrrole nitrogens (**Fig. 3.13 B**, **33** as an example), which are absent in the HOMO, since the pyrrole nitrogens lie on nodal planes. The central ions of **32** and **33** are in higher oxidation states than that of **31** and can withdraw more electron density from the ligand π-system.

The bulky aminophenoxy substituents interact significantly with the Pc π-system resulting in a lifting of the degeneracy of the LUMO and LUMO+1 of the optimized geometries that were determined for the D_{4h} positional isomers of **31-33**. Since the substitution is at the peripheral positions, similar trends in the MO energies and optical spectra of the four possible positional isomers are anticipated to be broadly similar in each case [**162**], so the spectra obtained for the mixture of isomers that are present in solution show no obvious evidence of spectral differences due to isomerism.

3.1.9.Complexes 34-36

The synthesis of complex **34-36** (**Scheme 3.8**) was accomplished by statistical condensation of 4-(4-(1,3-benzo[d]thiazol-2-yl)phenoxy)phthalonitrile(**5**) and 2-(4-(3,4-dicyanophenoxy)phenoxy) acetic acid (**9**)   in the presence of metal salt and 1-pentanol.
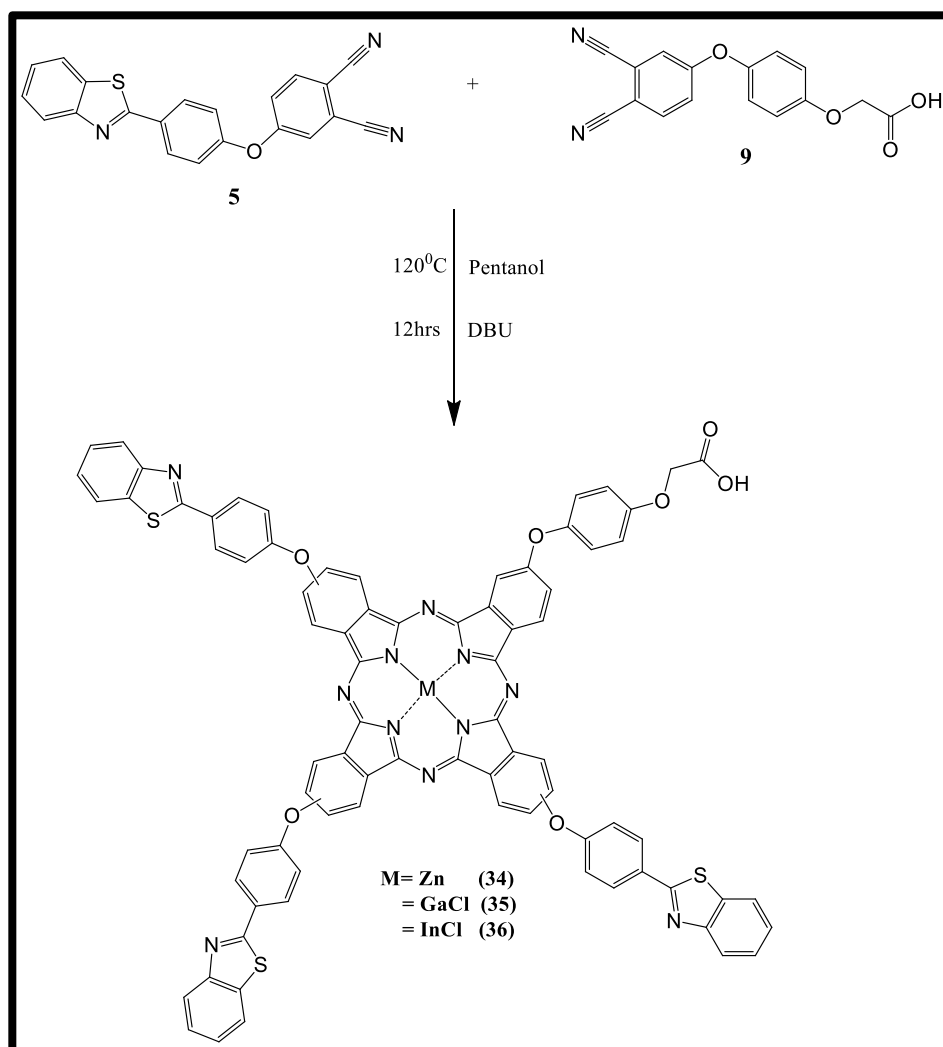
Scheme 3.8: Synthetic Route for complex 34-36

The disappearance of the C≡N peak at 2231 cm^{-1} and 2237 cm^{-1} in the respective phthalonitriles **5** and **9** showed complete cyclisation to form complexes **34**-**36**. Characterization of the complex using FTIR, ^{1}HNMR, UV-vis and elemental analysis confirmed the proposed structure. The broad peak of COOH group was observed in the FTIR between 3183-3395 cm^{-1}. The ^{1}HNMR (**Fig. A7, appendix**) showed the singlet proton of the carboxylic acid end resonating at 10.25-10.23 ppm while the rest of the aromatic protons were found between 8.25 – 7.30 ppm and integrated to give anticipated number of protons. The characteristic CH$_2$ proton of the phenoxyacetic acid was found between 4.18-4.00 ppm integrated into two protons. The MALDI TOF mass spectra of the complexes showed fragmentation with a molecular ion peak as [M + 1]$^{+}$ and the elemental analysis agreed with the proposed structure.

The ground state electronic absorption spectra of **34**-**36** revealed that the complexes were monomeric with single intense Q band at 680, 687 nm, 693 nm (**Fig. 3.14 A-C, Table 3.3**), respectively, as observed above for other MPcs. The absorption maxima of **35** and **36** lie at longer wavelength compared to that of **34** as discussed above.

 The MCD spectra of the complexes showed a distinct S-shaped sigmoid curve between 600-750 nm with a pseudo A_1 term in the Q band region at 682 nm, 688 nm, and 694 nm for **34**, **35** and **36** respectively, which essentially correspond to the absorption maxima of the complexes at 680, 687, and 693 nm (**Fig. 3.14 A-C**). A similar curve was observed in the B band region at 358 nm, 360 nm and 359 nm for **34**, **35** and **36**, respectively, similar to other Pcs discussed above.
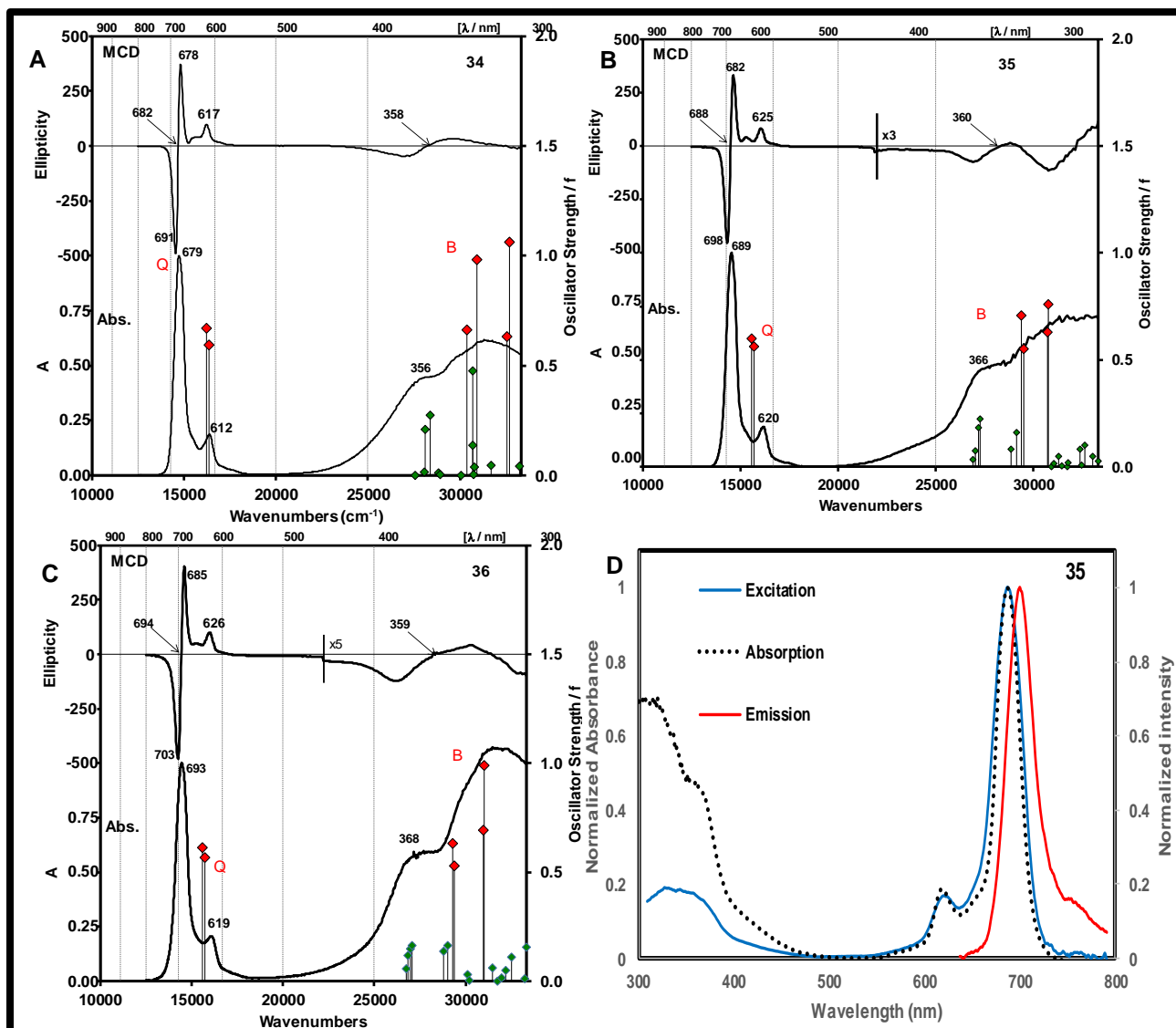
Figure 3.14: Absorption and MCD spectra of 34-36 in DMSO (A-C) and the calculated TD-DFT spectrum of the isomers is plotted against a secondary axis. Red diamonds are used to highlight bands associated with the Q and B bands of Gouterman's 4-orbital model while green diamonds are used for transitions associated with what would be the $2a_{2u}$ MO of the Pc rings. Absorption, excitation and emission spectra of 35 in DMSO (D)

The TD-DFT transition calculations are very close to the experimental (**Table A2, appendix**) and a single intense band arising from the Q and B band transitions were predicted in the TD-DFT calculations of the complexes (**Fig. 3.14**)

The absorption spectra are similar to excitation and both are mirror images of the emission (**Fig. 3.14**) indicating that the absorbing and emitting molecules are the same and not affected by excitation at selected wavelength.

3.1.10. Comparison of the spectra of ball-type with monomer MPcs (complexes 16-21, 22-24 and 28-30)

The Q band absorption maxima for the co-facial ball-type complexes **16**-**18, 19-21** and the corresponding monomers **22-24** and **28**-**30** are shown in **Table 3.4.**

Though a red-shifting with increase in atomic weight was observed both for the dimer and monomeric analogues, the Q band of the dimeric **16**-**18** lie at longer wavelength compared to the corresponding monomer (**Table 3.4**) except for **18** and **30**.

For the benzothiazole substituted dimers **19**-**21** and the corresponding **22**-**24** monomers, there was no difference in absorption maxima for the zinc complexes **19** and **22**, but significant red-shifting of 10 nm and 9 nm respectively for **20** and **21** was observed compared to **23** and **24**. This can be attributed to the presence of forbidden bands that arise from the co-facial arrangement of phthalocyanines [**164**] especially with axial ligated MPcs.

Table 3.4: effect of ball-type MPcs and monomeric derivatives spectra

Type	Complexes	Q band maximum absorption wavelength
Aldehyde substituted co-facial ball-type dimers	**16** (Zn)	682
	17 (GaCl)	691
	18 (InCl)	696
Aldehyde substituted monomers	**28** (Zn)	679
	29 (GaCl)	689
	30 (InCl)	695
Benzothiazole substituted co-facial ball-type dimers	**19** (Zn)	681
	20 (GaCl)	698
	21 (InCl)	701
Benzothiazole substituted monomers	**22** (Zn)	681
	23 (GaCl)	688
	24 (InCl)	692

3.2. Conjugation of metallophthalocyanine to nanomaterials

The amidation reaction was used to covalently linked complexes **10**-**12** and **31**-**36** with glutathione functionalized nanoparticles using DCC as activating agent [**165**], which activates the carboxylic acid groups for susceptible attack by the amine group and DMAP as a coupling agent. Complexes **10**-**12** were covalently linked to CdTe semiconductor QDs as well as carbon based GQDs and are represented as **10**-CdTe, **11**-CdTe and **12**-CdTe for semiconductor QDs and **10**-GQDs, **11**-GQDs and **12**-GQDs. **12** was further covalently linked CdTeSe (core), CdTeSe/ZnO (core shell), AgNPs and AuNPs. A complete list on **Table 3.5**.

Complexes **19**-**27**, **31** and **34** were surface assembled onto metallic AgNPs and AuNPs due to strong affinity of gold and silver to sulphur and nitrogen. The self assembled conjugates are listed in **Table 3.6**. Since **31** and **34** were self assembled as well as covalently linked to metallic Au and Ag NPs, the covalently linked conjugates are represented as **31**CB and **34**CB in **Table 3.5**, where CB stand for covalent bond. The nanoparticles were chosen for linkage to MPcs due to the following reasons.

1. Complexes **10**-**12** were linked to CdTe QDs and GQDs to evaluate the effect of semiconductor QDs and carbon based QDs on photophysical and nonlinear optical response.

2. Complex **12** was linked to CdTe (bare), CdTeSe (core) and CdTeSe/ZnO (core shell) QDs to investigate effect of bare, core and core shell on photophysical and nonlinear optical properties.

3. The comparative effect of semiconductor QDs and metallic AgNPS and AuNPs on photophysical and nonlinear optical behavior was investigated through linkage of **12**, **31** and **34** with the mentioned nanoparticles

4. Complexes **31** and **34** was covalently linked as well as self-assembled on AgNPs and AuNPs to investigate effect of self-assembly with covalent linkage on photophysical and nonlinear optical properties.

3.2.1. Covalent linkage of 10-12 and 31-36 with nanomaterials

Complexes **10**-**12** and **34**-**36** contain carboxylic acid functional group which can be activated using DCC and covalently coupled with the amine group of the nanoparticles using DMAP (**Scheme 3.9,** complex **12** as example). For complexes **31**-**33** that contain amino groups, the carboxylic acid of GSH functionalized

nanoparticles were activated instead using DCC and subsequently coupled with the amino group of **31**-**33** using DMAP (**Scheme 3.10**).
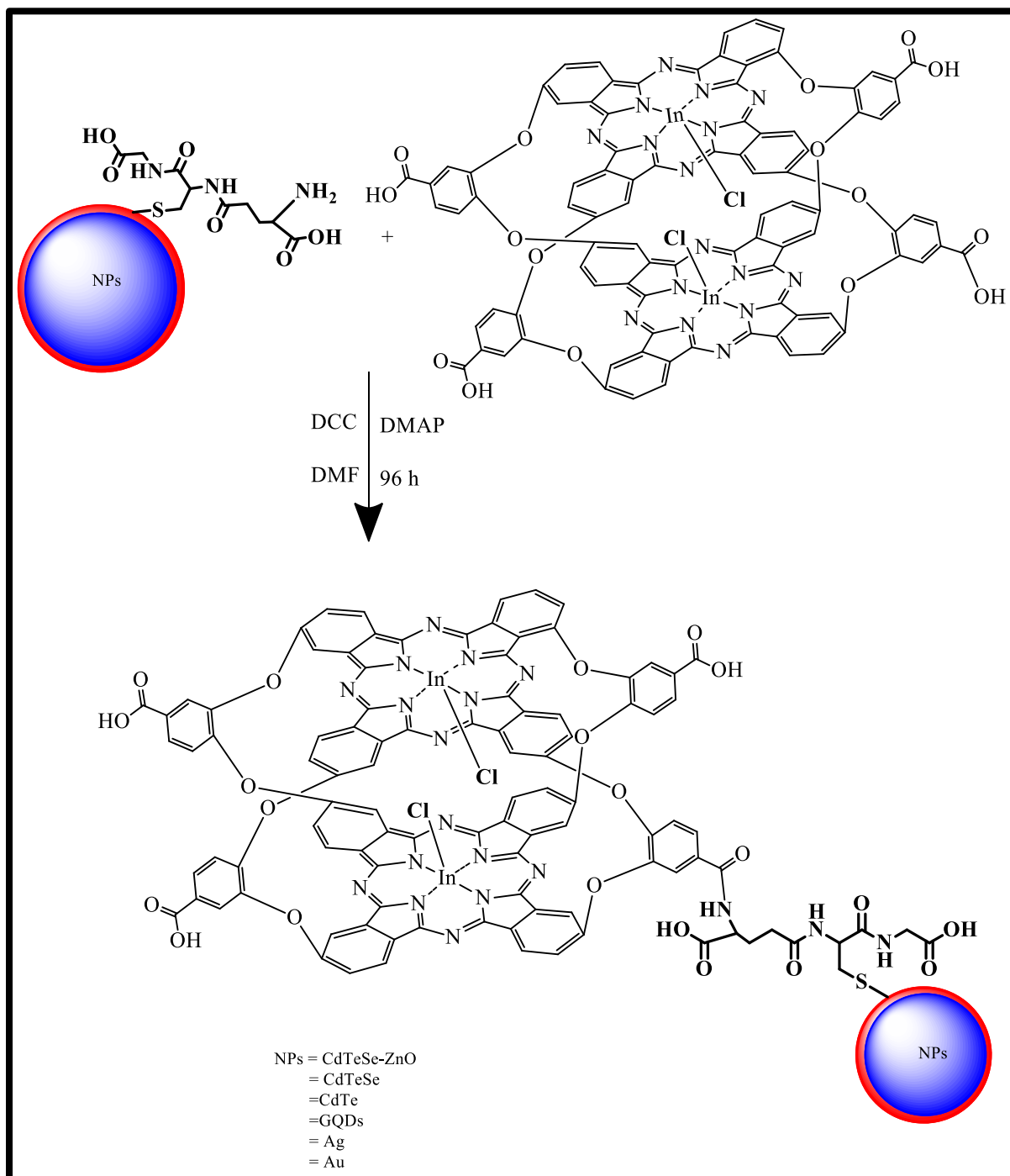
Scheme 3.9: Illustration of synthetic route for covalent linkage of 12 to nanomaterials as example.
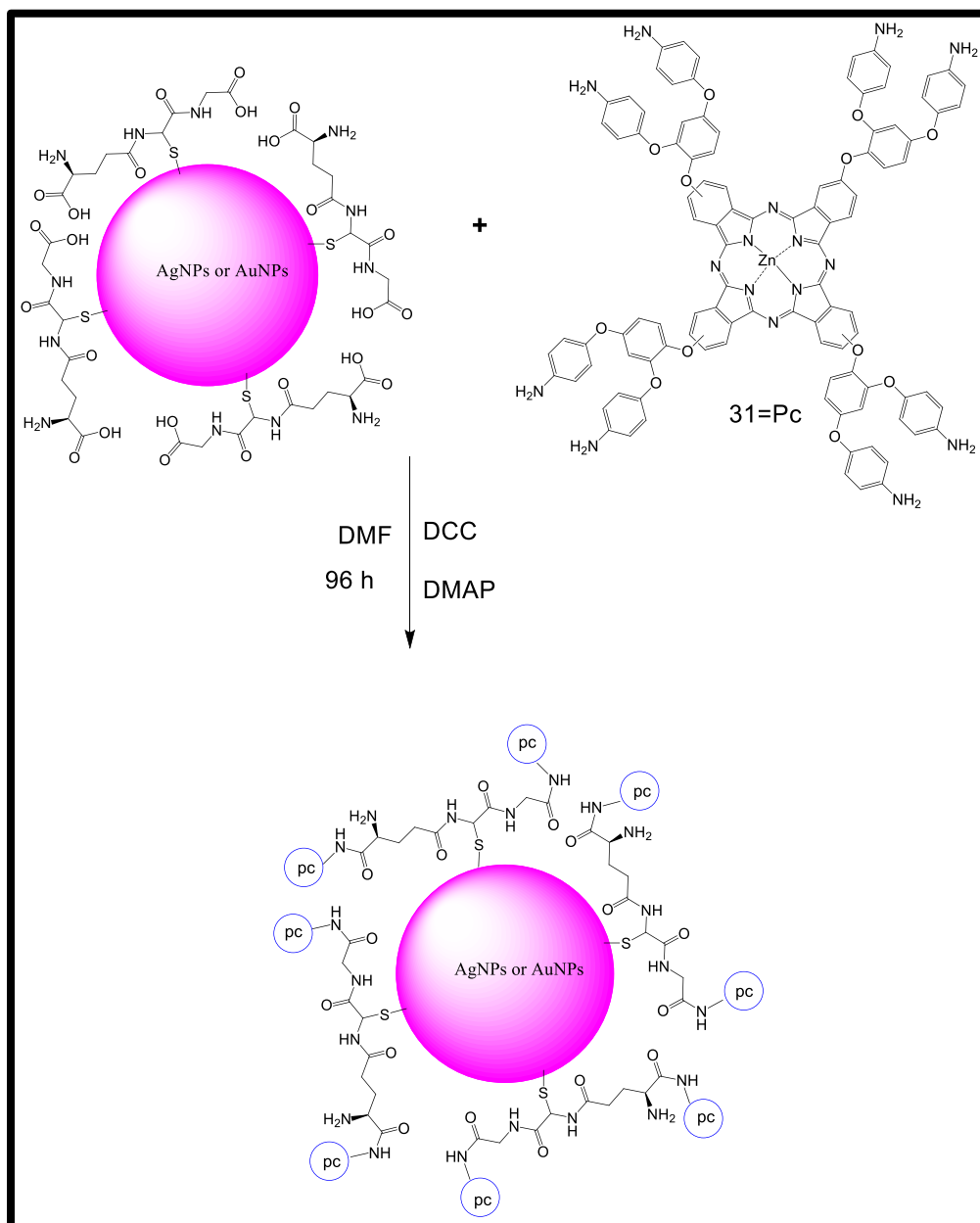
Scheme 3.10: Synthetic route for covalent linkage of 31 to metallic nanoparticles

3.2.1.1. FT-IR and Raman spectra

Fig. 3.15 shows the representative FT-IR spectra of complex **12**, CdTeSe/ZnO and **12**-CdTeSe/ZnO and Raman spectra of GQDs and **11**-GQDs.
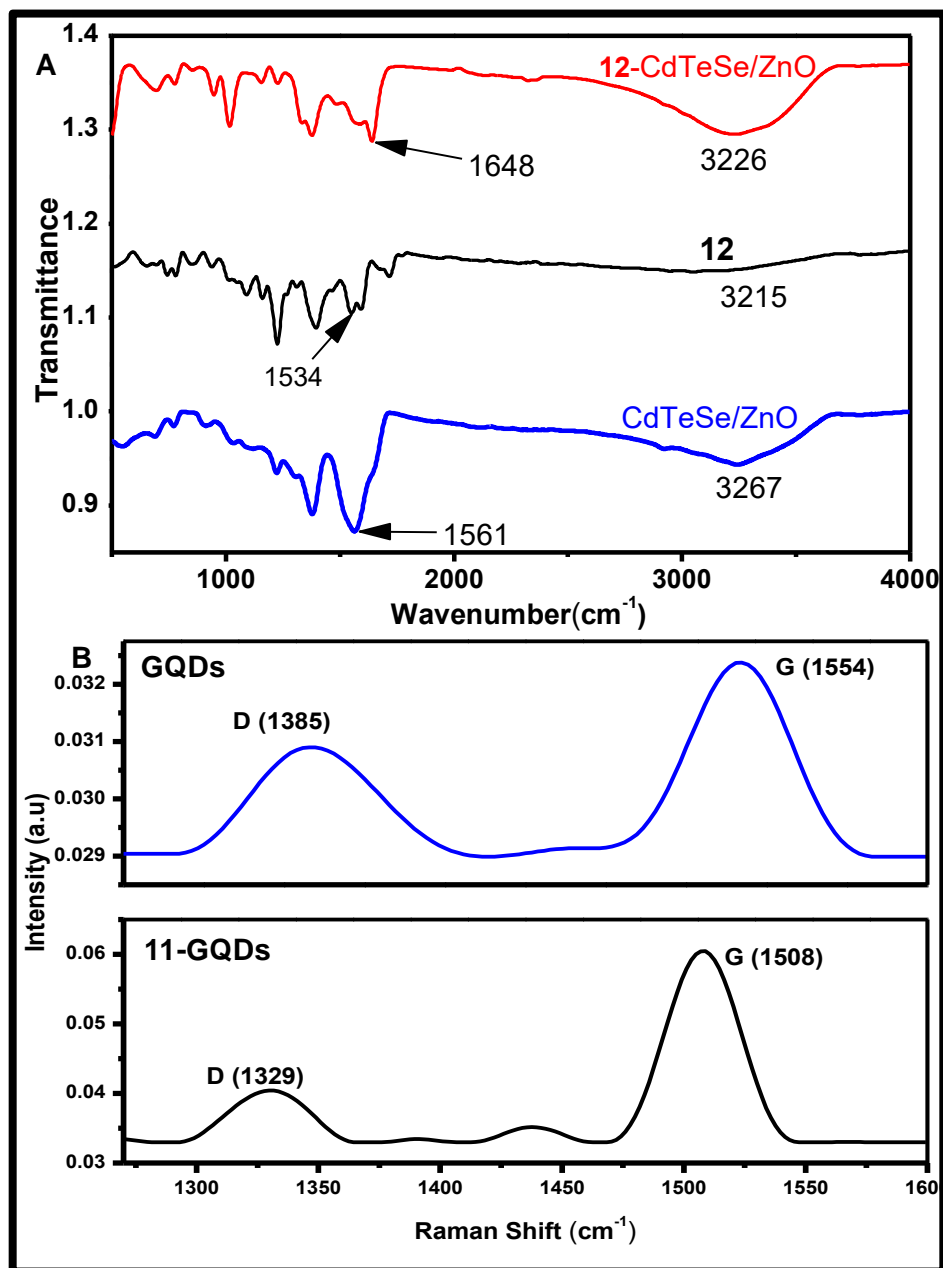
Figure 3.15: FTIR (A) and Raman (B) spectra of complex 11 and 12 when covalently linked to CdTeSe/ZnO and GQDs respectively

The carbonyl C=O stretches of primary amine of CdTeSe/ZnO and **12** were observed at 1561 and 1534 cm^{-1}. After covalent linkage, a distinct and sharp vibration band observed at 1648 cm^{-1} for **12**-CdTeSe/ZnO, which corresponds to the peak due to the amide bond (O=C-NH), and confirms the successful formation of the amide bond between the Pc and the NPs because this band was not present in either **12** or CdTeSe/ZnO.

The Raman spectrum obtained after conjugation of Pc complexes to GQDs displayed a shift in the characteristic D (disordered carbon atoms at the edges) and G (sp^2 bonded carbon atoms) bands of the GQDs (**Fig. 3.15 B**). The observed Raman shift after conjugation is an indication of the introduction of defects within the carbon framework in the GQDs and confirmation of the formation of a new nanocomplex.

3.2.1.2. TEM Micrograph analysis

The TEM images of the nanoparticles before and after covalent linkage reveal significant changes in the morphologies resulting from linkage (**Fig. 3.16**, using CdTeSe/ZnO, GQDs, AuNPs and conjugate of AuNPs as examples). Monodispersed particles were observed for the nanoparticles alone with average size of 5.9, 9.6, 9.1, 9.8, 8.2 and 15.1 nm respectively for GQDs, CdTe, CdTeSe, CdTeSe/ZnO, AgNPs and AuNPs (**Table 3.5**). Increase in size was observed for all the conjugates except for **31**CB-AuNPs and **34**CB-AuNPs, where a decrease in size was observed (**Table 3.5**). The increase in size for the nanoconjugates are probably due to aggregation resulting from interaction between the MPcs on adjacent NPs via π-π stacking. The interfacial interaction such as adsorption of the ligand as well as change in surface curvature for metallic nanoparticles has been shown to result in increase or decrease of size depending on orientation [**166–168**]. Decrease in size with higher number of adsorption sites and symmetry distortion has been reported [**169**]. Thus, the observed

decrease in size for **31**CB-AuNPs and **34**CB-AuNPs could be due to the presence of higher number of adsorption sites resulting from eight terminal amino nitrogen in **31** and symmetry distortion in asymmetric **34**.
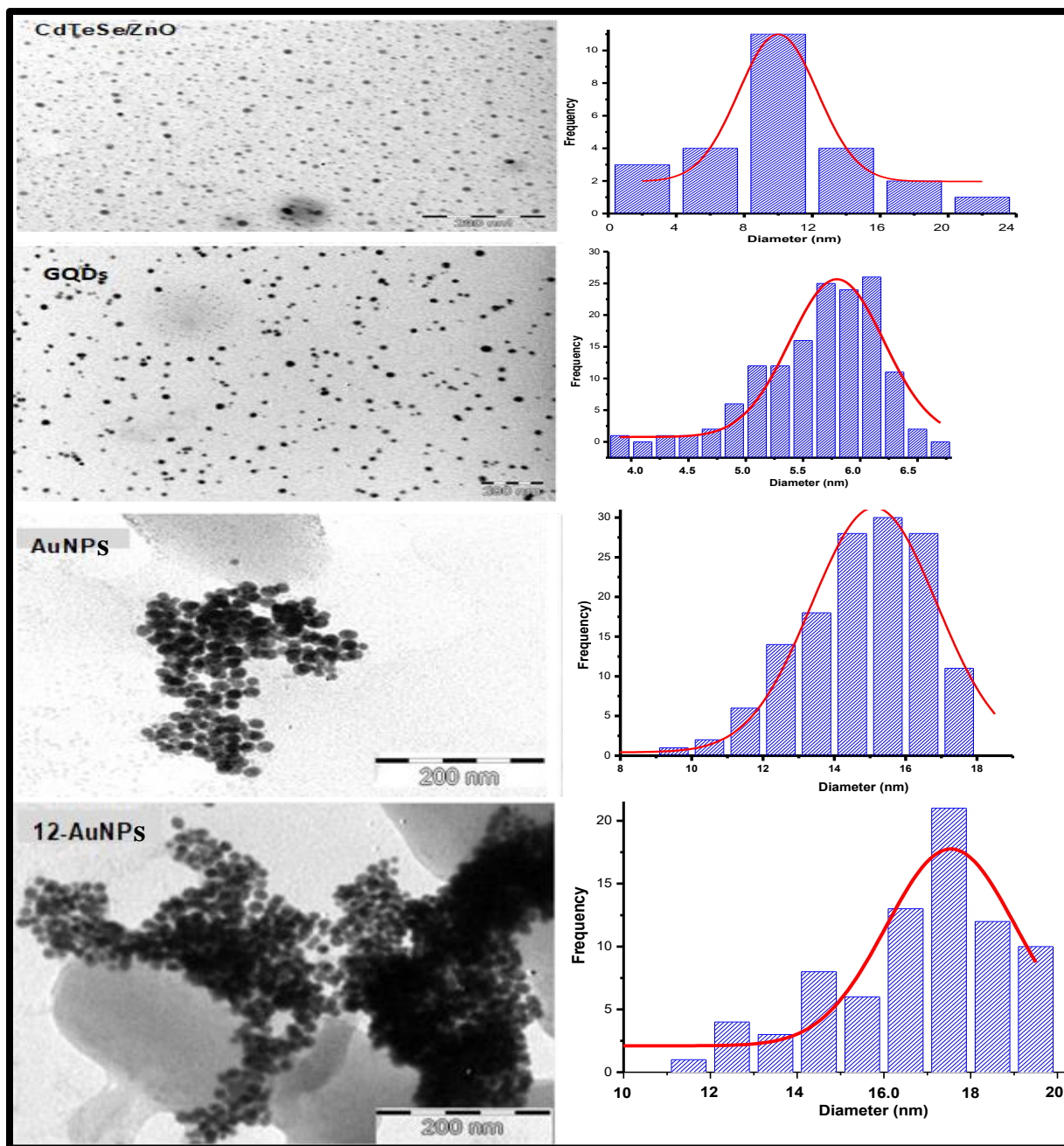
Figure 3.16: Representative TEM micrograph of nanoparticles before and after covalent linkage to MPcs complexes

Table 3.5: Absorption wavelengths and sizes of nanoparticles and the covalent conjugates

Compounds[b]	λ_{max} (nm)[a]	TEM sizes (nm)	XRD sizes (nm)	Loading (mg/mg)
Ball-type complexes 10-12				
10	682	-	-	-
11	689	-	-	-
12	695	-	-	-
GQDs	352	5.9	4.8	-
CdTe	561	9.6	8.3	-
CdTeSe	428	9.1	9.0	-
CdTeSe/ZnO	501	9.8	9.6	-
AgNPs	403	8.2	7.6	-
AuNPs	536	15.1	14.8	-
10-GQDs	682 (352)	9.3	10.1	12
11-GQDs	689 (358)	8.7	7.4	15
12-GQDs	697 (356)	7.2	5.9	7
10-CdTe	682 (561)	11.2	10.7	8
11-CdTe	689 (565)	10.1	9.8	11
12-CdTe	699 (567)	11.3	10.4	9
12-CdTeSe	690 (428)	11.6	9.1	19
12-CdTeSe/ZnO	701 (501)	12.9	10.3	25
12-AgNPs	697 (403)	13.1	10.5	5
12-AuNPs	697 (536)	17.9	15.3	16
aminophenoxy substituted complexes 31-33				
31	680	-	-	-
32	687	-	-	-
33	691	-	-	-
31-CdTe	684	10.5	8.9	10
32-CdTe	691	10.0	9.4	7
33-CdTe	694	11.2	11.5	3
31CB-AgNPs[b]	680 (473)	14.3	14.8	37
31CB-AuNPs[b]	680 (539)	12.3	11.7	30

Table 3.5 continued

Compounds[b]	λ_{max} (nm)[a]	TEM sizes (nm)	XRD size (nm)	Loading (mg/mg)
Asymmetric benzothiazole substituted complexes 34-36				
34	680	-	-	-
35	687	-	-	-
36	693	-	-	-
34-CdTe	684	10.2	9.1	9
35-CdTe	691	10.7	10.5	7
36-CdTe	696	9.8	8.4	4
34CB-AgNPs[b]	681(400)	15.3	13.8	11
34CB-AuNPs[b]	682 (529)	13.5	10.9	17

[a]**Numbers in bracket are for nanoparticles in the conjugate,**
[b]**CB = covalent bond**

3.2.1.3. XRD Diffraction pattern

An XRD peak was observed in the range of $2\theta = 17.8°$ to $28.5°$ for the Pcs (**Fig. 3.17**, using **20** for example), which is typical for phthalocyanine [**170**]. The diffraction peaks due to CdTeSe and CdTeSe/ZnO NPs alone were observed at $2\theta = 26, 42.8$ and $51°$, which correspond to cubic zinc-blend CdTe QDs [**171**]. The metallic Ag/Au showed diffraction peaks at 38.5, 44.8, 65.1, 77.9 corresponding to (111), (200), (220) and (311) for face centered cubic of Au or Ag NPs [**172**]. After covalent linkage of the complexes to MPcs, attenuated peak of MPcs was observed on the diffractogram of the nanoconjugates with peak due to nanoparticles showing significant presence (**Fig. 3.17**, using **12**-CdTeSe/ZnO and **20**-AuNPs as examples) The attenuation of the MPcs diffraction peaks could be adduced to the possible interaction between the MPc and NPs.
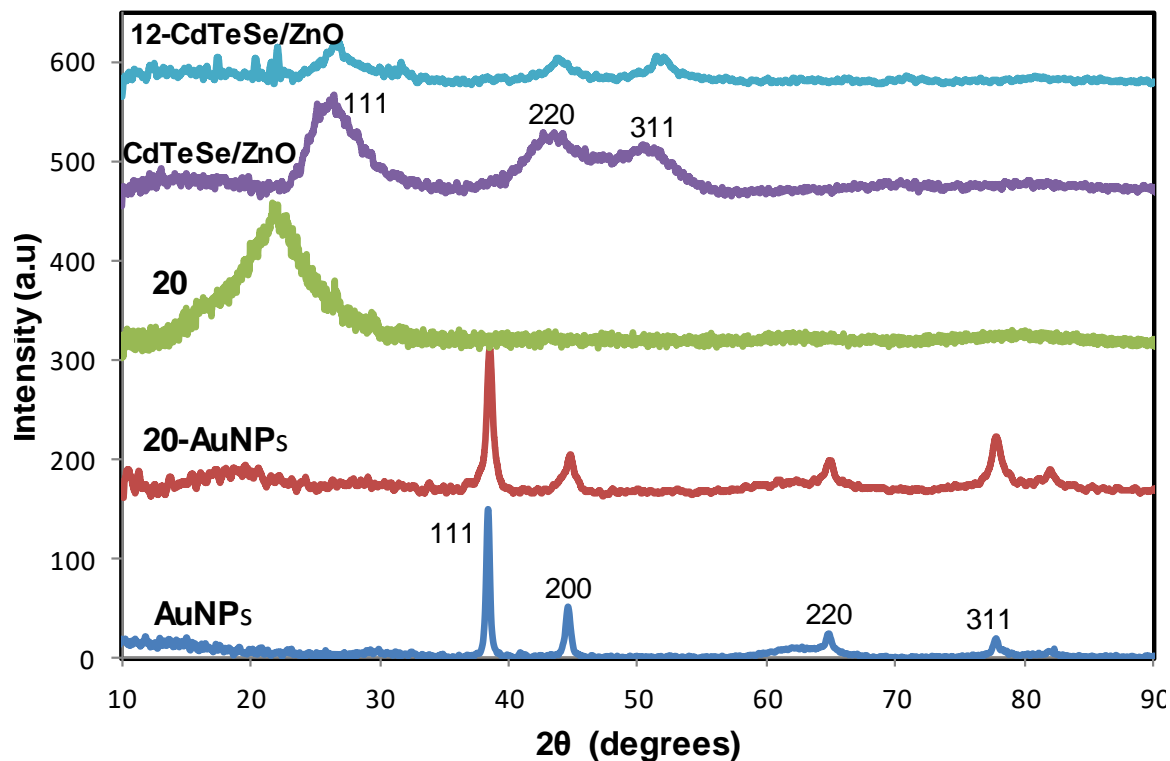
Figure 3.17: XRD Diffractogram of complex 20, NPs and corresponding nanoconjugates.

The crystallite diameter size of NPs was calculated using Debye–Scherrer's **equation:3.1** [173]

$$d = \frac{0.89\lambda}{\beta cos\theta} \tag{3.1}$$

where λ is the wavelength of the X-ray source ($\lambda = 1.5405$ Å), β is the full width at half maximum of the diffraction peak, and θ is the angular position. The sizes were determined by focusing on the (111) plane peak. The size calculated from XRD closely agreed with those obtained from TEM (**Table 3.5**).

3.2.1.4. EDX analysis

The energy dispersive X-ray spectrometer (EDX) was used to qualitatively ascertain the elemental compositions of the nanoparticles before and after covalent linkage with the complexes and the spectra is shown in (**Fig. 3.18** using **12,** CdTeSe and AgNPs as examples). The EDX of the NPs alone showed the expected atoms. After covalent linkage of the complexes to nanoparticles, additional peaks (In, Cl) were observed indicating the presence of the complexes in the nanoconjugates. The Cl is the axial ligand on the In central metal.
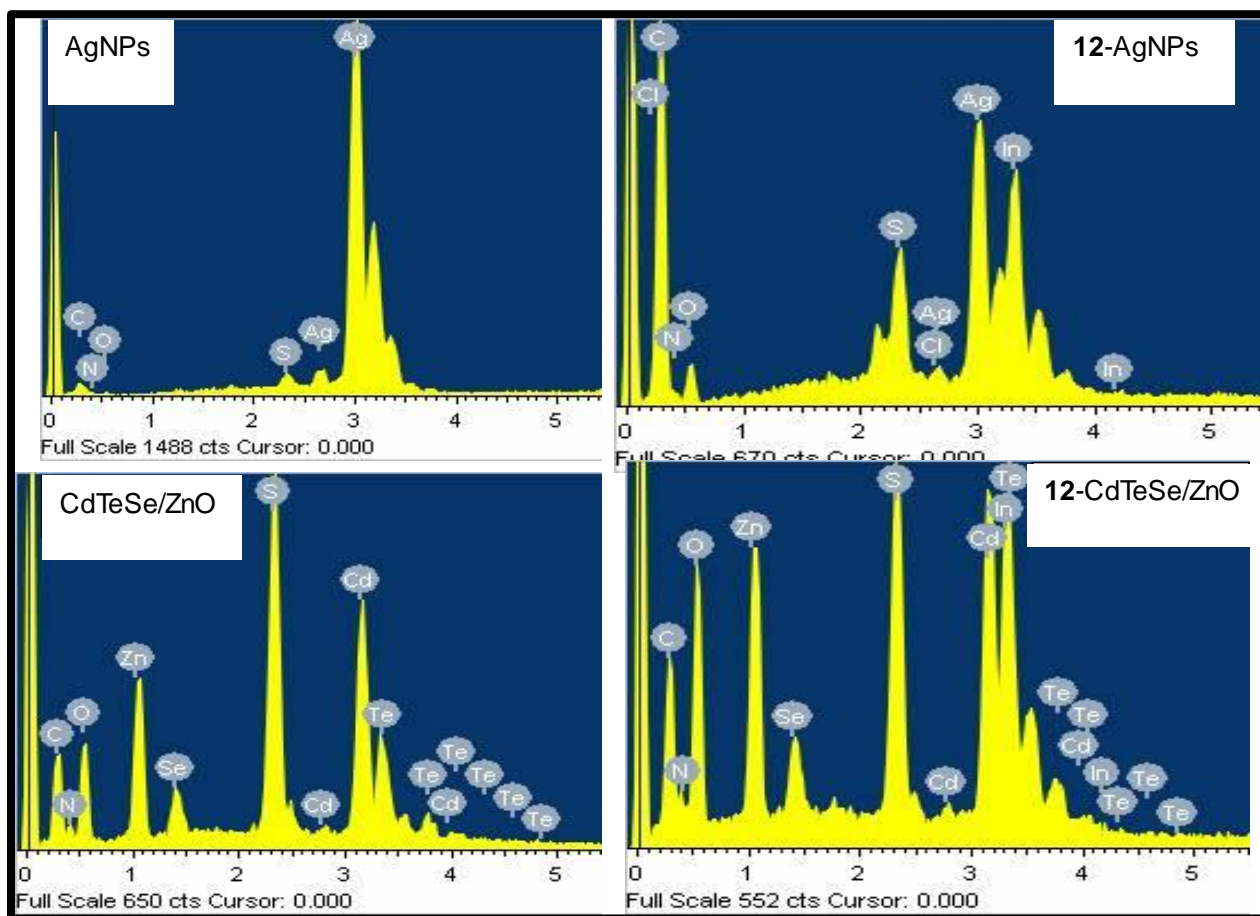
Figure 3.18: Representative EDX spectra of NPs before and after linkage to MPcs

3.2.1.5. UV-vis absorption spectra

Fig. 3.19 shows the absorption spectra of the nanoparticles in water for semiconductor and GQDs and toluene for metallic nanoparticles. The broad absorption spectral bands for semiconductor QDs [**174**] were observed at 561, 428 and 501 nm respectively for CdTe, CdTSe/ZnO and CdTeSe, while the carbon based GQDs displayed absorption band at 352 nm (**Table 3.5**). The surface plasmon resonance bands of the metallic nanoparticles were observed at 403 and 536 nm for AgNPs and AuNPs respectively (**Fig. 3.19, Table 3.5**). The absorption peaks of the nanoparticles alone in the conjugates were found to be either slightly red-shifted or remain the same apart **34**CB-AgNPs and **34**CB-AuNPs that showed a blue-shift. The red-shifting of the absorption bands of the nanoparticles could be attributed to increase in size following conjugation as shown in **Table 3.5**.
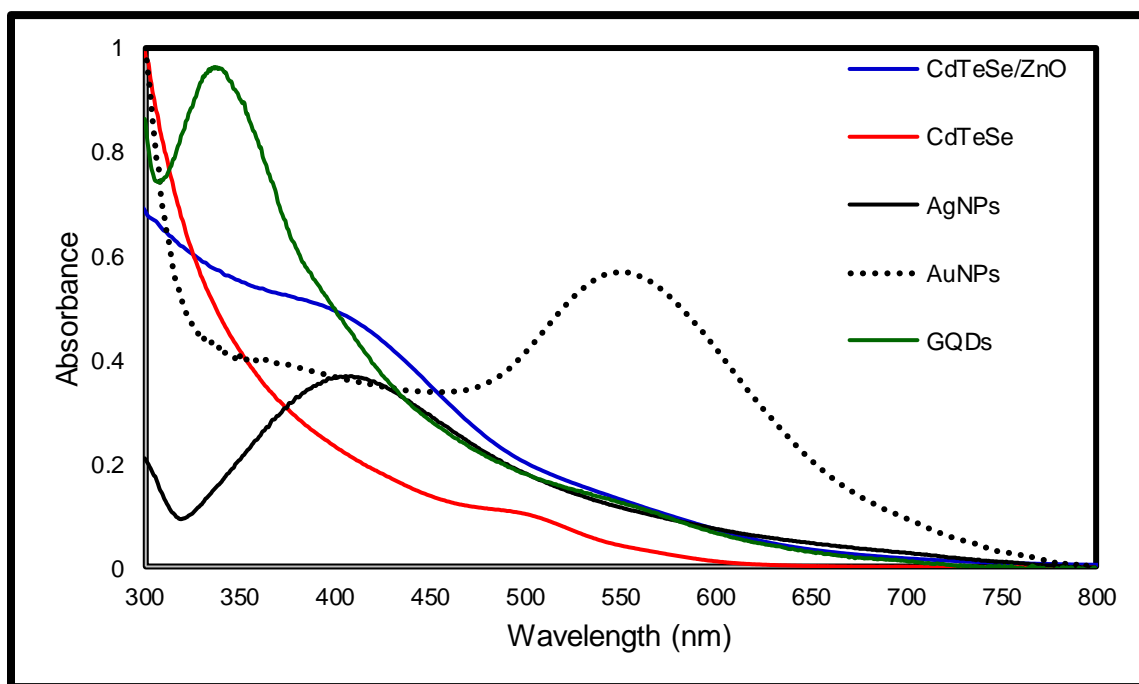
Figure 3.19: Uv-vis absorption spectra for different nanoparticles. Solvent: water for CdTeSe, CdTeSe/ZnO and GQDs, toluene for AgNPs and AuNPs.

Upon covalent linkage of these nanoparticles to MPcs, some significant changes in absorption spectra of the Pcs were seen (**Fig. 3.20**). **12**-CdTeSe showed a 5 nm blue shifting while a 6 nm and 4 nm red-shifting was observed for **12**-CdTeSe/ZnO and **12**-CdTe respectively. The conjugates of asymmetric **34**-**36** also showed a red shift of 4 nm each for **34**-CdTe and **35**-CdTe, and 3 nm for **36**-CdTe (**Table 3.5**). Blue or red shifting of MPcs conjugated to nanoparticles has been attributed to π-π interaction of the MPcs with the nanomaterials [**175**]. A slight red-shifting of 2 nm was also observed for **12**-AgNPs and **12**-AuNPs.
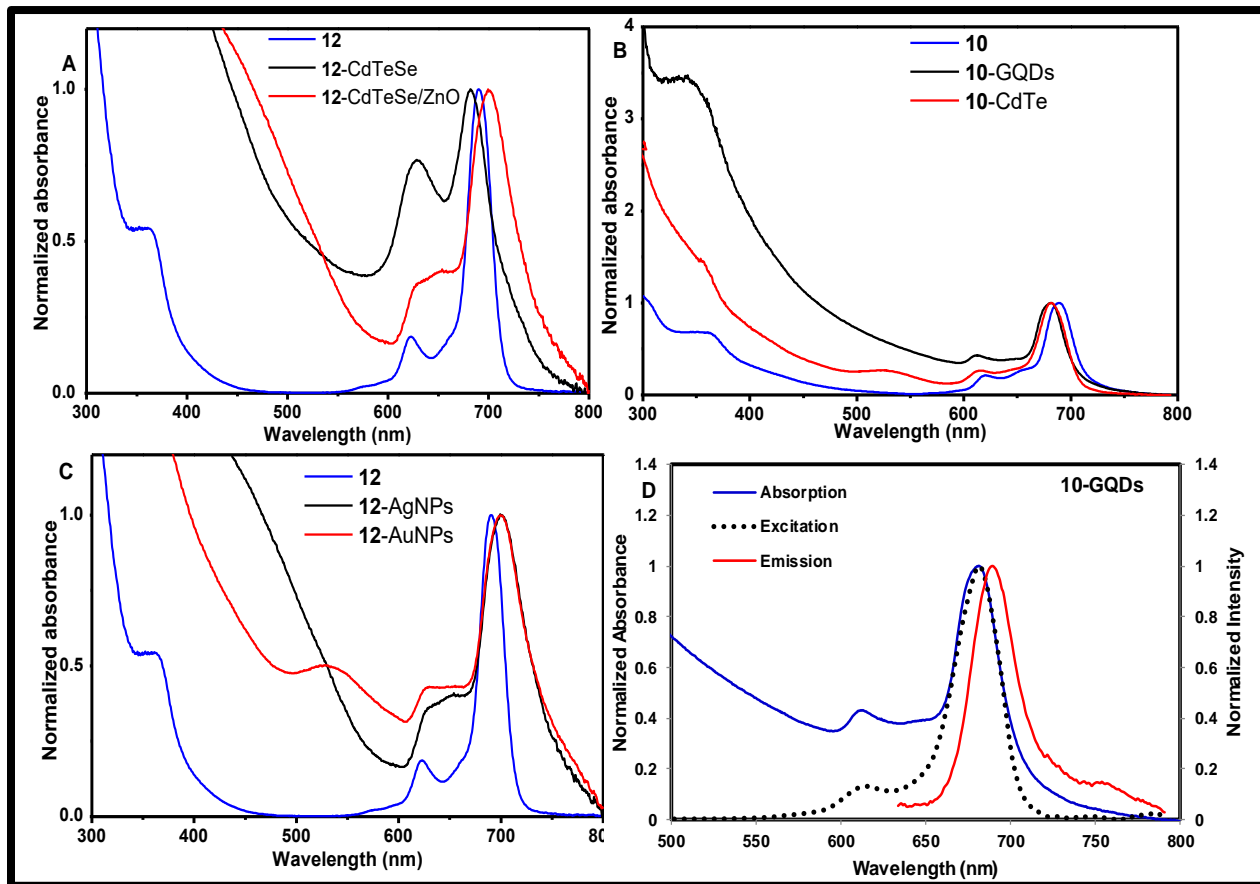
Figure 3.20: Representative absorption spectra of the complexes and corresponding nanoconjugates (A-C) and absorption, excitation and emission spectra of 10-GQDs (D)

The loading of complexes onto the nanoparticles was investigated following a literature report [**176**], but using absorption instead of fluorescence. This involves comparing the Q band absorbance intensity of the Pc in the conjugate with that of the initial Pc before the conjugation. Increased loading of 9, 19 and 25 mg/mg for **12**-CdTe, **12**-CdTeSe and **12**-CdTeSe/ZnO (**Table 3.5**) was observed as size increases from core (CdTe), core-shell (CdTeSe) and core-shell-shell (CdTeSeZnO). Though it is expected that smaller particle size should result in more loading due to higher surface to volume ratio, larger particles has been shown to possess core that allow more drugs to be loaded [**177**]. Higher loading was observed for **31**CB-AgNPs and **31**CB-AuNPs compared to other conjugates, which could be due to easy accessibility of the eight terminal amino group of **31**-**33** for nucleophilic attack.

The emission spectra of the nanoconjugates were mirror image of both the absorption and excitation and the latter two are similar (**Fig. 3.20 C**, using **10**-GQDs as example), suggesting that excitation at selected wavelengths does not affect the ground state nuclear configuration of the nanocomplexes.

3.2.1.6. X-ray photoelectron spectroscopy (XPS) Analysis

An important indication of amide linkage is characteristic carbonyl (-N=C=O) peak at binding energy between 396-404 eV in high resolution N1s deconvolution XPS [**178**]. The XPS high resolution N1s deconvolution of the glutathione functionalized nanoparticles before and after covalent linkage are shown in **Fig. 3.21**. The binding energies of GSH-AuNPs alone was observed at at 396.3 eV, 398.1 eV and 399.2 eV corresponding to N-C, N-H and N-C=O (**Fig. 3.21**). This is expected since glutathione also contain amide bond. The GSH-AgNPs alone showed similar trend with binding energy for N-C peak at 396.7 eV, N-H at 397.3 eV and N-C=O at 397.3 eV (figure not shown). After covalent linkage of **31** and **34** to the nanoparticles, there

was a significant increase in intensity of N-C=O from 152 cps in GSH-AuNPs to 8550, 3920 and 4732 cps in **31**CB-AuNPs, **31**CB-AgNPs and **34**CB-AuNPs respectively as well as shift in binding energy due to amide bond (N-C=O) from 399.2 eV for GSH-AuNPs alone to 401.5 and 399.5 eV in **31**CB-AuNPs and **34**CB-AuNPs. A similar trend was also observed for **31**CB-AgNPs and **34**CB-AgNPs with shift in amide amide bond to 399.8 and 399.7 eV respectively. Thus, the amide bond resulting from linkage with MPcs complexes lie at slightly longer binding energy than that resulting from glutathione alone.
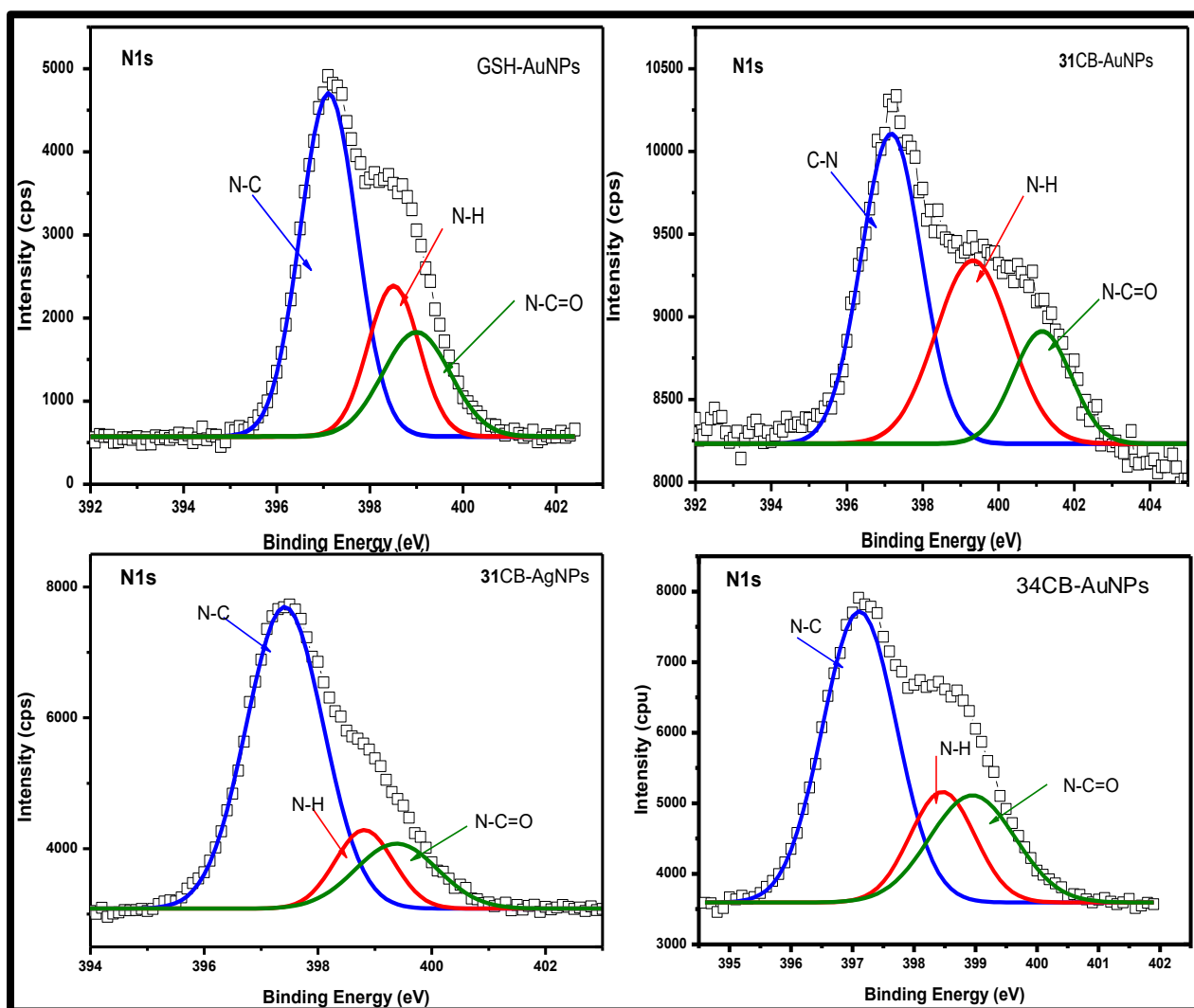
Figure 3.21: High resolution XPS N 1s spectra of GSH-AuNPs and nanoconjugates of complexes 31 and 34

3.2.2.Surface assembly of 19-27, 31 and 34 onto metallic nanoparticles

Scheme 3.11 illustrate the route used to assemble MPcs onto metallic gold and silver nanoparticles. Two batches of oleyamine functionalized AgNPs and AuNPs were employed, hence different sizes of Au/Ag NPs are presented in **Table 3.6**. The sulphur and nitrogen atoms within the benzothiazole ring for **22**-**27**, **34** or the terminal amino nitrogen for **31** were utilized due to strong affinity of gold and silver to sulphur and nitrogen. The ligand exchange between Ag/Au NPs and S or N of the complexes result in displacement of the loosely bound olyamine (OA) on surface of the NPs.
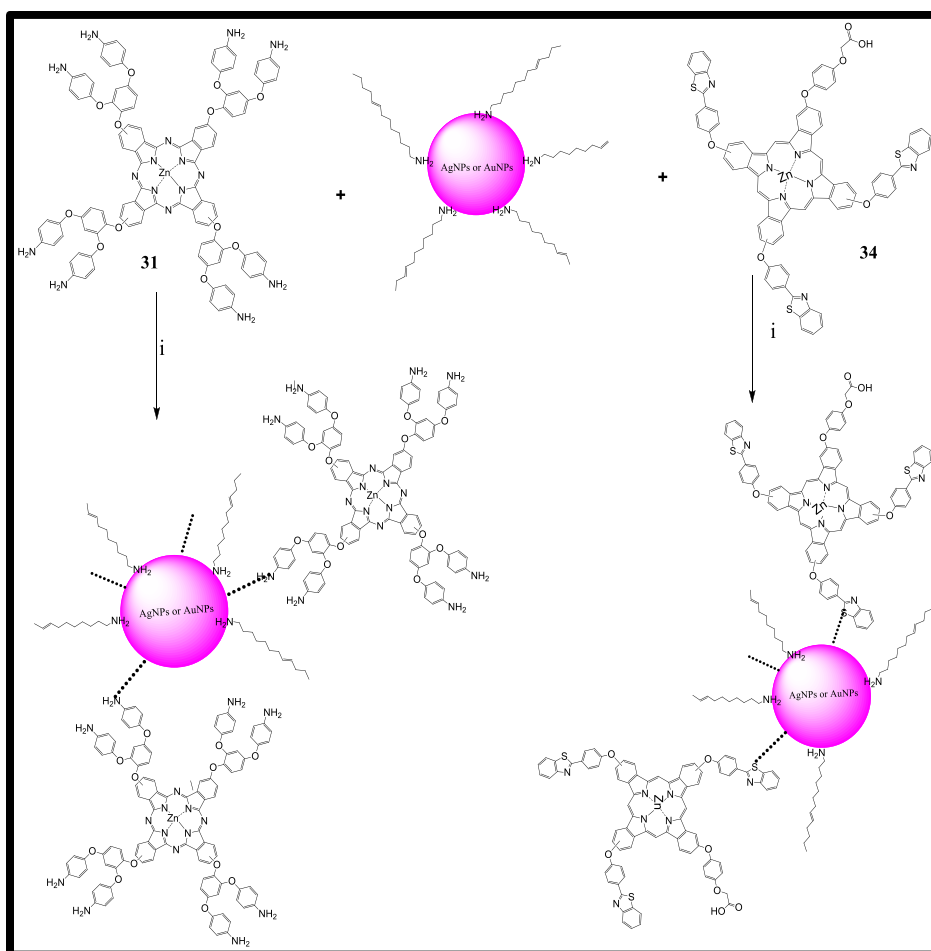
Scheme 3.11: Schematic illustration of surface assembly of the synthesized complexes onto metallic nanoparticles.

3.2.2.1. TEM/EDX

The TEM micrographs of the AuNPs and AgNPs (**Fig. 3.22**, first batch as examples) showed monodispersed particles with average size of 12.5 nm and 10.4 nm for first batch and 10.1 and 9.3 nm for second batch (**Table 3.6**,). Complexes **19**-**21** was conjugated to first batch while **22**-**27**, **31** and **34** were conjugated with the second batch. The size increases to 13.2, 13.0 and 12.7 nm for **19**-AuNPs, **20**-AuNPs and **21**-AuNPs after conjugation. Similarly, the corresponding silver nanocomposite also increases to 11.2, 10.8 and 11.7 nm respectively for **19**-AgNPs, **20**-AgNPs and **21**-AgNPs. Conjugates of complexes **22**-**27** as well as **31** and **34** also follow similar trend with increase in sizes after conjugation (**Table 3.6**) as discussed before.

The elemental compositions of the nanoparticles were qualitatively determined using energy dispersive X-ray spectrometer (data not shown). The EDX of the metallic NPs alone showed the expected atoms. On conjugation of the complexes AgNPs or AuNPs, additional peaks (Zn. Ga, In and Cl) were observed indicating the presence of the Pc in the nanoparticles.

3.2.2.2. XRD pattern

The XRD patterns shows crystalline face centred cubic of the metallic Ag/Au as observed in **Fig. 3.17**. Peak broadening around 23⁰ was observed after conjugation shows the presence of Pcs in the nanocomposite (**Fig. 3.17**, using **20** as example) The NP sizes from XRD were calculated using the Debye–Scherrer **equation 3.1** described above. The sizes of metallic AuNPs and AgNPs were found to be 12.0 and 9.4 nm for the first batch, slightly lower than the observed size using TEM (**Table 3.6**) while the second batch showed a size of 9.4 and 8.3 nm for Au and Ag NPs. As observed in TEM, the size increases to 11.9, 13.2 and 10.6 nm for **19**-AuNPs, **20**-AuNPs and **21**-AuNPs and 9.2, 11.3, and 8.7 nm for corresponding **19**-AgNPs, **20**-

AgNPs and **21**-AgNPs (**Table 3.6**). All other conjugates also showed increase in size following conjugation (**Table 3.6**) as discussed before.
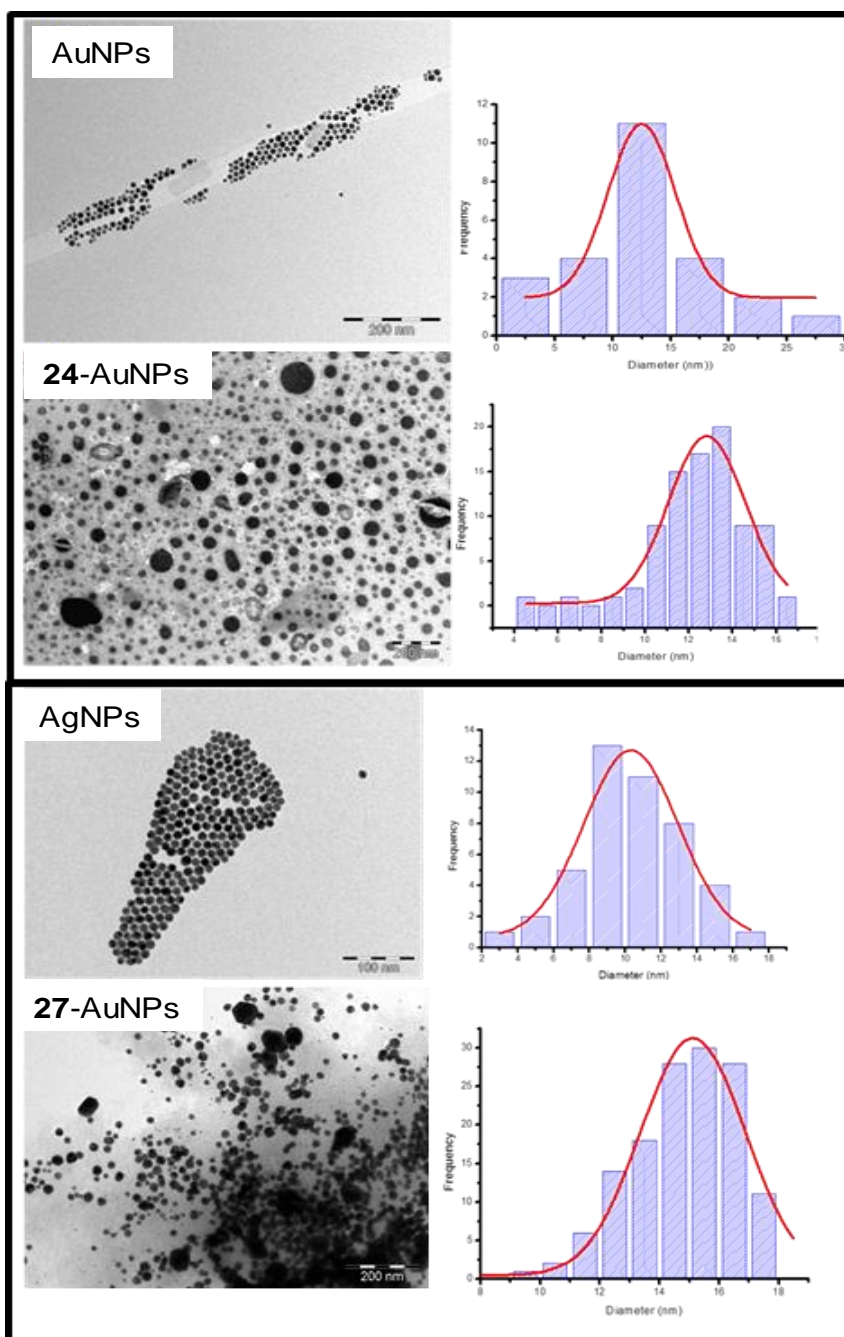
Figure 3.22. Representative TEM images of nanoparticles alone and when conjugated to the complexes

Table 3.6: Absorption maxima for complexes and corresponding self assembled nanoconjugates in DMSO with size determination parameters

Compound	λ_{max} (SPR)[a] (nm)	TEM sizes (nm)	XRD sizes (nm)	Loading (g/cm² NPs)
Ball-type complexes 19-21 and conjugates				
19	681	-	-	-
20	698	-	-	-
21	701	-	-	-
AgNPs	422	10.4	9.4	-
AuNPs	536	12.5	12.0	-
19-AgNPs	686 (392)	11.2	9.2	17
19-AuNPs	688 (536)	13.2	11.9	11
20-AgNPs	698 (415)	10.8	11.3	40
20-AuNPs	696 (554)	13.0	13.2	23
21-AgNPs	701 (422)	11.7	8.7	52
21-AuNPs	705 (540)	12.7	10.6	31
Benzothiazole substituted complexes 22-27 and conjugates				
22	681	-	-	-
23	688	-	-	-
24	692	-	-	-
25	685	-	-	-
26	692	-	-	-
27	697	-	-	-
AgNPs	417	9.3	8.3	-
AuNPs	536	10.1	9.4	-
22-AgNPs	681 (423)	13.8	12.1	9
22-AuNPs	682 (536)	13.4	13.4	14
23-AgNPs	689 (422)	15.3	14.9	6
23-AuNPs	696 (537)	14.2	11.5	11
24-AgNPs	692 (427)	14.3	15.0	7
24-AuNPs	695 (536)	12.4	17.1	22
25-AgNPs	686 (430)	17.9	13.2	13
25-AuNPs	685 (537)	17.5	15.1	23
26-AgNPs	691(422)	13.8	10.8	12
26-AuNPs	692 (540)	12.9	14.7	29
27-AgNPs	701 (422)	16.7	11.8	19
27-AuNPs	697 (538)	11.5	14.9	33

Table 3.6 continued

Compounds	λ_{max} (SPR) (nm)	TEM sizes (nm)	XRD sizes (nm)	Loading (g/cm² NPs)
aminophenoxy substituted complexes 31 and conjugates				
31	680	-		-
31-AgNPs	680 (417)	11.2	9.9	28
31-AuNps	681 (529)	13.1	12.5	16
Asymmetric benzothiazole substituted 34 and conjugates				
34	680	-		-
34-AgNPs	680 (407)	10.7	8.8	21
34-AuNPs	681(523)	10.4	9.6	33

[a]Values in bracket are for nanoparticles

3.2.2.3. Electronic absorption spectra

The metallic AgNPs and AuNPs shows characteristic surface plasmon resonance (SPR) bands at 422 nm and 536 nm for AgNPs and AuNPs respectively (**Fig. 3.23 A and B**, **Table 3.6**). Please note that Au/Ag NPs here are capped with OA unlike GSH capped ones in **Table 3.5**, hence the spectra may differ. The ball-type **19-21**, **20**-AuNPs and **21**-AuNPs showed a red-shift in the SPR peaks to 554 and 540 nm while **19**-AuNPs remain unchanged. On the other hand, **19**-AgNPs and **20**-AgNPs showed a blue-shift to 392 and 415 nm even with increased sizes while the SPR peak for **21**-AgNPs remain unchanged (**Table 3.6**). SPR peaks for all the other conjugates either red-shifted or remain unchanged apart from **31**-AuNPs, **34**-AgNPs and **34**-AuNPs that showed a blue shift (**Table 3.6**). A red-shift in SPR after conjugation has been reported [**166**] and was attributed to increase in size of the nanoparticles due to π-π interaction of the dye chromophore with the nanoparticles. The blue-shift in SPR peak with increase in size has been explained from the fact that the shifts in SPR bands in metallic nanoparticles can be affected by surface curvature and damping of electrons [**166,179**]. The orbital overlap can result in stiffness of surface plasmon and this occurs with a very low surface curvature (large particle size),

leading to a high energy resonance, and hence blue-shift in the SPR band. Link et al [**179**] observed blue shifts of the SPR peak in gold-silver nano-alloys with increasing particle size.
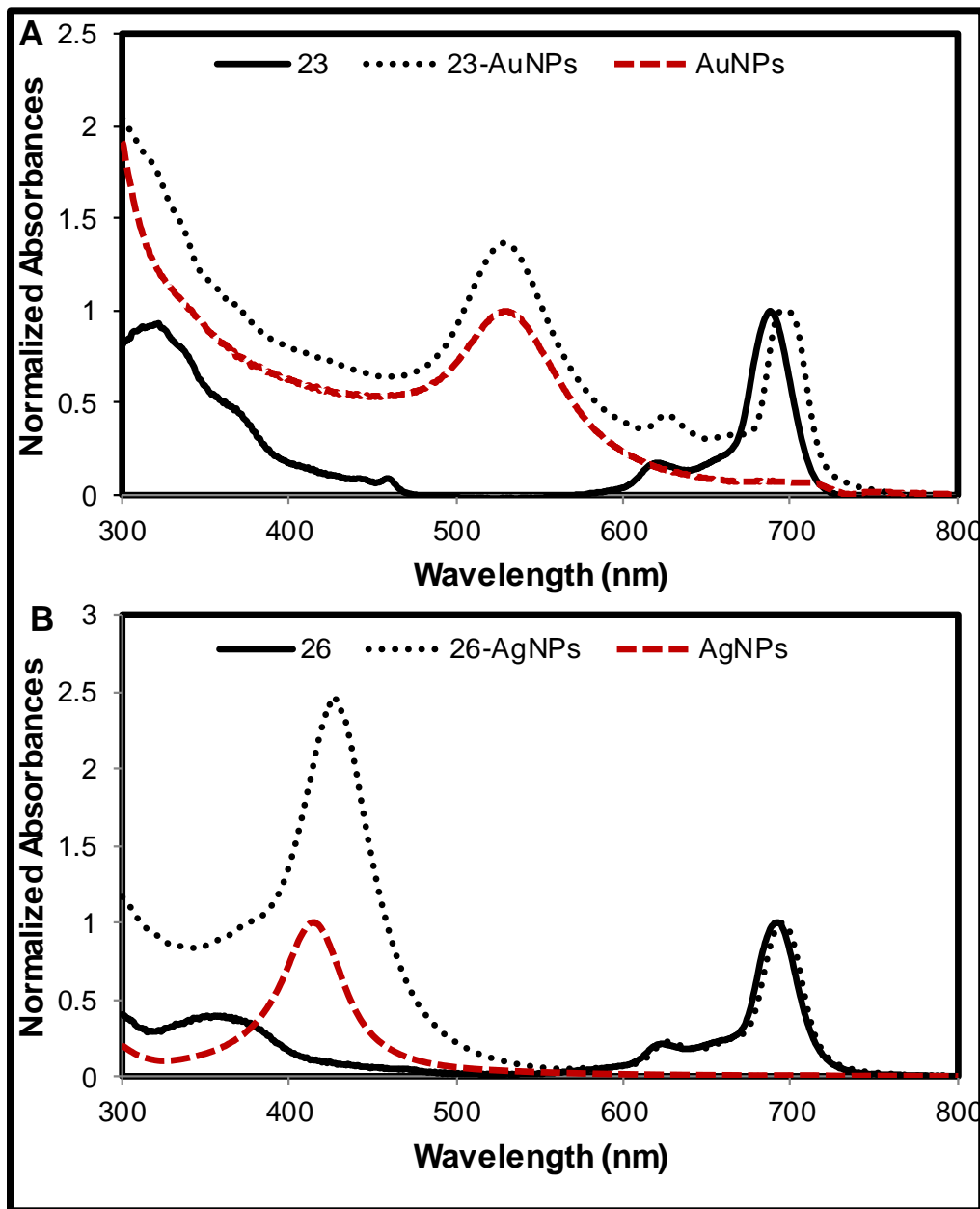
Figure 3.23: UV-vis absorption spectra of (A) 23, AuNPs and 23-AuNPs (B) 26, AgNPs and 26-AgNPs. Solvent = DMSO.

This stiffness of the surface plasmon is usually associated with close packing of chromophore onto the nanoparticles [166].

All the complexes either maintain their Q band maxima or predominantly red-shifted (Table 3.6). The shift in the Q band of the Pc could be attributed to the molecular orientation of the MPc to the NPs as reported elsewhere [180]

Because the interaction of the MPcs and Au/Ag NPs occurs through adsorption rather than covalent attachment, a different method for calculating loading was employed in this section. The loading of MPcs onto the nanoparticles was investigated according to reported procedure [181]. This involves investigating the ratio of metallic nanoparticles required to saturate the dyes molecule, hence resulting in almost disappearance of the Q-band (Fig. 3.24). The complete disappearance of the absorption band of 19-21 occurs at an [Au]/[complex] ratio of 5.2, 8.5 and 6.0 for 19, 20 and 21 respectively (Fig. 3.24 A and B using 19-AgNPs and 20-AuNPs as examples). The number of gold or silver atoms per particle (N_x) was determined using equation 3.2.

$$N_x = (59 \text{ nm}^{-3})(\pi/6)(DMS)^3 \hspace{3cm} (3.2)$$

where DMS is the mean diameter size of the particles as found from TEM and x is the metallic nanoparticles (i.e AgNPs or AuNPs). Thus, for a silver nanoparticle with 12.5 nm will have 35776.1 numbers of silver atoms. For complex 20 with the ratio [Ag]/[complex 20] of 5.2, the number of molecules of complex 20 per gold nanoparticle was determined to be 6880. With the known molecular weight of 20, the mass of the complex per unit area of nanoparticles was calculated to be 40 (Table 3.6).
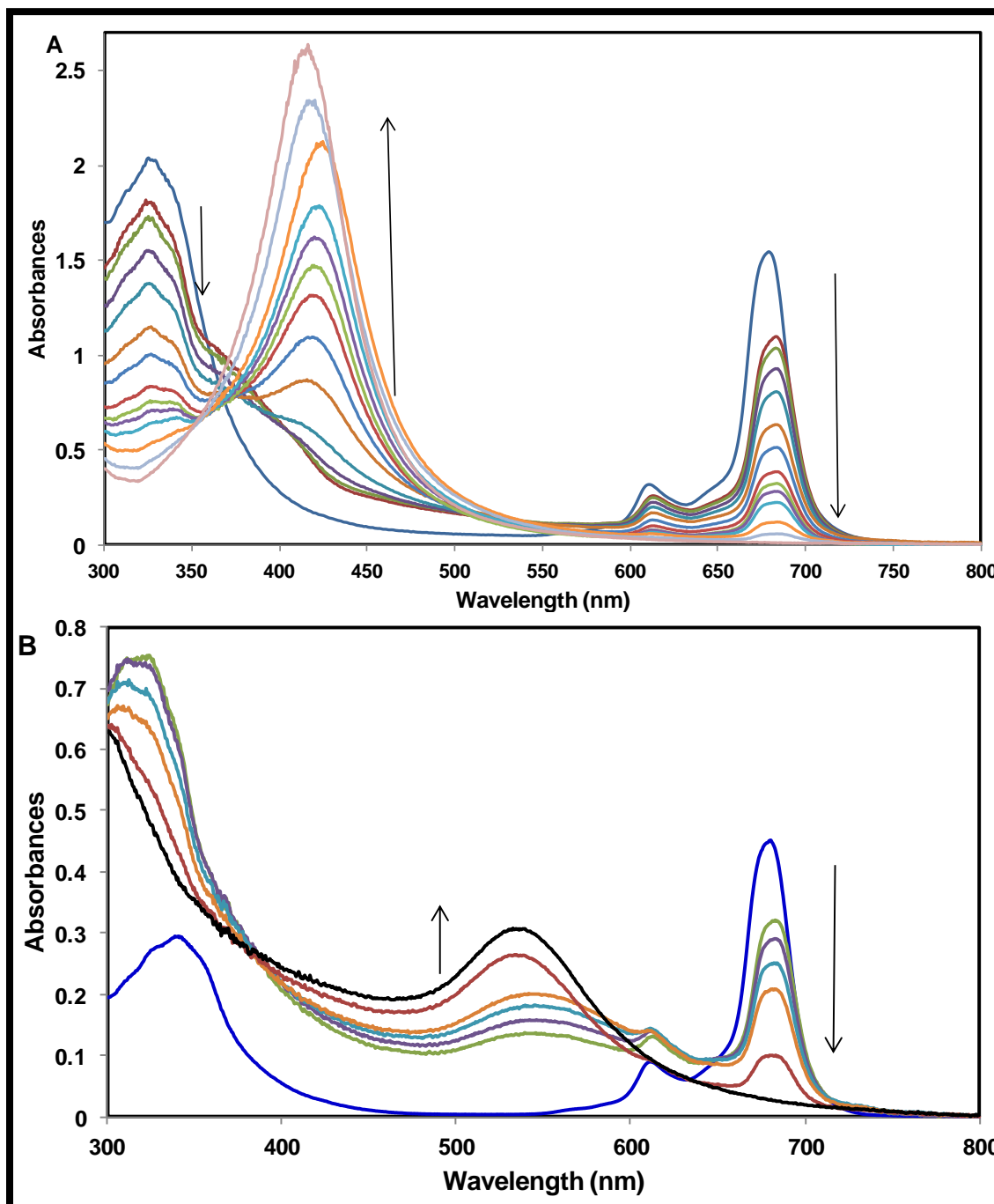
Figure 3.24: Absorption spectra of 3×10^{-6} M of (A) 19 and (B) 20 in aqueous solution containing different ratios of AuNPs or AgNPs, respectively.

For ball-type **19**-**21**, more loading of complexes was observed for the Ag conjugates compared to Au conjugates (**Table 3.6**) which could be attributed to smaller particles size, hence high surface area to volume ratio for the former compared to the latter. On the other hand, the Au conjugates of **22**-**27** displayed higher loading than the correspond Ag conjugates. A critical look at **Table 3.6** indicates larger particle size for Ag conjugates compared to that of Au, hence the Au conjugates in this case will have slight higher surface area to volume ratio resulting to higher loading. Conjugates of **31** and **34** also follow similar trend in that larger particle size conjugates showed lower loading (**Table 3.6**)

3.2.2.4. X-ray photoelectron spectroscopy (XPS)

The probable site of interaction of the nanoparticles with MPcs was investigated using XPS analysis.

The XPS survey spectra of the compounds exhibited the expected elemental compositions at their respective binding energies (eV). Ga (21 eV), Ga (101 eV), S (161 eV), C (285 eV), N (400 eV), and O (534 eV) were found in complex **26** for example while its conjugates with AuNPs (**26**–AuNPs) and AgNPs (**26**–AgNPs) depicted similar trends but with the presence of Au (665 eV) and Ag (575 eV and 606 eV) for the respective conjugates (**Fig. 3.25 A**).

Because sulfur to metal interaction is expected, the high-resolution spectra deconvolution of S 2p was performed. The S 2p peak of complex **26** was deconvoluted and it accounted for two sub peaks with binding energies at 169.91 eV and 165.08 corresponding to S–C and S. Similar patterns were observed for the conjugates with the appearance of a new peak which could be attributed to the interaction between S–Au or S–Ag. Upon deconvolution of **26**–AuNPs, three sub peaks were obtained, and they correspond to S–C, S and S–Au at 164.58 eV, 165.72

eV and 166.83 eV respectively, (**Fig. 3.25 B**). Deconvolution of **26**–AgNPs also showed three sub peaks which correspond to S–C, S and S–Ag at 165.10 eV, 167.07 eV and 169.05 eV respectively. The appearance of the additional sub peaks and chemical shift in the binding energy of S could suggest the successful formation of the S–Au or S–Ag. For all conjugates, there was no evidence from XPS of the involvement of nitrogen groups on the MPc substituents in the binding with AgNPs or AuNPs except for 31 without any sulphur atom within the structure.
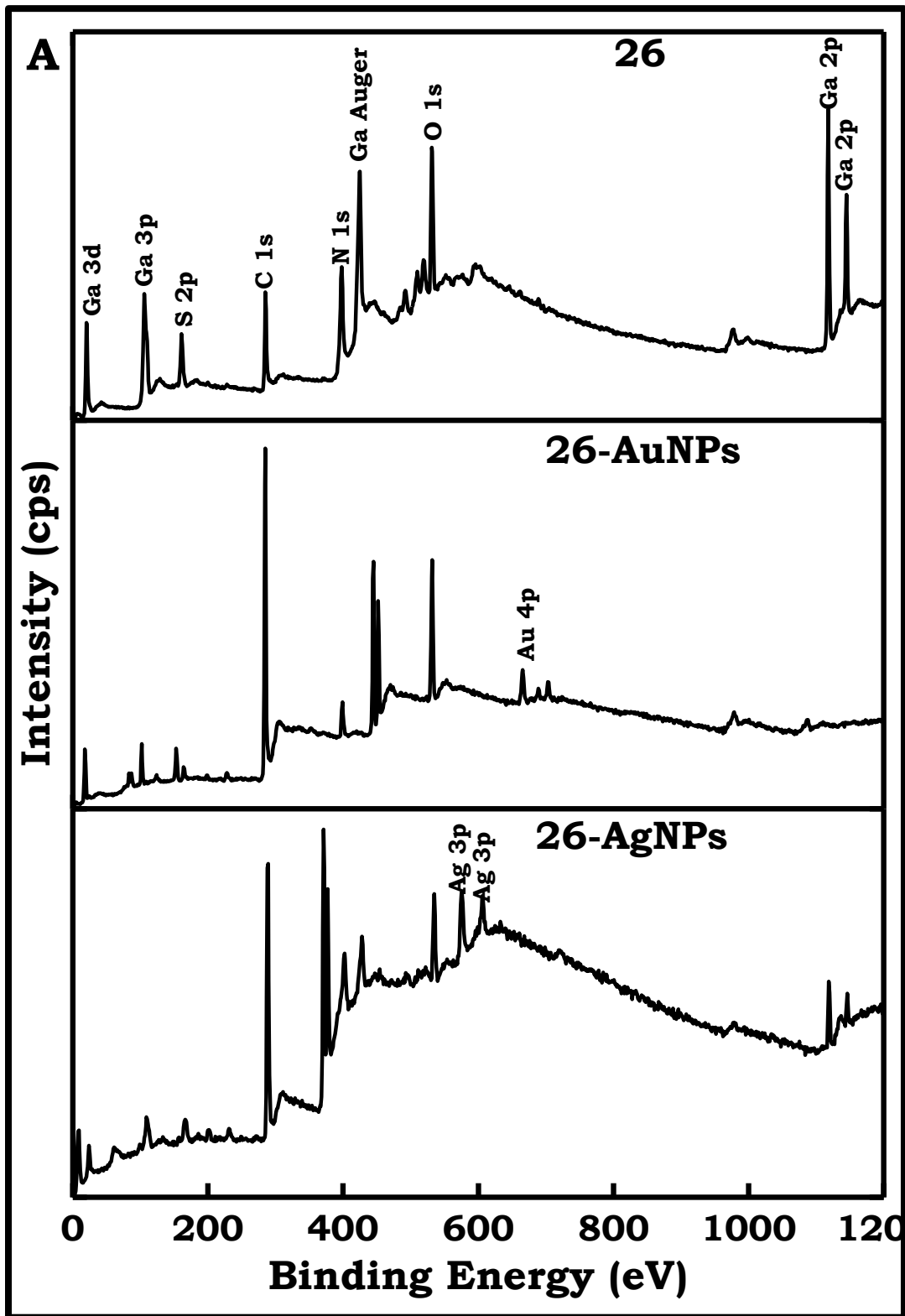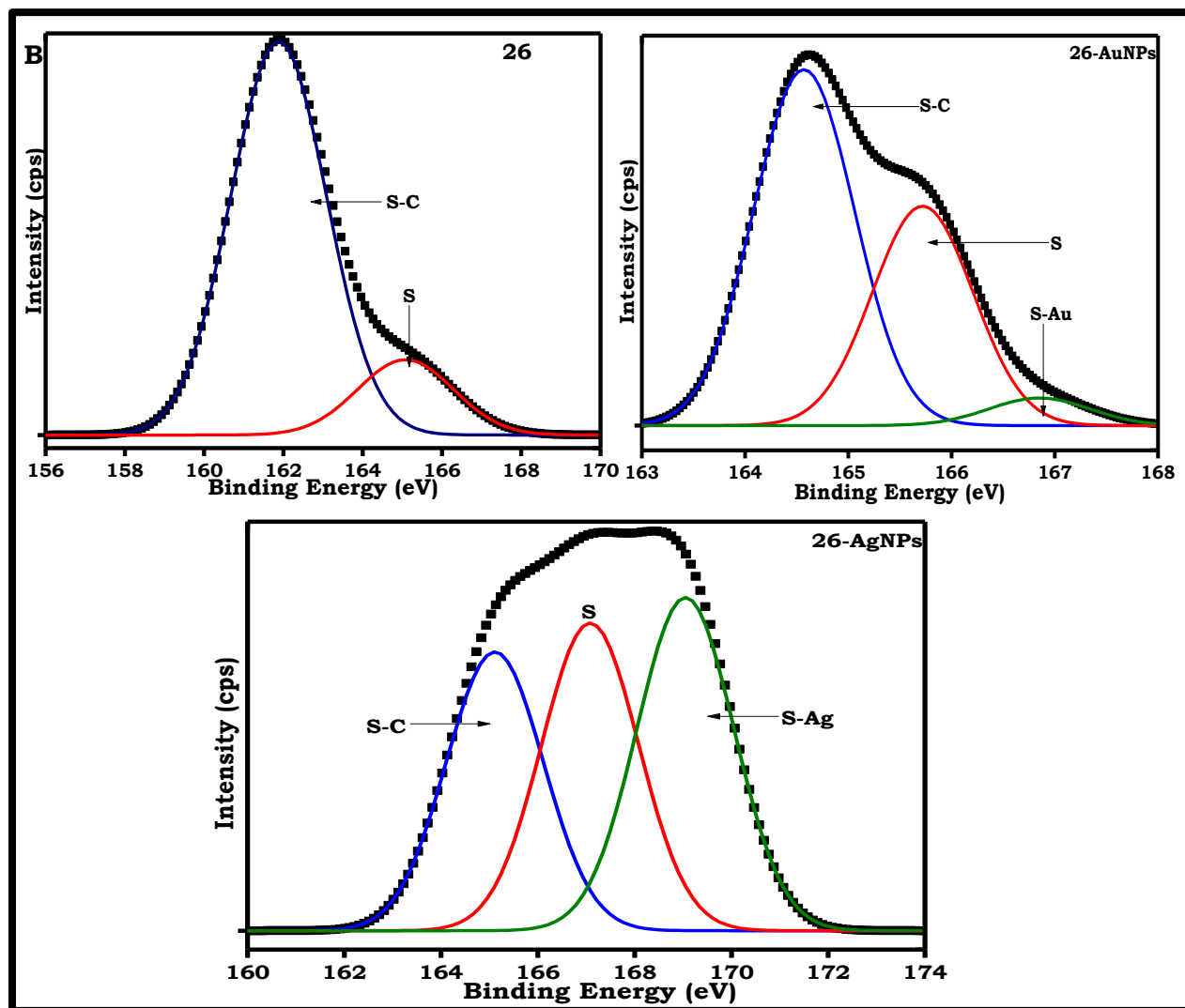
Figure 3.25: XPS spectra (A) Survey spectra for complex 26, 26–AuNPs and 26–AgNPs; and (B) High resolution spectra of S 2p for complex 26, 26–AuNPs and 26–AgNPs.

XPS N1s deconvolution of **31**-AuNPs showed two sets of N1s doublets, one centered around 397.7 eV and the other at 400.8 eV (**Fig. 3.26**, using **31**-AuNPs as example). The corresponding silver nanoconjugate also showed similar trend with binding energy at 397.3 eV and 399.7 eV (spectra not shown). The presence of two set of doublets following surface assembly, indicate the existence of the amino nitrogen N1s in two different environments. The most logical conclusion in this case would be that some amino 'arms' of complex **31** underwent N-Au or N-Ag interaction following surface

assembly while others did not. The set of doublets were resolved using peak fitting to investigate different nitrogen groups present. The peak at 400.8 eV is assigned as nitrogen bound to gold, while the peak at 397.7 eV could indicate unbound nitrogen. Xiao et al [**182**] reported a binding energy of 399.2 eV for unbound amino nitrogen and 401.7 eV for nitrogen bounded to gold while Zhang et al [**183**] also observed a binding energy of 398.8 eV and 401.5 eV for free amine and amine bounded to gold nanoparticles, respectively.
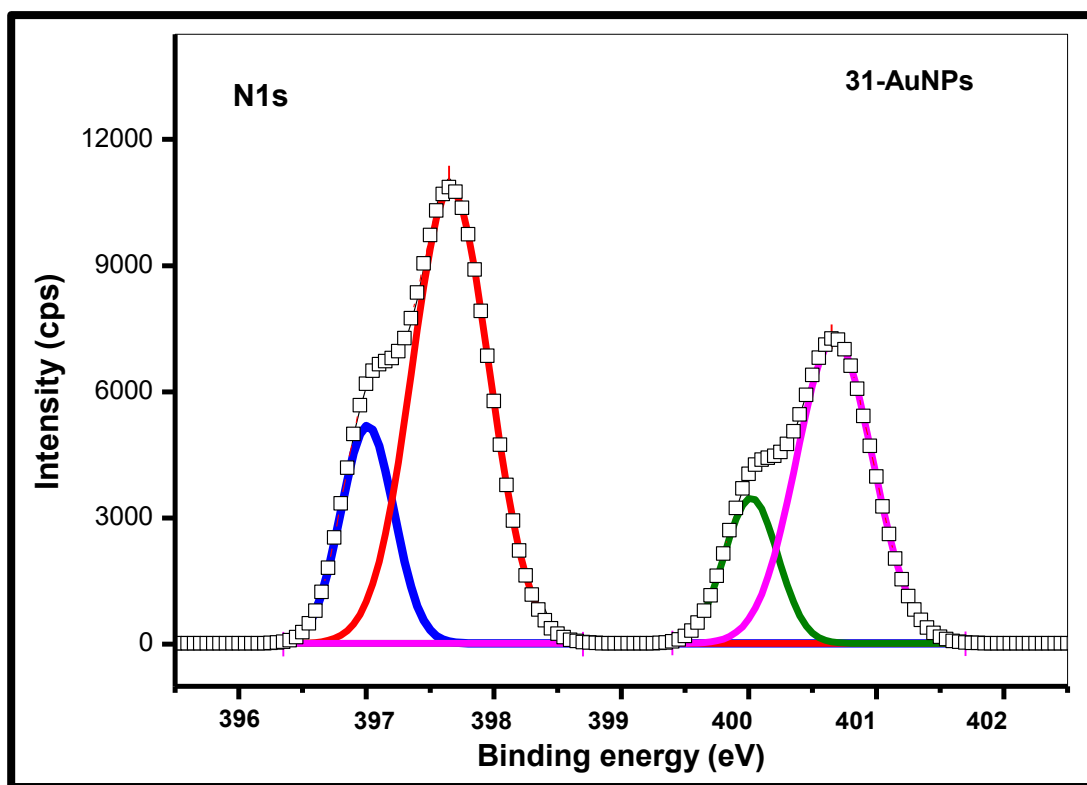
Figure 3.26: XPS High resolution spectra of N1s for 31–AuNPs.

3.3. Conclusion for the chapter

The different metallophthalocyanines synthesized in this work were characterized using various spectroscopic and analytical techniques. The complexes were either covalently or surface assembled onto different nanomaterials.

Evidence from XPS, FTIR, Uv-vis, XRD and EDX spectra showed successful linkage of these complexes to nanomaterials.

The origin of optical transitions in these molecules was investigated using TD-DFT calculation.

The Uv-vis absorption spectra showed spectral broadening for the ball-type complexes compared to their corresponding monomeric analogues. For all complexes with the same substituents, a red-shifting in order of Zn < Ga < In was observed in the Q band maxima, which was confirmed from TD-DFT to be due to narrowing of HOMO-LUMO gap with increase in atomic weight of the central metal. In most cases, the Q band absorption maxima of the nanoconjugates were red-shifted compared to that of the corresponding complex alone.

CHAPTER FOUR: PHOTOPHYSICAL AND PHOTOCHEMICAL PROPERTIES

The photophysical behavior of all the substituted phthalocyanine complexes **10**-**36** was investigated in DMSO. The effect of central metal was investigated by synthesizing zinc, gallium and indium bearing central metal for each functional substituent. The spin orbit interaction arising from heavy atom effect is expected to play indispensable role in the photophysical properties. It is expected that enhanced triplet population will be achieved for complexes possessing heavy central metal ion in comparison to their relatively lighter metal derivatives. Because one predominant aim of this work is to maximize the triplet population with the expectation of enhancing nonlinear optical response. Selected complexes possessing requisite functional groups were further combined with nanomaterials mainly containing heavy atoms. Improvement in photophysical properties when organic chromophores were combined with nanomaterials has been reported [**184**,**185**], hence selected complexes in this work were linked to different semiconductor QDs, metallic gold and silver nanoparticles as well as carbon based graphene QDs.

4.1. Complexes 10-36 alone

4.1.1.Fluorescence quantum yield (Φ_F) and lifetime (τ_F)

Table 4.1 showed the photophysical behavior of all complexes in DMSO. The Φ_F were calculated using **equation 4.1** (same as **equation 1.4**) with ZnPc ($\Phi_F = 0.2$ in DMSO) as standard [**186**]

$$\Phi_F = \Phi_F^{std} \cdot \frac{F.A_{std}.n^2}{F_{std}.A.n_{std}^2} \qquad\qquad (\textbf{4.1})$$

where F and F_{std} are the areas under the fluorescence emission curves of the sample and standard respectively. A and A_{std} are the respective absorbance of the sample and standard at the excitation wavelength, while n and n_{std} are the refractive indices of the solvents for the sample and standard, respectively.

Table 4.1: Photophysical parameters of 10-36 in DMSO

Complexes	Φ_F	τ_F (ns)	Φ_T	τ_T (µs)	k_r x 10^7 (s^{-1})	τ_{isc}
Carboxylic acid substituted ball-type complexes						
10 (Zn)	0.20	3.20	0.58	289	6.25	5.52
11 (Ga)	0.12	2.70	0.67	102	4.44	4.03
12 (In)	0.04	2.30	0.81	59	1.74	2.78
Long alkyl substituted ball-type complexes						
13 (Zn)	0.10	3.07	0.62	264	3.26	4.95
14 (Ga)	0.07	1.05	0.69	84	6.67	1.52
15 (In)	0.02	0.97	0.83	44	2.06	1.13
Aldehyde substituted ball-type complexes						
16 (Zn)	0.11	3.19	0.60	321	3.45	5.32
17A (Ga)	0.08	1.05	0.65	95	7.62	1.62
17B (Ga)	0.07	1.03	0.69	93	6.80	1.49
18 (In)	0.04	0.97	0.75	69	4.12	1.29
Benzothiazole substituted ball-type complexes						
19 (Zn)	0.17	3.27	0.58	289	5.20	5.64
20 (Ga)	0.11	2.30	0.64	112	4.78	3.59
21 (In)	0.05	1.09	0.71	61	4.59	1.54
Mononuclear Pcs complexes 22-36						
Phenoxylbenzothiazole substituted complexes 22-24						
22 (Zn)	0.24	2.86	0.56	130	8.39	5.11
23 (Ga)	0.16	2.73	0.68	193	5.86	4.01
24 (In)	0.03	0.78	0.75	55	3.85	1.04
Thiarylbenzothiazole substituted complexes 25-27						
25 (Zn)	0.18	1.92	0.65	148	9.38	2.95
26 (Ga)	0.12	2.45	0.72	205	4.90	3.40
27 (In)	0.02	0.73	0.78	48	2.74	0.93
Aldehyde substituted monomer complexes 28-30						
28 (Zn)	0.14	3.24	0.57	331	4.32	5.68
29 (Ga)	0.09	1.17	0.63	107	7.69	1.86
30 (In)	0.06	1.07	0.69	73	5.61	1.55

Table 4.1 continued

Complexes	Φ_F	τ_F (ns)	Φ_T	τ_T (μs)	k_r x 10^7 (s^{-1})	τ_{isc}
aminophenoxyl substituted complexes 31-33						
31 (Zn)	0.21	3.25	0.61	343	6.46	5.33
32 (Ga)	0.11	2.01	0.69	196	5.47	2.91
33 (In)	0.08	0.98	0.72	52	8.16	1.36
asymmetric benzothiazole substituted complexes 34-36						
34 (Zn)	0.15	3.82	0.59	347	3.93	6.50
35 (Ga)	0.09	1.92	0.64	239	4.69	3.00
36 (In)	0.03	1.02	0.70	95	2.94	1.46

Generally for each substituent, the Φ_F decreases with increase in atomic weight of the central metal ion attributed to heavy atom spin orbit coupling deactivation of the excited singlet state through intersystem crossing to populate the triplet [**185**].   For ball-type Pcs, **10**, **13**, **16** and **19** bearing zinc central metal, the fluorescence quantum yield (Φ_F) slightly decreases in order of **10** > **19** > **16** ≈ **13**, showing the lowest Φ_F value for long alkyl and aldehyde bridging substituents. For complexes bearing indium central metal, the Φ_F values were low due to heavy atom effect. The Φ_F for **11**, **14**, **17** and **20** bearing gallium central metal also follow the same trends as for zinc complexes, with decrease in fluorescence quantum yield in order of **11** > **20** > **17** ≈ **14**.

For monomeric Pcs **22**-**27** containing benzothizolylphenoxyl and benzothiazolylthiaryl substituents respectively, a lower Φ_F was observed for **25**-**27** compared to the corresponding **22**-**24** except **24** and **27** that showed almost the same order of magnitude (**Table 4.1**). It has been shown that MPcs with absorption peak at shorter wavelength show higher fluorescence quantum yield [**187**] and complexes **22**-**24** have shorter absorption wavelength compared to **25**-**27** (**Table 3.3**), hence lower Φ_F for the former than the latter.

 The Φ_F for aldehyde substituted **28**-**30** was found to be 0.14, 0.09 and 0.06, generally lower than for **22**-**27**, while those of the asymmetric **34**-**36** showed Φ_F of 0.15, 0.9 and 0.03 respectively (**Table 4.1**).

The fluorescence lifetime (τ_F) decay curve for the complexes are shown in **Fig. 4.1** (using **13** and **16** as examples). The complexes bearing indium showed biexponential decay with existence of two lifetimes while the rest of the complexes exhibit mono-exponential decay. Average lifetimes for the indium complexes and mono-exponential lifetimes for other complexes are presented in **Table 4.1.** The existence of two lifetimes in Pcs has been reported in terms of the presence of aggregates which quench fluorescence, resulting in quenched (shorter) and unquenched (longer) lifetimes [**188**].

Generally, for each substituent of Zn, Ga and In series, the τ_F also decrease with decrease in Φ_F, which is expected since quantum yield is directly proportional to lifetime.

Though the fluorescence lifetime for **10**-**21** directly relate to the quantum yield, complexes **11** and **20** showed fluorescence lifetime (τ_F) that were 2 times more than that of complex **14** and **17**. It is well known that the fluorescence lifetime will depend on other non-radiative processes that compete for deactivation of the excited state [**78**] as represented in **equation 4.2**.

$$\tau = \frac{1}{k_r + k_{nr}} \qquad\qquad (\textbf{4.2})$$

where k_r and k_{nr} are radiative and non-radiative rate constants. Thus, the presence of non-radiative processes will compete and decrease the radiative pathways. From **equation 4.2**, a decrease in fluorescence rate constant will increase the fluorescence lifetime. The radiative rate constant of fluorescence was calculated from the fluorescence quantum yield and fluorescence lifetime using $k_r = \Phi_F/\tau_F$ [**78**]. and presented in **Table 4.1**. The increased lifetime observed in **11** and **20** compared to

14 and **17** can be attributed to decrease in fluorescence rate constants in the former due to non-radiative competing processes.
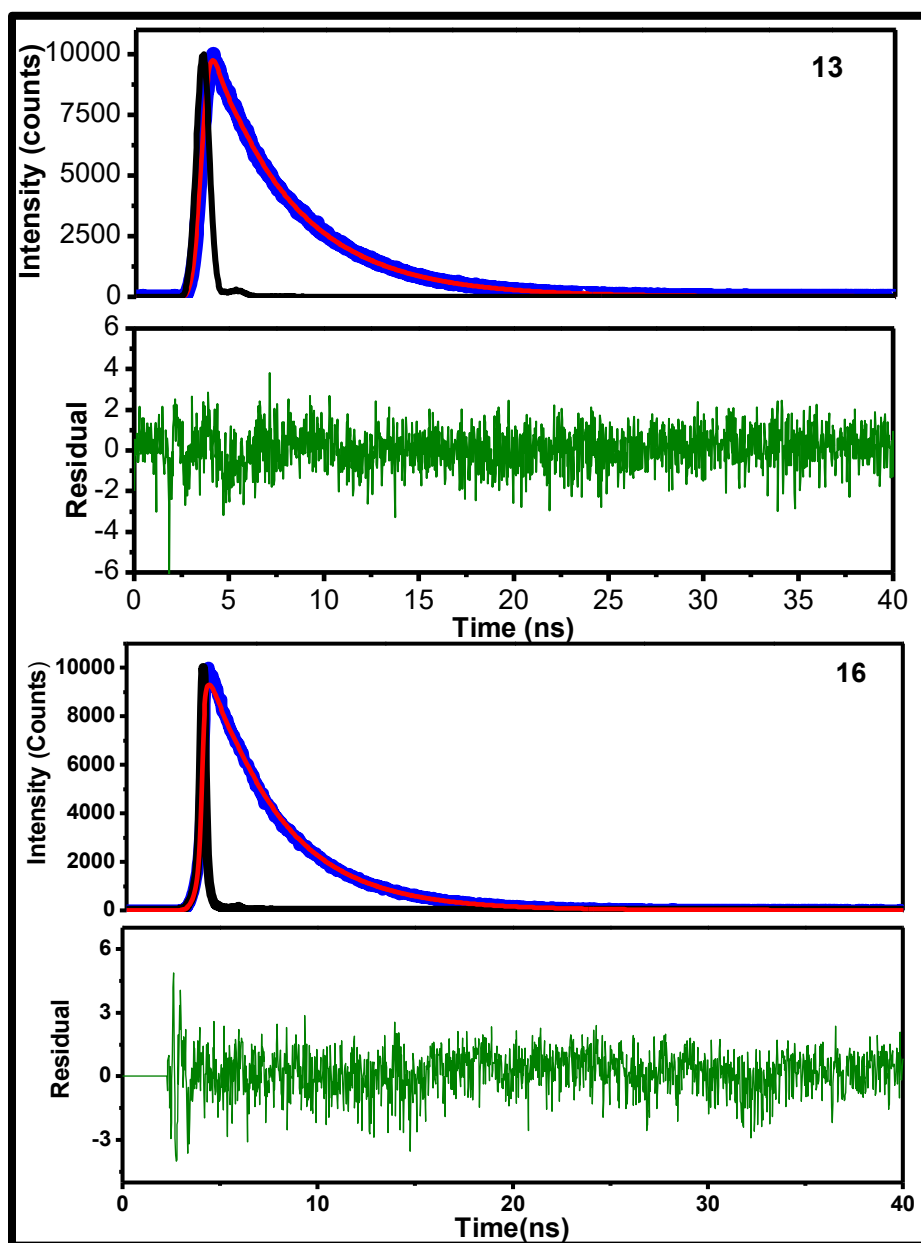
Figure 4.1: Fluorescence decay (blue), X^2 fitting (red) and IRF (black) curves of 13 and 16 in DMSO. Absorbances at Q band <0.04

4.1.2.Triplet quantum yield (Φ_T) and lifetime (τ_F)

4.1.2.1. Ball-type MPcs 10-21

The Φ_T were calculated using **equation 4.3** (same as **equation 1.1**) with ZnPc (Φ_T = 0.65 in DMSO) [**189**].

$$\Phi_T = \Phi_T^{std} . \frac{\Delta A_T . \varepsilon_T^{std}}{\Delta A_T^{std} . \varepsilon_T} \qquad\qquad (\mathbf{4.3})$$

where ΔA_T and ΔA_T^{std} are the changes in the triplet state absorbance of the sample and the standard, respectively. ε_T and ε_T^{std} are the respective triplet state molar extinction coefficients for the sample and the standard. Φ_T^{std} is the triplet quantum yield of the standard ZnPc.

A plot of Φ_T against the atomic weight of the central metal ions showed enhanced population of the triplet with increase in atomic weight (**Fig. 4.2** using **10-21** as example) for all the substituents.
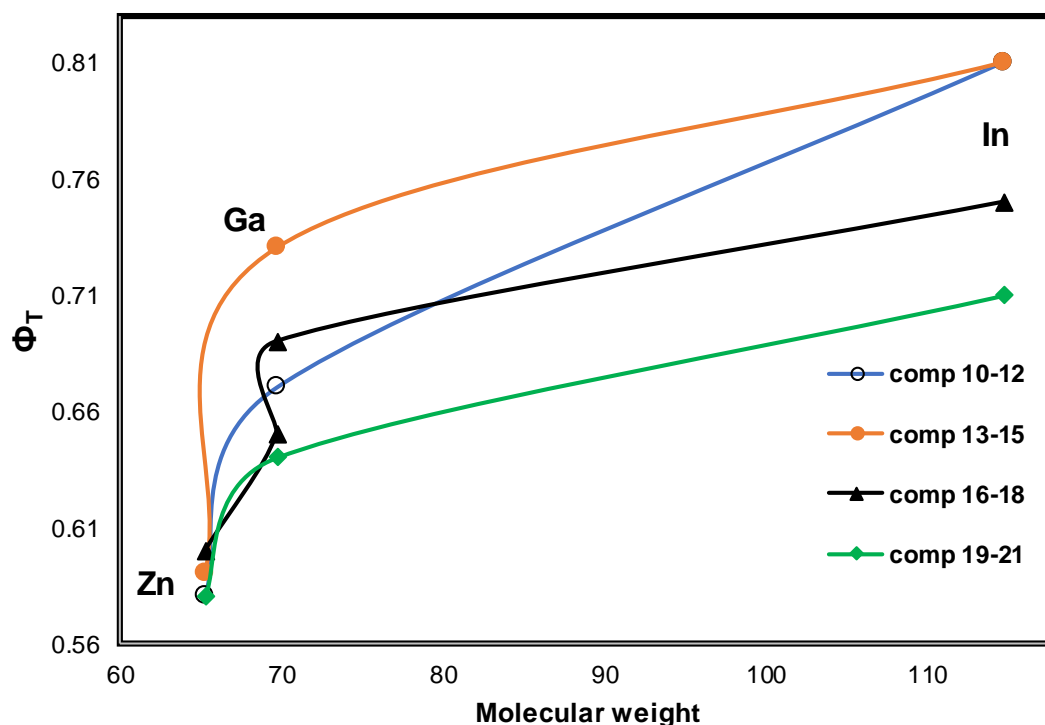
Figure 4.2: Plots of triplet population vs molecular weight of 10-21

The values for Φ_T was found to increase with decrease in Φ_F for complexes having the same central metal ion (**Table 4.1**). The triplet quantum yields (Φ_T) for long alkyl substituted Zn, Ga and In complexes **13**, **14** and **15** respectively were also found to be marginally higher than their corresponding carboxylic acid (**10**-**12**), aldehyde (**16**-**18**) and benzothiazole (**19**-**21**) substituted complexes corresponding to lower Φ_F. Though the Φ_F for **10** and **19** slightly differ, the Φ_T were found to be the same. In general, for the ball-type **10**-**21**, only complexes **13**, **14** and **15** with bridging long alkyl substituent showed significant effect on the photophysical properties. The electron donating effect of alkoxy long alkyl substituent that shows enhancement in rate of intersystem crossing to populate the triplet has been reported in porphyrin macrocycle [**190**], hence the consistent lower rate of fluorescence and higher triplet quantum yield for complexes **13, 14** and **15** could be attributed to electron donating effect of this complexes.

The relative lower Φ_F for complex **17** compared to **11** does not translate to higher Φ_T for the latter, suggesting that other excited singlet deactivation pathways such as internal conversion must have been involved in the observed low Φ_F, since such pathways do not actually enhance the intersystem crossing to the triplet. Brookfield et. al [**191**] have shown that for dimer molecules, the two rings may be close and the interaction can be sufficient to result in exciton coupling, which will provide extra pathway for non-radiative process. Thus, non-radiative process that did not populate the triplet must have been responsible for lower Φ_F as well as lower triplet population in **17** compared to **11**. Though the fluorescence quantum yield for **12** and **18** are the same, **12** possessed enhanced Φ_T.

Fig. 4.3 showed the transient absorption data of **12** as well as the triplet decay curve for the complexes (using **11**, **12**, **16** and **19** as examples). The triplet state absorption maxima for **12** was observed at 495 nm with a large negative band at 705 nm which could be attributed to the depletion or bleaching of the ground state [**192**]. The triplet

decay curves obey second order decay kinetics due to triplet-triplet recombination of MPcs at high concentration [**193**].

The triplet lifetime (τ_T) was obtained by fitting the triplet absorption data to rate **equation 4.4**

$$A_t = A_0 e^{\left(-\frac{t}{\tau_T}\right)} + kt \qquad\qquad (\textbf{4.4})$$

where A_t and A_0 are the relative absorbance at time t = t and t = 0 respectively; k is the triplet state absorption rate constant.
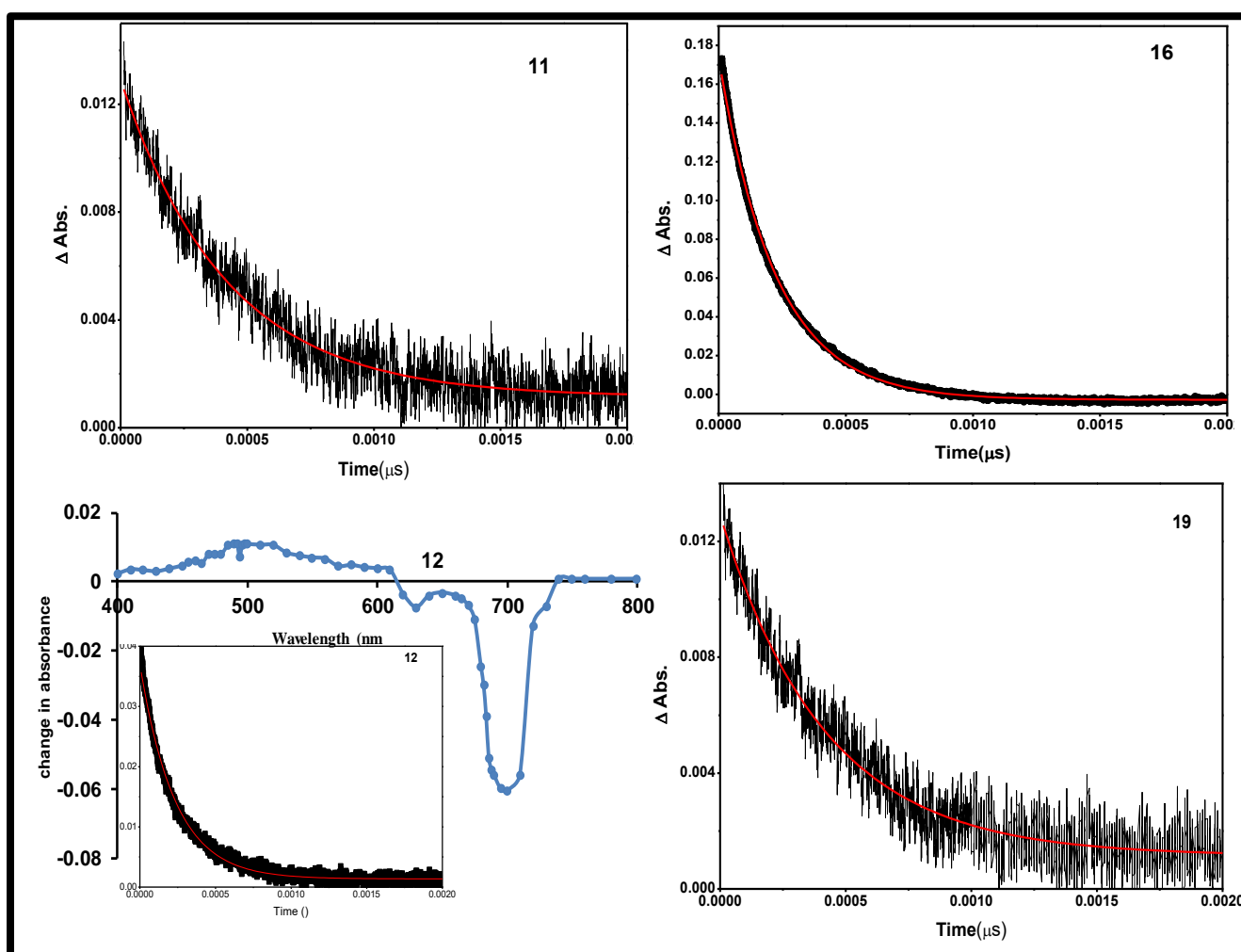
Figure 4.3: Transient absorption curve of 12 and triplet absorption decay of selected complexes in DMSO. The red solid curve depicts the fitting curve.

4.1.2.2. Mononuclear 22-36

For non ball-type **22**-**36**, the sulphur-bridged benzothiazole substituted complexes **25**-**27** showed higher Φ_T compared to corresponding benzothizolylphenoxyl **22**-**24**, bis(aminophenoxy)phenoxyl substituted **31**-**33**, aldehyde substituted **28**-**30** and the asymmetric **34**-**36** (**Table 4.1**). The Φ_T values for the bis(aminophenoxy)phenoxyl substituted **31**-**33** are higher than the corresponding aldehyde substituted **28**-**30** (**Table 4.1**). The presence of amino substituents has been shown to quench fluorescence [**194**], hence enhance intersystem crossing to populate the triplet.

The asymmetric **35** and **36** showed lower Φ_T compared to **23** and **24**, suggesting that other non-radiative pathways must have contributed to the lower Φ_F observed for the asymmetric **35** and **36**. Also, electron withdrawing substituents has been shown to decrease intersystem crossing [**187**,**195**], hence the presence of electron withdrawing carboxylic acid in the asymmetric complexes could be responsible for the lower triplet population. The intersystem crossing lifetime was calculated using **equation 4.5**

$$\tau_{isc} = \frac{\tau_F}{\Phi_T} \tag{4.5}$$

For each substituent, the τ_{isc} decreases in order of In < Ga < Zn, suggesting faster rate of intersystem crossing to populate the triplet by heavy atom (**Table 4.1**).

4.2. Metallophthalocyanine in combination with nanomaterials

Table 4.2: comparative photophysical parameters of complexes alone and when linked with nanomaterials. Solvent DMSO

Complexes	Loading (mg/mg)	$\Phi_{F(pc)}$	$\tau_{F(Pc)}$ (ns)	$\Phi_{F(QDs)}$[a]	$\tau_{F(QDs)}$ (ns)[a]	Φ_T	τ_F (µs)	τ_{isc} (ns)
Carboxylic acid substituted ball-type complexes 10-12								
10	-	0.20	3.20	-	-	0.58	289	5.52
10-GQDs	12	0.16	2.91	0.85 (0.89)	9.1 (10.4)	0.61	221	4.75
10-CdTe	8	0.13	2.50	0.47(0.63)	11.3 (18.5)	0.67	189	3.73
11	-	0.12	2.70	-	-	0.67	102	4.03
11-GQDs	15	0.10	2.40	0.82 (0.89)	8.7 (10.4)	0.69	93	3.48
11-CdTe	11	0.08	1.90	0.39(0.63)	10.9 (18.5)	0.72	72	2.64
12	-	0.04	2.30	-	-	0.81	59	2.78
12-GQDs	7	0.04	2.18	0.79 (0.89)	9.3 (10.4)	0.85	56	2.56
12-CdTe	9	<0.01	1.54	0.37(0.63)	8.8 (18.5)	0.90	48	1.71
12-CdTeSe	19	0.02	1.74	0.04 (0.09)	5.9 (12.6)	0.90	63	2.09
12-CdTeSe/ZnO	25	0.01	1.25	0.02 (0.14)	3.7 (11.3)	0.83	67	1.37
12-AgNPs	5	0.02	1.85	-	-	0.80	65	2.31
12-AuNPs	16	0.017	1.82	-	-	0.85	58	2.14
Benzothiazole substituted ball-type 19-21 and conjugates								
19	-	0.17	3.27	-	-	0.58	289	5.64
19-AgNPs	17	0.14	2.53	-	-	0.63	103	4.02
19-AuNPs	11	0.11	2.09	-	-	0.67	96	3.12
20	-	0.11	2.30	-	-	0.64	112	3.59
20-AgNPs	40	0.09	1.70	-	-	0.69	73	2.46
20-AuNPs	23	0.06	1.29	-	-	0.73	69	1.77
21	-	0.05	1.09	-	-	0.71	61	1.54
21-AgNPs	52	0.03	1.01	-	-	0.82	48	1.23
21-AuNPs	31	<0.01	0.85	-	-	0.88	39	0.97

Table 4.2 continued

Complexes	Loading (mg/mg)	$\Phi_{F(pc)}$	$\tau_{F(Pc)}$ (ns)	$\Phi_{F(QDs)}^a$	$\tau_{F(QDs)}$ (ns)^a	Φ_T	τ_F (μs)	τ_{isc} (ns)
Phenoxyl benzothiazole substituted 22-24 and conjugates								
22	-	0.24	2.86	-	-	0.56	130	5.11
22-AgNPs	9	0.11	1.82	-	-	0.58	107	3.14
22-AuNPs	14	0.09	1.71	-	-	0.63	119	1.85
23	-	0.16	2.73	-	-	0.68	193	4.01
23-AgNPs	6	0.07	1.39	-	-	0.67	158	2.01
23-AuNPs	11	0.05	1.26	-	-	0.73	172	1.73
24	-	0.03	0.78	-	-	0.75	55	1.04
24-AgNPs	7	<0.01	0.62	-	-	0.79	41	0.78
24-AuNPs	22	<0.01	0.59	-	-	0.87	47	0.68
Thiaryl benzothiazole substituted 25-27 and conjugates								
25	-	0.18	1.92	-	-	0.65	148	2.95
25-AgNPs	13	0.08	1.37	-	-	0.62	121	2.21
25-AuNPs	23	0.06	1.28	-	-	0.69	137	1.86
26	-	0.12	2.45	-	-	0.72	205	3.40
26-AgNPs	12	0.07	0.83	-	-	0.73	167	1.13
26-AuNPs	29	0.05	0.71	-	-	0.77	188	0.92
27	-	0.02	0.73	-	-	0.78	48	0.93
27-AgNPs	19	<0.01	0.57	-	-	0.83	34	0.69
27-AuNPs	33	<0.01	0.51	-	-	0.91	39	0.56
aminophenoxyl substituted 31-33 and conjugates								
31	-	0.21	3.25	-	-	0.61	343	5.33
31-AgNPs	16	0.15	3.12	-	-	0.63	325	4.95
31-AuNPs	28	0.13	2.64	-	-	0.66	312	3.94
31CB-AgNPs	37	0.10	3.02	-	-	0.68	303	4.44
31CB-AuNPs	30	0.09	2.05	-	-	0.75	298	2.73
31-CdTe	10	0.13	2.60	0.46 (063)	14.1 (18.5)	0.68	265	3.82
32	-	0.11	2.01	-	-	0.69	196	2.91
32-CdTe	7	0.09	0.98	0.42 (0.63)	12.8 (18.5)	0.73	76	1.34

Table 4.2 continued

Complexes	Loading (mg/mg)	$\Phi_{F(pc)}$	$\tau_{F(Pc)}$ (ns)	$\Phi_{F(QDs)}{}^a$	$\tau_{F(QDs)}$ (ns)^a	Φ_T	τ_F (µs)	τ_{isc} (ns)
33	-	0.08	0.98	-	-	0.72	52	1.36
33-CdTe	3	0.02	0.78	0.38 (0.63)	11.3 (16.8)	0.76	40	1.02
Low symmetry benzothiazole substituted 34-36 and conjugates								
34	-	0.15	3.82	-	-	0.59	347	6.50
34-AgNPs	21	0.10	3.84	-	-	0.67	329	5.7
34-AuNPs	33	0.08	2.35	-	-	0.71	353	3.3
34CB-AgNPs	11	0.13	3.20	-	-	0.61	331	5.2
34CB-AuNPs	17	0.11	2.90			0.63	349	4.6
34-CdTe	9	0.06	2.60	0.45 (0.63)	11.9 (18.5)	0.74	293	3.51
35	-	0.09	1.92	-	-	0.64	239	3.00
35-CdTe	7	0.05	1.50	0.41 (0.63)	10.2 (18.5)	0.74	192	2.02
36		0.03	1.02	-	-	0.70	95	1.46
36-CdTe	4	<0.01	0.98	0.39 (0.63)	9.5 (18.5)	0.80	41	1.23

^{a}Values in brackets are for QDs alone.

Excitation at Pcs absorption =615-620 nm, 400 nm for SQDs and 340 for GQDs

4.2.1.Fluorescence quantum yield (Φ_F) and lifetime (τ_F)

Due to the fluorescent nature of QDs, the nanohybrid of QDs were excited either at QDs or MPcs absorption wavelength. The metallic Au and Ag NPs nanocomposites were only excited at the MPcs absorption wavelength since Au and Ag NPs do not fluoresce.

For all the nanoconjugate when exciting at absorption wavelength of Pcs, the $\Phi_{F(pc)}$ decreased compared to the corresponding complexes alone (**Table 4.2**), suggesting deactivation of the excited singlet of MPc complexes and enhancement of intersystem crossing either through heavy atom effect from the SQDs or enhanced π-conjugated system for GQDs. The nanoconjugates of AuNPs showed lower Φ_F values compared to the corresponding AgNPs.

When exciting at QDs absorption wavelength, **equation 4.6** was used to determine the fluorescence quantum yields following the covalent linkage of complexes $\Phi_{F(Pc\text{-}QDs)}$)

$$\Phi_{(Pc-QDs)} = \Phi_{QDs} \frac{F_{(Pc-QDs)}}{F_{QDs}} \qquad\qquad (4.6)$$

where $F_{(Pc\text{-}QDs)}$ and F_{QDs} are the fluorescence intensities of QDs in Pc-QDs conjugates and QDs alone, respectively. $\Phi_{(QDS)}$ represents fluorescence quantum yield of the QDs alone and was used as a standard.

The semiconductor QDs showed lower $\Phi_{F(QDs)}$ compared to GQDs. A significant decrease in $\Phi_{F(QDs)}$ were observed for the nanoconjugates compared to QDs alone (**Table 4.2**), which can be attributed to energy transfer from the donor QDs to acceptor MPcs leading to excited state quenching of the former [**78**] as will be discussed below.

The fluorescence decay curves for all the nanoconjugates when exciting at absorption wavelength of MPcs showed biexponential decay with two lifetimes. Average lifetimes are presented in **Table 4.2**.

The $\tau_{F(QDs)}$ for GQDs, CdTe, CdTeSe and CdTeSe/ZnO alone was found to be 10.4, 18.5, 12.6 and 11.3 ns respectively (**Table 4.2**). Upon conjugation of the complexes to these nanoparticles, a significant reduction in lifetime was observed for all the nanoconjugates (**Fig. 4.4**, using CdTe and **33**-CdTe as examples, **Table 4.2**), which is the hallmark of Förster resonance energy transfer (FRET) [**76**].
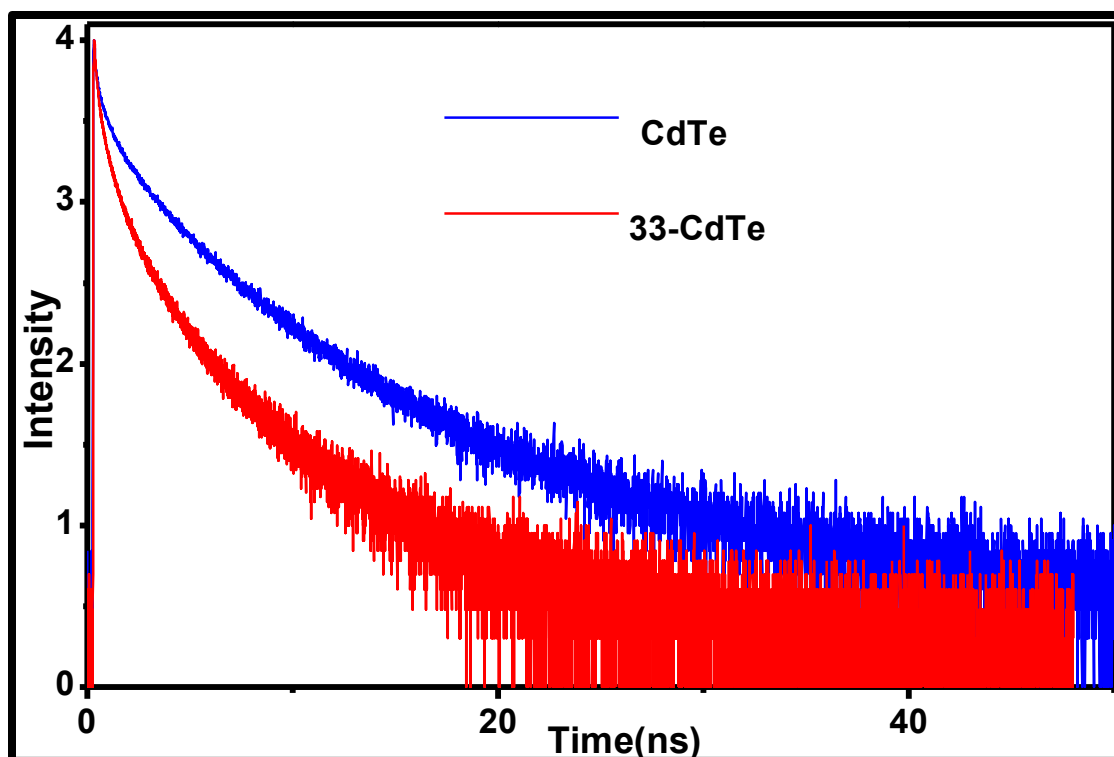
Figure 4.4:   **Fluorescence decay profile of CdTe QDs before and after covalent linkage to 33. Excitation wavelength = 560 nm.**

4.2.2.Förster resonance energy transfer (FRET)

The FRET study was carried out since energy transfer from QDs to MPcs is expected following excitation of the MPc-QDs nanohybrids. For FRET to occur, the emission spectra of donor fluorophore (QDs) must overlap the absorption spectra of the acceptor (MPcs) as shown in **Fig. 4.5A**. Upon excitation where QDs absorbs, the occurrence of FRET will result in fluorescence quenching for QDs and enhancement for Pcs (**Fig. 4.5B**)
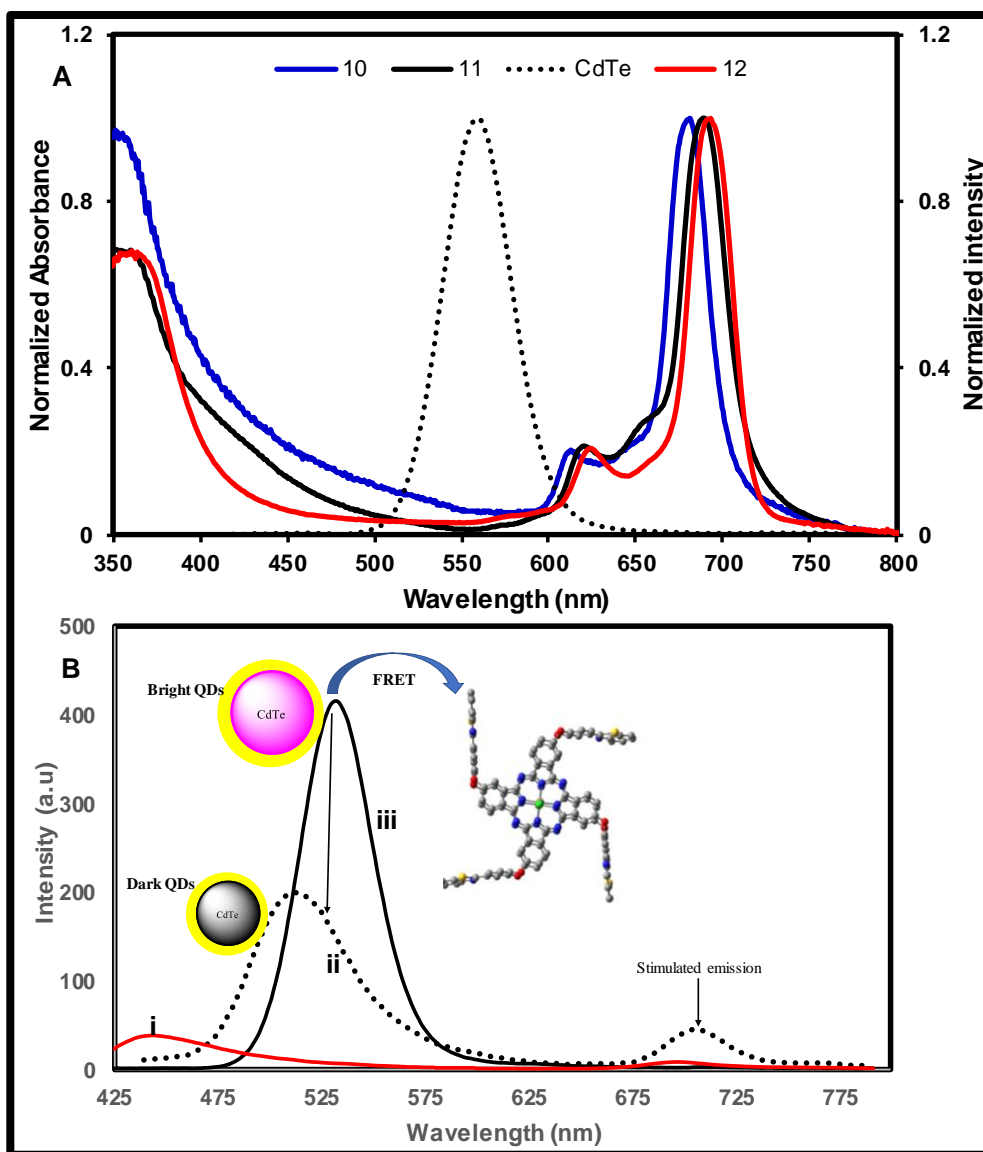
Figure 4.5: (A)Emission spectra (dotted line) of QDs and absorption spectra (solid lines) of 10–12 and (B) emission spectra of 35 (i), 35-CdTe (ii) and CdTe (iii). Excitation at 400 nm.

A significant quenching in emission spectra of CdTe QDs with emergence of new peaks around 650-700 nm was observed when MPc complexes was covalently linked with QDs at excitation wavelength of 400 nm (**Fig. 4.5B**, using **35** and conjugate as an example).

Table 4.3: Energy transfer parameters for QDs-Pc conjugates in DMSO using FRET Method

Conjugates	Loading mg/mg	Φ_F	$J(\lambda)$ (M^{-1} cm^{-1} nm^4)	Eff (%)	R_0 (Å)	r (Å)	k_T (r) (ns^{-1})
Carboxylic acid substituted ball-type complexes 10-12							
10-CdTe	8	0.13	5.70×10^{-14}	50.1	59.3	53.3	0.08
11- CdTe	11	0.08	2.60×10^{-14}	51.9	40.2	38.7	0.04
12- CdTe	9	<0.01	2.27×10^{-14}	49.5	40.5	36.2	0.07
10-GQDs	12	0.16	6.57×10^{-13}	19.2	64.5	92.7	0.012
11-GQDs	15	0.10	1.27×10^{-13}	16.3	49.1	78.9	0.006
12-GQDs	7	0.04	1.09×10^{-13}	14.6	41.3	73.5	0.014
Bis(aminophenoxyl)phenoxyl substituted complexes 31-33							
31-CdTe	10	0.13	3.20×10^{-14}	78.1	41.3	40.8	0.21
32-CdTe	7	0.09	4.02×10^{-14}	60.3	42.9	42.0	0.09
33-CdTe	3	0.02	7.20×10^{-14}	51.0	40.5	40.1	0.06
Low symmetry benzothiazole substituted complexes 34-36							
34-CdTe	9	0.06	6.58×10^{-14}	62.2	41.3	38.7	0.51
35-CdTe	7	0.05	6.67×10^{-14}	57.4	31.5	30.9	0.67
36-CdTe	4	<0.01	6.79×10^{-14}	53.3	35.8	35.5	0.24

This new peak around 650-700 is known as stimulated emission since it is not observed either in the CdTe or complex **35** alone at the same excitation wavelength. This stimulated emission can be attributed to a nonradiative energy transfer from the donor quantum dots to the acceptor Pcs. Excited state quenching is one major process that results in FRET for a donor-acceptor pair, and this process turns the

"bright" QDs into "dark" QDs due to attachment of the acceptor on the surface of donor [**196**].

The PHOTOCHEMCAD [**85**] was employed to compute the FRET parameter using **equations 1.5-1.10** and presented in **Table 4.3**. From **Table 4.3**, The FRET efficiencies (Eff) were found ranging from 15-78%. The semiconductor QDs showed higher transfer efficiency compared to the graphene based QDs. The efficiency of FRET is expected to increase with decrease in overlap integral (J) [**197**], which could be the reason for higher efficiency for semiconductor QDs compared to GQDs. Enhancement in FRET efficiency has been shown to occur in QDs-dyes conjugate with increase in number of acceptor molecules per donor [**198**], but this is not always in all case as seen in **Table 4.3** where **11**-GQDs has larger loading but low Eff compared to **10**-CdTe. It should be mentioned that the calculated FRET efficiency values are only estimates, since there are a wide variety of factors [**83**,**199**] which influences the decrease in QDs emission in addition to FRET.

4.2.3. Triplet quantum yield (Φ_T) and lifetime τ_T)

Generally, the Φ_T for the nanoconjugates were found to be higher compared to the corresponding complex alone (**Table 4.2**). The Φ_T values for **10**-CdTe, **11**-CdTe and **12**-CdTe were found to be 0.67, 0.72 and 0.90, higher than 0.61, 0.69 and 0.85 for the corresponding **10**-GQDs, **11**-GQDs and **12**-GQDs respectively (**Table 4.2**), due to heavy atom effect in the former compared to the latter.

For all the metallic nanoparticle conjugates, the Φ_T for the Au conjugates were higher compared to the corresponding Ag conjugates, which could be due to Au being heavier atom than Ag (**Table 4.2**). For complexes **31** and **34** that was covalently linked as well as surface assembled to Au and Ag NPs, the Φ_T for the covalently linked **31**CB-AuNPs and **31**CB-AgNPs were found to be 0.75 and 0.68, higher than 0.66 and 0.63 for self-assembled **31**-AuNPs and **31**-AgNPs (**Table 4.2**).

On the other hand, the Φ_T for the self-assembled **34**-AuNPs and **34**-AgNPs were 0.71 and 0.67, higher than 0.63 and 0.61 for **34**CB-AuNPs and **34**CB-AgNPs. These observations could be attributed to the loading of MPc complexes on the nanoparticles as higher loading was observer for the covalently linked conjugates of **31** and self-assembled conjugates of **34** (**Table 4.2**)

The τ_F generally decreases with increase in Φ_T as expected. The τ_{isc} was high where Φ_T were low.

4.2.4. Singlet oxygen (Φ_Δ) and photodegradation (Φ_{pd}) quantum yields

Though singlet oxygen generation is not required for materials intended for NLO application, the selected complexes in this section were studied to determine whether they would be suitable candidates for use as photosensitisers in other applications where singlet oxygen is required such as in photodynamic therapy (PDT).

The singlet oxygen quantum yield (Φ_Δ) was determined by monitoring the chemical photodegradation of singlet oxygen quencher 1,3-diphenylisobenzofuran (DPBF) (**Fig. 4.6,** using **31** and **34**CB-AuNPs as examples) and calculated using **equation 4.7**.

$$\Phi_\Delta = \Phi_\Delta^{std} . \frac{B I_{abs}^{std}}{B^{std} I_{abs}} \qquad (\textbf{4.7})$$

where $\Phi_\Delta{}^{std}$ is the singlet oxygen quantum yield of unsubstituted ZnPc standard in DMSO ($\Phi_\Delta = 0.67$)[**200**] , B and B^{std} are the coefficients of the sample and standard, I_{abs} and I_{abs}^{std} are the rates of light absorption by the complexes and the standard, respectively

I_{abs} is define by **equation 4.8**.

$$I_{abs} = \frac{\alpha A I}{N_A} \qquad (\textbf{4.8})$$

where $\alpha = 1 - 10^{-A(\lambda)}$ $A(\lambda)$ is the absorbance of the sensitizer at the irradiation wavelength, A is the irradiated area $(2.5\ cm^2)$, I is the intensity of light $(4.0 \times 10^{16} photons\ cm^{-2}\ s^{-1})$ and N_A is Avogadro's constant.

There was no significant change in Q-band intensity of the complexes or the nanoconjugates during irradiation showing stability over the irradiation period, while DPBF degraded. A significant increase in singlet oxygen generation as evidenced by singlet oxygen quantum yield (**Table 4.4**) was observed upon conjugation of complexes to the metallic nanoparticles corresponding to increase in triplet quantum yields. Conjugates with higher Φ_T also showed higher singlet oxygen generation capacity (**Table 4.4**).
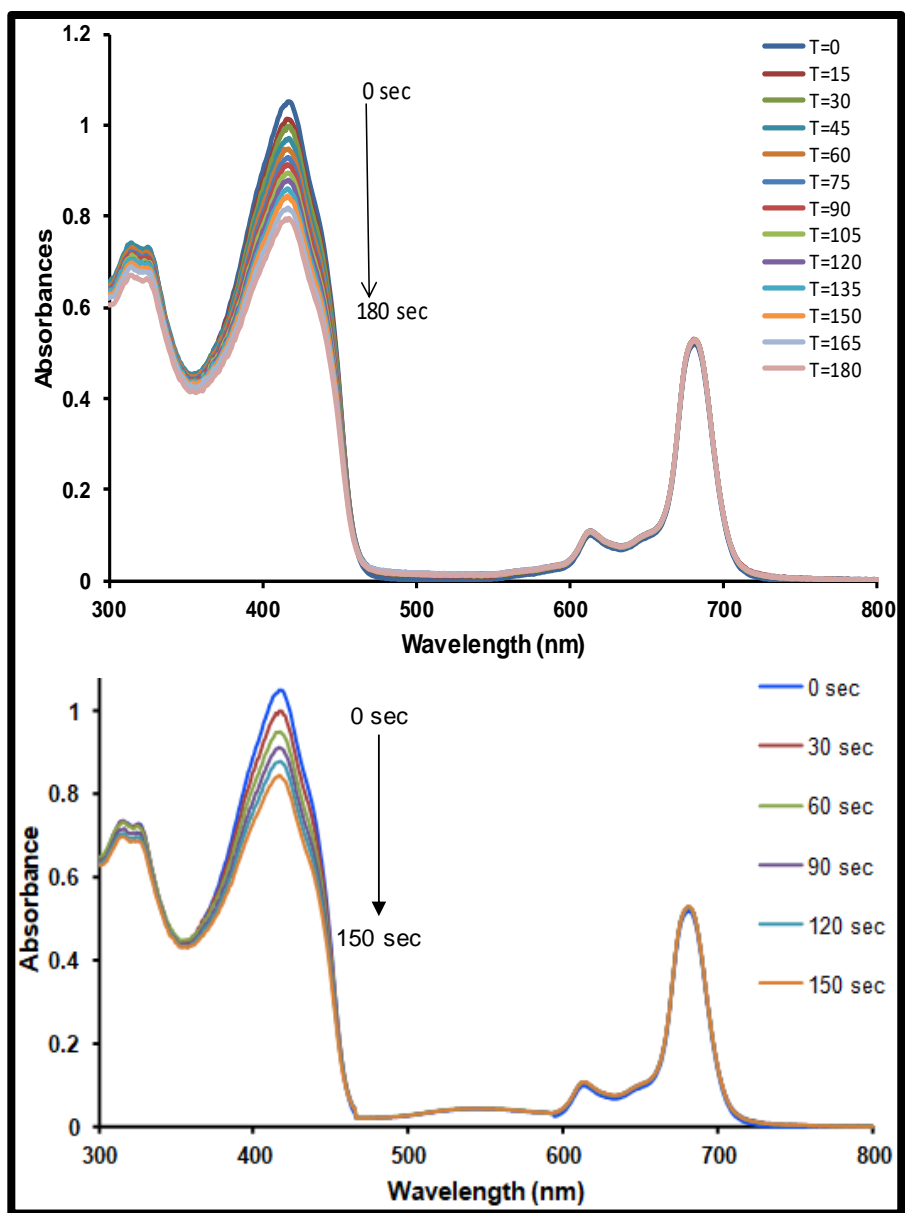
Figure 4.6: Typical spectra observed during the generation of singlet oxygen using DPBF as a singlet oxygen quencher for complex 31(top) and 34CB-AuNPs (bottom) in DMSO.

Table 4.4: Singlet oxygen generation of selected complexes and corresponding nanoconjugates.

Complexes	Loading (mg/mg)	Φ_T	Φ_Δ
Bis(aminophenoxyl)phenoxyl substituted complexes 31			
31	-	0.61	0.37
31CB-AgNPs	37	0.68	0.47
31-AgNPs	16	0.63	0.40
31CB-AuNPs	30	0.75	0.53
31-AuNPs	28	0.66	0.44
Low symmetry benzothiazole substituted complexes 34			
34	-	0.59	0.32
34CB-AgNPs	11	0.61	0.34
34-AgNPs	21	0.67	0.43
34CB-AuNPs	17	0.63	0.38
34-AuNPs	33	0.71	0.51

4.3.   Conclusions for the chapter

The photophysical and photochemical properties of MPcs complexes either alone or in combination with different nanomaterials were investigated.

A decrease in Φ_F and corresponding increase in Φ_T was observed for complexes having gallium and indium central metal compared to the corresponding zinc analogues. Further enhancement in Φ_T was observed when the complexes were linked to nanomaterials.

Excited state quenching of the luminescence properties of SQDs and GQDs was found to occur through FRET process and the efficiency of FRET was found to be higher in SQDs compared to corresponding GQDs.

CHAPTER FIVE: NONLINEAR OPTICAL (NLO) PROPERTIES

5. NLO parameters

5.1. Equations used

5.1.1. Conventional Sheik Bahae analysis

The difficulty in separating various nonlinear optical mechanisms such as: excited state absorption (ESA), two photon absorption (TPA), nonlinear scattering and nonlinear refraction responsible for reverse saturable absorption (RSA) or saturable absorption (SA) processes has been a serious limitation of the Z-scan technique. To solve this limitation, suitable equations for analysis of Z-scan data have been developed, and the explanation of results from such analysis is usually given based on the nature of the investigated material and the properties (pulse width and repetition rate) of the laser beam employed. The nonlinear absorption coefficient (β) is an important parameter for measuring optical limiting ability of materials. For molecules that have zero linear absorption at the laser wavelength of 532 nm, all the observed absorptions at that wavelength must be due to multi-photon absorption. However, when lasers with nanosecond pulses are employed as is the case in this study, the absorption may also be due to sequential TPA and ESA [201]. Therefore, the intrinsic value for β that is associated only with TPA cannot be determined, and an effective value (β_{eff}) is determined instead.   The β_{eff} measures the degree of nonlinear absorption and depends on the population of molecules in the first excited triplet state (T$_1$). The β_{eff} can be calculated by fitting the Z-scan data to the transmittance **equation 5.1** reported by Sheik-Bahae et al [89,140,141]

$$T_{(Z)} = \frac{1}{1+\beta_{eff}L_{eff}(I_{00}/(1+(z/z_0)^2))} \qquad (5.1)$$

where $T_{(Z)}$ is the normalized transmittance of the sample, I_{00} is the intensity of the light on focus, β_{eff} is the two-photon absorption coefficient, z_0 is the diffraction length of the beam, z is the sample position with respect to input intensity and L_{eff} is the effective length for 2 photon absorption using **equation 5.2**

$$l_{eff} = \frac{1-e^{-\alpha l}}{\alpha} \tag{5.2}$$

where α is the linear absorption coefficient. Since equation (**5.1**) is not generally suited to directly fit experimental data, a numerical form of the equation was employed to fit the experimental data, **equation 5.3** :

$$T_{(z)}=0.363e^{\left(\frac{-q_{(z)}}{5.60}\right)}+0.286e^{\left(\frac{-q_{(z)}}{1.21}\right)}+0.213e^{\left(\frac{-q_{(z)}}{24.62}\right)}+0.096e^{\left(\frac{-q_{(z)}}{115.95}\right)}+0.038e^{\left(\frac{-q_{(z)}}{965.08}\right)}$$

$$\tag{5.3}$$

Equation 5.3 describes reverse saturable absorption emanating from two-photon pumped excited state, hence the excited state cross-section (δ_{exc}) can be determined by fitting the experimental data from Z-scan to **equation 5.4**

$$T_{Norm} = \frac{In(1+(q/(1+X^2)))}{q/(1+X^2)} \tag{5.4}$$

where q is a dimensionless parameter given by **equation 5.5**

$$q = \frac{\alpha \delta_{exc}}{2h\nu} F_0 L_{eff} \tag{5.5}$$

where T_{Norm} is the normalized transmittance (T/T_0), and $T_0 = \exp^{(-\alpha L)}$, $F_0 = 2I_{00}$ (in J/cm^2), h is the Planck constant, $\chi = z/z_0$, ν is the frequency of the laser beam, α and L_{eff} are as defined above in **Equation 5.2**.

The imaginary third order susceptibility [$I_m(\chi^3)$], which measures the nonlinear absorption per mole can be determined by **equation 5.6**

$$I_m\left[\chi^{(3)}\right] = \frac{n^2 \varepsilon_0 C\lambda\beta_{eff}}{2\pi} \tag{5.6}$$

where n and c are the linear refractive index and the speed of light respectively, ε_0 is the permittivity of free space, β_{eff} is the nonlinear absorption coefficient, and λ is the wavelength of the laser beam.

The second-order hyperpolarizability (γ) values of the materials were calculated using **Equation 5.7**

$$\gamma = \frac{Im[\chi(3)]}{f^4 C_{mol} N_A} \qquad\qquad (\mathbf{5.7})$$

were, N_A is the Avogadro constant, C_{mol} is the concentration of the active species in the triplet state in mole and f is the Lorentz local field factor given as, $f = (n^2 + 2)/3$.

5.1.2. Five level rate equations

In phthalocyanines, it has been shown that upon excitation by intense laser, two-photon absorption (TPA) process is usually accompanied by excited state absorption [**202**] due to large excited state absorption cross-section in Pcs. This large cross section of two photon-induced excited state absorption (TPA-induced ESA) is directly related to the molecular structures [**203**,**204**]. Thus, understanding the relation between the molecular structures and the nonlinear absorption mechanisms is of paramount importance in the development of new materials with strong NLO properties. However, the existing Z-scan equations given above are inadequate to differentiate the contributions resulting from TPA and ESA. Additionally, since the ESA comprises of the singlet and triplet contributions, alternative model need to be invoked to track the individual contributions of each state to the RSA process.

A well-known five-level model can adequately explain the nonlinear absorption phenomenon in MPcs [**205**–**207**]. The necessity of five level models (**Fig. 5.1**) becomes imperative since transitions due to two photon absorption (TPA), the S_1-T_1 intersystem crossing process and T_1-T_n processes in the nanosecond time scale can be accounted for in this model. In this model, laser irradiation at 532 nm excites molecules from the ground state to either the S_1 or an S_n state with an excited state absorption cross-section δ_1. The population of the triplet state will depend on the rate of intersystem crossing as well as the lifetime of the triplet state. In phthalocyanines, the triplet lifetimes are far longer than the intersystem crossing lifetime, hence the rate of intersystem crossing to build up the triplet state are high. Molecules in the T_1

state can subsequently absorb laser radiation resulting in excitation from the T_1 state to a higher energy T_n state with excited state absorption cross-section, δ_2.
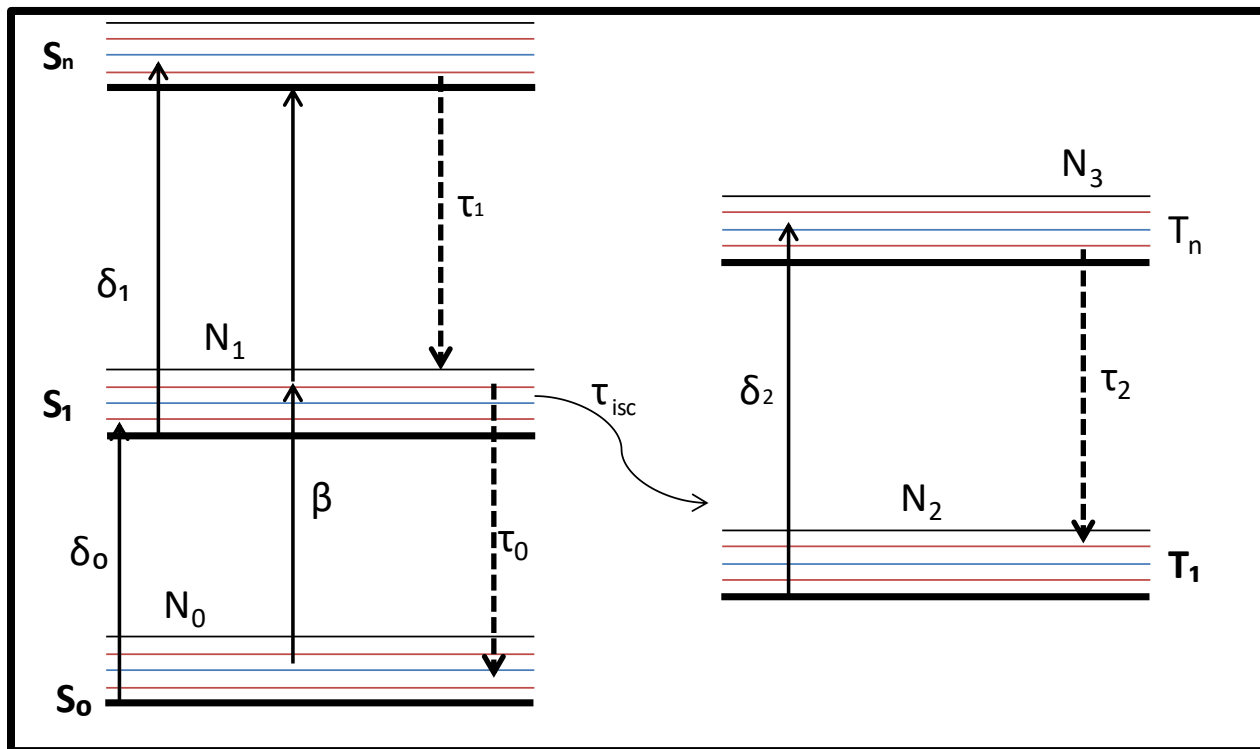
Figure 5.1. Five level energy diagrams explaining the dynamic of the excited state population (upward arrows), non-radiative relaxation (dashed arrows) in the studied complexes and nanoconjugates

The five-level systems in **Fig. 5.1** can be treated with 5-level model rate **Equations 5.8-5.11**

$$\frac{dN_o}{dt} = -\frac{\delta_0 I N_0}{\hbar\omega} - \frac{\beta I^2}{2\hbar\omega} + \frac{N_0}{\tau_0} + \frac{N_2}{\tau_1} \qquad (5.8)$$

$$\frac{dN_1}{dt} = \frac{\delta_1 I N_1}{\hbar\omega} + \frac{\delta_0 I N_0}{\hbar\omega} - \frac{N_0}{\tau_0} - \frac{N_0}{\tau_{isc}} + \frac{N_1}{\tau_1} \qquad (5.9)$$

$$\frac{dN_2}{dt} = \frac{\delta_1 I N_1}{\hbar\omega} + \frac{\beta I^2}{2\hbar\omega} - \frac{N_1}{\tau_1} \qquad (5.10)$$

$$\frac{dN_3}{dt} = -\frac{\delta_2 I N_3}{\hbar\omega} - \frac{N_2}{\tau_2} + \frac{N_0}{\tau_{isc}} + \frac{N_3}{\tau_3} \tag{5.11}$$

where δ_0, δ_1 and δ_2 are the absorption cross section for the ground, singlet and triplet excited respectively, $\hbar$ is Planck's constant, ω is the frequency of light, the N_i values represent the populations in the different states; β is the two-photon absorption (TPA) cross-section, the τ_i values are the lifetimes of the excited states, and τ_{isc} is the intersystem crossing lifetimes.

The intensity transmitted through the sample is represented as I and is given by **equations** (**5.12-5.14**):

$$\frac{dI}{dt} = \frac{c}{n_r}\frac{dI}{dz} = \frac{cI}{n_r}[\delta_0 N_1 + \delta_1 N_2 + \delta_2 N_3] \tag{5.12}$$

$$\text{with } I = I_{00}\left(\frac{\omega_0^2}{\omega^2(z)}\right)exp\left(-\frac{t^2}{\tau_p^2}\right)exp\left(-\frac{2r^2}{\omega^2(z)}\right) \tag{5.13}$$

$$\omega(z) = \omega_0\sqrt{\left\{1 + \left(\frac{z}{z_0}\right)^2\right\}}; \quad z_0 = \frac{\pi\omega_0^2}{\lambda} \tag{5.14}$$

where n_r is the refractive index ($n_r = 1.479$ in DMSO), c is the speed of light in vacuum, I_{00} is the peak intensity at the focus of Guassian beam; τ_p is the input pulse width; w_0 is beam waist at focus, z_0 is Rayleigh range and r is the radius of the aperture. dI/dz in **equation. 5.12** describes the change of photon flux with propagation of laser light through the sample with z as the position of the sample in the beam profile.

These equations are numerically solved using the ordinary differential equation (ODE45) function in Matlab with the boundary condition that each electron must be either in the ground or the excited state. Also in nanosecond regime, the rate equations can be analytically solved with all the time derivatives of the upper excited state being set to zero [**208**]. In this case, the steady state approximation becomes

the valid approach of solving the above equations [**38,49**] and the intensity dependent absorption coefficient can be given as **equation 5.15.**

$$\alpha(I) = \frac{\sigma_0 N}{1+\frac{I}{I_{sat}}}\left[1 + \frac{\sigma_1}{\sigma_2}\cdot\frac{\tau_{isc}}{\tau_2}\cdot\frac{I}{I_{sat}} + \frac{\sigma_2}{\sigma_0}\cdot\frac{I}{I_{sat}}\right] \qquad (5.15)$$

where the ground state linear absorption coefficient $\alpha_0 = \sigma_0 N$ (N is the total number density of the dissolved molecules). $I_{sat} = \frac{hv}{(\sigma_0\tau_0)}$ the intensity of saturation and k is is the ratio excited state to ground state cross-sections.

It is pertinent to note that in Pcs, σ_2 and σ_1 are approximately the same order when $\tau_{isc} \ll \tau_2$. Then the term with σ_1 on the numerator can be eliminated and the intensity dependent absorption coefficient can be now defined as

$$\alpha(I, I_{sat}.k) = \frac{\alpha_0}{1+\frac{I}{I_{sat}}}\left(1 + k\frac{I}{I_{sat}}\right) \qquad (5.16)$$

The excited state absorption cross-section σ_2 can be replaced with σ_{ex} since the excited state absorption is mostly due to triplet state. Thus, the ratio of excited to ground state absorption cross-section k is $\frac{\sigma_{ex}}{\sigma_0}$. The parameter I/I_{sat} in the equation can be replaced with F/F_{sat} where F and F_{sat} are respectively fluence per pulse and the energy density of saturation defined as the energy density at which the output reaches saturation value. The $\alpha(I, I_{sat}.k)$ must be substituted back to the propagation formalism **equation 5.12** before fitting the open aperture data to obtain the optical limiting parameters k and F_{sat}. Integration over a homogenous sample of thickness L yields a transcendental equation for transmission T as $T = I_{out}/I_{in}$ [**209**]. In this work, both the five energy model rate equations and/or the conventional Sheik Bahae Z-scan equations were employed for the analysis of the experimental data to understand the proper mechanism responsible for the nonlinear optical response.

5.2. Metallophthalocyanine alone

5.2.1. Ball-type complexes 10-21 (Effect of bridging substituents)

This section compares the ball-type complexes **10**-**21** having carboxylic acid, long alkyl, aldehyde and benzothiazole bridged substituents. Each of the four substituent bear zinc-zinc (**group 1**), gallium-gallium (**group 2**) and indium-indium (**group 3**) central metals.

Reverse saturable absorption (RSA) process is dependent on absorption cross-section [**210,211**] and can only occur when the excited state absorption cross-section is greater than that of the ground state. Complexes **10**-**21** all showed a RSA behavior as evidenced by valley dip decrease in transmittance around the focus (z = 0) along the z-position (**Fig. 5.2**, using **10**, **13**, **19** and **20** as examples).
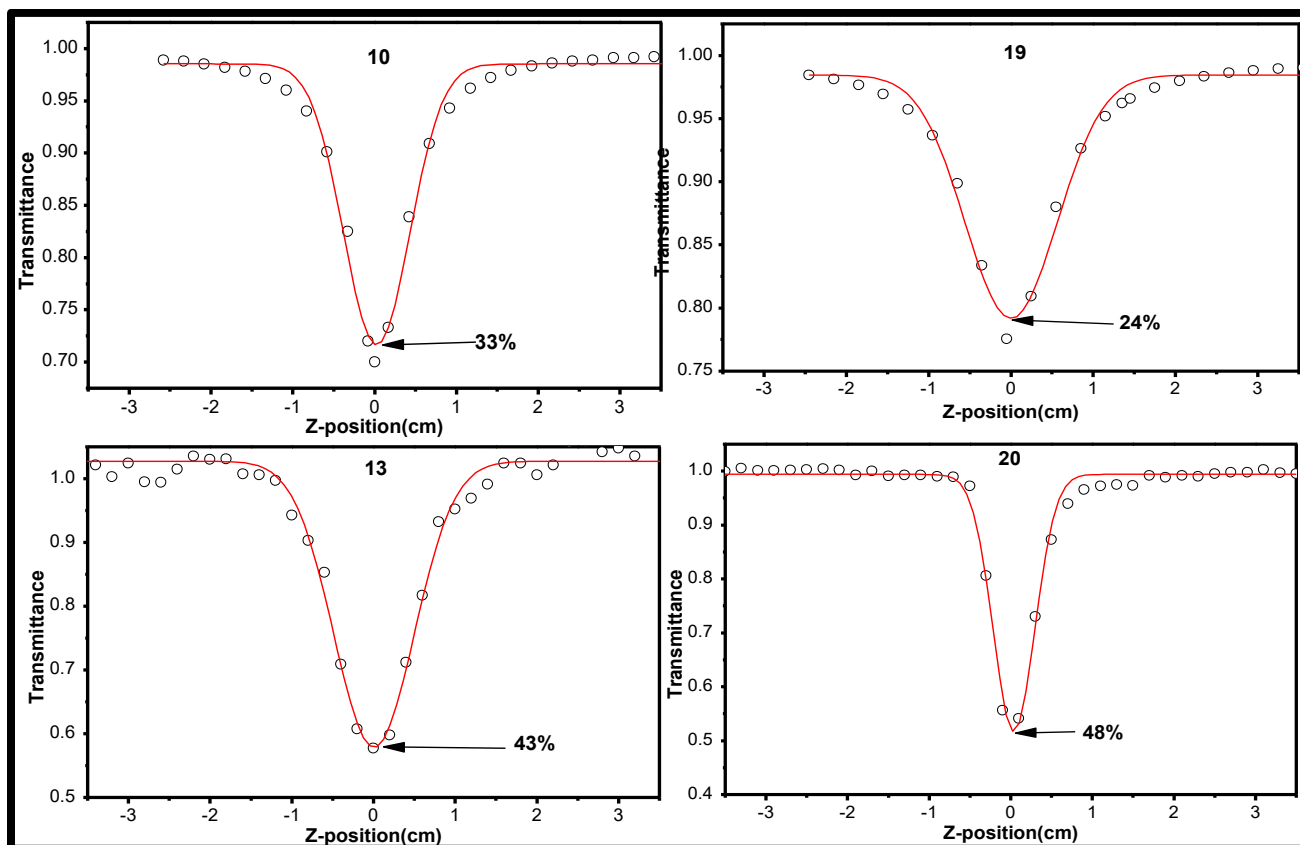
Figure 5.2: RSA profile of zinc ball-type complexes with different bridging substituents. Solvent: DMSO

For **group 1** complexes containing zinc, the RSA reduction in transmittance was found in order of **13** (43%) > **16** (35%) > **10** (33%) > **19** (24%) (**Fig. 5.2**) corresponding to the triplet population as evidenced by triplet quantum yield (**Table 5.1**). For **group 2** complexes, the reduction in transmittance was found in order of **14** (59%) > **11** (56%) > **17** (49%) ≈ **20** (48%) while that of **group 3** were in order of **15** (63%) > **18** (59%) > **12** (57%) > **21**(56%) (**Table 5.1**). The above values show that **13**, **14** and **15** having long alkyl substituents showed highest RSA dip. The benzothiazole substituted complexes showed the lowest reduction in transmittance compared to other complexes. The β_{eff} values were obtained by fitting z-scan data to the TPA-assisted ESA **equations 5.2** and **5.3** described above.

The improvement in nonlinear absorption coefficient ($\beta_{eff.}$) for the group 1 zinc complexes was found in order of **13** (35.1 cm/GW) > **16** (23.2 cm/GW) > **19** (18.3 cm/GW) > **10** (12.8 cm/GW), suggesting better enhancement in nonlinear absorption properties for the long alkyl substituted complex **13** followed by the aldehyde substituted complex **16**. Though complex **10** showed higher percentage transmittance (33%) compared to **19** (24%), the latter displayed higher β_{eff} value than the former. This could be attributed in slight increase in beam waist ($\mathbf{w_0}$) for **19** compared to **10** (**Table 5.1**),which has been shown to increase absorption coefficient [**38**]. There was no clear trend between the carboxylic and benzothiazole substituted complexes. Generally, the value of β_{eff} increases with increase in atomic weight of the central metal in order of **group 3** (In) > **group 2** (Ga) > **group 1**(Zn), which could be attributed to heavy atom effect that enhances population of the excited triplet hence improving RSA behavior.

Table 5.1: Optical limiting parameters of 10-21 in DMSO

Comp	Φ_T	% T	β_{eff} (cm/GW)	$I_m[\chi^3]$(esu)	γ(esu)	F_{sat} (J. cm^{-2})	k(δ_{ex}/δ_g)	w_0 (μm)
Zinc containing complexes with different bridging substituents (Group 1)								
10	0.58	33	12.8	2.99×10^{-8}	3.23×10^{-27}	34.2	13.7	19.2
13	0.62	43	35.1	8.19×10^{-8}	1.20×10^{-26}	26.4	10.3	19.2
16	0.60	35	23.2	5.41×10^{-8}	3.57×10^{-27}	29.3	5.2	17.6
19	0.58	24	18.3	2.35×10^{-8}	2.82×10^{-27}	35.1	17.2	20.1
Gallium containing complexes with different bridging substituents (Group 2)								
11	0.67	56	21.5	5.01×10^{-8}	5.42×10^{-27}	25.2	27.9	18.7
14	0.69	59	78.9	1.84×10^{-7}	2.81×10^{-26}	20.0	16.1	19.6
17A	0.66	49	47.3	1.27×10^{-7}	1.41×10^{-26}	23.8	8.1	19.3
17B	0.69	51	49.7	1.25×10^{-7}	1.42×10^{-26}	20.2	11.0	19.3
20	0.64	48	48.2	1.12×10^{-7}	7.42×10^{-27}	25.9	9.5	18.9
Indium containing complexes with different bridging substituents (Group 3)								
12	0.81	57	52.4	1.22×10^{-7}	1.32×10^{-26}	16.3	17.8	18.2
15	0.83	63	101.2	2.35×10^{-7}	3.59×10^{-26}	11.8	18.3	17.1
18	0.75	59	63.1	1.72×10^{-7}	2.56×10^{-26}	14.2	10.8	18.5
21	0.71	56	49.9	1.16×10^{-7}	7.68×10^{-27}	18.1	23.4	17.3

The plot of β_{eff} against absorbance (**Fig. 5.3**, using **13**-**15** as examples) shows the dependence of β_{eff} on the concentration. It was observed that β_{eff} values increase with the concentration [**212,213**], indicating a strong dependence of β_{eff} on the number of available active excited state molecules.
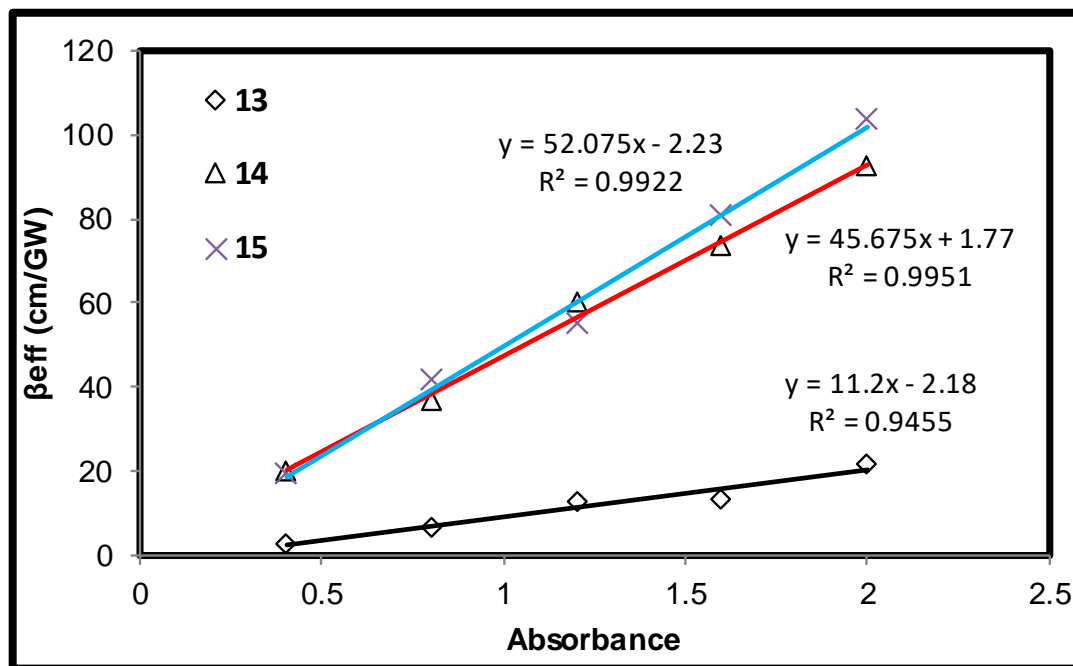
Figure 5.3: Plots of absorbance versus β_{eff} for 13–15. Each data point represents an independent z-scan measurement. $I_{00} \approx 360$ MW cm^{-2} for each measurement. Solid lines are theoretical fits.

The energy density of saturation (F_{sat}) as well as the ratio of excited state to ground state absorption cross-section (k) were obtained by plotting the normalized transmittance against incident energy density per pulse (J. cm^{-2}) (**Fig. 5.4**), where k and F_{sat} were treated as free parameters in the fitting algorithm **equation 5.16**. The F_{sat} for the lead complexes **13**, **14** and **15** that exhibited higher β_{eff} and also saturate at the lowest energy density (**Table 5.1**), indicating the superior nonlinear optical properties of these complexes. All the complexes showed 5-28 times higher excited state absorption cross-section than that of the ground (**Table 5.1**). Apart from **15** that showed superior nonlinear absorption coefficient, the observed F_{sat}, β_{eff} and k for **10-21** agreed with reported values of 40 optical limiting materials, where F_{sat} ranges

from 5 - 150 J cm^{-2}, k ranges from 2-27 and β_{eff} of 1.52 x 10^{-9} – 8.3 x10^{-8} cm W^{-1} (15.2-83 cm/Gw) in solution [**38**].
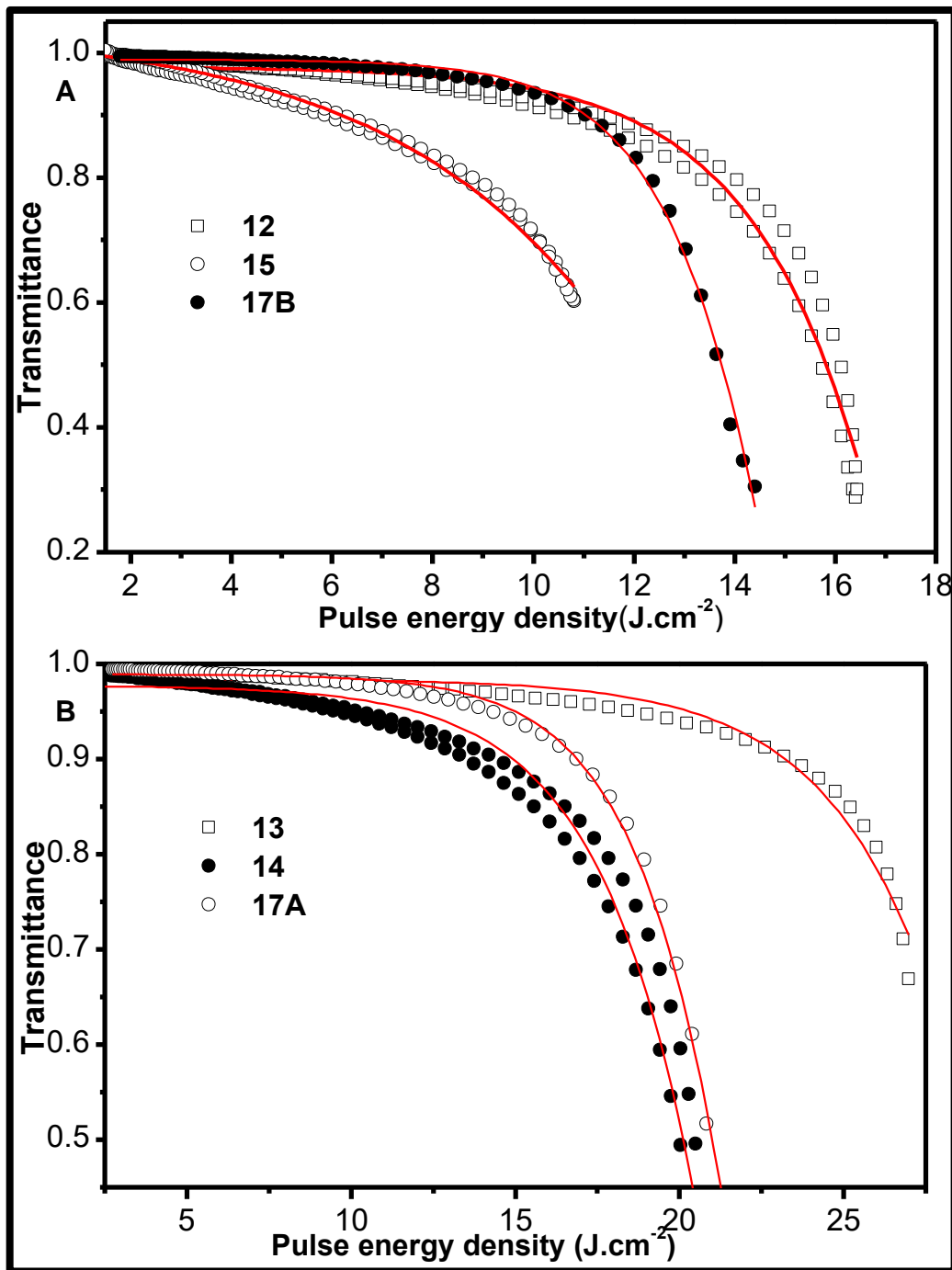
Figure 5.4: Representative plot of normalized transmission against pulse energy density for selected complexes. Solid lines are theoretical fits.

An important measure of a good nonlinear optical material is the value of the imaginary component of the third-order nonlinear susceptibility ($Im[\chi^3]$) since this provides a measure of the speed of the response of an optical material to the perturbation initiated by an intense laser beam [77]. The $Im[\chi^3]$ is directly related to hyperpolarizability (γ), which measures the polarizability experienced by a molecule when it is exposed to light.

The $Im[\chi^3]$ and γ obtained from **equation 5.6** and **equation 5.7** showed that complexes with high β_{eff} also displayed high third order susceptibility as well as high hyperpolarizability with complexes having alkyl substituent still exhibiting better activity (**Table 5.1**).

It is pertinent to note that the excited state absorption cross-section used to determine the k value in **Table 5.1** arise from both excited singlet and triplet together, hence does not give information of which of the excited state is dominating the RSA observed in the complexes.

To probe into the singlet (S_1) and triplet (T_1) contribution to the observed RSA, the five level model (**Fig. 5.1**) **rate equations 5.8**-**5.11** [214] were employed to map out the population dynamics in ball-type **10**-**21** as well as the monomeric **22**-**36**. The ground state absorption cross-section (δ_0) was obtained from absorption spectroscopy using **equation 5.17**

$$\delta_{0=} \alpha/_{N_0} \qquad\qquad (\textbf{5.17})$$

The best fit to equations showed the excited singlet state absorption cross-section (δ_1) arising from the singlet in the range of 8.01×10^{-19} cm^2 – 5.08×10^{-17} cm^2 (2– 4 times higher than the ground state absorption cross-section) (**Table 5.2**) for **group 1** complexes**.**

Table 5.2: RSA ground and excited state population dynamics of 10-37 in DMSO

Comp	Φ_T	TPA	δ_0 (cm^2)	δ_1 (cm^2)	δ_2 (cm^2)	k_1 (δ_1/δ_0)	k_2 (δ_2/δ_0)	I_{lim} (J.cm^{-2})
Zinc containing complexes with different bridging substituents (Group 1)
10	0.58	928	2.37×10^{-18}	1.02×10^{-17}	1.80×10^{-16}	4.3	7.6	-
13	0.62	805	2.52×10^{-19}	1.04×10^{-18}	1.19×10^{-18}	4.1	4.7	-
16	0.60	883	3.49×10^{-19}	8.01×10^{-19}	1.23×10^{-18}	2.3	3.5	-
19	0.58	1002	1.19×10^{-17}	5.08×10^{-17}	1.14×10^{-16}	4.3	9.6	-
Gallium containing complexes with different bridging substituents (Group 2)
11	0.67	721	2.95×10^{-18}	6.37×10^{-17}	5.00×10^{-16}	21.6	16.9	0.63
14	0.69	633	2.07×10^{-19}	9.41×10^{-19}	1.79×10^{-18}	4.5	8.6	0.35
17A	0.65	925	1.70×10^{-19}	4.51×10^{-19}	1.05×10^{-18}	2.7	6.1	0.44
17B	0.69	700	1.59×10^{-19}	4.93×10^{-19}	1.65×10^{-18}	3.1	10.4	0.37
20	0.75	509	2.01×10^{-17}	3.02×10^{-17}	1.18×10^{-16}	1.5	5.9	0.40
Indium containing complexes with different bridging substituents (Group 3)
12	0.81	192	8.10×10^{-17}	9.27×10^{-16}	9.83×10^{-16}	11.4	12.1	0.41
15	0.83	106	1.64×10^{-19}	1.14×10^{-18}	1.58×10^{-18}	7.0	9.7	0.18
18	0.75	245	1.57×10^{-19}	5.11×10^{-19}	9.55×10^{-19}	3.2	6.1	0.29
21	0.71	273	6.07×10^{-17}	7.72×10^{-17}	1.12×10^{-15}	1.2	18.5	0.31
Phenoxylbenzothiazole substituted 22-24
22	0.56	1020	1.35×10^{-17}	2.79×10^{-17}	4.94×10^{-17}	2.1	3.7	- (Zn)
23	0.68	717	9.8×10^{-18}	1.83×10^{-17}	5.78×10^{-17}	1.8	5.9	0.67 (Ga)
24	0.75	119	2.77×10^{-17}	8.31×10^{-17}	2.02×10^{-16}	3.0	7.3	0.24 (In)
Thiarylbenzothiazole substituted 25-27
25	0.65	702	1.81×10^{-17}	9.82×10^{-17}	3.39×10^{-16}	2.8	5.1	- (Zn)
26	0.72	627	1.69×10^{-17}	1.03×10^{-16}	1.86×10^{-16}	6.1	11.0	0.47 (Ga)
27	0.78	292	3.03×10^{-17}	8.72×10^{-17}	3.78×10^{-16}	5.0	12.5	0.22 (In)

Table 5.2 continued

comp	Φ_T	TPA (GM)	δ_0 (cm^2)	δ_1 (cm^2)	δ_2 (cm^2)	k_1 (δ_1/δ_0)	k_2 (δ_2/δ_0)	I_{lim} (J.cm^{-2})
			Monomeric aldehyde substituted 28-30					
28	0.57	342	3.08×10^{-19}	6.11×10^{-19}	1.04×10^{-18}	2.0	3.3	- (Zn)
29	0.63	263	1.52×10^{-19}	3.90×10^{-19}	7.50×10^{-19}	2.6	4.9	0.61 (Ga)
30	0.69	174	1.28×10^{-17}	2.82×10^{-17}	5.79×10^{-17}	2.2	4.5	0.45 (In)
			Aminophenoxyl substituted complexes 31-33					
31	0.61	216	2.97×10^{-17}	2.02×10^{-16}	3.97×10^{-16}	6.8	13.4	- (Zn)
32	0.69	155	3.24×10^{-19}	2.11×10^{-18}	1.29×10^{-18}	6.5	4.0	- (Ga)
33	0.72	113	1.63×10^{-19}	3.08×10^{-18}	1.61×10^{-18}	18.9	9.9	0.18 (In)
			Asymmetric benzothiazole substituted complexes 34-36					
34	0.59	392	2.40×10^{-16}	1.00×10^{-16}	5.8×10^{-16}	42	24.2	- (Zn)
35	0.64	211	1.92×10^{-16}	5.81×10^{-17}	9.4×10^{-16}	30.3	48.9	- (Ga)
36	0.70	195	1.1×10^{-16}	2.80×10^{-16}	1.3×10^{-16}	2.6	11.8	0.38 (In)

The corresponding triplet absorption cross-section, on the other hand, ranges from 1.19×10^{-18} cm^2–1.80×10^{-16} cm^2 (4–10 times higher than the ground state absorption cross-section). **Group 2** complexes also showed (δ_1) ranging from 4.51×10^{-19} cm^2 – 6.37×10^{-17} cm^2 (2–22 times higher than the ground state absorption cross-section) and (δ_2) ranging from 1.05×10^{-18} cm^2 – 5.00×10^{-16} cm^2 (5–17 times higher than the ground state absorption cross-section) while **group 3** showed the (δ_1) ranging from 5.11×10^{-19} cm^2 – 9.27×10^{-16} cm^2 (1–11 times higher than the ground state absorption cross-section) and (δ_2) from 9.55×10^{-19} cm^2 – 1.12×10^{-15} cm^2 (6–19 times higher than the ground state absorption cross-section). It can be seen from **Table 5.2** that the observed RSA behavior was dominated by the triplet population, which is expected since at higher fluence and longer pulse durations, Pcs exhibit RSA resulting from the strong absorption from the singlet and/or triplet

manifold [**214**]. Though the singlet and triplet manifold showed higher absorption cross-section than the ground state, there was no clear trend for the substituent effect. A close look at the sum of the k_1 and k_2 values for singlet and triplet contribution showed that the rate equation values (**Table 5.2**) are relatively close to the values obtained from steady state approximation (**Table 5.1**).

5.2.2. Mononuclear complexes 22-36

Fig. 5.5 shows the open aperture Z-scan profile of **22**-**24** as examples. The RSA profile dips are higher for indium and gallium containing complexes compared to the corresponding zinc due to heavy atom effect as discussed before.
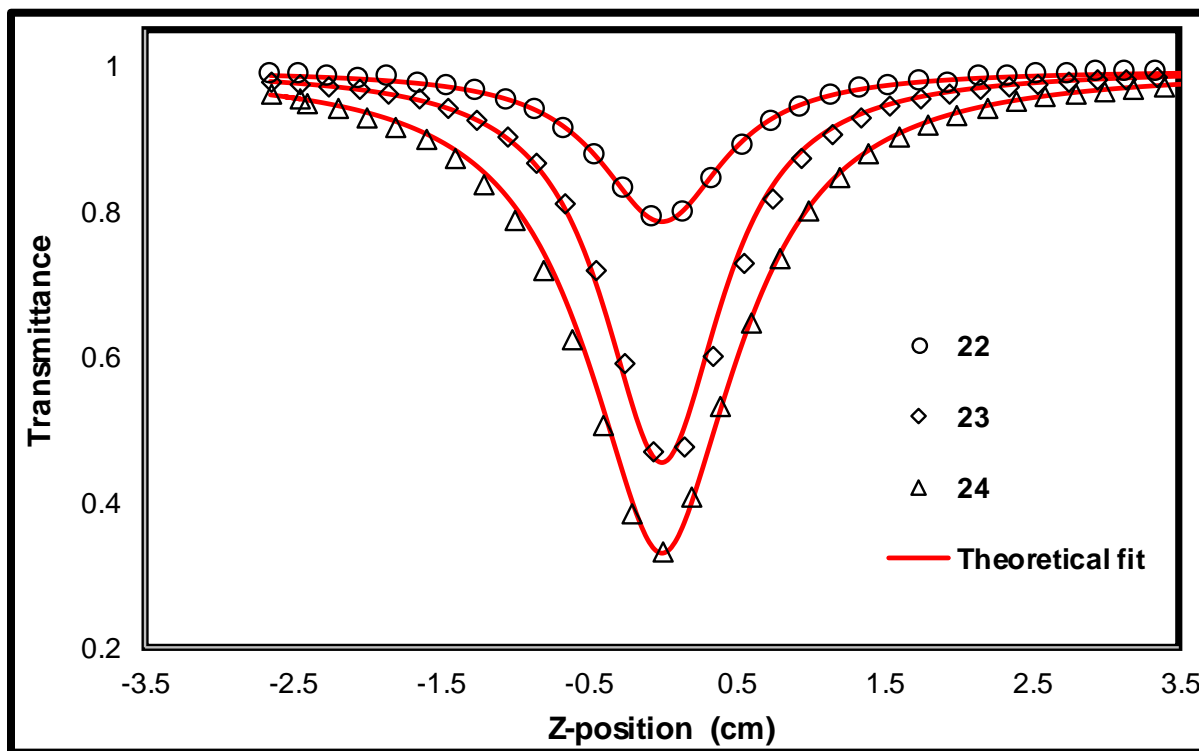
Figure 5.5: Representative open-aperture Z-scans of complexes 22-24 in THF. Input 60 μJ

The symmetrical complexes **22**-**33** showed values of k_1 ranging from 2-19 and k_2 ranging from 3-13, indicating higher excited state absorption cross-sections than that of the ground state (δ_0) (**Table 5.2**). The asymmetric complexes **34**-**36** showed k_1 value of 42, 30.3 and 2.6 for **34**, **35** and **36** respectively while the correspond k_2 were 24.2, 48.9 and 11.8

The absorption cross-section due to two photon absorption (TPA) pathways for all complexes ranges from 106 - 1020 GM ($1GM = 10^{-50}$ cm^2). It has been shown that at 532 nm and using nanosecond pulse regime, the nonlinear absorption response of phthalocyanines is dominated by excited state absorption from the singlet and/or triplet excited states rather than two-photon absorption [**215**], which account for the low TPA (1.06×10^{-48}-1.020×10^{-47} cm^2) observed for **22**-**27** compared to δ_1 or δ_2 (order of 10^{-19} - 10^{-18} cm^2).

A plot of Φ_T versus TPA as well Φ_T versus ratio of triplet to ground state absorption cross-section (k_2) (**Fig. 5.6**, using **13**-**15** and **25**-**27** as examples) predominantly showed significant depopulation of TPA cross-section with attendance increase in k_2. This is reasonable since triplet population will reduce the number of available molecules for TPA.
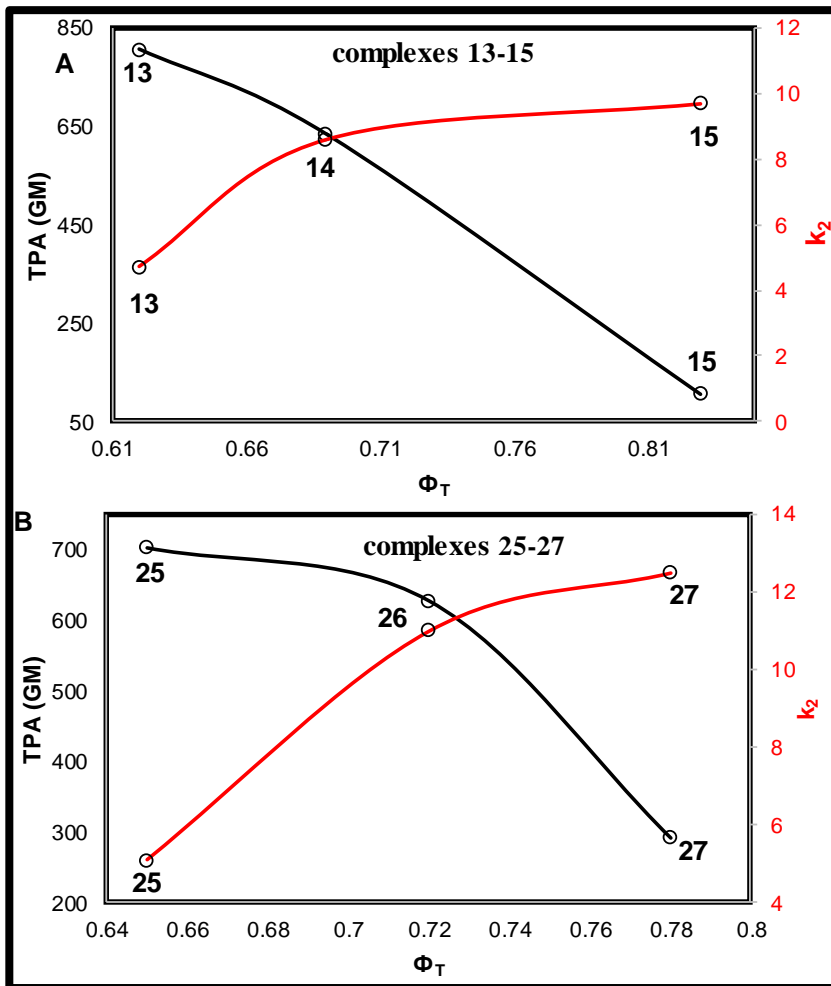
Figure 5.6: Plots of Φ_T vs TPA (black) and Φ_T vs k_2 (red)

The limiting threshold (l_{lim}) is an important term in optical limiting measurements and can be defined as the input fluence at which the transmittance is 50% of the linear transmittance value [**216**]. **Fig. 5.7** (using **31**-**33** as examples) shows the plot of input fluence against transmittance from which the limiting threshold (l_{lim}) was determined.
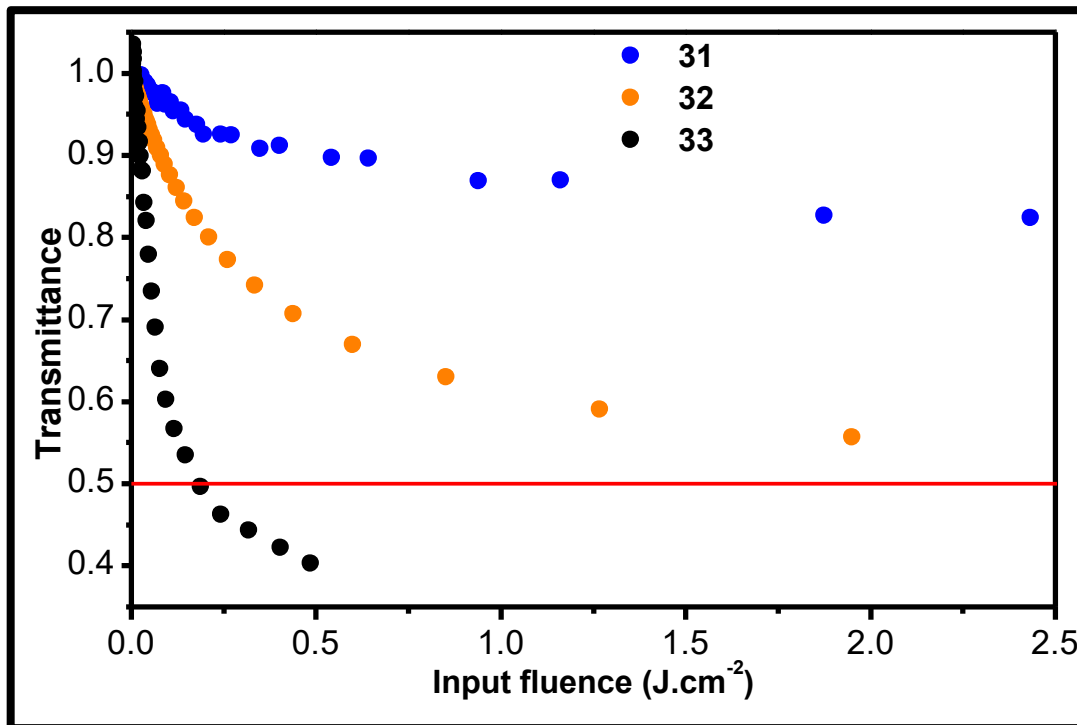
Figure 5.7: Plot of normalized transmittance vs input fluence for 31-33. Solid red line indicates 50% linear transmittance

For all zinc complexes, the l_{lim} could not be determined since the transmittance did not reach 50%. For complexes with the same substituents, the l_{lim} decreases in order of $In < Ga$, suggesting lower limiting threshold, hence better NLO performance with incorporation of heavy atom. Lower limiting threshold, hence better NLO response was observed for **26** and **27** containing sulfur bridge and no phenyl bridging ligand compared to corresponding **23** and **24**, which could be attributed to enhanced k_2 (**Table 5.2**) corresponding to higher triplet quantum yield for **26** and **27** (**Table 5.2**).

5.2.3. Comparative effect of co-facial ball-type and symmetry (complexes 16-18, 19-21, 22-24 and 28-30)

The aldehyde and benzothiazole substituted complexes **28**-**30** and **22**-**24** are monomeric analogue of the ball-type complexes **16**-**18** and **19**-**21**, respectively. On the other, **22**-**24** are symmetric analogue of asymmetric **34**-**36** hence the comparative effect of their optical limiting properties is hereby discussed.

Comparing the ball-type aldehyde (**16**-**18**) and with **28**-**30**, k_2 values were found to be 3.5, 6.1, 10.4 and 6.1 for **16**, **17A**, **17B** and **18**, higher than 3.3, 4.9 and 4.5 for the monomeric **28**, **29** and **30** (**Table 5.2**). Comparing **19**-**21** with **22**-**24**, complex **20** and the monomeric analogue **23** show the same k_2. However, the k_2 values for **19** and **21** were significantly higher than corresponding **22** and **24** (**Table 5.2**). The limiting threshold (l_{lim}) for the ball-type **16**-**18** and **19**-**21** were found to be lower compared to the corresponding monomeric **28**-**30** and **22**-**24** respectively. These observations suggest that dimerization could be a potential means of tuning NLO response.

For the asymmetric **34**-**36** and the symmetric **22**-**24**, the former showed higher k_2 and lower l_{lim} for **35** compared to corresponding symmetric **22**-**24** (**Table 5.2**).

Lack of symmetry in Pcs molecules, which result in uneven peripheral substitution has been shown to result in enhanced nonlinear optical response compared to the symmetric analogue [**47**]. The symmetric **22**-**24** showed higher TPA pathway than the asymmetric 34-36, suggesting that enhanced TPA for 22-24 could have lower the excited absorption cross-section.

5.3.   Combination of phthalocyanines and nanomaterials.

5.3.1. Covalently linked complexes 10-12, 31-33 and 34-36

Fig. 5.8 shows the open aperture Z-scan profile of selected complexes and the corresponding nanoconjugates. Results obtained by fitting the experimental data into five level rate equations described before showed decrease in transmittance around the focus (z = 0), signifying RSA behavior. The nanoconjugates displayed higher percentage reduction in transmittance compared to the corresponding Pc complexes alone showing the important of formulation of complexes into nanohybrid in improving the nonlinear absorption behavior.
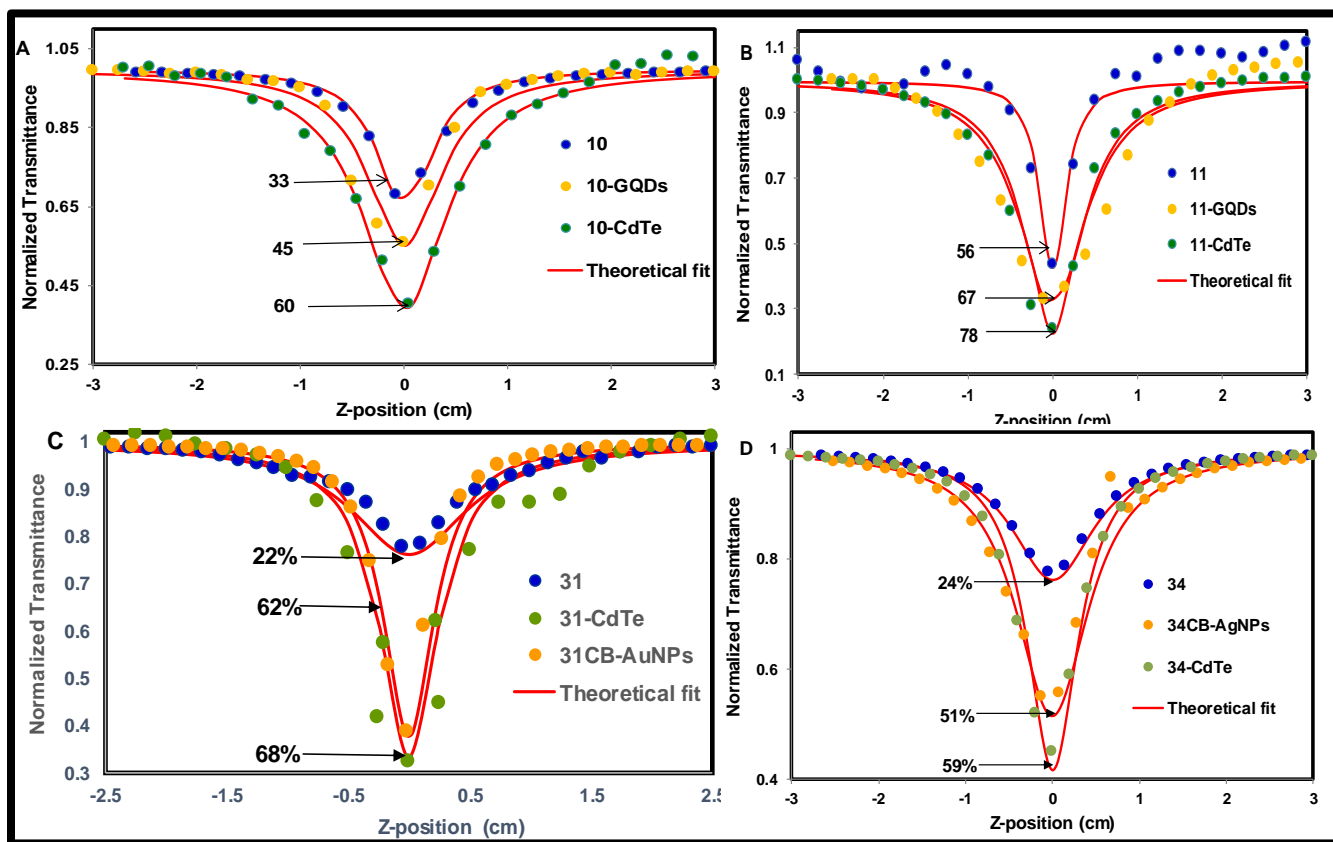
Figure 5.8: Open aperture Z-scan profile of selected complexes and corresponding nanoconjugates in DMSO. Scattered circles are experimental data.

Table 5.3: Nonlinear optical parameters of complexes and nanoconjugates in DMSO

Complex	TPA (GM)	δ_0 (cm²)	δ_1 (cm²)	δ_2 (cm²)	k_1 δ_1/δ_0	k_2 δ_2/δ_0	Loading (mg/mg)	I_{lim} (J cm^{-2})
Carboxylic acid substituted ball-type complexes 10-12								
10	928	2.37×10^{-18}	1.02×10^{-17}	1.80×10^{-16}	4.3	7.6		-
10-CdTe	1088	2.41×10^{-18}	3.15×10^{-17}	4.00×10^{-16}	13.1	16.2	8	0.85
10-GQDs	186	2.37×10^{-18}	2.47×10^{-17}	2.80×10^{-16}	10.4	11.8	12	**-**
11	721	2.95×10^{-18}	6.37×10^{-17}	5.00×10^{-16}	21.6	16.9		0.63
11-CdTe	917	3.90×10^{-18}	3.11×10^{-17}	1.01×10^{-16}	8.0	25.9	11	0.42
11-GQDs	202	2.88×10^{-18}	4.23×10^{-17}	5.10×10^{-17}	14.7	17.7	15	0.67
12	192	8.10×10^{-17}	9.27×10^{-16}	9.83×10^{-16}	11.4	12.1		0.41
12-CdTe	543	8.10×10^{-17}	8.65×10^{-16}	1.53×10^{-15}	10.7	18.9	9	0.32
12-CdTeSe	213	2.03×10^{-16}	6.34×10^{-15}	3.81×10^{-14}	31.2	187.7	19	0.50
12-CdTeSe/ZnO	305	1.94×10^{-16}	7.18×10^{-15}	4.24×10^{-14}	37.0	218.5	25	0.40
12-GQDs	272	8.10×10^{-17}	9.30×10^{-16}	1.03×10^{-14}	11.5	12.7	7	0.48
12-AgNPs	134	5.50×10^{-17}	9.75×10^{-16}	8.15×10^{-15}	17.7	14.8	5	0.68
12-AuNPs	312	1.94×10^{-16}	4.29×10^{-15}	3.94×10^{-15}	22.1	20.4	16	0.55
Bis(aminophenoxyl)phenoxyl substituted complexes 31-33								
31	216	2.97×10^{-17}	2.02×10^{-16}	3.97×10^{-16}	6.8	13.4	-	-
31CB-AgNPs	189	2.27×10^{-17}	3.15×10^{-16}	4.09×10^{-16}	13.9	18.0	37	0.42
31CB-AuNPs	449	3.03×10^{-17}	6.33×10^{-16}	6.01×10^{-16}	11.5	29.6	30	0.36
31-CdTe	348	5.36×10^{-19}	8.60×10^{-19}	2.96×10^{-18}	2.0	5.2	10	0.38
32	155	3.24×10^{-19}	2.11×10^{-18}	1.29×10^{-18}	6.5	4.0	-	-
32-CdTe	309	3.24×10^{-19}	9.50×10^{-19}	1.99×10^{-18}	2.9	6.1	7	0.50
33	113	1.63×10^{-19}	3.08×10^{-18}	1.61×10^{-18}	18.9	9.9	-	0.18
33-CdTe	437	1.63×10^{-19}	1.92×10^{-18}	2.32×10^{-19}	11.8	14.2	3	0.04

Table 5.3 continued

Complex	TPA (GM)	δ_0 (cm²)	δ_1 (cm²)	δ_2 (cm²)	k_1 δ_1/δ_0	k_2 δ_2/δ_0	Loading (mg/mg)	I_{lim} (J cm⁻²)
Asymmetric benzothiazole substituted complexes 34-36								
34	392	2.40×10^{-16}	1.00×10^{-16}	5.8×10^{-16}	42	24.2		-
34CB-AgNPs	186	2.98×10^{-18}	3.15×10^{-18}	1.09×10^{-16}	10.6	36.6	11	0.82
34CB-AuNPs	249	3.73×10^{-18}	6.23×10^{-17}	1.01×10^{-16}	18.5	30.0	17	0.77
34-CdTe	623	7.93×10^{-18}	5.83×10^{-17}	7.30×10^{-17}	23.7	21.7	9	0.75
35	211	1.92×10^{-16}	5.81×10^{-17}	9.40×10^{-16}	30.3	48.9		0.56
35-CdTe	501	5.40×10^{-18}	9.80×10^{-18}	1.11×10^{-18}	1.8	20.3	7	0.44
36	115	1.10×10^{-16}	2.80×10^{-16}	1.30×10^{-16}	2.6	11.8		0.31
36-CdTe	432	2.60×10^{-18}	7.20×10^{-18}	7.63×10^{-17}	2.8	29.1	12	0.25

Generally, for complex **12** that was linked to CdTe (core), CdTeSe (core shell), CdTeSe/ZnO (core shell shell), the ratio of δ_1/δ_0 and δ_2/δ_0 was found in order of CdTeSe/ZnO > CdTeSe > CdTe (**Table 5.3**) showing that either larger core/shell QDs are advantageous to optical limiting behavior of phthalocyanines or due to higher loading of complex **12** on CdTeSe/ZnO (**Table 5.3**).

The semiconductor QDs also predominantly showed higher TPA cross-section compared to the carbon based GQDs. The metallic **12**-AuNPs showed k_1 and k_2 to be 22.1 and 20.4 respectively, higher than 17.7 and 14.8 for **12**-AgNPs. **12**-AuNPs also showed higher TPA than **12**-AgNPs, which could be attributed to SPR band of Au being in resonance with the 532 nm excitation wavelength of the laser employed. Enhancement in TPA for AuNPs compared to AgNPs when both were coupled to conjugated polymers has been reported [**217**].

Though the values of I_{lim} for all the nanoconjugates are lower than the Pc complexes alone, which indicate superior optical limiting response, **12**-CdTe with lower ratio

of δ_1/δ_0 and δ_2/δ_0 showed better limiting threshold of 0.32 J. cm^{-2} compared to 0.5 and 0.4 J. cm^{-2} for **12**-CdTeSe and **12**-CdTeSe/ZnO, which could be due to faster response time for core CdTe than its core-shell derivatives as described elsewhere [**218**–**220**].

The conjugates of the aminophenoxyl **31**-**33** and the asymmetric benzothiazole **34**-**36**, **31**CB-AgNPs showed a δ_1 of 3.15×10^{-16} and δ_2 of 4.09×10^{-16} (14 and 18 times higher) than δ_0. The corresponding **31**CB-AuNPs showed a δ_1 of 6.33×10^{-16} and δ_2 of 6.01×10^{-16} (12 and 29 times higher) than δ_0. Thus, the Au conjugate showed enhanced NLO performance irrespective of higher loading in Ag conjugate (**Table 5.3**). The δ_1 and δ_2 for **31**-CdTe was found to be 8.60×10^{-19} and 2.96×10^{-18} (2-5 times higher) than δ_0. The limiting threshold was found in order of **31**CB-AuNPs (0.36) < **31**-CdTe (0.38) < **31**CB-AgNPs (0.42) (**Table 5.3**). Similar trends were observed for Au and Ag conjugates of **34**. However, **34**-CdTe showed enhanced NLO performance as evidenced by lower I_{lim} compared to corresponding Au and Ag conjugates.

5.3.2. Surface assembly of complexes 19-27, 31 and 34 onto metallic gold and silver nanoparticles.

The open aperture Z-scan profile of these complexes and the corresponding nanoconjugates showed downward dipping curve symmetrical about the focus as observed for the covalently linked conjugates (spectra not shown) which signify RSA behavior. All the nanoconjugates showed enhanced RSA behavior than the corresponding Pc complexes alone as was the case for the covalently linked conjugates.

k_1 and k_1 values of dimeric benzothiazole ball-type **19**-**21** respectively range from 2–5 and 8-31 (**Table 5.4**).

It should be noted that while other complexes and nanoconjugates shown in **Table 5.4** were studied in DMSO, **22**-**27** and the nanoconjugates were studied in THF to avoid high light scattering observed when DMSO was employed, hence comparison of the NLO data for **22**-**27** and conjugates with other nanoconjugates may not be entirely accurate.

Comparing the asymmetric nanoconjugates **34-**AgNPs and **34**-AuNPs with the corresponding the dimeric ball-type nanoconjugate of **19**-AgNPs and **19**-AuNPs, the k_2 were higher for the asymmetric derivatives, indicating enhanced NLO response for the asymmetry than the ball-type analogues.

Table 5.4: Nonlinear optical parameters of complexes and nanoconjugates in DMSO unless otherwise stated

Complex	TPA (GM)	δ_0 (cm^2)	δ_1 (cm^2)	δ_2 (cm^2)	k_1 δ_1/δ_0	k_2 δ_2/δ_0	I_{lim} (J cm^{-2})
Ball-type benzothiazole bridged complexes 19-21							
19	1030	1.19×10^{-17}	4.92×10^{-17}	1.29×10^{-16}	4.1	10.8	-
19-AgNPs	133	3.05×10^{-17}	5.10×10^{-17}	2.42×10^{-16}	1.7	7.9	-
19-AuNPs	2247	3.08×10^{-17}	9.48×10^{-17}	4.60×10^{-16}	3.1	14.9	-
20	509	2.01×10^{-17}	3.28×10^{-17}	2.51×10^{-16}	1.6	12.5	0.18
20-AgNPs	161	7.04×10^{-17}	3.37×10^{-16}	7.02×10^{-16}	4.8	10.0	0.19
20-AuNPs	692	4.02×10^{-17}	7.91×10^{-17}	6.96×10^{-16}	2.0	17.3	0.10
21	273	6.07×10^{-17}	8.99×10^{-17}	1.49×10^{-15}	1.5	24.5	0.12
21-AgNPs	110	1.06×10^{-17}	3.07×10^{-17}	3.01×10^{-16}	2.9	28.4	0.10
21-AuNPs	489	4.22×10^{-17}	2.17×10^{-16}	1.32×10^{-15}	5.1	31.2	0.09
Tetra-substituted benzothiazole complexes 22-27[a]							
22	1020	1.35×10^{-17}	2.79×10^{-17}	4.94×10^{-17}	2.1	3.7	-
22-AgNPs	106	1.01×10^{-17}	2.92×10^{-17}	8.57×10^{-17}	2.9	8.5	0.59
22-AuNPs	22900	1.45×10^{-17}	9.98×10^{-17}	9.22×10^{-17}	2.0	6.4	0.53
23	717	9.8×10^{-18}	1.83×10^{-17}	5.78×10^{-17}	1.8	5.9	0.67
23-AgNPs	340	1.08×10^{-17}	2.21×10^{-17}	1.29×10^{-16}	2.0	12.0	0.47
23-AuNPs	9700	1.61×10^{-17}	2.73×10^{-17}	1.53×10^{-16}	1.7	9.5	0.41

Table 5.4 continued

Complex	TPA (GM)	δ_0 (cm^2)	δ_1 (cm^2)	δ_2 (cm^2)	k_1 δ_1/δ_0	k_2 δ_2/δ_0	I_{lim} (J cm^{-2})
24	129	2.77×10^{-17}	8.31×10^{-17}	2.02×10^{-16}	3.0	7.3	0.34
24-AgNPs	172	2.38×10^{-17}	4.05×10^{-17}	1.50×10^{-16}	1.7	6.3	0.28
24-AuNPs	307	2.52×10^{-17}	6.30×10^{-17}	2.07×10^{-16}	2.5	8.2	0.19
25	702	1.81×10^{-17}	9.82×10^{-17}	3.39×10^{-16}	2.8	5.1	-
25-AgNPs	235	2.16×10^{-17}	2.89×10^{-17}	1.53×10^{-16}	1.3	7.1	0.56
25-AuNPs	32900	2.45×10^{-17}	3.77×10^{-17}	1.72×10^{-16}	1.5	7.0	0.33
26	627	1.69×10^{-17}	1.03×10^{-16}	1.86×10^{-16}	6.1	11.0	0.47
26-AgNPs	1020	3.02×10^{-17}	6.03×10^{-17}	2.07×10^{-16}	2.0	6.9	0.28
26-AuNPs	40300	3.17×10^{-17}	5.62×10^{-17}	2.12×10^{-16}	1.8	6.7	0.25
27	292	3.03×10^{-17}	8.72×10^{-17}	3.78×10^{-16}	5.0	12.5	0.22
27-AgNPs	2330	2.98×10^{-17}	1.19×10^{-16}	2.10×10^{-16}	4.0	7.0	0.14
27-AuNPs	289020	3.42×10^{-17}	1.76×10^{-16}	3.35×10^{-16}	5.1	9.8	0.12
Bis(aminophenoxyl)phenoxyl substituted complex 31							
31	216	2.97×10^{-17}	2.02×10^{-16}	3.97×10^{-16}	6.8	13.4	-
31-AgNPs	137	1.78×10^{-17}	3.37×10^{-16}	5.30×10^{-16}	6.6	10.3	-
31-AuNPs	39100	2.05×10^{-17}	4.47×10^{-16}	4.40×10^{-16}	21.8	21.5	0.68
Asymmetric benzothiazole substituted complex 34							
34	392	2.40×10^{-16}	1.00×10^{-16}	5.8×10^{-16}	42	24.2	-
34-AgNPs	194	2.95×10^{-18}	6.37×10^{-17}	1.30×10^{-16}	21.6	44.0	0.42
34-AuNPs	661	2.87×10^{-18}	4.47×10^{-17}	1.40×10^{-16}	15.6	48.8	0.39

[a]Solvent =THF

The limiting threshold (I_{lim}) values for asymmetric **34**-AgNPs and **34**-AuNPs were found to be 0.42 and 0.39 J.cm^{-2} respectively, while the I_{lim} for **19**-AgNPs and **19**-AuNPs could not be determined since the conjugates did not reduce transmittance up to 50% (**Table 5.4**). The enhanced NLO performance for **34**-AgNPs and **34**-AuNPs could be attributed to effect of asymmetry, which has been shown to improve dipole moment, hence provide faster optical limiting response [**221**–**223**]. Comparing the NLO performance of the metallic nanoparticles the conjugates of AuNPs consistently showed higher RSA dip as well as lower limiting threshold compared to the corresponding AgNPs derivatives.

5.3.3. Comparative effect of covalent linkage and surface assembly onto metallic nanoparticles (complexes 31 and 34)

The effect type of linkage on the optical limiting performance was investigated using complexes **31** and **34**, which were covalently linked as well as surface assembled onto metallic gold and silver nanoparticles to form the respective conjugates and the NLO parameters are presented in **Table 5.5**.

Table 5.5: Nonlinear optical parameters of nanoconjugates in DMSO.

Complex	TPA (GM)	δ_0 (cm²)	δ_1 (cm²)	δ_2 (cm²)	δ_1/δ_0	δ_2/δ_0	Loading (mg/mg)	I_{lim} (J cm⁻²)
Bis(aminophenoxyl)phenoxyl substituted complex 31								
31CB-AgNPs	286	2.27×10^{-17}	3.15×10^{-16}	4.09×10^{-16}	13.9	18.0	37	0.42
31-AgNPs	137	1.78×10^{-17}	3.37×10^{-16}	5.30×10^{-16}	6.6	10.3	16	-
31CB-AuNPs	449	3.03×10^{-17}	6.33×10^{-16}	6.01×10^{-16}	11.5	29.6	30	0.36
31-AuNPs	391	2.05×10^{-17}	4.47×10^{-16}	4.40×10^{-16}	21.8	21.5	28	0.68
Asymmetric benzothiazole substituted complexes 34								
34CB-AgNPs	98.6	2.98×10^{-18}	3.15×10^{-18}	1.09×10^{-16}	10.6	36.5	11	0.59
34-AgNPs	93.6	2.95×10^{-18}	6.37×10^{-17}	1.30×10^{-16}	21.6	44.0	21	0.42
34CB-AuNPs	249	3.73×10^{-18}	6.23×10^{-17}	1.01×10^{-16}	18.5	30.0	17	0.52
34-AuNPs	261	2.87×10^{-18}	4.47×10^{-17}	1.40×10^{-16}	15.6	48.8	33	0.39

For complexes **31**, the minimum transmittance values of 62% and 53% respectively were observed for the covalently linked **31**CB-AuNPs and **31**CB-AgNPs, higher than 51% and 35% for the corresponding surface assembled **31**-AuNPs and **31**-AgNPs, respectively (figure not shown), which could be due to more Pcs being loaded on the surface of the nanoparticles through the covalent route compared with the surface assembled route (**Table 5.5**). Additionally, these covalently linked conjugates show enhancement in TPA as well as lower limiting threshold compared to the surface assembled analogues (**Table 5.5**).

For the asymmetric conjugates, the minimum transmittance value of 66% and 60% was observed for the surface assembled **34**-AuNPs and **34**-AgNPs respectively, which is higher than 58% and 51% for the corresponding covalently linked derivative. The limiting threshold for surface assembled conjugates were lower, hence superior NLO response compared to the covalently linked conjugates (**Table 5.5**). The loading of complexes onto the nanoparticles also showed more loading of

complex **34** through the surface assembly route with accompanying high triplet quantum yield. Thus, none of the linking route could be categorically said to offer better optical limiting behavior since it greatly dependent on the number of complexes loaded.

5.3.4. Effect of formulation into thin films (complexes 13-15, 16-18, 22-27 and 28-30)

Fig. 5.9 shows the open aperture results of the complexes in solution and in polymer thin-films (TF), using polystyrene as the polymer sources.
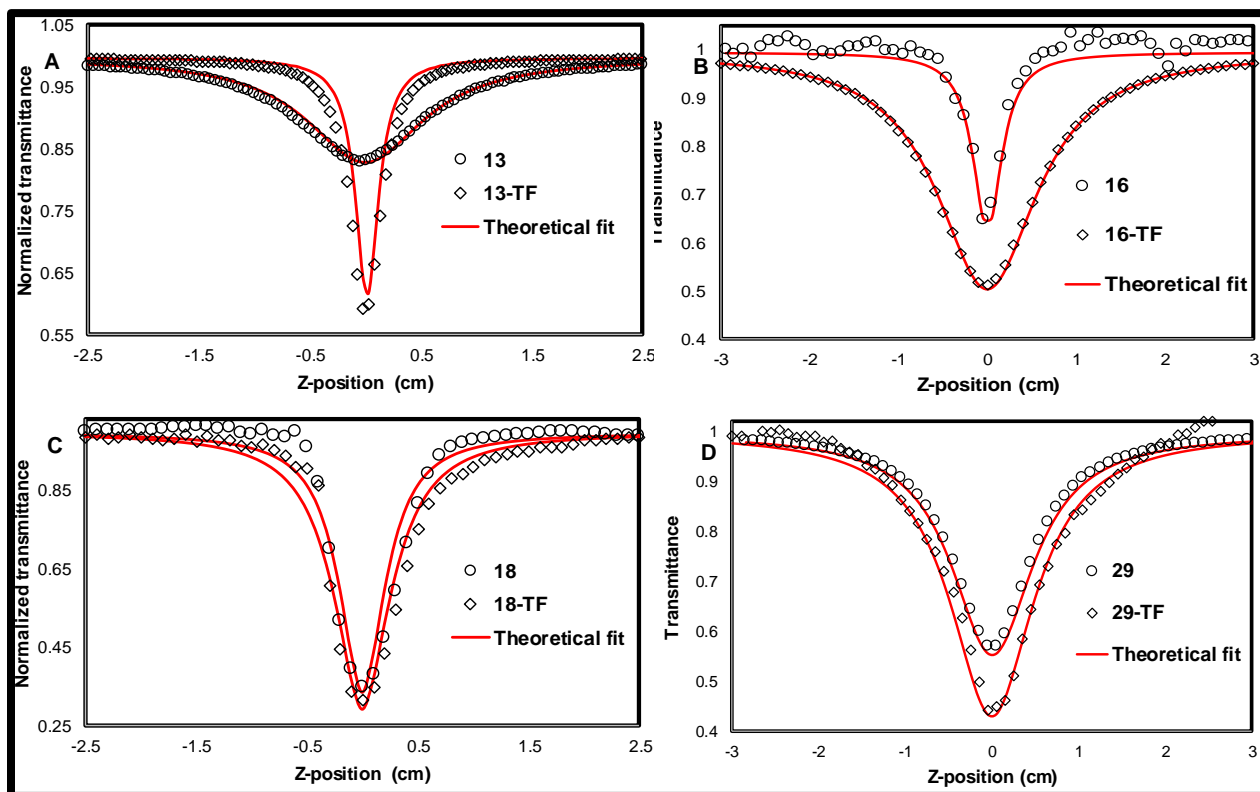
Figure 5.9: RSA profile of selected complexes in solution and thin films. Scattered circles are experimental data. Input energy 50 µJ.

The RSA behavior shows significant reduction in transmittance when the complexes were fabricated into thin films. The optical limiting parameters for the complexes and corresponding thin films are presented in **Table 5.6**. The observed value of β_{eff} for the thin films **13**-TF, **14**-TF and **15**-TF are 38.9, 80.7 and 108.4 cm/GW respectively, higher than 35.1, 78.9 and 101.2 cm/GW for **13**, **14** and **15** respectively in solution (**Table 5.6**). Similarly, the thin films of complexes **16**-**18** and **22**-**30** follow similar trend by displaying higher absorption coefficient in polymer support than in solution. The enhanced NLA may generally be related to the high photodegradation threshold of Pcs in solid state compared to when they are in solution where they tend to degrade faster [**224**].

The energy density of saturation (F_{sat}) values when the complexes were formulated into thin films were lower than for the complexes in solution (**Table 5.6**). Thus, the thin films exhibit highest nonlinear absorption coefficient and saturates at the lowest energy density, suggesting better optical response for the thin films.

Table 5.10: optical limiting parameters of complexes in solution and thin films

Comp	β_{eff} (cm/GW)	$I_m [\chi^3]$(esu)	γ(esu)	F_{sat} ($J.$ cm^{-2})	$k(\delta_{ex}/\delta_g)$	w_0 (µm)
Long alkyl-substituted ball-type complexes 13-15 and thin films						
13	35.1	8.19×10^{-8}	1.20×10^{-27}	16.4	10.3	19.2
13-TF	38.9	9.07×10^{-8}	5.99×10^{-27}	14.3	9.9	17.1
14	78.9	1.84×10^{-7}	2.81×10^{-26}	15.0	16.1	19.6
14-TF	80.7	1.88×10^{-7}	3.24×10^{-26}	14.3	18.9	18.9
15	101.2	2.35×10^{-7}	3.59×10^{-26}	11.8	18.3	17.1
15-TF	108.4	2.53×10^{-7}	3.67×10^{-26}	11.3	15.2	18.9
Aldehyde substituted ball-type complexes 16-18 and thin films						
16	23.2	5.41×10^{-8}	3.57×10^{-27}	25.3	5.2	17.6
16-TF	52.5	1.22×10^{-7}	8.08×10^{-27}	7.30	3.1	20.8
17	48.5	1.13×10^{-7}	1.22×10^{-26}	24.8	7.1	19.3
17A-TF	62.7	1.46×10^{-7}	2.73×10^{-26}	5.19	9.2	18.9
17B-TF	69.1	1.62×10^{-7}	3.01×10^{-26}	3.94	5.7	20.1
18	60.1	1.42×10^{-7}	3.26×10^{-26}	14.2	10.8	18.5
18-TF	114.0	2.66×10^{-7}	2.89×10^{-26}	3.01	11.2	19.8
Phenoxyl benzothiazole substituted complexes 22 and 23						
22	43.0	4.46×10^{-8}	4.62×10^{-27}	30.2	3.7	20.2
22-TF	48.2	6.87×10^{-8}	5.81×10^{-27}	15.8	9.3	23.2
23	89.0	5.11×10^{-8}	7.07×10^{-27}	24.7	2.4	20.1

Table 5.10 continued

Comp	β_{eff} (cm/GW)	$I_m[\chi^3]$(esu)	γ(esu)	F_{sat} (*J.* cm^{-2})	$k(\delta_{ex}/\delta_g)$	w_0 (µm)
23-TF	97.0	7.28×10^{-8}	7.93×10^{-27}	21.4	7.8	24.6
24	92.2	6.93×10^{-8}	7.95×10^{-27}	18.9	10.2	19.8
24-TF	98.5	8.11×10^{-8}	9.07×10^{-27}	18.6	10.8	22.7
25	47.2	5.22×10^{-8}	6.02×10^{-27}	27.8	8.1	20.2
25-TF	53.7	6.39×10^{-8}	7.05×10^{-27}	23.8	13.5	23.9
26	96.1	5.99×10^{-8}	8.25×10^{-27}	26.1	9.5	20.4
26-TF	112.0	7.78×10^{-8}	1.17×10^{-26}	23.2	11.2	21.7
27	101.3	7.34×10^{-8}	9.82×10^{-27}	24.1	5.4	20.2
27-TF	119.4	8.33×10^{-8}	1.88×10^{-26}	23.3	15.2	23.4
Monomeric aldehyde substituted 28-30						
28	16.1	3.75×10^{-8}	2.48×10^{-27}	13.8	4.5	19.0
28-TF	17.8	4.15×10^{-8}	2.74×10^{-27}	6.8	9.2	20.7
29	18.9	4.41×10^{-8}	2.91×10^{-27}	11.5	7.5	18.9
29-TF	20.3	4.74×10^{-8}	3.13×10^{-27}	5.9	7.4	19.4
30	63.8	1.49×10^{-7}	9.82×10^{-27}	9.7	10.4	20.1
30-TF	46.9	1.09×10^{-7}	7.22×10^{-27}	4.2	13.1	21.6

5.4.   Conclusion for the chapter

The nonlinear optical study ball-type, symmetric and asymmetric MPcs complexes alone, when combined with nanomaterials or formulated into polymer thin films was investigated using the Z-scan technique at 532 nm.

The nonlinear optical response showed reverse saturable absorption behavior. The origin of RSA behavior was investigated using the Sheik Bahae Z-scan analysis equations. The five-energy level model was employed to map out the population dynamics resulting from TPA, excited singlet or excited triplet states. The NLO analysis result showed that the observed RSA behavior originates mainly from the excited triplet manifold.

The enhancement in NLO response was observed for complexes having Ga and In central metals compared to corresponding zinc analogues. The ball-type MPcs predominantly showed better optical limiting performance than the corresponding monomeric analogues

Formulation of the complexes with nanomaterials or polymer thin films results in improved NLO response compared to the complexes alone.

Chapter six: Conclusion and future work

Conclusion

The synthesis of ball-type, asymmetric and symmetric phthalocyanine complexes with zinc, gallium and indium central metals was successfully accomplished and the synthesized complexes were characterized with various analytical and spectroscopic techniques. The origin of optical absorption from the complexes was investigated using time dependent density functional theory.

A decreased in Φ_F and τ_F with accompanied increase in Φ_T was observed as the atomic weight of the central metal increases and this attributed to heavy atom effect. The ball-type complexes showed enhanced Φ_T compared with the corresponding monomeric analogues.

The formation of amide bond through the covalent linkage of selected complexes to CdTe, CdTeSe, CdTeSe/ZnO, GQDs, AuNPs and AgNPs as well as surface assembly of the complexes onto metallic AuNPs and AgNPs was confirmed using FTIR and XPS analysis. The changes in photophysical parameters of the employed semiconductor quantum dots and carbon based GQDs was found to occur through Förster resonance energy transfer process. A significant improvement in the photophysical properties was observed when the complexes was linked to nanoparticles.

The optical limiting performance was investigated with either the complexes alone, when linked to nanoparticles or when embedded into polystyrene thin films. The effect of central metal in nonlinear optical performance was found in order of Zn < Ga < In corresponding to Φ_T enhancement. The ball-type Pc complexes showed high absorption coefficient (β_{eff}) and lower energy density of saturation (F_{sat}) compared to corresponding monomeric derivatives, hence exhibit better optical limiting behavior. The asymmetric complexes **34**, **35** and **36** display better optical limiting properties compared to the symmetric complexes **22**, **23** and **24**. A significant

improvement in optical limiting behavior was found when the complexes were linked to nanoparticles or formulated in polystyrene thin films.

The dominant mechanism resulting in NLO response was found to be strong absorption from the triplet excited state manifold.

Future prospect

It is pertinent that more researches are carried out with the aim to answering the following questions that emerge from the findings in this work.

1. At what wavelength range of light can NLO material considered sensitivity?
2. What types of laser beams can the material limit, femtosecond, picosecond, nanosecond, or all?
3. Could incorporation of two different central metal in ball-type phthalocyanine give better optical limiting response?
4. Could the solution of phthalocyanine-nanoconjugate fabricated into thin films offer greater advantage in nonlinear response?

References

1. G. P. Agrawal, Nonlinear fiber optics, 4th edition, Academic press, 2007, pp.62-100

2. N Bloembergen, 'Nonlinear optics of polymers: fundamentals and applications', *JNOPM.,* 5 (1996) 1.

3. T. Yohannes, O. Inganäs, *Synth met.*, 107 (1999) 97.

4. K. D. Belfield, K. J. Schafer, *Chem. Mat.*, 14 (2002) 3656.

5. A.B.P. Lever, In: Advances in Inorganic Chemistry and Radiochemistry, H.J. Emeleus, A.G. Sharpe (Eds) Academic Press, New York, vol. 7 (1965) 28

6. N.B. McKeown, In: Phthalocyanine Materials-Synthesis, Structure and Function, Cambridge University Press, Uk, 1998, pp. 126-135

7. K. Kadish, K. M. Smith, R. Guilard (eds), In: The Porphyrin Handbook, 1st edition, Academic Press, San Diego CA, USA, (2003).

8. F. H. Moser, A. L. Thomas, in: The Phthalocyanines, Properties, A. L. Thomas (Ed), CRC, Boca Raton, Florida, 1983, vol. 1, ch. 11, pp. 79-104.

9. J.J. Cid, J.H. Yum, S.R. Jang, M.K. Nazeeruddin, E. Martinez-Ferrero, E. Palomares, J. Ko, M. Graetzel, T. Torres, *Angew. Chem. Int*., *Ed*. 46 (2007) 8358.

10. K. Sakamoto, E. Ohno-Okumura, *Materials*, 2(2009) 1127

11. K.C. Honeychurch, L. Gilbert, J.P. Hart, *Anal. Bioanal. Chem*., 396 (2010) 3103

12. R. Bonnett, in Chemical Aspects of Photodynamic Therapy, Gordon and Breach Science, Amsterdam, 2000.

13. G. de la Torre, P. Vázquez, F. Agulló-López, T. Torres, *Chem. Rev*., 104 (2004) 3723.

14. S. Vilakazi, T. Nyokong, *Polyhedron*, 19 (2000) 229

References

15. O. Adegoke, T. Nyokong, *J. Photochem. Photobiol. A: Chem*., 265 (2013) 58

16. K. Morishige, S. Tomoyasu, G. Iwani, *Langmuir* 3 (1997) 5184

17. H. Eichhorn, *J. Porphy. Phthalocya*., 4 (2000) 88

18. A. Y. Tolbin, A. V. Ivanov, L. G. Tomilova and N. S. Zefirov, *Mendeleev Commun.*, 12 (2002) 96

19. A. Y. Tolbin, A. V. Ivanov, L. G. Tomilova and N. S. Zefirov, *J. Porphy. Phthalocya*., 7 (2003) 162

20. M. A. Özdağ, T. Ceyhan, H. Ünver, A. Elmali, Ö. Bekaroğlu, *Opt. Comm*., 283 (2010) 330

21. A. Wang, L. Long, C. Zhang, *Tetrahedron*, 68 (2012) 2433

22. M.J.F. Calvete, D. Dini, S.R. Flom, M. Hanack, R.G.S. Pong, J.S. Shirk, Eur. *J. Org. Chem*., (2005) 3499.

23. R.W. Boyd Nonlinear Optics; 3rd ed. Academic Press: San Diego, CA, 1992

24. M.S. Rodriguez-Morgade, G. de la Torre, T. Torres, in The Porphyrin Handbook, K.M. Kadish, K.M. Smith, R. Guilard (Eds.), Academic Press, Elsevier Science, vol.15 (2003) pp. 125-160

25. Y. Liu, Y. Xu, D. Zhu, T. Wada, H. Sasabe, L. Liu, W. Wang, *Thin Solid Films*, 244 (1994) 943.

26. Y. Liu, D. Zhu, T. Wada, A. Yamada, H. Sasabe, *J. Hetero. Chem*., 31 (1994) 1017.

27. C.F. van Nostrum, R.J.M. Nolte, *Chem. Comm*., (1996) 2385

28. M. Ando, Y. Mori, *Chem. Abstr*., 113 [1990] 255558c

29. N. Kobayashi, R. Kondo, S.I. Nakajima, T. Osa, *J. Am. Chem. Soc*., 112 (1990) 9640.

30. W. M. Sharman, J. E. Van lier, *J. Porphy. Phthalocya*., 9 (2005) 651.

31. W.A. Nevin, W. Liu, S. Greenberg, M.R. Hempstead, S.M. Marcuccio, M. Melnik, C.C. Leznoff, A.B.P. Lever. *Inorg. Chem*., 26 (1987) 891.

32. C.C. Leznoff, A.B.P. Lever, (Eds.) Phthalocyanines. Properties and Applications; VCH Publishers (LSK) Ltd.: Cambridge, U.K., 1989, Vol. 1, pp 403.

33. M. Hanack, H. Heckman, R. Polley, In: Methods in Organic Chemistry (HoubenWeyl); Schuman, E., Ed.; Georg Thieme Verlag: Stuttgart, 1997; Vol. E 9d, 4th edition, pp 717-833.

34. K.A. Vishnumurthy, M.S. Sunitha, A. Vasudeva Adhikari, *Eur. Polym. J.*, 48 (2012) 1575.

35. G. de la Torre, M. Nicolau, T. Torres, In Supramolecular Photosensitive and Electroactive Materials; H.S. Nalwa, (Ed.), Academic Press: San Diego, CA, 2001.

36. K.M. Kadish, K.M. Smith, R. Guilard, (Eds.), Porphyrin handbook: Phthalocyanines synthesis; Academic Press: Boston, MA, Vols. 15, Ch. 97 2003; pp. 125-136.

37. T. Wei, T. Huang, *Appl. Phys. Lett.*, 72(1998) 2505

38. S.M. O'Flaherty, S.V. Hold, M.J. Cook, T. Torres, Y. Chen, M. Hanack, W.J. Blau, *Adv. Mater.*, 15 (2003) 19.

39. R.S.S. Kumar, S.V. Rao, L. Giribabu, D.N. Rao, *Chem. Phys. Lett.*, 447 (2007) 274

40. M. Yüksek, A. Elmali, M. Durmuş, H.G. Yaglioglu, H. Ünver, T. Nyokong, *J. Opt.*, 12(2010) 1-6

41. E.M. García-Frutos, S.M. O'Flaherty, S.V. Hold, G. de la Torre, S. Maier, P. Vázquez, W. Blau, T. Torres, *Synth. Met.*, 137 (2003) 1479.

42. S.J. Mathews, S.C. Kumar, L. Giribabu, S.V. Rao, *Opt. Commun.*, 280 (2007), 206.

43. S.V. Rao, P.T. Anusha, T.S. Prashant, D. Swain, S.P. Tewari, *Mater. Sci. Appl.*, 2(2011) 299.

44. M.C. Larciprete, R. Ostuni, A. Belardini, M. Alonzo, G. Leahu, E. Fazio, C. Sibilia, M. Bertolotti, *Photon. Nanostr. Fundamen. Appl.*, 5 (2007) 73.

45. H. Liu, C. Chen, F. Xi, P. Wang, S. Zhang, P. Wu, C. Ye, J. Nonli. *Opt. Phys. Mater.*,10 (2001) 423

46. Y. Wang, L. V. Mingzhe, J. Guo, T. Wang, J. Shao, D. Wang, Y. Yang, *Sci China Chem.*, 12 (2015) 1782

47. S.V. Rao, P.T. Anusha, L. Giribabu, S.P. Tewari, Pramana J. Phys., 75 (2010) 1017.

48. Y. Chen, D. Wang, Y. Li, Y. Nie, *Opt. Mater.*, 24 (2003) 581

49. J.S. Shirk, R.G.S. Pong, S.R. Flom, H. Heckmann, M. Hanack, *J. Phys. Chem. A*,104 (2000) 1438

50. Y. Chen, L. Gao, M. Feng, L. Gu, N. He, J. Wang, Y. Araki, W.J. Blau, O. Ito, *Mini-Rev. Org. Chem.*, 6 (2009) 55

51. D. O. Oluwole, A. V. Yagodin, N. C. Mkhize, E. K. Sekhosana, A. G. Martynov, Y. G Gorbunova, A. Y. Tsivadze, T. Nyokong, *Chem. Eur. J.*, 23(2017) 2820.

52. J. Britton, C. Litwinski, M. Durmuş, V. Chauke, T. Nyokong, *J. Porphyr. Phthalocya.*, 15 (2011) 1239.

53. Y. Liu, S. M. O'Flaherty, Y. Chen, Y. Araki, J. Bai, J. Doyle, W. J. Blau, O. Ito, *Dyes and pigments*, 75(2007) 88.

54. K.E. Sekhosana, E. Nyokong, *Inorg. Chem. Acta*, 450(2016), 87-91.

55. L. Liu, C. Tai, A. T. Hu, T. Wei, *J. Porphyr. Phythalocya*, 8 (2004)984.

56. K.E. Sekhosana, E. Amuhaya, J. Mack, T. Nyokong, *J. Mater. Chem. C*, (2014), 5431.

57. Y. Chen, M. Hanack, Y. Araki, O. Ito, *Chem. Soc. Rev.*, 34 (2005) 517

58. E.M. García-Frutos, S.M. O'Flaherty, E.M. Maya, G. de la Torre,W. Blau, P. Vázqueza, T. Torres, *J. Mater. Chem.*, 13 (2003) 749.

59. J.W. Perry, K. Mansour, S.R. Marder, D. Alvarez Jr., K.J. Perry I. Choong, *J. Opt. Lett*., 19 (1994) 625-627.

60. J.S. Shirk, R.G.S. Pong, F.J. Bartoli, A.W. Snow, *Appl. Phys. Lett*., 63 (1993) 1880

61. I.V. Khudyakov, Y.A. Serebrennikov, N. Turro. *Chem. Rev*., 93 (1993) 537

62. M. S. Ağirtaş, U. Yildiko, *J. Coord. Chem*., 61 (2008) 2781

63. A. Aktaş, M. Durmuş, L. Değrmencioğlu, *Polyhedron*, 48 (2012) 80

64. B. S. Singh, H. R. Lobo, J. K. Podagatlapalli, S. V. Rao, G. S. Shankarling, *Opt. Mat*., 35 (2013) 962.

65. M. Gouterman, Optical Spectra and Electronic Structure of Porphyrins and Related Rings. In: The Porphyrins; Dolphin, D., Ed.; Academic Press: New York, NY, USA, 1978; Volume III, pp. 1–165

66. A.M. Schaffer, M. Gouterman, E.R. Davidson, *Theoret. Chim. Acta*, 30 (1973) 9

67. O. Bekaroğlu, S*truct. Bonding*, 135 (2010) 105

68. Z. Odabaş, F. Dumludağ, A.R. Ozkaya, S. Yamauchi, N. Kobayashi, O. Bekaroğlu, *Dalton Trans*., 39 (2010) 8143.

69. Z. Odabaş, I. Koc, A. Altindal, A.R. Ozkaya, B. Salih, O. O. Bekaroğlu, *Synth. Met*., 160 (2010) 967.

70. J. Kleinwächter and M. Hanack, *J. Am. Chem. Soc*., 119(1997), 10684

71. G. S. S. S. Saini, S.D. Dogra, S. Singh, S. Kaur, S.K. Tripathi, *Vibrational Spec*., 56(2011) 61

72. K.A. Nguyen, R. Pachter, *J. Chem. Phys*., 114 (2001) 10757

73. S. A. Fischer, C. J.Cramer, N. Govind, *J. Phys. Chem. Lett*., 7(2016) 1387

74. R.J. Magyar, S. Tretiak, *J. Chem. Theory Comput*., 3 (2007) 976.

75. A. Gilbert and J. Baggott, Essentials of Molecular Photochemistry, Blackwell Scientific, Oxford, 1991.

References

76. P. Kubat, J. Mosinger, *J. Photochem. Photobiol. A*, 96 (1996) 93

77. R.L. Sutherland. Handbook of Nonlinear Optics, 2nd Edn, Marcel Dekker, New York, (2003).

78. J.R. Lakowicz, In: Principles of Fluorescence Spectroscopy, 3rd ed., Kluwer Academic/Plenum Publishers, New York, 2006, pp. 63-95

79. S. Dhami, D. Phillips, *J. Photochem. Photobiol*. *A*, 100 (1996) 77.

80. T. Minami, M. Kawahigashi, Y. Sakai, K. Shimamoto, S. Hirayama, *J. Lumin*., 35(1986) 247.

81. G. Valduga, E. Reddi, G. Jori, R. Cubeddu, P. Taroni, G. Valentini, *J. Photochem. Photobiol. B: Biol*., 16 (1992) 331.

82. T. Nelson, S. Fernandez-Alberti, A. E. Roitberg, S. Tretiak, *J. Phys. Chem. Lett*., 8 (2017) 3020

83. J.S. Hsiao, B.P. Krueger, R.W. Wagner, T.E. Johnson, J.K. Delaney, D.C. Mauzerall, G.R. Fleming, J.S. Lindsey, D.F. Bocian, R.J. Donohoe, *J. Am. Chem. Soc*., 118 (1996) 11181

84. T.H. Förster, *Disc. Far*. *Soc*., 27 (1959) 7

85. H. Du, R.-C.A. Fuh, J. Li, L.A. Cockan, J.S. Lindsey, *Photochem. Photobiol*., 68 (1998) 141

86. J.M. Dixon, M. Taniguchi, J.S. Lindsey, *Photochem. Photobiol*., 81 (2005) 212-213

87. G.L. Hornyak, J. Dutta, H.F. Tibbals, A. K. Rao, in Introduction to Nanoscience, CRC Press, Taylor and Francis Group, Boca Raton, (2008).

88. O. Salata, *J. Nanobiotech*., 2 (2004) 1

89. A.A. Said, M. Sheik-Bahae, D.J. Hagan, T.H. Wei, J. Wang, E.W. Van Stryland, *J. Opt. Soc. Am*. *B*, 9 (1992) 405

90. S. V. Gaponenko, U. Woggon, M. Saleh, W. Langbein, A. Uhrig, M. Müller, and C. Klingshirn, *Opt. Soc. Am*., 10 (1993) 1947

References

91. W. Xie, *Solid state comm.*, 151(2011) 545

92. M.Y. Han,W. Huang, C.H. Chew, L.M. Gan, X.J. Zhang,W. Ji, *J. Phys. Chem. B*, 102 (1998) 1884

93. J.T. Seo, S. Ma, Q. Yang, L. Creekmore, R. Battle, H. Brown, A. Jackson, T. Skyles, B. Tabibi, W. Yu, S. Jung, M. Namkung, *J. Phys.* (Conf. Series) 38 (2006) 91.

94. C.-P. Huang, Y.-K. Li, T.-M. Chen, *Biosens. Bioelectron.*, 22 (2007), 1835

95. S.-H. Choi, H. Song, I.K. Park, J.-Ho Yum, S.-S. Kim, S. Lee, Y.-E. Sung, *J. Photochem. Photobiol. A: Chem.*, 179 (2006), 135

96. Y. Zheng, S. Gao, J. Ying, *Adv. Mater.*, 19 (2007) 376

97. C.-P. Huang, S.-W. Liu, T.-M. Chen, Y.-K. Li, *Sens. Actua.*, 130 (2008), 338

98. I. B. Bwatanglang, F. Mohammad, N. A. Yusof, J. Abdullah, M. Z. Hussein, N. B.Alitheen, N. Abu, *Int. J. Nanomedicine*, 11 (2016) 413.

99. S. Hohng, T. Ha, *Chem. Phys. Chem.*, 6 (2005) 956

100. D. Gerion, W.J. Parak, S.C. Williams, D. Zanchet, C.M. Micheel, A.P. Alivisatos, *J. Am. Chem. Soc.*, 124 (2002) 7070.

101. C. S. Anna, S. X. Chen, C. Burda, *J. Am. Chem. Soc.*, 125 (2003) 15736

102. N. He, Y. Chen, J. Bai, J. Wang, W. J. Blau, J. Zhu, *J. Phys. Chem. C.*, 113 (2009) 13029

103. K. Sathiyamoorthy, C. Vijayan, Shikha Varma, *Langmuir*, 24 (2008) 7485

104. E. Jiang, C. He, X. Xiao, Y. Dong, Y. Gao, Z. Chen, Y. Wu, W. Song, *Opt. Mat.*, 64 (2017) 193

105. Z. Wang, C. He, W. Song, Y. Gao, Z. Chen,Y. Dong, C. Zhao, Z. Li, Y. Wu. *RSC Adv.*, 5 (2015) 94144

106. K. Sanusi, S. Khene, T. Nyokong, *Opt. Mat.*, 37(2014) 572

107. K. Sanusi, J. M. Stone, T. Nyokong, *New J. Chem.*, 39(2015) 1665

108. K. Sanusi, T. Nyokong, *Opt. Mat.*, 38(2014) 17

References

109. O. M. Bankole, O. J. Achadu, T. Nyokong, *J. Flores*., 27 (2017) 755

110. O. M. Bankole, T. Nyokong, *New J. Chem*., 40(2016) 10016

111. O. M. Bankole, O. Osifeko, T. Nyokong, *J. Photochem. Photobiol. A*, 329(2016) 155

112. Y. Li, J. Zhu, Y. Chen, J. Zhang, J. Wang, B. Zhang, Y. He, W. J. Blau, *Nanotech*., 22 (2011) 205704

113. H. Sun, L. Wu, W. Wei, X. Qu, *Mater. Today* 11 (2013) 433

114. L. Li, G. Wu, G. Yang, J. Peng, J. Zhao, J.J. Zhu, *Nanoscale*, 5 (2013) 4015

115. L. Lin, M. Rong. F. Luo, D. Chen, Y. Wang, X. Chen, *Trends Anal. Chem*., 54 (2014) 83

116. J. Yao, Y. Sun, M. Yang, Y. Duan, *J. Mater. Chem*., 22 (2012) 14313

117. C. Chung, Y.-K. Kim, D. Shin, S.-R. Ryoo, B.H. Hong, D.H. Min, *Accounts Chem. Res*., 46 (2013) 2211

118. V. Georgakilas, M. Otyepka, A.B. Bourlinos, V. Chandra, N. Kim, K.C. Kemp, P. Hobza, R. Zboril, K.S. Kim, *Chem. Rev*., 112 (2012) 6156.

119. J.H. Shen, Y. Zhu, X.Yang, C.Li, *Chem. Commun*., 48 (2012)3686.

120. K. Tanabe, *Mat. Lett*., 61 (2007) 4573

121. J. H. Fendler (Ed.) Nanoparticles and Nanostructured Films: Preparation, Characterization and Applications; Wiley-VCH: New York, 1998, pp. 429-461.

122. C. M. Lieber, *Solid State Commun*., 107 (1998) 607.

123. Y. Xiong, Q. Zhang, X. Sun, W. Tan, X. Xin, W. Ji, *Appl. Phys. A*, 70 (2000) 85

124. Y.P. Sun, J.E. Riggs, H.W. Rollins, R. Guduru, *J. Phys. Chem. B*, 103 (1999) 77

125. R. Philip, G.R. Kumar, N. Sandhyarsni, T. Pradeep, *Phys. Rev. B*, 62 (19) (2000) 13160

References

126. M. Anija, J. Thomas, N. Singh, A.S. Nair, R.T. Tom, T. Pradeep, R. Philip, *Chem. Phys. Lett*., 380 (2003) 223

127. H. Zhang, David E. Zelmon, L.G. Deng, H.K. Liu, K.T. Boon, K. Teo, *J. Am. Chem. Soc*., 123 (2001) 11300

128. R. West, Y. Wang, T. Goodson, *J. Phys. Chem. B*, 107 (2003) 3419

129. S.L. Qu, C.M. Du, Y.L. Song, Y.X. Wang, Y.C. Gao, S.T. Liu, Y.L. Li, D.B. Zhu, *Chem. Phys. Lett*., 356 (2002) 403

130. Y.C. Gao, Y.X. Wang, Y.L. Song, Y.L. Li, S.L. Qu, H.B. Liu, *Opt. Commun*., 223 (2003) 103

131. L. Francois, M. Mostafavi, J. Belloni, J.-F. Delouis, J. Delaire, P. Feneyrou, *J. Phys. Chem. B*, 104 (2000) 6133

132. M. Chen, L. Yu, L. R. Dalton, Y. Shi, W. H. Steier, *Macromolecules*, 24 (1991), 5421

133. T. Verbiest, S. Houbrechts, M. Kauranen, K. Clays, A. Persoons, *J. Mat. Chem*., 7 (1997), 2175.

134. U. Gubler, C. Bosshard, In: *Polymers for Photonics Applications I*, K. Lee (Ed.), Springer Berlin Heidelberg, 2002, 123-191

135. S. A Jenekhe, W. Chen, S. Lo, S. R. Flom, *Appl. Phys. Let.,* 57 (1990) 126

136. J. L. Bredas, C. Adant, P. Tackx, A. Persoons, and B. M. Pierce, *Chem. Rev.*, 94 (1994) 243

137. R.W. Hellwarth, *Prog. Quant. Electr.,* 5 (1979) 1.

138. M.C. Spaeth, W.R. Sooy, *J. Chem. Phys*., 48 (1968) 2315

139. M. Sheik-Bahae, A.A. Said, T. –H. Wei, D.J. Hagan, E.W. Van Stryland*, IEEE, J. Quant. Electr.*, 26 (1990) 760.

140. M. Sheik-Bahae, A.A. Said, E.W. Van Stryland*, Opt. Lett.,* 14 (1989) 955

References

141. E.W. Van Stryland, M. Sheik-Bahae, In: Characterization techniques and tabulations for organic nonlinear materials, M.G. Kuzyk and C.W. Dirk *(Eds.), Marcel Dekker, Inc.,* (1998) 655-692.

142. M.J. Frisch, G.W. Trucks, H. B. Schlegel, G. E. Scuseria, M. A. Robb, G. Cheeseman, J. R.; Scalmani, V. Barone, B. Mennucci, H. Petersson, G. A.; Nakatsuji, M. Caricato, X. Li, H.P. Hratchian, A.F. Izmaylov, J. Bloino, G. Zheng, J.L. Sonnenberg, K. Hada, M.; Ehara, M.; Toyota, R. Fukuda, J. Hasegawa, M. Ishida, T. Nakajima, Y. Honda, O. Kitao, H. Nakai, T. Vreven, J.E. Montgomery, J. A., Jr.; Peralta, F. Ogliaro, M. Bearpark, J.J. Heyd, E.. Brothers, K.N. Kudin, R. Staroverov, V. N.; Kobayashi, K. Normand, J.; Raghavachari, A. Rendell, J.C. Burant, S.S. Iyengar, J. Tomasi, M. Cossi, N. Rega, J.M. Millam, M. Klene, J.E. Knox, J.B. Cross, V. Bakken, C. Adamo, J. Jaramillo, R. Gomperts, R.E. Stratmann, O. Yazyev, A.J. Austin, R. Cammi, C. Pomelli, J.W. Ochterski, R.L. Martin, K. Morokuma, V.G. Zakrzewski, G.A. Voth, P. Salvador, S. Dannenberg, J. J.; Dapprich, A.D. Daniels, Ö. Farkas, J.B. Foresman, J.V. Ortiz, J. Cioslowski, D.J. Fox, Gaussian 09, Revision E. 01; Gaussian, 2009

143. P. Sen, G.Y. Atmaca, A. Erdogmuş, N. Dege, H. Genç, Y.S.Z. Atalay Yildiz, *J. Fluoresc*. 25 (2015) 1225

144. David O. Oluwole, Earl Prinsloo, Tebello Nyokong, Polyhedron 119 (2016) 434

145. N. Gaponik, D. V. Talapin, A. L. Rogach, K. Hoppe, E. V. Shevchenko, A. Kornowski, A. Eychmüller, H. Weller, *J. Phys. Chem. B,* 106 (2002) 7177

146. D. O. Oluwole, C. M. Tilbury, E. Prinsloo, J. Limson, T. Nyokong, *Polyhedron*, 106 (2016) 92

147. X. Liu, L. Hua-Ji, F. Cheng, Y. Chen, *Nanoscale* 6 (2014) 7453

148. H. Hiramatsu, F. Osterloh, *Chem. Mat*., 16 (2004) 2509

References

149. M. J. Stillman, T. Nyokong T. In: Leznoff CC, Lever ABP, editors. Phthalocyanines. Principles and properties, vol. 1; 2003. New York

150. Gurel, E., M. Pişkin, S. Altun, Z. Odabaş, M. Durmuş, *Dalton Trans*. 44 (2015), 6202

151. Z. Odabaş, F. Dumludaĝ, A. R. Özkaya, S. Yamauchi, N. Kobayashi, Ö. Bekaroğlu, *Dalton Trans*. 39 (2010), 6202

152. M. Canlıca, A. Altındal, T. Nyokong, *J. Porphyr. Phthalocyanines*. 16 (2012) 826.

153. A. Y. Tolbin, A. V. Dzuban, E. V. Shulishov, L. G. Tomilovaa, N. S. Zefirov, *New J. Chem*., 40 (2016) 8262

154. L. Alagna, A. Capobianchi, M. P. Casaletto, G. Mattogno, A. M. Paoletti, G. Pennesi and G. Rossi, *J. Mater. Chem*., 11 (2001) 1928.

155. E. Glimsdal, M. Carlsson, T. Kindahl, M. Lindgren, C. Lopes and B. Eliasson, *J. Phys. Chem. A*, 114 (2010) 3431.

156. T. Nyokong, Z. Gasyna and M. J. Stillman, *Inorg. Chem*., 26 (1987)1087.

157. J. Mack, N. Kobayashi and M. J. Stillman, *J. Inorg. Biochem*., 102 (2008) 472.

158. J. Mack, J. Stone and T. Nyokong, *J. Porphyr. Phthalocyanines*, 18 (2014) 630

159. L. Guo, D. Elis, B. M. Hoffman, Y. Ishikawa, porphyrazines, *Inorg. Chem*. 35(1996) 5304

160. Nyokong T. In Structure and Bonding: Functional Phthalocyanine Molecular Materials, Vol 135, Jiang J and Mingos DMP. (Eds.) Springer, 2010; pp. 45–87.

161. J. Mack and M. J. Stillman, , *Coord. Chem. Rev*. 219-221 (2001) 993-1032.

162. J. Michl, Tetrahendron, 40 (1984) 3845

References

163. J. Mack and N. Kobayashi, *Chem. Rev*. 111 (2011) 281

164. M. Gouterman, Optical spectra and electronic structure of porphyrins and related rings, in: D. Dolphin (Ed.), The Porphyrins, III, Academic Press, New York, 1978, 1–165 (Part A).

165. W. Chidawanyika, T. Nyokong, *Carbon* 48 (2010) 2831

166. S. Thomas, S. K. Nair, E. A. Jamal, S. H. Al-Harthi, M. R. Varma and M. R. Anantharaman, *Nanotechnology*, 19 (2008) 075710

167. Y. Fleger and M. Rosenbluh, *Res. Lett. Opt*., (2009) 4759415

168. E. Villarreal, G. G. Li, Q. Zhang, X. Fu and H. Wang, *Nano Lett*., 17 (2017) 4443

169. B. C. Han, C. R. Miranda, and G. Ceder, *Phys. Rev. B*, 77 (2008) 075410

170. A. W. Snow, J. R. Griffith, N. P. Marullo, *Macromolecules* 17 (1984)1614

171. U. T. Thuy, P. S. Toan, T. T. Chi, D. D. Khang, N. Q. Liem, *Adv. Nat. Sci: Nanosci. Nanotech*. 045009

172. C. Malarkodi, S. Rajeshkumar, M. Vanaja, K. Paulkumar, G. Gnanajobitha G. Annadurai, *J. Nanostruct. Chem*., 3 (2013) 1

173. J.H. Chang, K.H. Kang, J. Choi, Y.K. Jeong, Superlatt. Microstruct. 44 (2008), 442.

174. A. C. S. Samia, S. Dayal, S. Burda, *Photochem. Photobiol*., 82 (2006) 617

175. C. G. Claessens, M. V. Mart´ınez-D´ıaz, T. Torres, Supramolecular Phthalocyanine-Based Systems. In Supramolecular Chemistry; John Wiley & Sons, Ltd: 2012

176. L. Li, J. F. Zhao, N. Won, H. Jin, S. Kim, J. Y. Chen, *Nanoscale Res Lett*., 7 (2012) 386.

177. S. Avnesh, M. D. Thakor, S. Sanjiv, M. D. Gambhir. *CA. J. Cancer Clin*., 63 (2013) 395

References

178. H. J. Kim, I. Bae, S. Cho, J. Boo, B. Lee, J. Heo, I. Chung, B. Hong *Nanoscale Res. Let*., 7(2012) 1

179. S. Link, C. Burda, M. A. El-Sayed, *J. Chem. Phys*., 111 (1999) 1256

180. Vukovic V, Corni S, Mennucci B. *J Phys Chem C*. 113 (2009) 121

181. N. Chandrasekharan, P. V. Kamat, *J. Phys. Chem. B* 104 (2000) 11103

182. S. J. Xiao, M. Textor, N. D. Spencer, J. Mat. Sci. Mat. Medic., 8 (1997) 867

183. H. Zhang, S. D. Evans, J. R. Henderson, R. E. Miles, T. Shen, *J. Phys. Chem. B* 107 (2003) 6087

184. D. Modal, S. Bera, *Adv. Nat. Sci: Nanosci. Nanotechnol*. 5 (2014) 033002

185. J. A. Kloepfer, S. E. Bradforth, J. L. Nadeau, *J. Phys. Chem. B* 109 (2005) 9996.

186. S. Fery-Forgues and D. Lavabre, *J. Chem. Educ*., 76 (1999) 1260

187. N. Kobayashi, H. Ogata, N. Nonaka, E. A. Luk'yanets, Chem. Eur. J. 9 (2003) 5123

188. Z. Petrasek and D. Phillips, *Photochem. Photobiol. Sci*., 2 (2003) 236

189. T. H. Tran-Thi, C. Desforge, C. Thies, J. Phys. Chem., 93 (1989) 1226

190. C. Byeon, M. Mckerns, W. Sun, T. M. Nordlund, C. M. Lawson, Appl. Phys. Lett., 84 (2004) 5174

191. R. L. Brookfield, H. Ellul, A. Harriman, G. Porter, *J. Chem. SOC., Faraday Trans. 2*, 82 (1986) 219

192. H. Abramczyk, Introduction to laser spectroscopy. second ed. New York: Elsevier; 2005.

193. F. X. Sauvage, *Laser Chem* 8(988)1.

194. X.-F. Zang, X. Li, L. Niu, L. Sun, L. Liu, J. Fluoresc. 19 (2009) 947

195. S. Z. Topal, I. Ümit, U. Kumru, D. Atilla, A. G. Gürek, C. Hirel, M. Durmuş, J. Tommasino, D. Luneau, S. Berber, F. Dumoulin, V. Ahsen, *Dalton Trans*., 43 (2014) 6897

References

196. C. Dong, H. Qian, N. Fang, J. Ren, *J. Phys. Chem. B*. 110 (2006) 11069

197. C. Berney, G. Danuser, *Biophys. Jour*., 84 (2003) 3992

198. A.M. Dennis, W.J. Rhee, D. Sotto, S.N. Dublin, G. Bao, *ACS Nano*., 6 (2012) 2917

199. E.Z. Chong, D.R. Matthews, H.D. Summers, K.L. Njoh, R.J. Errington, P.J. Smith, *J. Biomed. Biotechnol*. 2007 (2007) 1.

200. T. Nyokong, E. Antunes, In the handbook of porphyrin science: Kadish KM, Smith KM, Guilard R (Eds.). Academic Press New York, 7 (2010) 247.

201. M. Frenette, M. Hatamimoslehabadi, S. Bellinger-Buckley, S. Laoui, J. La, S. Bag, S. Mallidi, T. Hasan, B. Bouma, C. Yelleswarapu, J. Rochford, *J. Am. Chem. Soc.* 136 (2014) 15853

202. M. Drobizhev, N. S. Makarov, *J. Chem. Phys*., 124 (2006), 224701

203. M. Charlot, N. Izard, O. Mongin, D. Riehl, M. Blanchard- Desce*, Chem. Phys. Lett*., 417 (2006), 297

204. R. R. Tykwinski, U. Gubler, R. E. Martin, F. Diederich, C. Bosshard, P. Günter, *J. Phys. Chem*., B, 102 (1998), 4451

205. T.-H. Wei, T.-H. Huang, T.-C. Wen, *Chem. Phys. Lett*. 314 (1999) 403

206. S.V. Rao, D.N. Rao, J.A. Akkara, B.S. DeCristofano, D.V.G.L.N. Rao, *Chem. Phys. Lett*. 297 (1998) 491

207. K. Tanigaki, T.W. Ebbesen, S. Kuroshima, *Chem. Phys. Lett*. 185 (1991) 189

208. F. Li, P. Lu, H. Long, G. Yang, Y. Li, Q. Zheng, *Opt. Exp*., 16 (2008) 14571

209. S. M. O'Flaherty, J. J. Doyle, W. J. Blau, J. *Phys. Chem. B*, 108 (2004) 17313.

210. L. Dai, Intelligent Macromolecules for Smart Devices: From Material Synthesis to Device Applications, Springer-Verlag, Berlin, 2004.

211. G. L. Wood, M. J. Miller, A. G. Mott, *Opt. Lett*., 20 (1995) 973

212. L. De Boni, L. Gaffo, L. Misoguti and C. R. Mendonca*, Chem. Phys. Lett*., 419 (2006) 417

References

213. K. Sanusi, E. Antunes and T. Nyokong, Dalton Trans., 43 (2014) 999

214. C. Zhang, Y. Wang, J. Zhao, Q. Gary, G.M. Lawson, *Opt. Spec. Am.*, 2017 paper NW4A.23

215. S.V. Rao, D.N. Rao, J.A. Akkara, B.S. DeCristofano, D.V.G.L.N. Rao, *Chem. Phys. Lett.*, 297 (1998) 49.

216. Y. Chen, L.R. Subramanian, M. Fujitsuka, O. Ito, S. O'Flaherty, W.J. Blau, T. Schneider, D. Dini, M. Hanack, *Chem. Eur. J.*, 8 (18) (2002) 4248.

217. Z. Guan, L. Polavarapu, Q. Xu, *Langmuir*, 26 (2010) 18020

218. V. D. Kulakovskii, G. Bacher, R. Weigand, T. Kümmell, A. Forchel, *phys. Rev. let.*, 82 (1999) 1780

219. J. Kobak1, T. Smoleński1, M. Goryca1, J. Rousset, W. Pacuski, A. Bogucki, K. Oreszczuk, P. Kossacki, M. Nawrocki, A. Golnik, J. Płachta, P. Wojnar, C. Kruse, D. Hommel, M. Potemski, T. Kazimierczuk, *J. Phys. Condens. Matt.*,, 28 (2016) 265302

220. L. Besombes, K. Kheng, L. Marsal, H. Mariette, *Phys. Rev. B*, 65 (2002) 121314.

221. P. Fischer, F. Hache, *Chirality*, 17 (2005) 1

222. G. Yang, Z. Su, C. Qin, *J. Phys. Chem. A*, 110 (2006) 4817

223. M. G. Kuzyk, K. D. Singer, G. I. Stegeman, *Adv. Opt. Phot.*, 5 (2013) 4

224. S.J. Mathews, S. Chaitanya Kumar, L. Giribabu, S. V. Rao, *Mat. Lett.*, 61 (2007) 4426
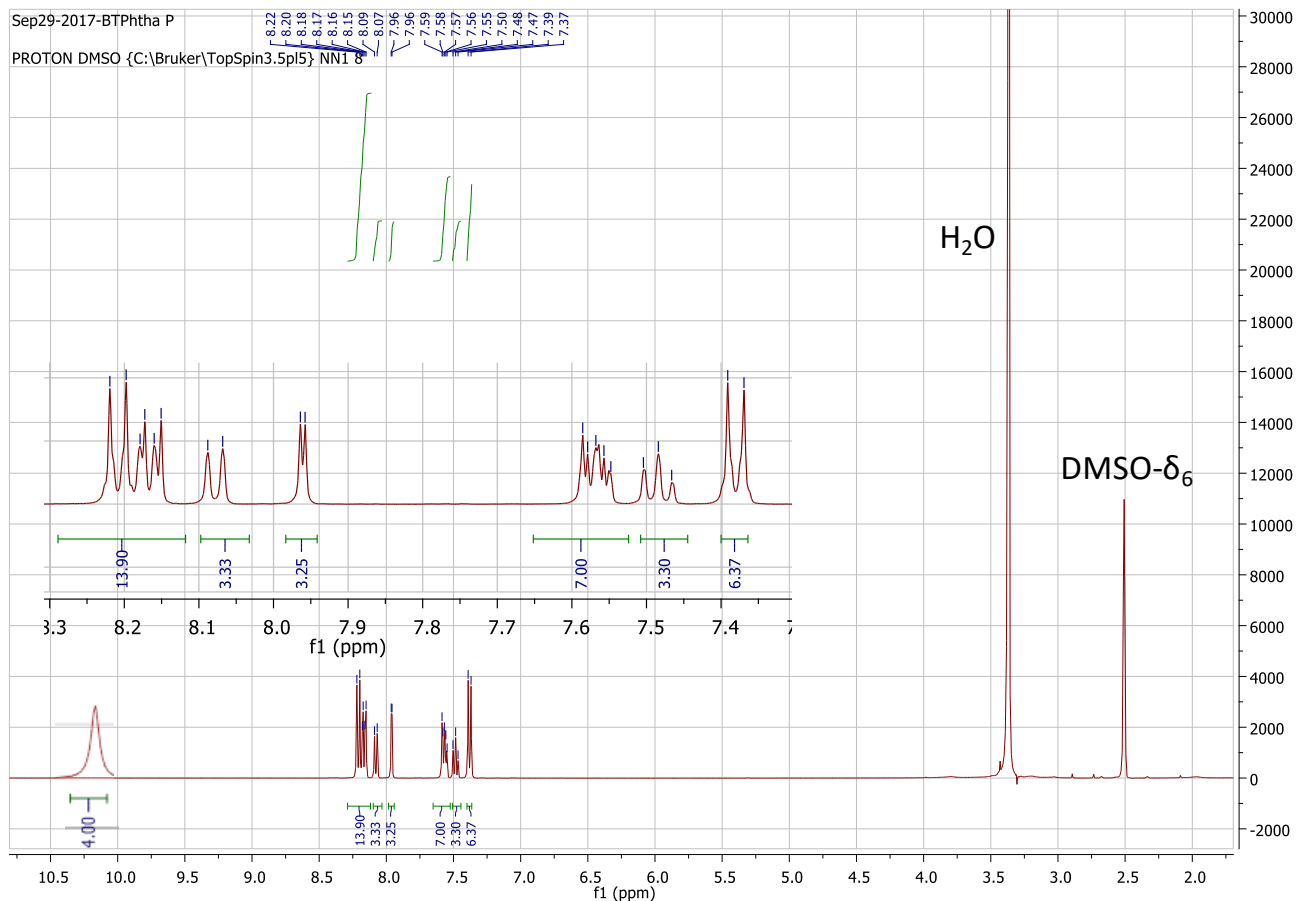
Figure A1: ^{1}NMR Spectrum of complex 11 in DMSO-δ$_6$ as a representative for 10-12 (insert, expanded section of aromatic proton between 8.22-7.39 ppm for clarity)

Appendix
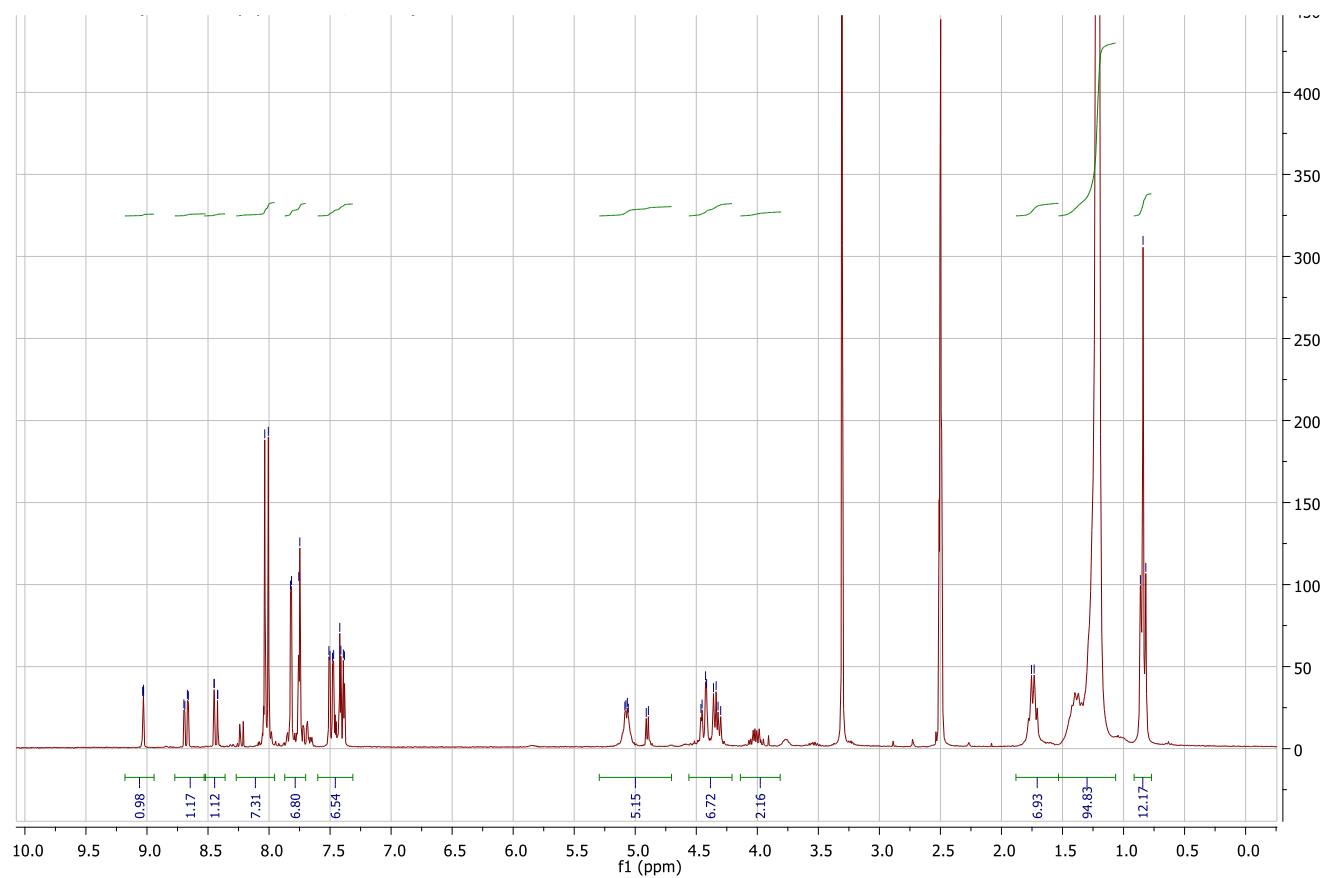
Figure A2: ¹NMR Spectrum of complex 15 in DMSO-δ₆ as a representative for 13-15

Appendix
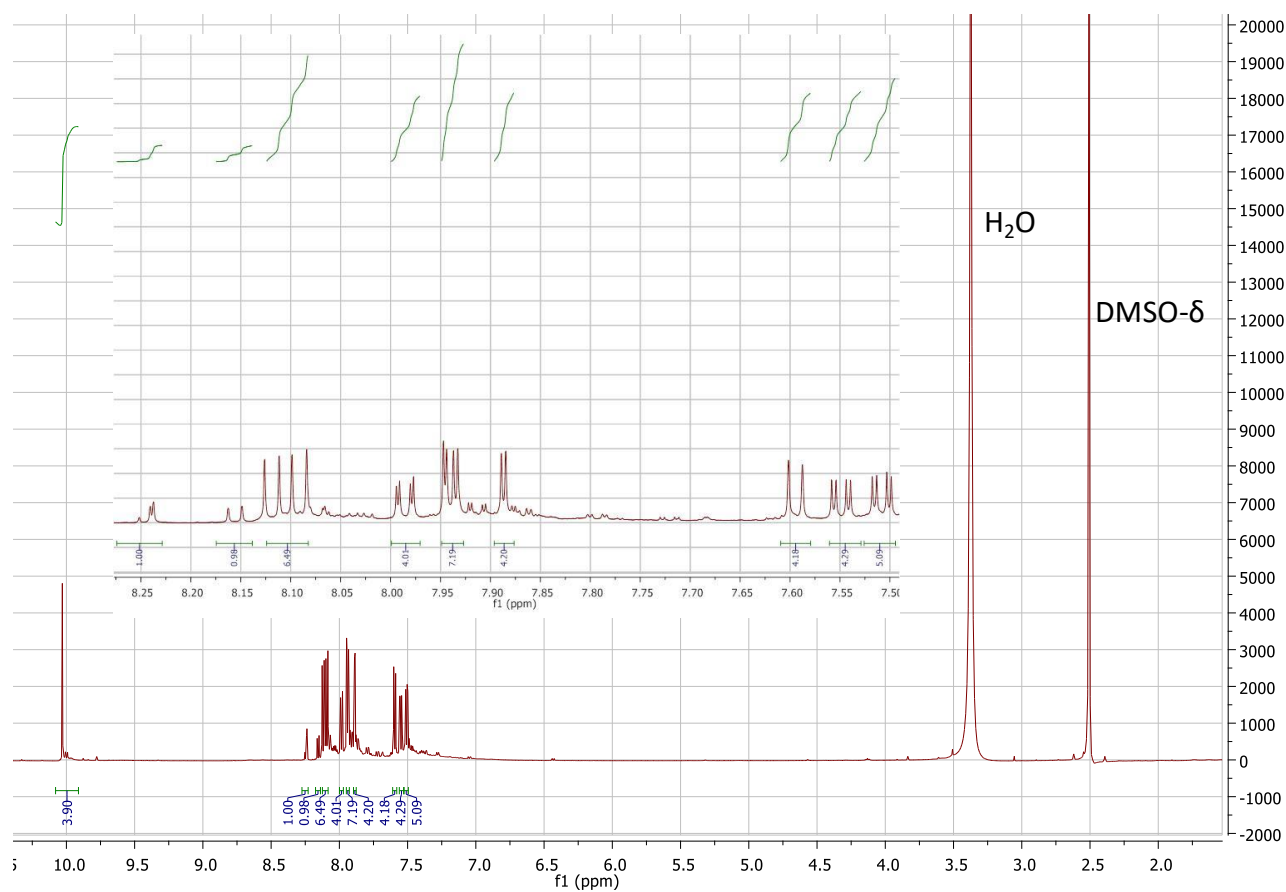
Figure A3: ¹NMR Spectrum of complex 16 in DMSO-δ₆ as a representative for 16-18

Appendix
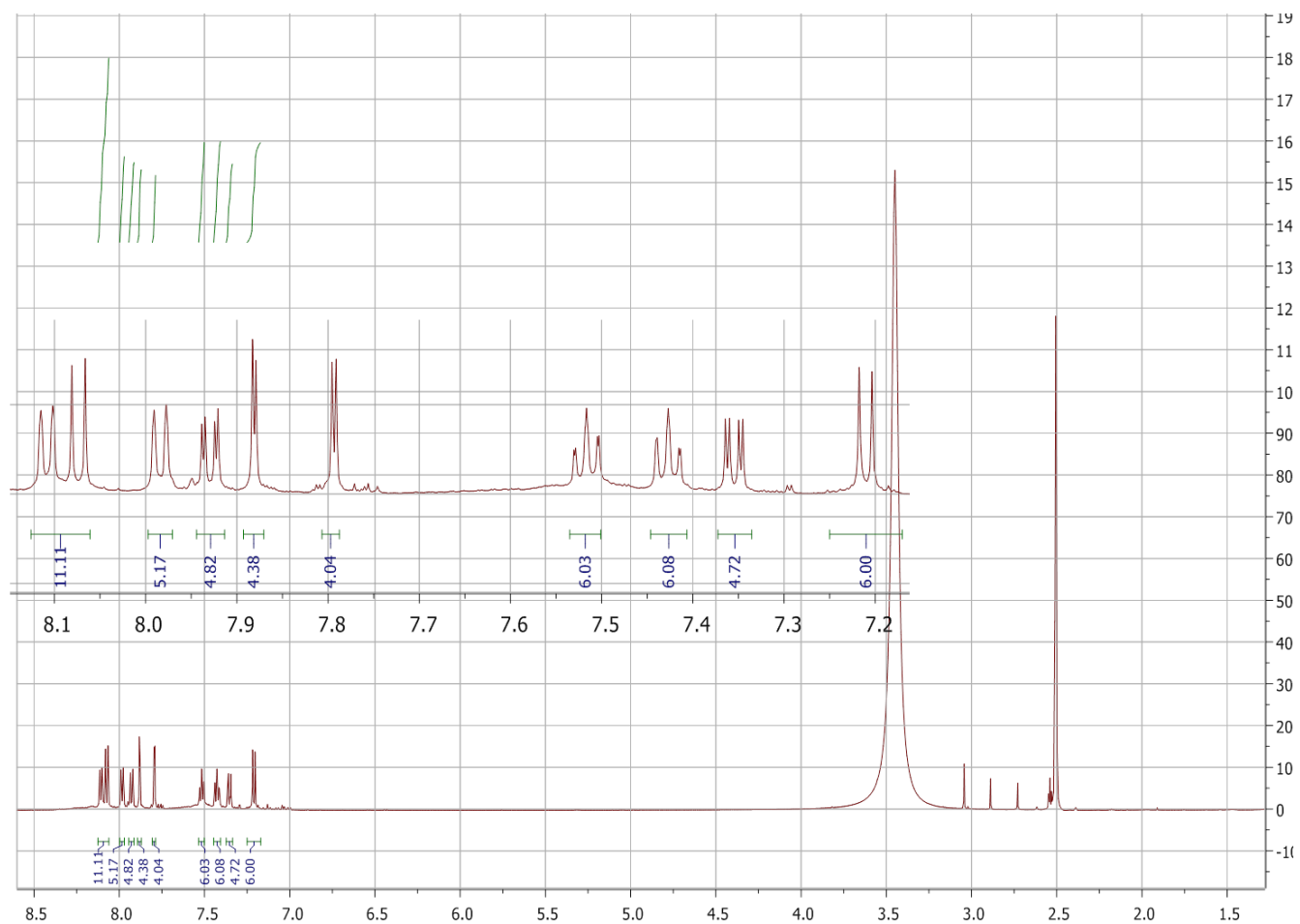
Figure A4: ^{1}NMR Spectrum of complex 19 in DMSO-δ_6 as a representative for 19-21

Appendix
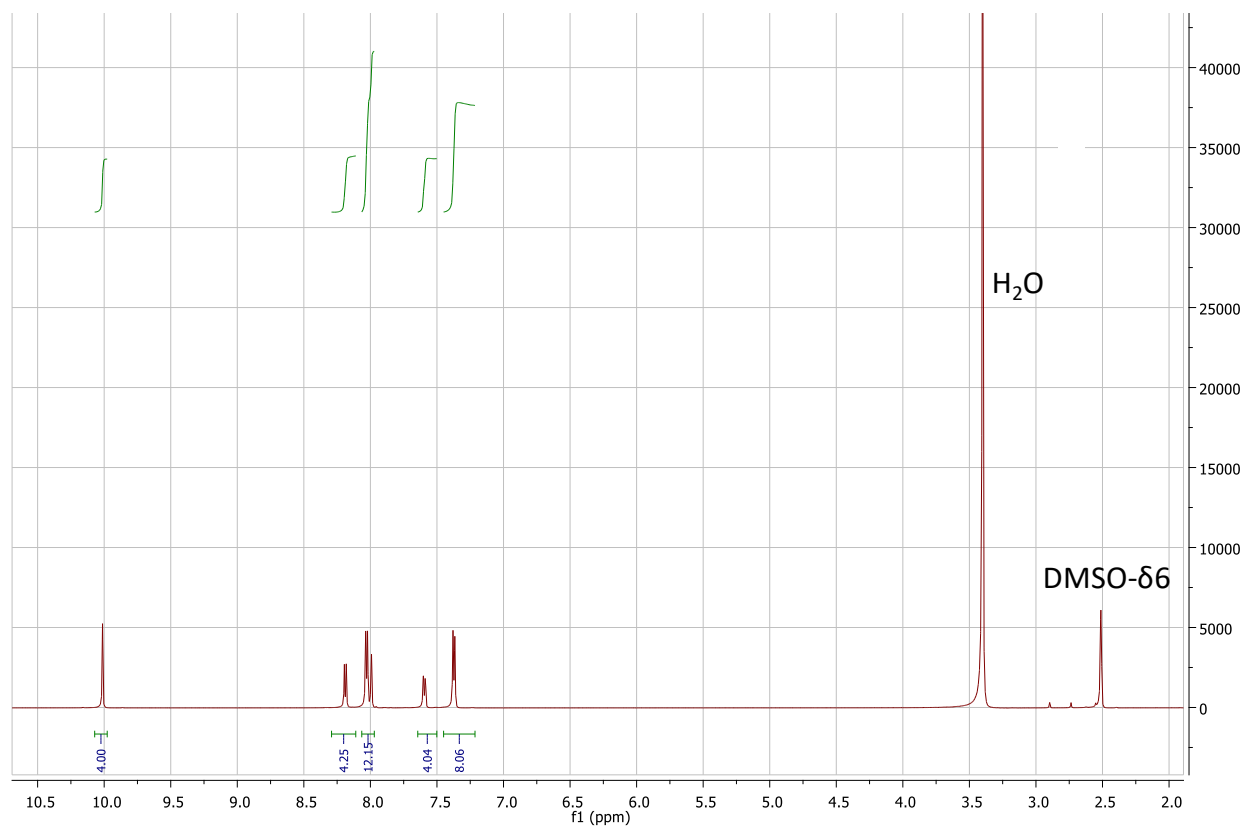
Figure A5: ^{1}NMR Spectrum of complex **28** in DMSO-δ$_6$ as a representative for **28-30**
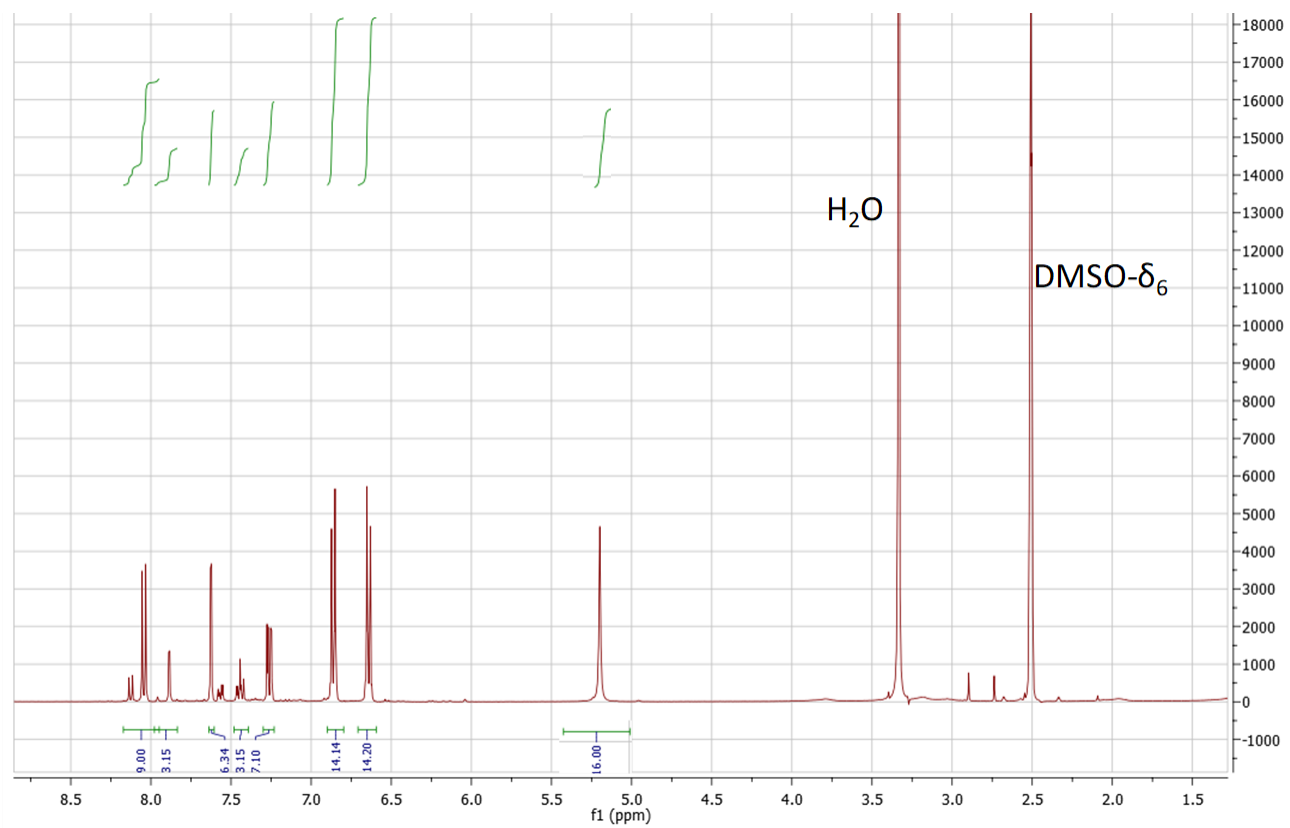
Figure A6: ^{1}NMR Spectrum of complex **32** in DMSO-δ_6 as a representative for **31-33**
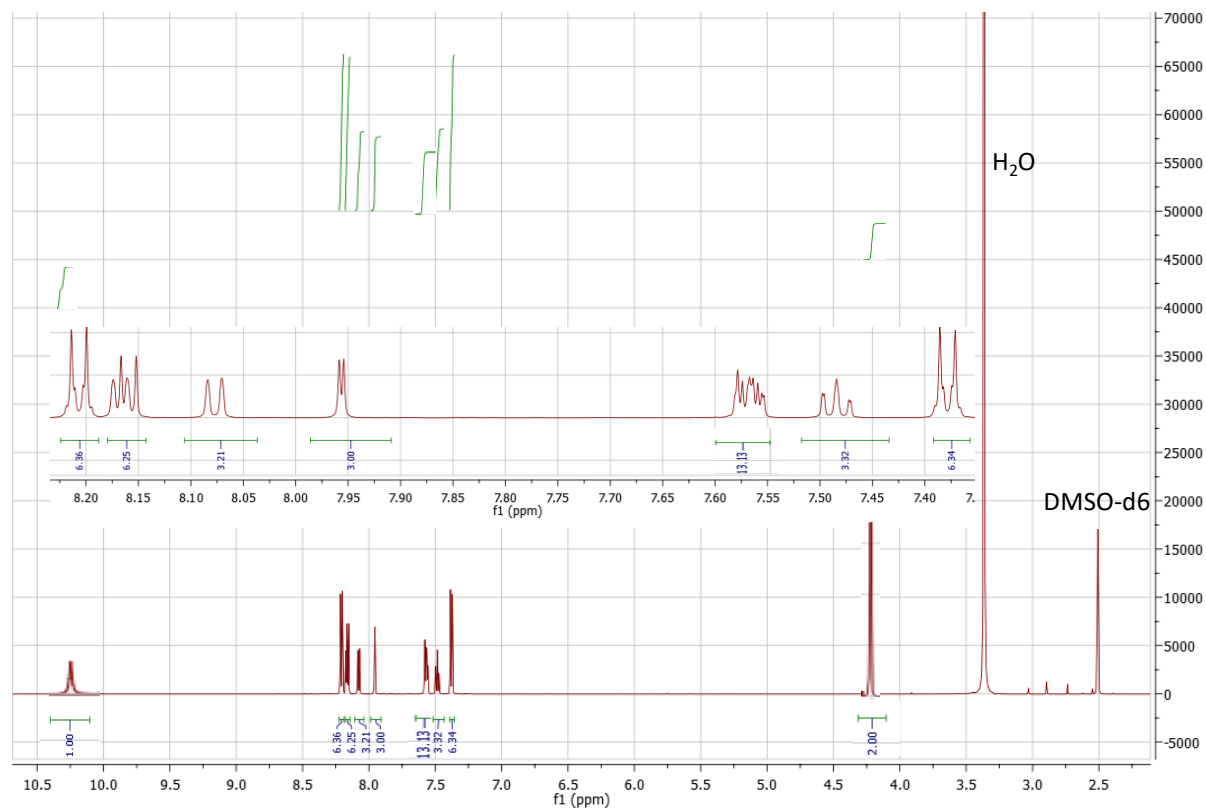
Appendix

Figure A7: ^{1}NMR Spectrum of complex 34 in DMSO-δ_6 as a representative for 34-36

Table A1: TD-DFT spectra of the B3LYP optimized geometries for the isomers of 13-15 with with four 3,3-position attachments calculated with the CAM-B3LYP functional and SDD basis sets.

13						
Band[a] #[b]		**Calc[c]**		**Exp[d]**		**Wave Function[e] =**
----	**1**	---- ---- ----		----	----	Ground State
Q	**4**	16.9 590 (0.65)		14.7 681		**89% $1a_{1u} \rightarrow 1e_g^*$**; …
	5	16.9 590 (0.65)		14.7 681		**90% $1a_{1u} \rightarrow 1e_g^*$**; …
B	**33**	32.0 312 (0.97)		28.7 348		**30% $1a_{2u} \rightarrow 1e_g^*$**; 26% $1b_{2u} \rightarrow 1e_g^*$; …
	34	32.1 311 (0.81)		28.7 348		**42% $1a_{2u} \rightarrow 1e_g^*$**; …
14						
Band[a] #[b]		**Calc[c]**		**Exp[d]**		**Wave Function[e] =**
----	**1**	---- ---- ----		----	----	Ground State
Q	**4**	16.8 594 (0.58)		14.3 697		**90% $1a_{1u} \rightarrow 1e_g^*$**; …
	5	16.8 594 (0.58)		14.3 697		**90% $1a_{1u} \rightarrow 1e_g^*$**; …
--	**18**	29.6 338 (0.05)		--- ---		**68% $1a_{2u} \rightarrow 1e_g^*$**; 13% $1b_{2u} \rightarrow 1e_g^*$; …
	19	29.6 338 (0.05)		--- ---		**68% $1a_{2u} \rightarrow 1e_g^*$**; 13% $1b_{2u} \rightarrow 1e_g^*$; …
--	**24**	31.4 319 (0.48)		--- ---		**38% $1a_{2u} \rightarrow 1e_g^*$**; 31% $2a_{2u} \rightarrow 1e_g^*$; …
	25	31.4 319 (0.48)		--- ---		**38% $1a_{2u} \rightarrow 1e_g^*$**; 31% $2a_{2u} \rightarrow 1e_g^*$; …
B	**33**	32.7 306 (0.59)		28.2 355		**31% $1a_{2u} \rightarrow 1e_g^*$**; 27% $1b_{1u} \rightarrow 1e_g^*$; 16% $2a_{2u} \rightarrow 1e_g^*$; …
	34	32.7 306 (0.59)		28.2 355		**31% $1a_{2u} \rightarrow 1e_g^*$**; 27% $1b_{1u} \rightarrow 1e_g^*$; 16% $2a_{2u} \rightarrow 1e_g^*$; …
--	**36**	32.9 304 (0.68)		--- ---		37% $2a_{2u} \rightarrow 1e_g^*$; 28% $1b_{1u} \rightarrow 1e_g^*$; **19% $1a_{2u} \rightarrow 1e_g^*$**; …
15						
Band[a] #[b]		**Calc[c]**		**Exp[d]**		**Wave Function[e] =**
----	**1**	---- ---- ----		----	----	Ground State
Q	**4**	16.4 611 (0.61)		14.2 705		**88% $1a_{1u} \rightarrow 1e_g^*$**; …
	5	16.4 611 (0.61)		14.2 705		**88% $1a_{1u} \rightarrow 1e_g^*$**; …
--	**18**	29.3 341 (0.08)		--- ---		**67% $1a_{2u} \rightarrow 1e_g^*$**; …
	19	29.3 341 (0.08)		--- ---		**67% $1a_{2u} \rightarrow 1e_g^*$**; …
--	**27**	30.8 325 (0.46)		--- ---		**34% $1a_{2u} \rightarrow 1e_g^*$**; 31% $2a_{2u} \rightarrow 1e_g^*$; …
	28	30.8 325 (0.46)		--- ---		**34% $1a_{2u} \rightarrow 1e_g^*$**; 31% $2a_{2u} \rightarrow 1e_g^*$; …
	31	31.5 317 (0.33)		--- ---		56% $2a_{2u} \rightarrow 1e_g^*$; …
--**B**	**32**	31.5 317 (0.33)		--- ---		56% $2a_{2u} \rightarrow 1e_g^*$; **12% $1a_{2u} \rightarrow 1e_g^*$**; …
	34	32.0 312 (1.21)		28.4 352		45% $2a_{2u} \rightarrow 1e_g^*$; **15% $1a_{2u} \rightarrow 1e_g^*$**; …

a − Band assignment described in the text. b − The number of the state assigned in terms of ascending energy within the TD-DFT calculation. c − Calculated band energies (10^3.cm^{-1}), wavelengths (nm) and oscillator strengths in parentheses (f). d − Observed energies (10^3.cm^{-1}) and wavelengths (nm) in **Figures 3.6,** e − The wave functions based on the eigenvectors predicted by TD-DFT. One-electron transitions associated with MOs associated with the four frontier π-MOs of Gouterman's 4-orbital model are highlighted in bold. The symmetry notations used refer to the D_{4h} symmetry of the parent monomeric complexes

Appendix

Table A2: TD-DFT spectra of the B3LYP optimized geometries for 34-36 calculated with the CAM-B3LYP functional and 6-31G(d) basis sets.

34						
Band[a]	**#[b]**	**Calc[c]**		**Exp[d]**		**Wave Function[e] =**
Q	1	16.2	616 (0.67)	14.7	680	**91% $1a_{1u} \rightarrow 1e_g$*;** …
	2	16.4	615 (0.60)			**91% $1a_{1u} \rightarrow 1e_g$*;** …
B	11	30.4	329 (0.67)	28.1	356	**31% $1a_{2u} \rightarrow 1e_g$*;** …
	16	30.9	323 (0.98)			**32% $1a_{2u} \rightarrow 1e_g$*;** …
35						
Band[a]	**#[b]**	**Calc[c]**		**Exp[d]**		**Wave Function[e] =**
Q	1	15.6	641 (0.61)	14.5	687	**92% $1a_{1u} \rightarrow 1e_g$*;** …
	2	15.7	637 (0.57)			**92% $1a_{1u} \rightarrow 1e_g$*;** …
B	40	30.9	341 (0.63)	27.3	366	**53% $2a_{2u} \rightarrow 1e_g$*;** …
	41	30.9	340 (0.52)			**52% $2a_{2u} \rightarrow 1e_g$*;** ……
36						
Band[a]	**#[b]**	**Calc[c]**		**Exp[d]**		**Wave Function[e] =**
Q	1	15.6	641 (0.61)	14.5	687	**92% $1a_{1u} \rightarrow 1e_g$*; 15% $1a_{2u} \rightarrow 1e_g$*;** …
	2	15.7	637 (0.57)			**92% $1a_{1u} \rightarrow 1e_g$*; 7% $1a_{2u} \rightarrow 1e_g$*;** …
B	10	29.3	342 (0.63)	27.3	366	53% **$1a_{2u} \rightarrow 1e_g$*;** …
	14	29.4	340 (0.52)			52% **$1a_{2u} \rightarrow 1e_g$*;** …

a − Band assignment described in the text. b − The number of the state assigned in terms of ascending energy within the TD-DFT calculation. c − Calculated band energies (10^3.cm^{-1}), wavelengths (nm) and oscillator strengths in parentheses (f). d− Observed energies (10^3.cm^{-1}) and wavelengths (nm). e − The wave functions based on the eigenvectors predicted by TD-DFT with one electron transitions associated with Gouterman's 4-orbital model highlighted in bold.